Experimental investigations of interactions between saltwater and ultramafic rocks in hydrothermal systems

Dissertation zur Erlangung des
Doktorgrades der Naturwissenschaften
am Fachbereich Geowissenschaften
der Universität Bremen

vorgelegt von

Heike Anders

Bremen, April 2012

Für Martin und meine drei Mädels.

Gutachter der Dissertation:

Prof. Dr. Wolfgang Bach

Prof. Dr. Reinhard X. Fischer

Prüfer:

Prof. Dr. Gerhard Bohrmann

Prof. Dr. Cornelia Spiegel

Tag der mündlichen Prüfung: 25. Juni 2012

Name: Heike Anders **Datum:** 24.04.2012

Anschrift: Am Deichschart 1b, 27751 Delmenhorst

Erklärung

Hiermit versichere ich, dass ich

1. die Arbeit ohne unerlaubte fremde Hilfe angefertigt habe,

2. keine anderen als die von mir angegebenen Quellen als Hilfsmittel benutzt habe und

3. die den benutzten Werken wörtlich oder inhaltlich entnommenen Stellen als solche kenntlich gemacht habe.

Bremen, den 24.04.2012

_____

(Unterschrift)

Danksagung

Einen großen Dank geht an meinem Doktorvater, Professor Dr. Wolfgang Bach, der mir die Möglichkeit gab diese Dissertation anzufertigen. Ohne seine Anleitung und Unterstützung wäre eine Fertigstellung meiner Arbeit nicht vorstellbar gewesen.

Herr Professor Dr. Reinhard X. Fischer danke ich für seine Tätigkeit als Zweitgutachter.

Niels Jöns danke ich für die Messungen an der Mikrosonde in Kiel sowie seiner unermüdlichen Geduld, mich in die Petrologie einzuführen. Er war stets ein geduldiger und kompetenter Ansprechpartner in vielen Dingen, insbesondere in der Endphase dieser Dissertation.

Für die Unterstützung bei der Durchführung meiner Experimente und bei den thermodynamischen Modellierungen bedanke ich mich ganz herzlich bei Michael Hentscher.

Bei allen Mitgliedern der Arbeitsgruppe „Petrologie der Ozeankruste“ möchte ich mich für das angenehme Arbeitsklima und für ihre stetige Hilfsbereitschaft bedanken.

Silvana Pape half mir bei der Analyse der Fluide. Michael Wendschuh führte die thermogravimetrischen und pulverdiffraktometrischen Messungen durch. Yu-Shi Lin und Eoghan Reeve unterstützten mich bei der Wasserstoff-Analytik. Petra Witte machte die Aufnahmen am Rasterelektronenmikroskop. Wolfgang Fulda und Mitarbeiter aus der Werkstatt des FB2, Biologie/Chemie, fertigten den Titanverschluss. Klaus Dehning und Mitarbeiter der Mechanischen Werkstatt vom MARUM – Zentrum für Marine Umweltwissenschaften waren stets hilfsbereit, wenn es um tatkräftige Mitwirkung ging. Ihnen allen danke ich sehr für die Unterstützung und Hilfsbereitschaft.

Abschließend bedanke ich mich besonders bei meiner Familie. Meinen Eltern und Schwiegereltern, die meine Kinder betreut haben. Martin, der mir in vielen Dingen den Rücken freigehalten hat und mir damit die Zeit gab, diese Arbeit fertig zu stellen. Ohne Martin wäre die hier vorliegende Arbeit nicht zustande gekommen. Lena, Mara und Lia die mich oft entbehren mussten und viel Verständnis zeigten.

Table of contents

Zusammenfassung

Zirkulation von Fluiden in ultramafischen Hydrothermalsystemen findet größtenteils an langsam spreizenden mittelozeanischen Rücken statt, wo durch tektonische Prozesse Meerwasser durch die ozeanische Kruste befördert wird. Dieses ist ein grundlegender Vorgang, der die chemische Zusammensetzung sowohl der ozeanischen Lithosphäre als auch der Hydrosphäre beeinflusst. In Bereichen des Meeresbodens, an denen Mantelperidotit aufritt, finden starke Wasser-Gesteins-Wechselwirkungen statt, durch die Olivin und Pyroxen hydratisiert werden. Die resultierenden Serpentingesteine bestehen hauptsächlich aus Serpentin und Magnetit. Bei diesem Prozess wird zweiwertiges Eisen in den Ausgangsmineralien unter Freisetzung von Wasserstoff zu dreiwertigen Eisen im gebildeten Magnetit oxidiert. Die Konzentrationen von Wasserstoff und Schwefelwasserstoff des interagierenden Fluides werden sowohl von der Mineralogie der Gesteine als auch von der Temperatur bei der Serpentinisierung gesteuert. Sulfide in serpentinisierten Peridotiten (z. B. Pentlandit, Pyrit, Godlevskit oder Heazlewoodit) sind potentielle Indikatoren für die Bedingungen der Serpentinisierungsreaktionen. Jedoch sind die Mineralreaktionen, die die Wasserstoffaktivität kontrollieren, noch wenig verstanden. Experimentelle Untersuchungen von sulfidischen Serpentinisierungs-Systemen können helfen, unser Verständnis für Sulfid-Phasenbeziehungen in natürlichen Systemen zu erweitern. Das Ziel dieser Forschungsarbeit ist, Wasser-Gesteins-Wechselwirkungen von ultramafischen Systemen zu simulieren und die Reaktionspfade, Wasserstoffbildung, Elementaustausch während des Reaktionsfortschrittes zwischen Gestein und Fluid, sowie die Bildung neuer Minerale zu untersuchen. Der Schwerpunkt liegt dabei auf Wasserstoff- und Schwefelwasserstoffaktivitäten sowie auf Änderungen in der Vergesellschaftung von Fe-Ni-S Mineralphasen, welches bisher noch nicht experimentell untersucht wurde. Für diesen Zweck wurde eine Hydrothermal-Apparatur entwickelt und in Betrieb genommen, welche die Beprobung von Fluiden während der Laufzeit eines Experiments erlaubt. Nachfolgend wurden vier Langzeit-Experimente von Wechselwirkungen zwischen Salzwasser und ultramafischen Gesteinen bei 320 °C und 400 bar durchgeführt: zwei identische Experimente mit Olivin, ein Experiment mit Orthopyroxen und ein Experiment mit Harzburgit zusammengesetzt aus 80 % Olivin und 20 % Orthopyroxen. In allen Experimenten wurden 30 Gramm Gesamtmineral mit 65 Gramm 3,2%-iger Natriumchloridlösung eingesetzt. Im Startmaterial aller

Experimente war synthetischer Pentlandit als Schwefelquelle enthalten. Die Lösungen wurden während der Experimente in regelmäßigen Abständen beprobt, um die chemische Entwicklung der Fluide zu beobachten. Die Startmaterialien Olivin und Orthopyroxen waren gut charakterisierte natürliche Minerale. Identifizierung und chemische Charakterisierung aller Reaktionsprodukte wurde durchgeführt mit potentiometrischer pH-Messung, Gaschromatographie, Ionenchromatographie, Fließinjektionsanalyse, photometrische Analyse, induktiv gekoppelte Plasma Atomemissions- sowie Massenspektrometrie für die Fluide und thermogravimetrische Analyse, Rasterelektronenmikroskop, Mikrosonde und Röntgendiffraktometrie für die Minerale. Zusätzlich wurden Fluid-Speziierungen und chemische Reaktionspfade mit der EQ3/6 Software berechnet. Phasendiagramme wurden mit der Software Geochemist`s Workbench® (GWB®) erstellt.

Magnetit bildete sich in allen vier Experimenten unter Wasserstoffbildung während fortschreitender Reaktion. Weitere Reaktionsprodukte von Olivin sind Chrysotil und Bruzit. Das Orthopyroxen-Experiment bildete Magnetit, Chrysotil und Talk, während im Harzburgit-Experiment nur Chrysotil und Magnetit entstanden sind. Das Olivin-Experiment erreichte den höchsten pH-Wert der Reaktionslösung, obwohl die Konzentrationen an gelösten SiO_2 und Magnesium viel niedriger waren als in den Orthopyroxen-Experimenten. Die durch Modellierungen vorhergesagten Phasenbeziehungen sind in guter Übereinstimmung mit den Experimenten. Ein beachtenswertes Ergebnis dieser Arbeit war, dass im Harzburgit-Experiment der Orthopyroxen viel schneller reagierte als der Olivin, was durch die Abwesenheit von Bruzit gezeigt wurde. Außerdem reagierte der Orthopyroxen im Olivin-Experiment schneller als in dem Experiment ohne Olivin. Offenbar ist die Reaktionsgeschwindigkeit von Orthopyroxenen stark erhöht in Olivin-führenden Gesteinen. Dieses Ergebnis deutet darauf hin, dass der große Unterschied der Kieselsäureaktivität von Orthopyroxen und Olivin der maßgebende Schlüssel ist, um die gesamte Reaktionsrate zu bestimmen. Gesteinszusammensetzungen, insbesondere (Mg+Fe)/Si-Verhältnisse, spielen eine große Rolle bei der Wasserstoffbildung. Die vorhergesagten Mg-Fe-Verhältnisse in den Sekundärmineralen unterscheiden sich geringfügig von den gemessenen Zusammensetzungen, was zu Unterschieden in der Wasserstoffbildung zwischen Vorhersagen und Experimenten führt.

Thermogravimetrische Analysen von Gehalten an Bruzit und Serpentin zusammen mit Mineralanalysen erlauben eine verbesserte Abschätzung der Wasserstofferzeugung.

Vorhergesagte und beobachtete Wasserstofferträge stimmen allgemein miteinander überein und zeigen, dass der theoretische Rahmen zu Vorhersagen von Wasserstoffproduktionen während der Serpentinisierung schlüssig ist. Die Zunahme von Wasserstoff mit fortschreitender Serpentinisierung treibt die Zersetzungsreaktion des ursprünglichen Pentlandits voran. Neben Spuren von übrig gebliebenen Pentlandit wurden metastabiler Ni-reicher Pentlandit und Heazlewoodit als Sulfide in dem Olivin-Experiment gefunden. Der Pentlandit im Orthopyroxen- und Harzburgit-Experiment zeigte aufgrund der kürzeren Laufzeiten der Experimente nahezu keine Reaktionen. Thermodynamisch basierte Vorhersagen der Stabilitäten von Sulfiden sagen Heazlewoodit und Godlevskit voraus und deuten an, dass Ni-reicher Pentlandite metastabil ist.

Abstract

Fluid circulation in ultramafic-hosted hydrothermal systems occurs mostly at slow-spreading mid-ocean ridges, where tectonic processes promote fluid ingress into the crust. This is a fundamental process that impacts transfer of energy and affects the chemical composition of both the ocean lithosphere and the hydrosphere. The presence of outcrops of mantle peridotite at the seafloor allows for intense fluid-rock interaction, during which primary olivine and pyroxene are hydrated. The resulting serpentinite rocks consist mainly of serpentine and magnetite. Oxidation of divalent iron primary minerals to trivalent iron in secondary magnetite results in the release of hydrogen. Levels of H_2 (aq) and H_2S (aq) of the interacting fluid are controlled by the mineralogy of the reacting rocks as well as the temperature of serpentinization. Sulfides present in serpentinized peridotites (e.g., pentlandite, pyrite, godlevskite or heazlewoodite) are potential indicators for the serpentinization conditions. However, the mineral reactions that control hydrogen activity are not well understood. Experimental investigations of sulfide-bearing serpentinization systems can help further our understanding of the sulfide phase relations at temperature conditions relevant for natural systems. The purpose of the research presented in this dissertation is to simulate fluid-rock interactions in ultramafic-hosted systems and to investigate reaction pathways, hydrogen generation, elemental exchange during reaction progress between rock and fluid, and formation of alteration minerals. The focus lies on the activities of H_2 (aq) and H_2S (aq) and changes in the assemblages of Fe-Ni-S mineral phases, which had never been tested by experimental work prior to this study.

For this purpose, a hydrothermal apparatus allowing fluid sampling during an experiment was developed and constructed. Subsequently, four long-term experiments of interactions between saltwater and ultramafic rocks were carried out at 320 °C and 400 bar: two identical experiments with olivine, one experimental run with orthopyroxene and one experiment with harzburgite composed of 80 wt. % olivine and 20 wt. % orthopyroxene. In all experiments, 30 grams of total mineral were reacted with 65 gram of sodium chloride solution (3.2 wt. %). The starting material of all experiments contains synthetic pentlandite ($Fe_{4.5}Ni_{4.5}S_8$) as sulfur source to investigate phase relations in the Fe-Ni-O-S system. Samples of the solutions were retrieved during the experiments to monitor the chemical evolution of the fluid. Olivine and orthopyroxene used as starting material were well-characterized natural minerals.

Identification and chemical characterization of secondary reaction products (minerals and fluids) was done using potentiometric pH measurement, gas chromatography, ion chromatography, flow injection analysis, photometric analysis, inductively coupled plasma atomic emission spectroscopy, inductively coupled plasma mass spectrometry for the fluids and thermogravimetric analysis, scanning electron microscope, electron microprobe and X-ray diffraction for the minerals. In addition, fluid speciation calculations and chemical reaction path modeling was performed using the EQ3/6 code; phase diagrams were constructed with Geochemist`s Workbench® (GWB®).
Magnetite formed as secondary mineral in all four experiments and substantial amounts of hydrogen were generated during reaction progress. Chrysotile and brucite formed as additional reactions products after olivine. The orthopyroxene experiment produced chrysotile and talc in addition to magnetite, while only chrysotile and magnetite were produced in the harzburgite experiment. The pH attained the highest level in the olivine experiments, while dissolved SiO_2 and magnesium concentrations were much lower than in the orthopyroxene experiments. The predicted silica-dependent phase relations are in good agreement with experimental findings. However, a remarkable finding of this study was that orthopyroxene in the harzburgite reacted much faster than olivine, as indicated by the absence of brucite. It also reacted much faster than the orthopyroxene in the experiment that was lacking olivine. Apparently, the reaction rate of orthopyroxene is strongly increased in rocks that also contain olivine. This result suggest that the strong contrasts in silica activity between orthopyroxene and olivine is key in controlling the overall reaction rates.
Rock compositions, especially (Mg+Fe)/Si-ratios, also play an important role in hydrogen generation. The predicted Mg-Fe-ratios in the secondary minerals differ slightly from measured compositions and this results in differences in hydrogen generation between predictions and experiments. Thermogravimetric analysis of brucite and serpentine abundances combined with mineral analysis allows improved estimation of hydrogen generation. Overall, predicted and observed hydrogen yields correspond to each other, indicating that the theoretical framework for predicting hydrogen production during serpentinization is sound. Build-up of hydrogen in the course of progressive serpentinization drives break-down reactions of the primary pentlandite. Besides traces of relict pentlandite, metastable Ni-rich-pentlandite and heazlewoodite were found as sulfides in the olivine experiments. The pentlandite in the orthopyroxene and harzburgite experiment was nearly unreacted owing to the shorter experimental run

time. Thermodynamic predictions of sulfide stability predict heazlewoodite and godlevskite, suggesting that the Ni-rich-pentlandite is metastable.

1. Introduction

1.1 Motivation

Interaction of seawater with rocks from the oceanic lithosphere in the course of hydrothermal circulation is a major factor influencing global thermal and geochemical budgets (e.g., Mottl and Wheat, 1994; Stein and Stein, 1994). The chemical composition of both the oceanic lithosphere and the seawater is affected by this process (Janecky and Seyfried, 1986; Allen and Seyfried, 2003; Bach et al., 2004). Hydrothermal rock interaction occurs in a variety of tectonic settings, such as along spreading centers, in back-arc basins, at seamounts, subduction zones and submerged island-arcs (Fig. 1.1). These settings feature distinct boundary conditions for hydrothermal circulation. Most mid-ocean ridge vent fields are hosted in basalt. Fluids venting at the seafloor are relatively oxidizing and acidic (pH 3 to 5). In felsic rock-hosted systems, which are found in submerged island-arc volcanoes, back-arc basins and rifted arcs, oxidizing conditions with a pH ≤ 1 to 3 prevail. Finally, peridotite-hosted systems, which are the topic of this study, occur where ultramafic mantle rocks are exposed along slow- and ultraslow spreading mid-ocean ridges. When these ultramafic rocks (e.g., harzburgite, lherzolite or dunite), undergo serpentinization as a consequence of infiltrating seawater at temperatures < 400 °C (e.g., Mével, 2003), the resulting fluids are characterized by enriched S and metals (e.g., Cu, Fe, Mn, Zn) and high hydrogen and methane concentrations. Serpentinites, the alteration products of peridotite alteration, consists dominantly of serpentine-group minerals (e.g., lizardite, chrysotile). Further alteration phases include magnetite and brucite, but also talc, hematite, chlorite and others are occasionally observed (e.g., Cannat et al., 1992; Mével, 2003; Bach et al., 2004). Additionally, sulfide assemblages and Ni-Fe alloys occur as accessories in serpentinites (Dick, 1974; Albertsen et al., 1978; Frost, 1985). During the past decades, researchers have shown increased interest in the process of serpentinization, which is found to be fundamental importance: it dramatically changes physical and chemical properties of the host rocks (e.g., rheological, magnetic susceptibility, gravimetry and seismic velocities (e.g., Oufi and Cannat, 2002; Mével, 2003). Compared to unaltered peridotites, serpentinites have a high magnetic susceptibility and a low density. The drop in density causes a volume expansion of the peridotites, which affects the permeability (e.g., O'Hanley, 1992). Apart from properties of the rocks, fluids discharged from ultramafic-hosted hydrothermal systems are highly

enriched in hydrogen and methane, show reducing conditions and a large pH range from 3 to 12 (Douville et al., 2002; Allen and Seyfried, 2003; Frost and Beard, 2007; McCollom and Bach, 2009). Water is reduced to dihydrogen (H_2), driven by the oxidation of ferrous iron (Fe^{2+}) in primary minerals to ferric iron (Fe^{3+}) in secondary minerals. Methane and other hydrocarbons are formed by the reduction of dissolved inorganic carbon (CO, CO_2, HCO_3^-, and CO_3^{2-}). In natural hydrothermal systems also sulfur- and nitrogen-bearing reactants (e.g., NH_3, H_2S etc.) might also play a role and potentially contribute to formation of a variety of organic compounds (e.g., Hennet et al., 1992; Yanagawa and Kobayashi, 1992; Marshall, 1994; Heinen and Lauwers, 1996; Rushdi and Simoneit, 2005). High concentrations of hydrogen and methane strongly influence the nature of the fauna associated with ultramafic-hosted hydrothermal system. Hydrogen acts as a source of energy and electrons for a wide range of chemosynthetic organisms (e.g., Perner et al., 2007; Petersen et al., 2011) in the deep sea, where light is absent and photosynthetic life thus not possible. Communities of chemolithoautotrophic microorganisms have been found in surface and subsurface seafloor environments at ultramafic hosted hydrothermal systems (Takai et al., 2004; Kelley et al., 2005; Alt et al., 2007; McCollom and Seewald, 2007). These systems can be viewed as potential analogs for early ecosystems on earth. Because the rock compositions in ultramafic-hosted systems are similar to komatiite lava flows that were abundant on the early earth, it is proposed that the first life on earth developed in submarine hydrothermal systems via abiotic synthesis of organic compounds (e.g., Chapelle et al., 2002; Takai et al., 2004; Schulte et al., 2006; Martin and Russell, 2007; Martin et al., 2008;).

Numerous field studies dedicated to deciphering serpentinization processes have been carried out (Cannat et al., 1992; Bach et al., 2006; Paulick et al., 2006), but the interrelations between peridotite alteration processes and associated compositions of intergranular fluids cannot be faithfully reconstructed solely by petrological methods. Various stages of alteration at different temperatures and across a wide range of fluid compositions occur in these processes. Thermodynamic reaction path models for interactions of aqueous fluids with ultramafic rocks can be applied to understand the influence of pressure, temperature, water-to-rock ratio and hydrogen formation (e.g., Klein and Bach, 2009; Klein et al., 2009; McCollom and Bach, 2009). These models are suited to make predictions, but uncertainties in thermodynamic and kinetic data restrict their use in understanding serpentinization in natural systems. The ability to examine

the state of equilibrium in mineral-fluid reactions is a pre-requisite for all these theoretical studies. Experimental investigations of water-rock interactions are useful in assessing changes in fluid compositions linked to the mineral alteration processes. The variations observed under controlled conditions are measurable and can be compared with predicted equilibrium conditions to help understand the reaction mechanisms involved in the rock transformation. To date, only few hydrothermal experiments simulating subseafloor serpentinization reactions were performed (Moody, 1976; Janecky and Seyfried, 1986; Berndt et al., 1996; Allen and Seyfried, 2003; Seyfried et al., 2007). Detailed knowledge of the reaction mechanisms and mineralogical changes during serpentinization is still lacking. Further experimental investigations of water-rock interactions are needed to help furthering our understanding of serpentinization. In this work, experiments simulating subseafloor serpentinization reactions were carried out. The specific focus was on investigation of the fate of primary sulfides in the course of serpentinization. Theoretical work (Frost, 1985; Klein and Bach, 2009) predicts specific changes in the assemblages of Fe-Ni phases as the extent of serpentinization increase. Prior to this study, these predictions were never tested by experimental work. Compositions of primary and altered minerals were determined and time series changes of fluid composition were monitored. The experimental data in terms of fluids and mineral compositions were compared to predicted results from theoretical geochemistry and with those observed in field studies. This study was aimed at making specific use of solution chemistry data and comprehensive characterization of the solid reaction product to contribute to a better understanding of the conditions and mass transfer processes during serpentinization.

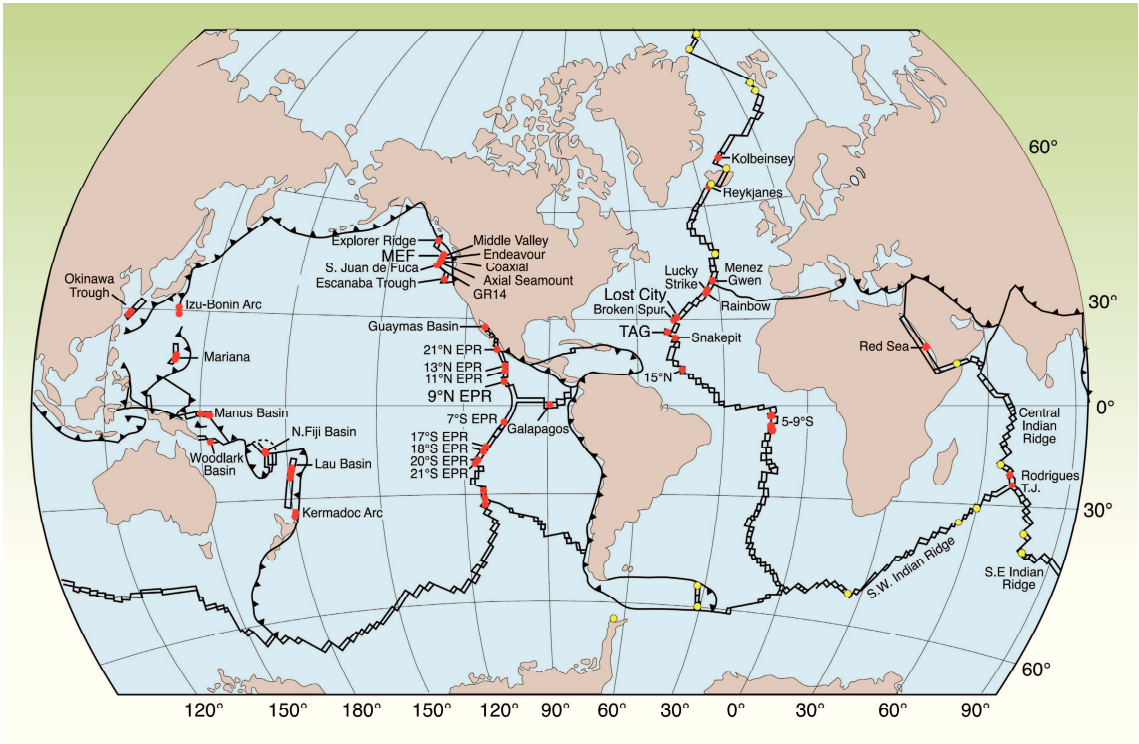

Fig. 1.1. Map of known hydrothermal vent systems along mid-ocean ridges, in back-arc basins, rifted arcs and at submerged island-arc volcanoes (red), and areas of activity as indicated by mid-water chemical anomalies (yellow). EPR = East Pacific Rise. TAG = Trans Atlantic Geotraverse, MEF = Main Endeavour Field, and GR-14 = Sea Cliff hydrothermal field on the northern Gorda Ridge. Figure taken from Tivey, 2007, Oceanography, Vol. 20, No.1, page 51. Figure after Baker et al., 1995; German and Von Damm, 2004; Hannington et al., 2005; Koschinsky et al., 2006.

1.2 Course of the PhD project

This project was divided into three phases. First an apparatus on the laboratory scale for the simulation of geochemical reactions under hydrothermal conditions was established. The apparatus was built from a high-pressure autoclave, a hydraulic unit used as pump and a heater arrangement to set the desired pressure-temperature-conditions. The reactions to be investigated took place in a flexible gold-cell with an attached titanium valve for sampling the fluid (Seyfried, 1979; see Fig. 2.1 in chapter 2 “Experimental setup”). In the second phase, several long-term serpentinization experiments with olivine, orthopyroxene, a mixture of olivine and orthopyroxene (representative of harzburgite composition) in artificial sodium chloride solution were executed. Synthetic pentlandite was added to all experiments to investigate the fate in the course of serpentinization. The primary mineral compositions were characterized by X-ray-

powder diffraction and electron microprobe analyses. Samples of the reacted fluid were taken periodically throughout the experimental run-time. Hydrogen concentrations and pH were determined immediately after sampling and further aliquots of the fluid were prepared for later analyses of cations, anions, ammonium and hydrogen sulfide. At the end of the experiments the reaction products were examined using X-ray powder diffraction (XRD), electron microprobe analyses (EPMA), scanning electron microscope (SEM), thermogravimetric analyses (TG) and magnetic susceptibility measurements. Also tests for the useability of the hydrothermal apparatus in experiments with rare earth elements distribution in hydrothermal fluids were carried out. In the last phase of this study the data obtained were compared with theoretical predictions of reaction pathways during serpentinization and with those observed in field studies in natural samples. Calculated mineral stabilities were compared with experimental results.

2. Experimental setup

2.1 Introduction

The principal aim of this work is carrying out simulations of geochemical reactions under hydrothermal conditions. The first step was the development and construction of the experimental apparatus. Hydrothermal reactions occur under extreme conditions of temperature and pressure at seafloor depth in the oceans. As hydrothermal fluids are high corrosive, the required facilities have to be sufficient inert to be suitable for the desired experiments and, in addition, contaminations of the run products have to be avoided. Periodic sampling and monitoring of the reaction in progress must be possible. Besides, reliability and convenience in handling, operational safety is an important criterion.

There are two different autoclave systems for hydrothermal experiments: the fixed-volume system and the flexible reaction cell system (Ulmer and Barnes, 1987). In the fixed-volume system, the starting materials (water and rock) are filled directly in an autoclave bomb with a constant internal volume. The system is then heat and pressure in the constant volume autoclave builds up as the water expands. The disadvantage of this system is that the experimentalist cannot choose pressure and temperature independent of each other. Also, the hydrothermal fluids are in contact with the inner surface of the pressure bomb, so that corrosion may be a problem and must be considered. For the experiments in this study the construction of the flexible reaction cell system was realized, because pressure and temperature can be chosen freely within the certified pressure-temperature range and the materials reside in an inert flexible gold bag and are not exposed to the inner surface of the steel autoclave.

2.2 History of flexible reaction cell systems

Dickson et al. (1963) designed an apparatus for hydrothermal experiments with a deformable reaction cell fitted in a pressure bomb and encased by pressurized water. The deformable sample cell is sealed and the inner is completely separated from the pressurized water in the pressure vessel. A tube connects the reaction cell to a valve, which allows for sampling of fluid while the experiment runs. Fluid samples could be taken at regular intervals by wringing off the deformation cell with the pressure of the

surrounding water. The internal pressure of the flexible reaction cell is equal to the outer pressurized water in the bomb, because the shape of the sample cell changes in response to the pressure of the surrounded water in the autoclave. The deformable reaction cell was made of polytetrafluorethylene resin (Teflon®). Teflon® is flexible and chemically inert, but its mechanical properties degrade above 260 °C. Furthermore, Teflon® is permeable to gases such as carbon dioxide, hydrogen sulfide and others, and high temperatures tend to increase this permeability. To overcome the problems of Teflon®, reaction cells made of gold were developed (Rytuba and Dickson, 1974). The handling of this gold cell is inconvenient. Subsequent to an experiment the cell is cut and re-sealed after removing the reactants. Every time the volume of the cell decreases and the procedure is time consuming. In later years, Seyfried (1979) have designed a new reaction cell for hydrothermal experiments which uses a commercial available pressure vessel in combination with a reaction cell consisting of gold and a resealable titanium closure (see Fig. 2.1). This system is still state-of-the art and is used in numerous labs around the world (e.g., Berndt et al., 1996; McCollom and Seewald, 2003; Seyfried et al. 2007). It was also the prototype for the system built in the course of this thesis.

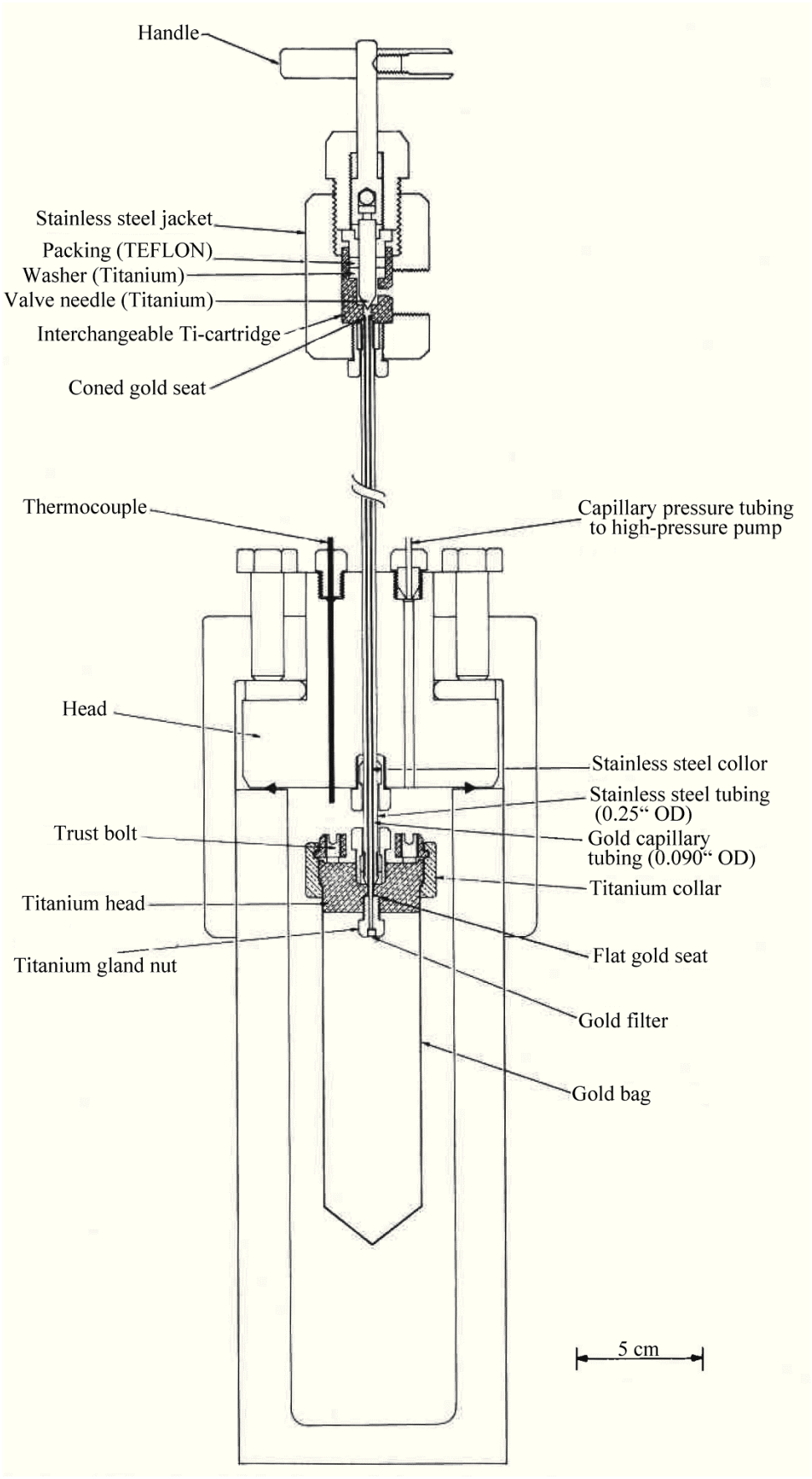

Fig. 2.1. Schematic illustration of experimental equipment with a gold-titanium reaction cell (Seyfried, 1979). Prototype for the system built in the course of this thesis.

2.3 Configuration of the experimental apparatus

2.3.1 High pressure bomb

A commercially available high-pressure and high-temperature vessel was purchased from Parr Instrument Company. The maximum pressure and temperature for this vessel are 565 bar at 400 °C. The cylindrical vessel is made of stainless steel T316 with an inner volume of 335 ml, an inside diameter of 50.8 mm and an inside height of 165.1 mm (see Fig. 2.2). The pressure vessel is equipped with a split ring closure. Two hardened steel split ring halves are clamped around the head and cylinder flanges with eight cap screws. A flat O-ring gasket is positioned between the cylinder and the head of the vessel. The material of the O-ring gaskets is variable depending on the maximum working temperature. For this work a flexible form of graphite (Grafoil®) was used. Graphite is a high temperature sealing material with practical unlimited temperature range and has a good corrosion resistance as well. Before the vessel was sealed by tightening the compression bolts, a metal compression ring (drop band) was attached around the split ring halves to lock their position. The bolts in the split ring halves have to be well-lubricated to avoid seizing. The compression bolts were tightened crosswise in small increments with a torque wrench to an intensity depending on the type of gasket.

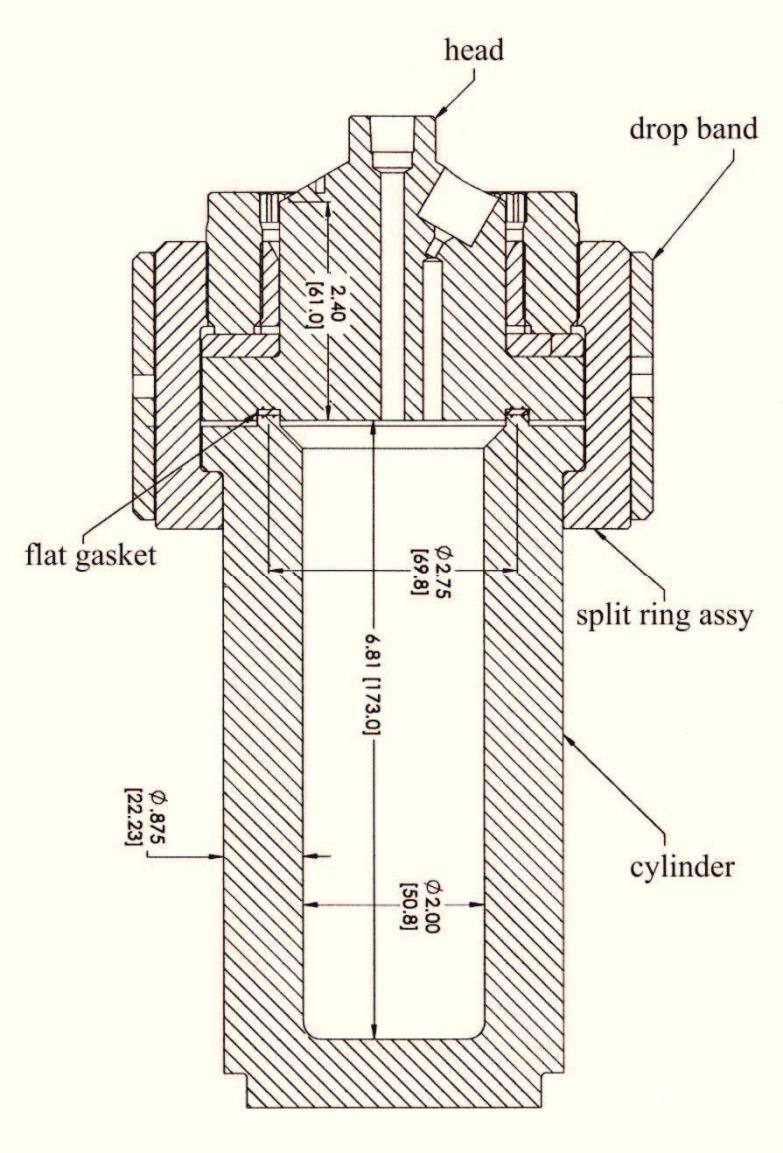

Fig. 2.2. Schematic drawing of the high-pressure and high-temperature vessel assembly (up to 565 bar at 400 °C). Figure is based on the original technical drawing of Parr Instrument Company. Values are in inches and values in brackets are in millimeters. The head openings are not all shown in this figure (all head openings are shown in Fig. 2.3)

The head of the pressure vessel contains various openings to insert a thermo couple and to connect a pump, a pressure gauge and a safety rupture disc. The opening in the middle of the head is for sealing the sample titanium tube to the gold reaction cell (see Fig. 2.3).

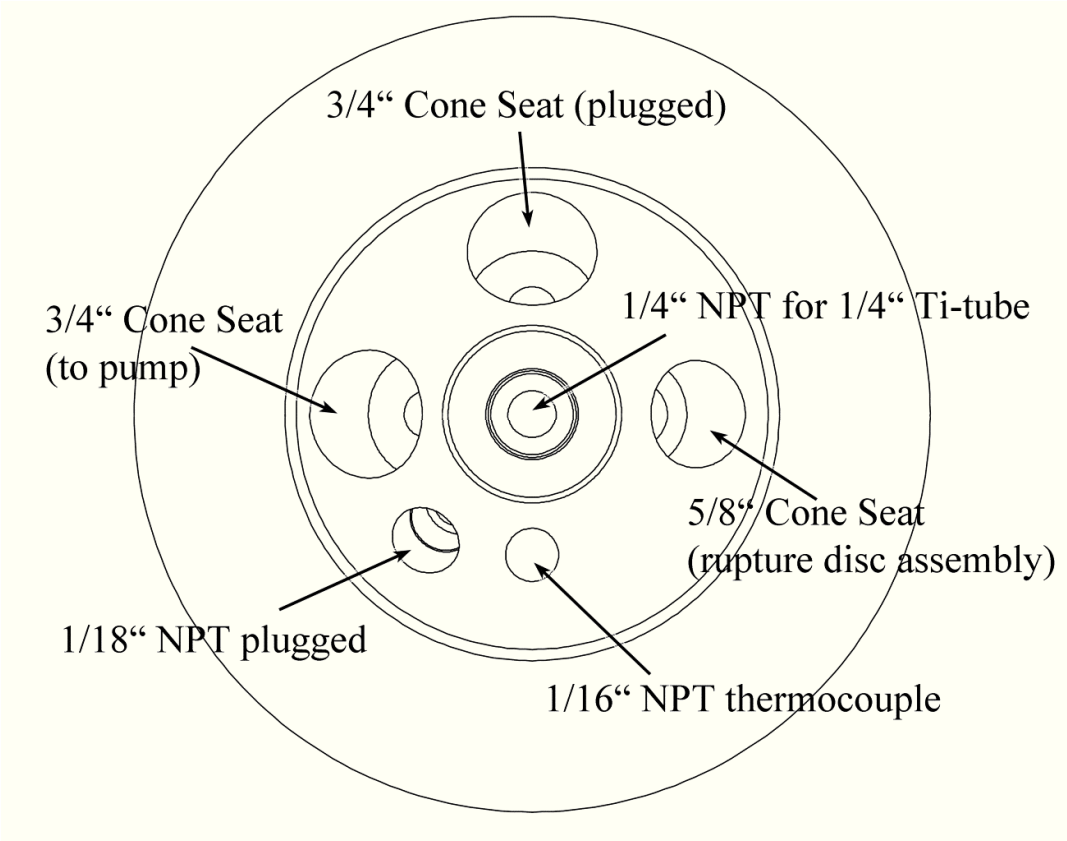

Fig. 2.3. The openings in the head of the pressure vessel are shown. Schematic illustration based on the original technical drawing of Parr Instrument Company. Abbreviation NPT = National Pipe Thread (U.S. standard for tapered threads). Values are in inches.

2.3.2 Heater arrangement

The well-tightened pressure vessel is placed in a heater arrangement (Fig. 2.4). Two electric band heaters are embedded in a ceramic body which is held within an insulated metal housing. The ceramic body is suitable shaped for the pressure vessel cylinder and a formed isolation made of Dotherm® 1100 (a calcium silicate material with carbon fiber reinforcement) covers the pressure vessel in the heater arrangement. A proportional-integral-derivative controller (PID controller) regulates the temperature during the experiment. The temperature is measured with a thermocouple positioned inside of the pressure vessel. The readout and setpoint resolution of the controller is 1 °C and the system accuracy is ± 2 °C. The controller is equipped with a lockout relay for over temperature protection.

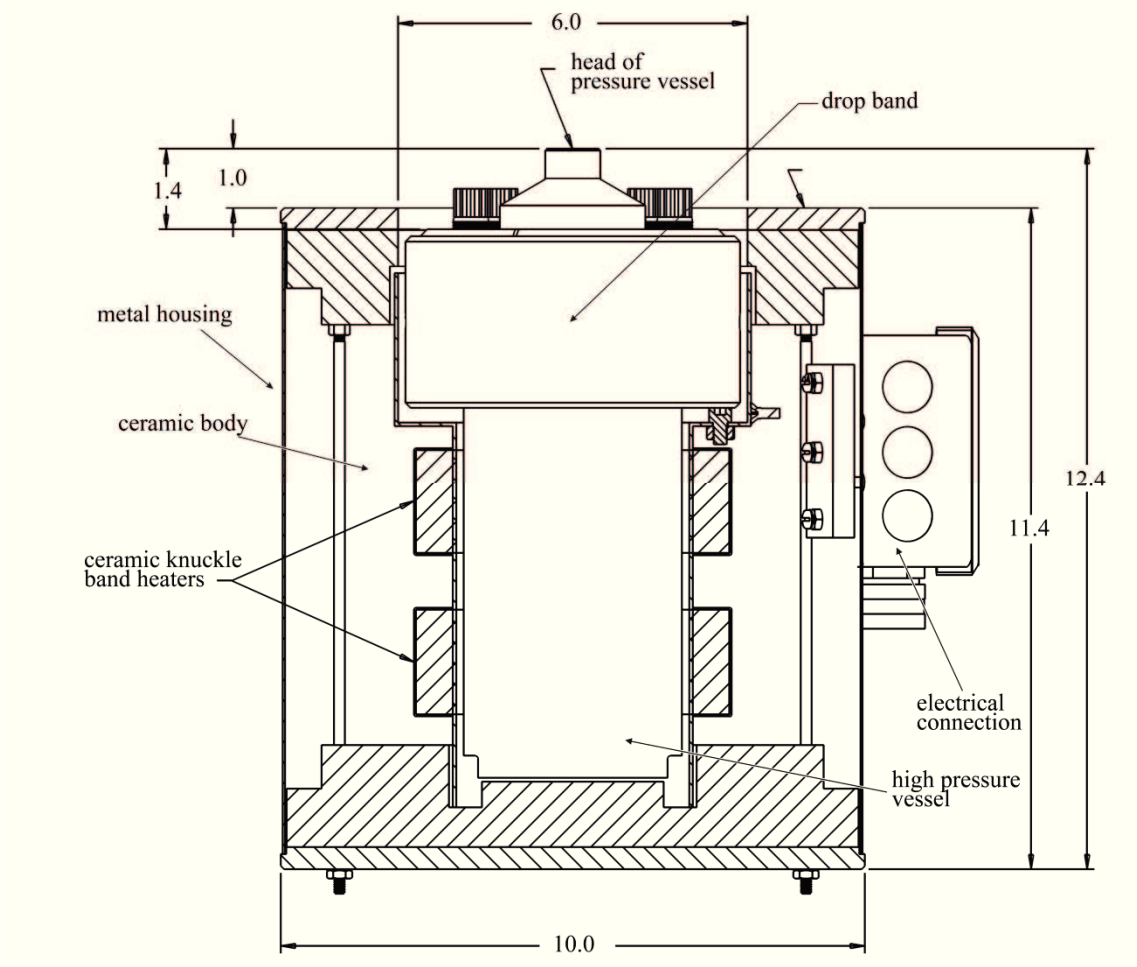

Fig. 2.4. Pressure vessel placed in a heater arrangement. Head isolation, connected thermocouple and tubings are not shown. Values are in inches. Schematic sketch based on the original technical drawing of Parr Instrument Company.

2.3.3 Pump

A hydraulic unit was used as pump (manufacturer: Maximator GmbH Germany, hydraulic unit for water, Type M111). The hydraulic unit is mounted in a portable rack made of stainless steel (Fig. 2.5). The pressure is built up with compressed air; alternatively, a hand drive is also available for pressurization. The air control unit is equipped with a filter regulator, control gauge and shut-off valve. An air safety valve is installed to the air control unit to limit the outlet pressure.

Fig. 2.5. Picture of the air driven pump with hand lever installed in a portable metal frame (Maximator GmbH, type M111). Equipped with an air control unit which combines a filter pressure regulator, control pressure gauge and shut-off valve. The metal frame is 26 cm wide and 67 cm height. Tank volume of the operating liquid (water) is 6.5 liter.

The Maximator hydraulic unit has an air drive pressure range of 1 to 10 bar (10 bar delivers a calculated outlet of 1300 bar, pressure ration 1:130). The outlet pressure is set through an air regulator. The displacement volume of water per double stroke is 1 cm^3 and the approximate flow at an air drive of 6 bar is 0.48 l/min (Fig. 2.6). Inlet and outlet valves control the liquid to be pumped. The pump stops automatically when the desired output pressure is reached (Fig. 2.6).

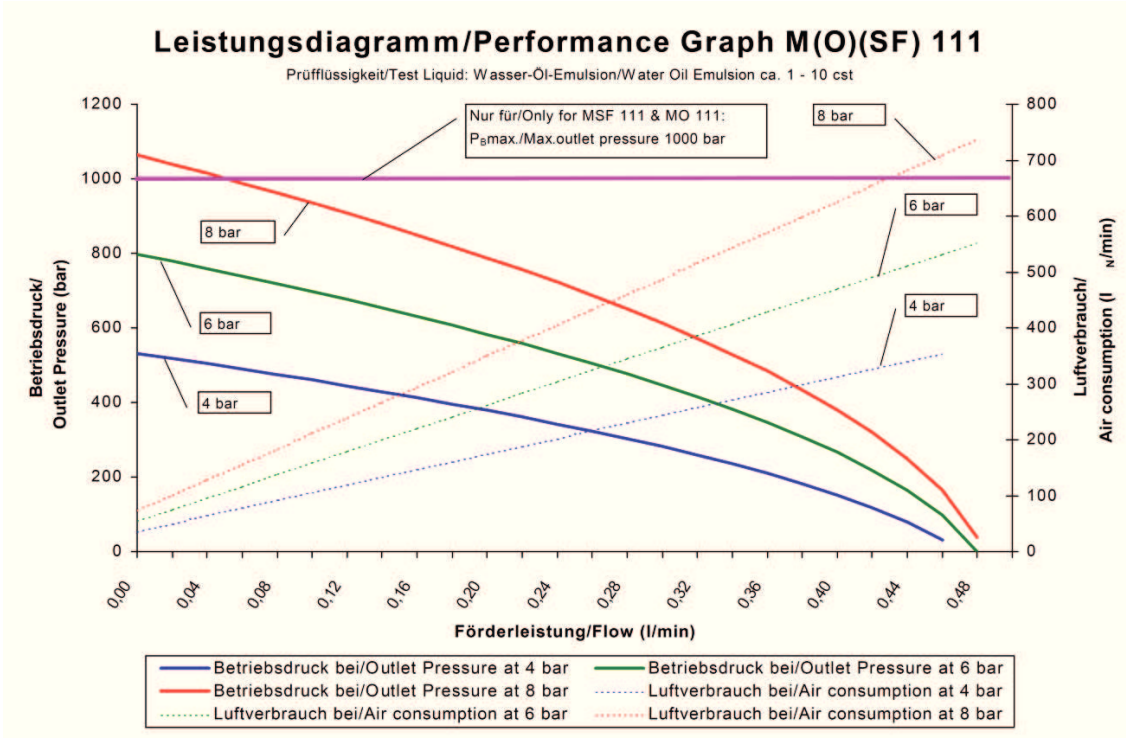

Fig. 2.6. Performance graph of hydraulic unit M111 used as pump in the experimental setup (Maximator GmbH).

The mode of operation is corresponding to an oscillating pressure transmitter. A supplied pressure increases to a higher final pressure. Two different sizes of plungers are interconnected with a pump rod. When plunger area A1 is pressurized with a pressure of p1 by air, a force F1 is exerted to a larger diameter plunger. This force is transmitted by the pump rod to the smaller plunger and to the smaller diameter plunger area A2 at the liquid side. Thereby pressure p2 is greater than pressure p1. In a pressure transmitter, pressures are reciprocal to the piston areas (Fig. 2.7).

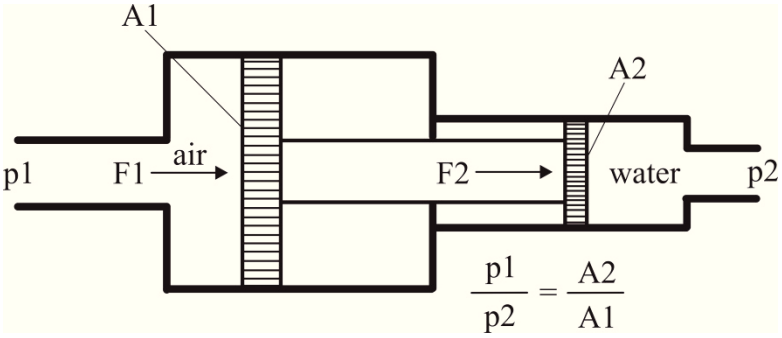

Fig. 2.7. Principle of operation of a pressure transmitter.

2.3.4 Gold reaction cell

The gold bag was made to our specifications by Heraeus Materials Technology GmbH. It is a welded cylindric crucible with an outer diameter of 35 mm, a height of 120 mm and wall thickness of 0.25 mm.

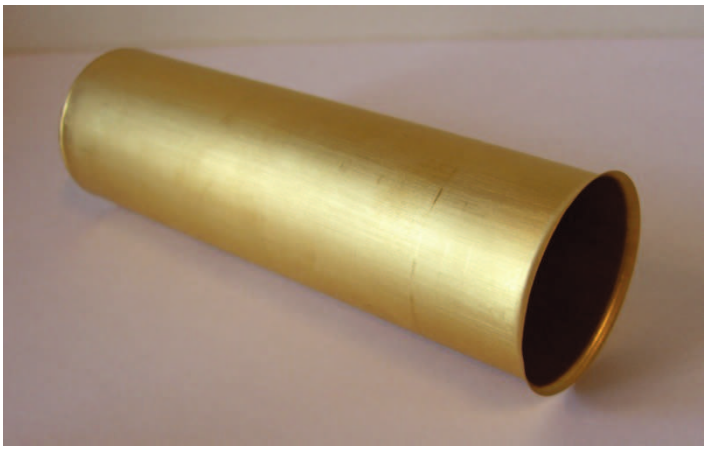

Fig. 2.8. Gold reaction cell used in the experiments (length: 120 mm, outside diameter 35 mm and wall thickness 0.25 mm).

The total volume of the gold bag is 115 ml, but fitting the Ti-closure, leads to decrease of the effective volume by 15 ml, leaving about 100 ml of volume for the experimental charges. Before use, the gold bag was cleaned with diluted hydrochloric acid and flushed with ultrapure water. The gold bag was annealed at 600 °C for one hour in a muffle furnace and slowly cooled down to make the gold soften. Before loading the gold cell, it is important to calculate the fluid expansion at the experimental temperature and pressure to prevent damage to the gold bag. The wall thickness of the gold reaction cell is a compromise between flexibility and stability. After several experiments the surface develops little cracks and final leaky ruptures due to repeated deformation (see Fig. 2.9).

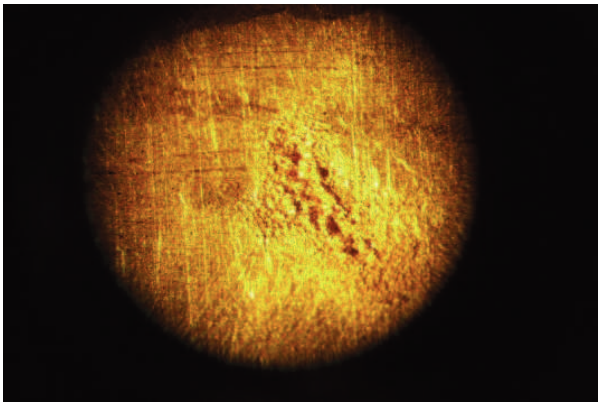

Fig. 2.9. Picture of tiny holes on the gold reaction cell surface after several usages in experiments. The photo was made under a binocular microscope with 40-fold magnification. The rounded field of view is 2 cm.

Soldering with applied filler gold is possible to plug the holes formed, but during deformation in following experiments, stress fractures occur at the boundary interfaces and the repaired cracks become leaky again.

2.3.5 Titanium closure

During an experimental run the reactants reside in the gold reaction cell and are physically separated from the pressurized fluid in the pressure bomb. After filling the gold reaction cell, a closure is needed to seal the gold cylinder. A reusable titanium closure was first constructed by Seyfried (1979). It consists of three parts: head, retainer plate and collar. Six pressing screws are needed to make an effective pressure seal. In cooperation with the machine shop of the Faculty of Biology and Chemistry at the University of Bremen, we developed a similar titanium closure. Instead of using six pressing screws, we constructed a bayonet connector to generate pressure needed to make a seal (see Fig. 2.10). The titanium bayonet connector consists of three pieces and was lathed from a titanium rod. The titanium plug fits well in the opening of the gold cylinder and has a flanged rim, which was fitted to the flanged rim of the gold bag. A titanium ring is pushed from below over the gold cylinder and the second counterpart titanium ring section is nested from the top. Metal bars of the top titanium ring gear into the corresponding cut outs of the bottom titanium flange ring. The metal bars are gently sloped. Both ring parts are pressed against each other through a plug rotary motion. Pressure sealing was accomplished with two special ring spanner wrenches. The bayonet closure works like a thread. The gold between the rims is used as gold gasket and seals the gold reaction cell against the outer pressurized fluid in the pressure vessel. Before starting an experiment, the titanium closure was tested for leakage by pressurizing the gold reaction cell with the installed titanium closure to one bar. The advantage of the bayonet sealing is that the force on the gold rim flange is equal in all places. In addition, it is more comfortable to close and especially to open the titanium closure after a long running experiment, where seizing of bolts is often a problem.

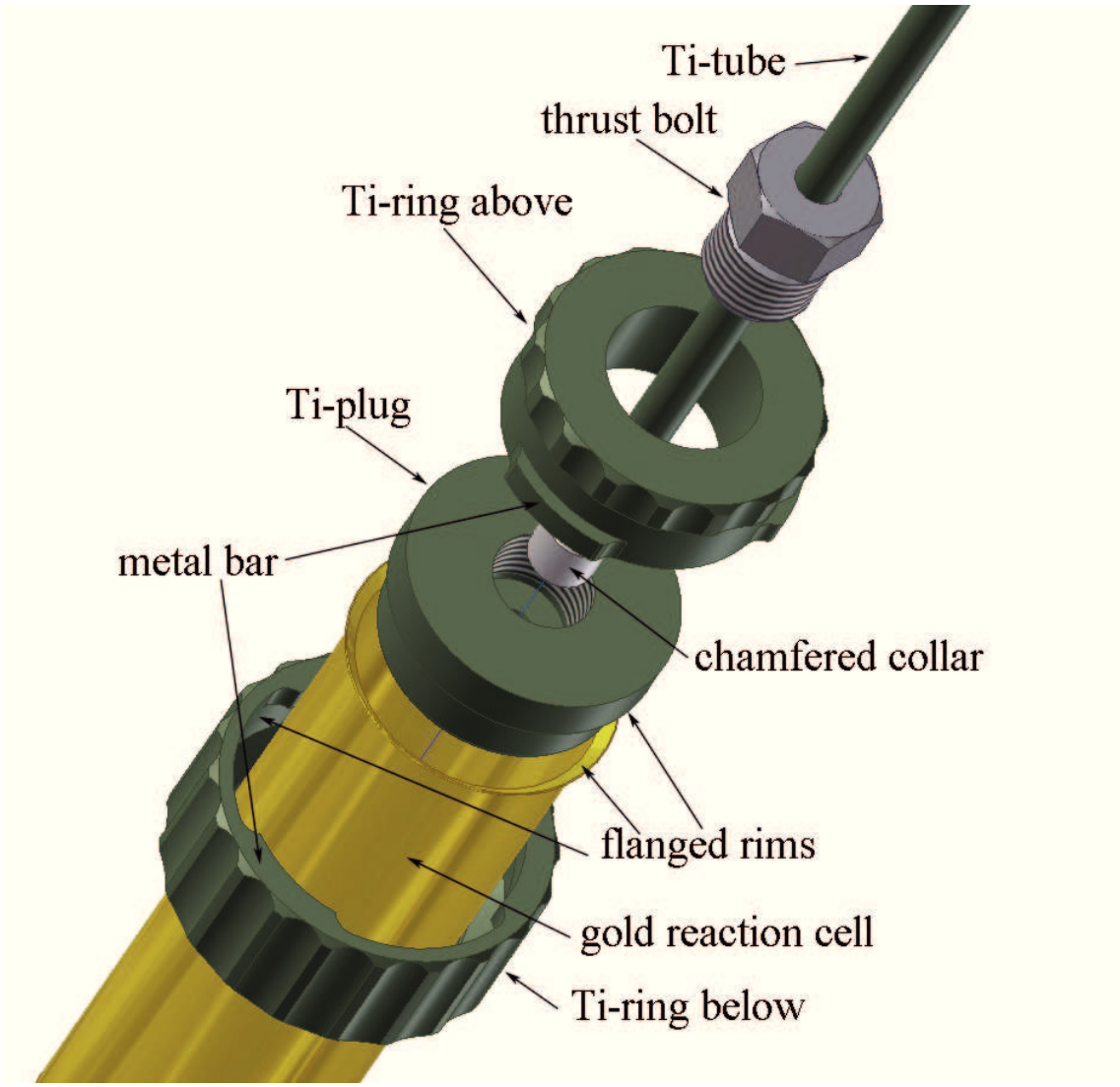

Fig. 2.10. Bayonet titanium closure connected to the gold reaction cell. Outer diameter of the Ti-ring below is 48.9 mm. Constructed in cooperation with the machine shop of the Faculty of Biology and Chemistry at the University of Bremen.

2.3.6 Titanium tube and valve

A titanium tube with a titanium valve is connected for sampling into the connecting bore hole in the middle of the titanium plug. The connection is a conventional high pressure stainless steel fitting, which uses a coned titanium tube, thrust collar and thrust bolt (see Fig. 2.11). The collar is chamfered at both ends and left-hand threaded to prevent unthreading as the right-hand threaded gland nut is tightened. The thrust bolt is pushed over the tube and the thrust collar is screwed so that 1-2 threads are free between sealing cone and thrust collar. The thrust bolt is screwed into the connecting bore hole of the titanium plug and it is tightened.

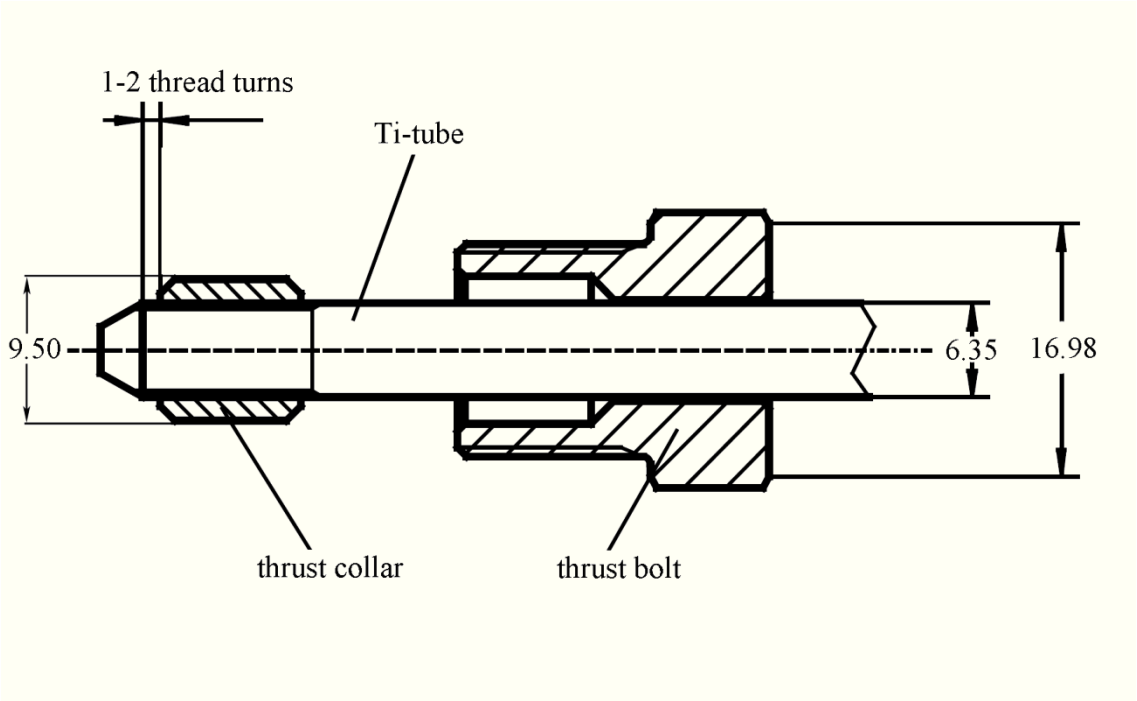

Fig. 2.11. Schematic sketch of the high pressure stainless steel connection with coned Ti-tube, thrust collar and thrust bolt. Values are in mm.

A high-pressure sampling titanium valve (Fig. 2.12) is connected to the titanium tube with the same conventional high pressure fitting as described before (see Fig. 2.11). It is a basic type of mini valve, in which all surfaces in contact with the experimental charge are made of titanium by Nova Werke Deutschland GmbH. The valve is gastight and has a minimal dead volume. A ¼- inch titanium frit prevents particles greater than two micrometer from entering the valve when sampling the fluid during an experiment. The replacement titanium frit is positioned in the bore hole of the titanium plug in direction to the inside of the gold reaction cell. A short piece of titanium tube is adapted behind the valve equipped with a flangeless fitting to a luer connection for adaption of a sample syringe.

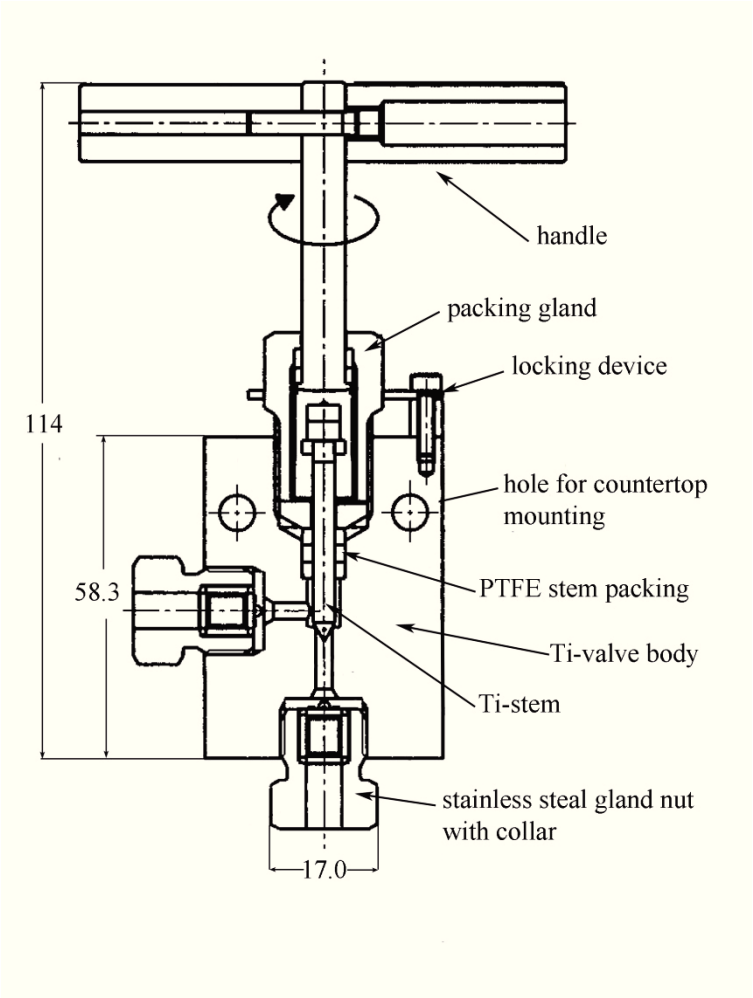

Fig. 2.12. Schematic sketch of the titanium valve used to sample the fluid during an experiment. Values are in mm.

2.3.7 Titanium tube sealing

The titanium tube with the installed Ti-valve has to pass from the outside to the inside of the high-pressure vessel in order to connect the gold reaction cell. A compression seal fitting from Conax Technologies, Model MK-250-A, was used to seal the Ti-tube in the pressure vessel head (see Fig. 2.13). The single sealing element consists of a cap, a ferrule and a body with a ¼ inch NPT thread. The stainless steel ferrule is deformed against the tube to make a gastight seal without cutting surface. The compression seal fitting is freely adjustable to the first tightening from whereon it has to be resealed at the fixed same position, because the ferrule is arrested. The Conax compression seal fitting can be used to a temperature of 870 °C and the pressure range is from vacuum to 690 bar.

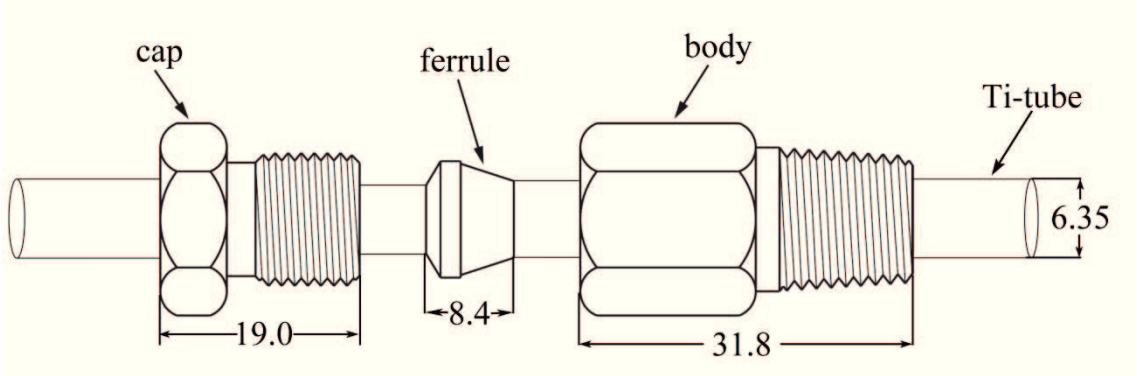

Fig. 2.13. Schematic sketch of the single sealing element MK-250-A (Conax Technologies). Values are in mm.

2.3.8 Safety equipment

High-pressure and high-temperature experiments are generally dangerous. The operational safety is important to avoid personal injury. The operator should be aware of the potential dangers of hot high-pressure fluids and should be experienced as well as trained in correct use of the apparatus. The pressure vessel must be protected against heating over 400 °C and against pressures greater than 565 bar to avoid bursting during operating. The controller used in the experiments (Parr Instrument Company, Controller 4836) was equipped with a lockout relay for over temperature and for over pressure protection. The alarm setpoint of the controller for temperature and pressure was adjustable. If the set limit of the pressure and / or temperature was reached the lockout relay interrupts the electric current. A thermocouple was positioned in the pressure vessel and must be connected to the controller to allow heating. A pressure transducer was installed in a pressure line away from the hot reactor vessel for continuous monitoring of the pressure. A direct connection of the pressure transducer to the head of the reactor is not possible because the operating temperature is higher than the allowed maximum operating temperature of 120 °C for the pressure transducer. Another backup safety feature was an adjustable proportional relief valves in the pressure lines. The valve opens gradually as the pressure increases. This was convenient too by starting an experiment to relieve the rising pressure during heating. A rupture disc was directly installed in the head of the pressure vessel, for the case that all aforementioned safety devices fail. Upon an unexpected overpressure, the disc will rupture at a pre-determined burst range and releases the vessel pressure to protect the vessel from bursting. The rupture disc is a domed thin metal foil, which is installed with the concave side facing

the pressurized side of the apparatus. A suitable rupture disc material must be chosen in view of temperature, pressure and reactants. The expected life of a rupture disc is about 5000 pressurization cycles. A stainless steel tube was attached to the rupture disc assembly to carry any discharge away from working area where vapor can be released safely if the rupture disc should burst.

Before the high pressure vessel can be used in experiments the Technical Inspection Agency has to inspect the system and to grant a permit.

2.3.9 System configuration

The complete flexible cell system is illustrated in figure 2.14. The pressure vessel is placed in the heater arrangement. The gold reaction cell with the titanium closure and the titanium sampling valve is installed. The thermocouple and the pressure transducer are connected to the controller. A valve system is attached. Besides the shut-off valves, the valve system contains the pressure relief valve, pressure transducer and the link to the pump.

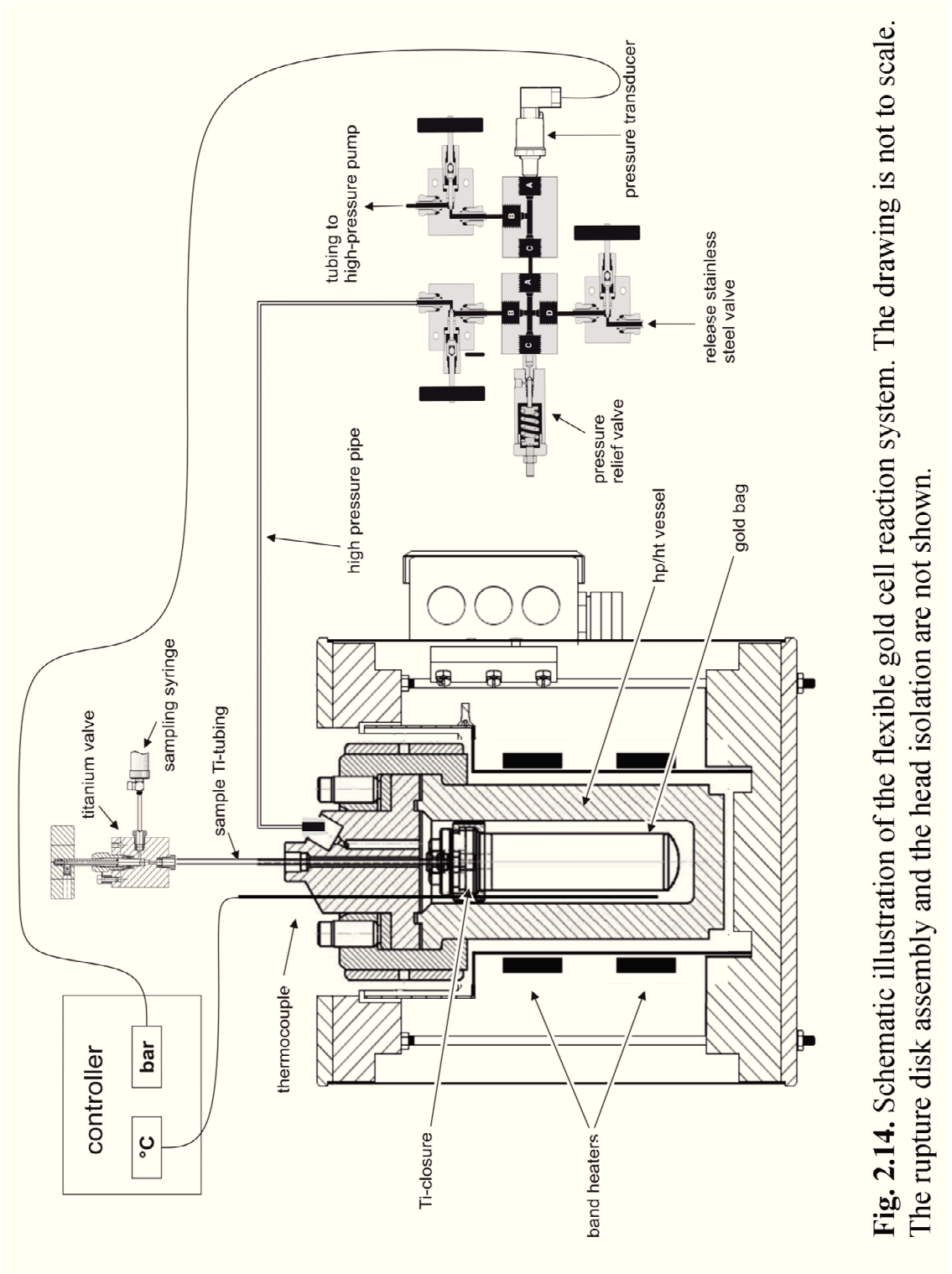

Fig. 2.14. Schematic illustration of the flexible gold cell reaction system. The drawing is not to scale. The rupture disk assembly and the head isolation are not shown.

2.3.10 Start of an experiment

The required amounts of reactants were weighted into the gold reaction cell and the titanium closure with the bayonet connector was attached. Before the deformable sample cell was fitted in the high-pressure vessel, leak testing by pressurizing with nitrogen to 1 bar is done. It is also important to remove oxygen (in trapped air) from the system by thorough flushing with nitrogen. Fluid expansion at the experimental temperature and pressure must be considered and overfilling of the gold bag must be avoided. The gold reaction cell was installed in the high-pressure vessel and the equipment was sealed. The bolts of the pressure head should be lubricated with a high-temperature antiseize grease so that they move freely during tightening to obtain the desired torque value and to prevent seizing of the bolts during the runtime of the experiment. The amount of torque depends on the used O-ring gasket and the experimental pressure. Even-tightening in small increments to the desired amount of torque of all eight bolts is important. The pressure vessel was then positioned in the heater arrangement and the pressure line to the pump was adapted. Additionally, a stainless steel tube was attached to the safety rupture disc assembly to carry away any discharge from the operator in case of failure. The thermocouple and pressure transducer were connected to the controller. The system was carefully pressurized manually by the hydraulic pump with an open sampling valve to remove nitrogen gas from the reaction cell into a syringe. When fluid was visible, the valve was closed immediately and the system was pressurized to the desired operating pressure. Then the heater was switched on. While the temperature rises, the pressure also increases and the installed relief valve was limiting the pressure to the desired value. Careful observation during heating-up the experiment was essential to make sure that everything runs faultless and to take a corrective action when necessary.

2.3.11 Sampling an experiment

Samples were taken using the installed titanium valve to carefully fill fluids into syringes attached to the valve. The first 1.5 ml of fluid extracted flushes the titanium tube and titanium valve (dead volume of the titanium tubes and titanium valve is 1.15 ml) and was discarded. For analyses of gases two separate aliquots of about 0.5 ml fluid were taken into a gastight syringe. Further fluid was sampled to analyze additional desired parameters like pH, and concentration of sulfide, chloride, sulfate, ammonium, and various cations. More information on analytical methods employed in the course of

this work is provided in chapter 3 “Analytical methods”. All fluid samples were weighted to determine the amount of residual fluid in the reaction cell and to calculate concentrations of dissolved species. During sampling, the high-pressure pump must be worked simultaneously to maintain a nearly constant pressure to compensate the pressure loss due to the decreasing volume in the flexible gold reaction cell.

3. Analytical methods

3.1 Potentiometric pH measurement

The pH-value expresses the acidity of a solution by measurement of the activity of hydrogen ions. It is defined as the negative logarithm to the base 10 of the molar hydrogen activity in a solution:

$$\mathrm{pH} = -\lg \frac{\mathrm{a}\,(\mathrm{H}^{+})}{\mathrm{mol} * \mathrm{l}^{-1}}$$

The pH-scale is defined in the range from 0 to 14. Pure water has a pH of 7.0 and it is named neutral. A pH below 7.0 is acidic and above 7.0 is alkaline. The lower the number, the stronger is the acidity. The pH measurement of a sample is accomplished by measuring the cell potential of the unknown sample in comparison to a standard cell potential. The electrode solution is separated from the solution to be measured by the thin glass membrane and the difference in potential, between the two is proportional to the hydrogen ion activity.

After sampling the experiment, the pH-values of the fluid were measured immediately to avoid pH-value changes, for example caused by absorption of carbon dioxide from the air. The pH-values were measurement with a pH-Meter, SCHOTT® Instrument Lab 850 and a micro-pH-combination electrode A-157 with integrated temperature sensor Pt1000 for measuring in small vessels and little sample quantities. Reference electrolyte was 3 mol/l potassium chloride solution and the reference system was Silamid® (Ag / AgCl system). The electrode was always calibrated with buffer solutions (slope and zero point with buffers 4.01 and 7.00) before a pH-measurement was done.

3.2 Gas chromatography for the analysis of hydrogen

Gas Chromatography (GC) is a method for the separation and quantification of volatile components of a sample. An inert gas transports the sample through a column packed with a selective adsorbent and the separated components are recorded by a detector.

The resulting graph indicates the presence of a particular component and the peak area is used to quantify the amount of the component in comparison with the peak area of a standard substance.

The fluid sample with the dissolved dihydrogen, H_2 (aq), was taken with a glass gastight syringe connected to the titanium valve at the high pressure bomb. The weight of the fluid sample retrieved was determined with a balance. Volatile components from the sample were extracted in the headspace of the syringe and the whole gas in the headspace was injected with a specially designed headspace valve extraction system (developed by Jeffrey S. Seewald, Woods Hole Oceanographic Institution) into the GC to determine dihydrogen concentrations (see Fig. 3.1).

The dihydrogen content in the gas phase was measured with an Agilent 7820A Gas Chromatograph using a thermal conductivity detector (TCD). The stationary phase was a packed, 60/80 Mol Sieve A column and the carrier gas was nitrogen. EZChrom Compact Software was used to quantify the peak area. Concentrations of dihydrogen dissolved in the solution were calculated from the concentrations in the gas phase and the weight of the solution sample.

Operating Conditions:

GC	Agilent 7820A Gas Chromatograph
Data system	EZChrom Compact Software
Injection:	Headspace valve extraction system
Column:	Supelco 13823, packed, 60/80 Mol Sieve 5A Column
Carrier gas:	Nitrogen 15 ml/min
Oven temperature:	40 °C isothermal
Detector:	TCD and FID at 350 °C
Make up gas:	no make up gas
Reference gas TCD:	Nitrogen 10 ml/min
H_2-flow FID:	40 ml/min
Air flow FID:	400 ml/min
Calibration:	point to point

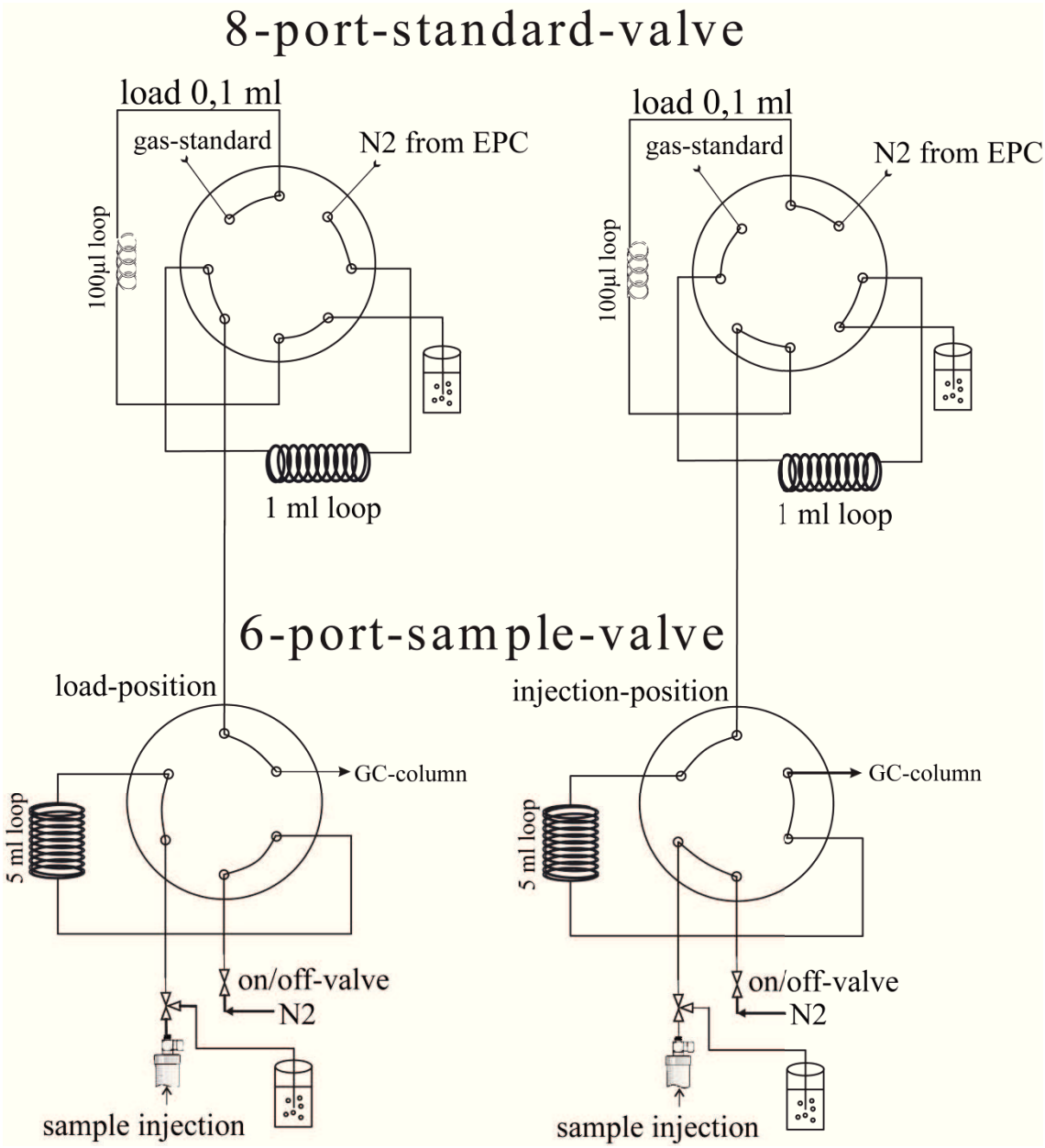

Fig. 3.1. Schematic sketch of the special headspace valve extraction system to inject gaseous phases directly from a syringe headspace to the GC (developed by Jeffrey S. Seewald, Woods Hole Oceanographic Institution). The drawing is not to scale. The two smaller loops (100 µl and 1 ml) are used for calibration with a gas standard.

A gas standard (Supelco®) with carbon monoxide, carbon dioxide, hydrogen, methane and oxygen each component at 1.0 % (w/w) in nitrogen, analytical accuracy ± 2 %, was used for the calibration of hydrogen. The relative standard deviation of the used hydrogen method is better than 5 %.

3.3 Ion chromatography (chloride and sulfate)

Ion chromatography was used for separation and analysis of anions. A known volume of sample is injected with the help of a sample loop. A pumped liquid solvent (eluent) carries the sample ions to a separation column. In the column, cations interact with the anions of the sample. The anions are separated and detected by changing the electrolytic conductivity of the eluate. The detected peaks are integrated with chromatograph`s software and quantified using calibrations with standards of known concentrations. An ion chromatograph from Methrom, IC Advanced Compact 861, was used to quantify chloride and sulfate concentrations. The column packing was polyvinyl alcohol with quaternary ammonium groups and a particle size of 5 µm (detailed operating condition are given below). The fluid samples were transferred in a glass vial, 100-fold diluted with ultrapure water (MilliQ®, 18.2 MΩ * cm @ 25 °C), closed by a septum-cap for automated introduction of the samples into the ion chromatograph.

IC operating conditions:

Injected volume:	5 µl
Precolumn:	METROSEP A SUPP 4/5 Guard
Column:	METROSEP A SUPP 5 - 100
Eluent:	3.2 mmol/l Na_2CO_3 / 1.0 mmol/l $NaHCO_3$
Flow:	0.70 ml/min
Temperature:	20 °C
Pressure:	5.9 MPa

A four point calibration curve in the range from 0 to 300 mg/kg chloride and from 0 to 10 mg/kg sulfate was used for quantification in the ion chromatography (see Fig. 3.2 and 3.3).

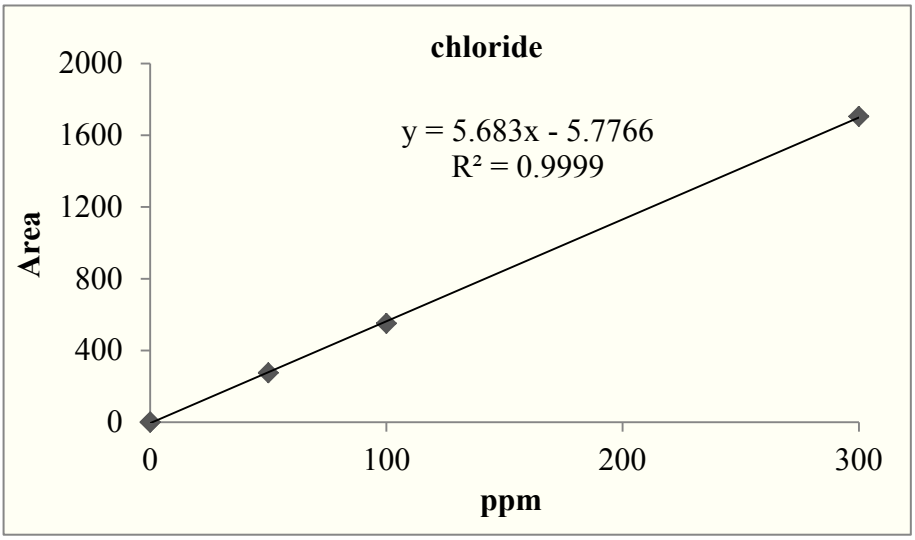

Fig. 3.2. IC calibration curve of chloride.

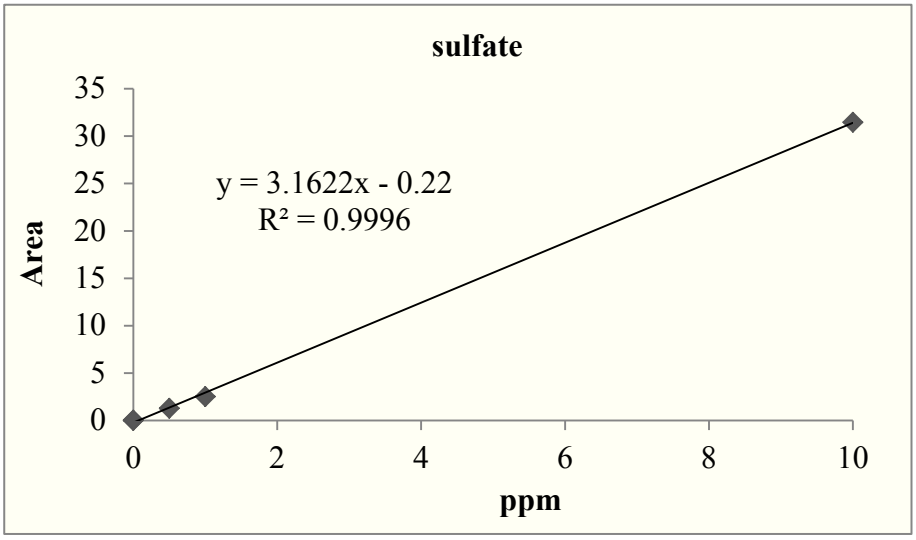

Fig. 3.3. IC calibration curve of sulfate.

A seawater standard IAPSO, P-Series from Osil (Ocean Scientific International ltd.) was used to check the accuracy of the method. IAPSO is a certificated standard seawater which is accurately calibrated in electrical conductivity ratio (K15) and in salinity. The concentration of chloride is 19354 mg/kg and of sulfate is 2712 mg/kg (Summerhayes and Thorpe, 1996). The relative error in measurement of chloride was better than 0.1 % and the relative error in measurement of sulfate was better than 1 % in comparison with the standard seawater IAPSO. The concentration range of chloride in the IAPSO standard was comparable with the sample fluids. The sulfate concentration in the fluids were 100-fold lower, so that the relative error of sulfate in the samples

maybe higher. The measured sulfate values of the fluids were considerable higher than the quantification limit of sulfate (0.03 mmol/kg).

3.4 Flow injection analysis system (ammonium)

A flow injection analysis system (FIA) was used for the quantification of ammonium (Hall and Aller, 1992; see Fig. 3.2). The sample is injected into a sodium citrate buffer solution stream, in which ammonium $(NH_4)^+$ is transformed to ammonia (NH_3). The ammonia passes through a gas-permeable hydrophobic membrane (Teflon®) into a hydrochloric acid solution on the other side of the membrane (see Fig. 3.4 and 3.5). In the hydrochloric acid, ammonia reacts to ammonium, and the concentration of the transferred ammonia is measured as conductivity change due to ammonium addition to the obtaining stream.

The ammonium fluid samples were taken directly after measurement of pH from the pH samples to save sample volume. The sample fluids were diluted 1:1 with ultrapure water (MilliQ®, 18.2 MΩ * cm @ 25 °C) in a 1.5 ml microcentrifuge tube with a conical bottom and sealed with an integral snap cap. These diluted sample fluids were inserted directly into the flow injection analysis system.

FIA operating conditions and measurement settings:

Pump: Ismatec peristaltic pump with 2-stop tygon tubing color coded white-white

Injector:	Common HPLC sample injector with a 100 µl sample loop
Detector:	Conductivity Detector with a strip chart recorder
Membrane:	Standard Teflon® pipe tape (10 x 0.1 mm)
Carrier stream:	0.2 mol/l sodium citrate dihydrate $C_6H_5O_7Na_3$ * 2 H_2O in 10 mmol/l sodium hydroxide solution
Receiver stream:	1 mmol/l hydrochloric acid
Standards:	0.5 / 1.0 / 5 / 10 mg/l ammonium in MilliQ® water

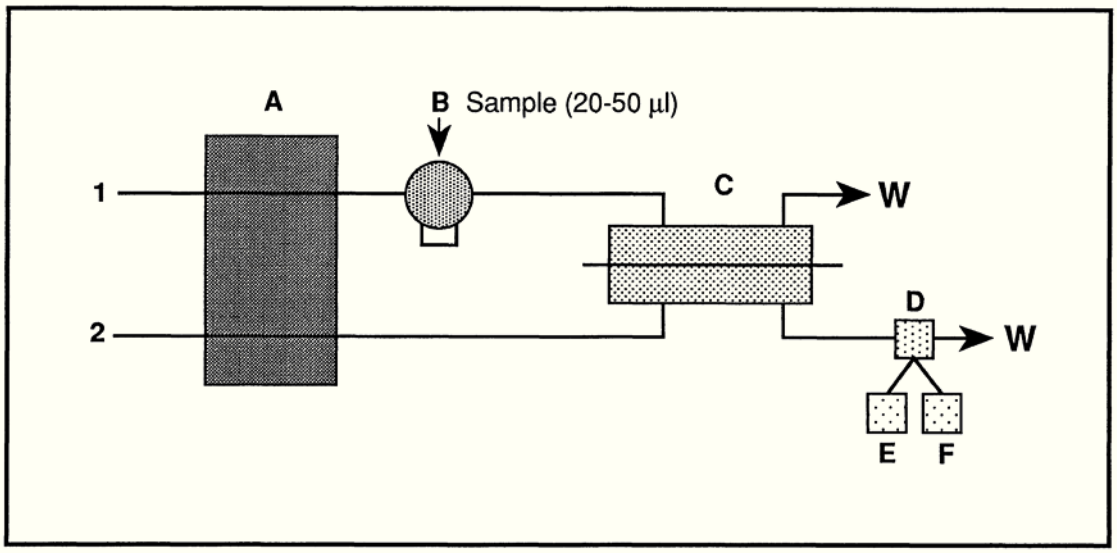

Fig. 3.4. Schematic sketch of basic FIA setup. A = multichannel peristaltic pump with reagent streams 1 and 2. In $\sum NH_3$ analyses, for example, stream 1 is 1 mmol/l HCl and stream 2 is 0.2 mol/l sodium citrate dihydrate $C_6H_5O_7Na_3 * 2 H_2O$ in 10 mmol/l sodium hydroxide solution. B = sample injection valve with 20 - 100 µl sample loop. C = gas exchange cell (see Fig. 3.5). D = conductivity detector with microflow-through cell. E. and F = strip chart recorder or computer readouts. W = waste. (Hall and Aller, 1992).

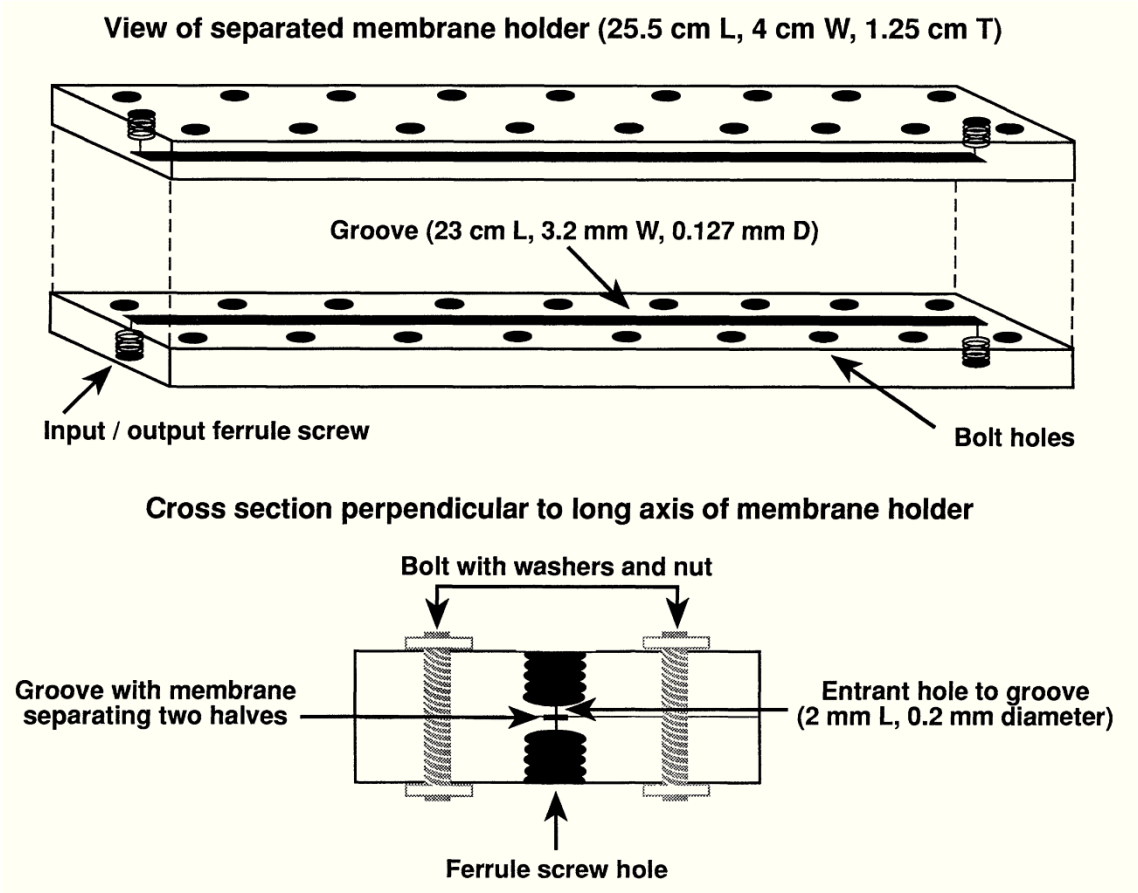

Fig. 3.5. Design and dimensions of gas diffusion cell. An acrylic sheet, stainless bolts and porous Teflon membrane are the materials used (Hall and Aller, 1992).

A six point calibration was done using concentrations which range from 0.03 to 1.08 mmol/kg. For evaluation the peak heights on the strip chart were measured and plotted against the concentrations in mmol per kilogram. A good linearity was obtained (see Fig. 3.6).

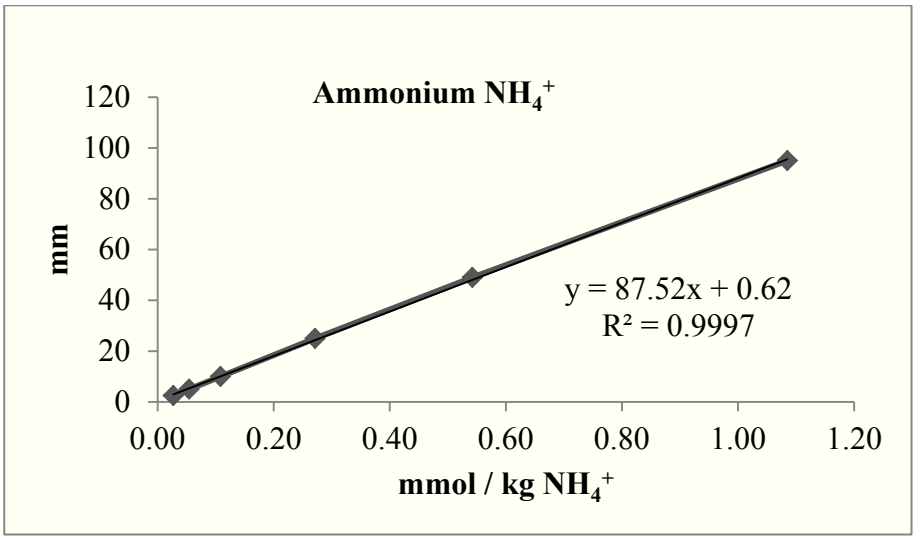

Fig. 3.6. Calibration function of flow injection analysis (FIA) for ammonium.

The measured ammonium concentrations of the diluted fluids were all inside the calibration range. The typical analytical precision is 1.4 % (rel. std. dev.) for NH_4^+ concentrations of 50 µM and the quantification limit is < 0.1 µM.

3.5 Photometric analysis of sulfide

The quantitative analysis of total sulfide was carried out using the Methylene Blue Method (Fogo and Popowski, 1949; Cline, 1969). Sulfide reacts with N,N-Dimethyl-p-phenylenediamine-dihydrochloride via the intermediate product 3-Mercapto-N,N-Dimethyl-p-phenylenediamine to colorless Leucomethylene blue. Leucomethylene blue oxidizes through Fe^{3+} to chromatic Methylene blue (see Fig. 3.7).

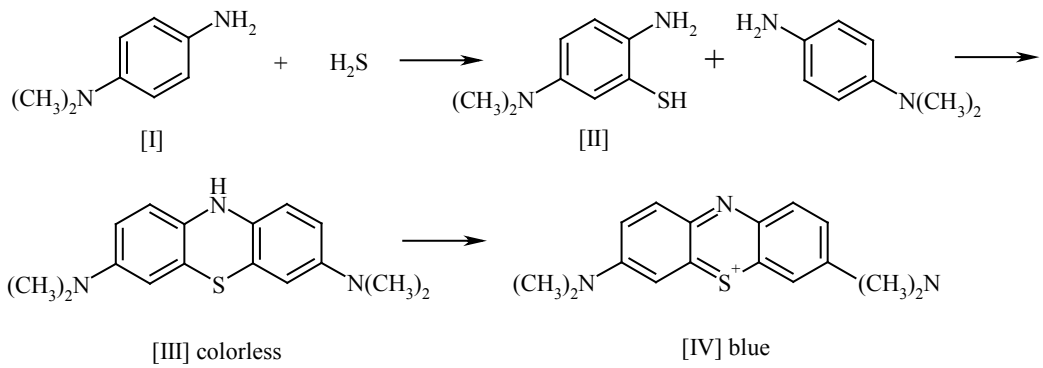

Fig. 3.7. Reaction equation of Methylene Blue Method. [I] N,N-Dimethyl-p-phenylenediamine-dihydrochloride, [II] 3-Mercapto-N,N-Dimethyl-p-phenylenediamine, [III] Leucomethylene blue, [IV] Methylene blue.

The amount of total sulfide (hydrogen sulfide H_2S, sulfide ion HS^- and sulfide S^{2-}) is quantified with this method. The quantitative evaluation of sulfide concentration is based on the Lambert-Beer-Law. A beam of light passing through a colored medium is absorbed proportional to the concentration of the colored substance in the light path. Measurement of light intensity before passage of the sample and measurement of light intensity after passage through the sample is necessary to quantify the amount of sulfide. The absorbance is directly proportional to the concentration:

$A = f\ (c)$ A = Absorbance
c = Concentration

$A = \lg \frac{Io}{I}$ Io = Intensity of light before passage of the sample
I = Intensity of light after passage of the sample

A single beam DR 5000™ UV-Vis Laboratory Spectrophotometer by Hach® was used for the determination of sulfide in the fluid samples. The wavelength of the emitted light was 670 nm. As hydrogen sulfide is volatile, the sample fluids must be preserved immediately after retrieval from the hydrothermal apparatus by precipitation with zinc acetate. After sampling the experimental fluid, 0.5 ml of the samples were instantly pipetted into 0.2 ml of zinc acetate reagent in a glass vial to form zinc sulfide by precipitation (dilution factor 1.4). The glass vials were closed with a screw cap, mixed thoroughly and stored in a refrigerator (at 4 °C to 8 °C) until measurement.

Reagent preparation:

color reagent:	0.4 g N,N-Dimethyl-p-phenylenediamine-dihydrochloride in 100 ml hydrochloric acid 30 % for analysis (storage cool and in a dark bottle)
catalyzer reagent:	1.6 g $FeCl_3$ * 6 H_2O in 100 ml hydrochloric acid 30 % for analysis

zinc acetate reagent: 1.04 g Zinc acetate dehydrate in 100 ml ultrapure water (from a MilliQ® system, 18.2 MΩ * cm @ 25 °C)

dilution water reagent: 14 ml Zinc acetate reagent in 50 ml ultrapure water (from a MilliQ® system, 18.2 MΩ * cm @ 25 °C)

Standard preparation:

The stock solution and the dilutions derived from it must always be prepared freshly. 75 mg of sodium sulfide nonahydrate, $Na_2S * 9 H_2O$ (stored in a desiccator) was dissolved in 100 ml of MilliQ® water (18.2 MΩ * cm @ 25 °C, turned oxygen-free by bubbling nitrogen through it) to obtain a 100 mg/l stock solution. Dilutions of 0.2, 0.5, 0.7, 1.0, 1.2 and 1.5 mg/l were prepared with anoxic MilliQ®-water for calibrating the instrument. 30 µl diamine reagent (color reagent) and 60 µl ferric chloride reagent (catalyzer reagent) were added to 2 ml of the standards solutions in cuvettes. The cuvettes were sealed and shaken well. After one hour reaction time the absorbance was measured at 670 nanometer wavelength with the spectrophotometer.

The linearity of the photometric sulfide calibration curve with 6 points had a good linear correlation (see Fig. 3.8). All concentrations of the diluted samples were inside the calibration range and far above the detection limit of about 1 µmol/kg. The photometric sulfide method has a precision of ± 2 % by determining replicate sulfide standards (n=98, Cline. 1969).

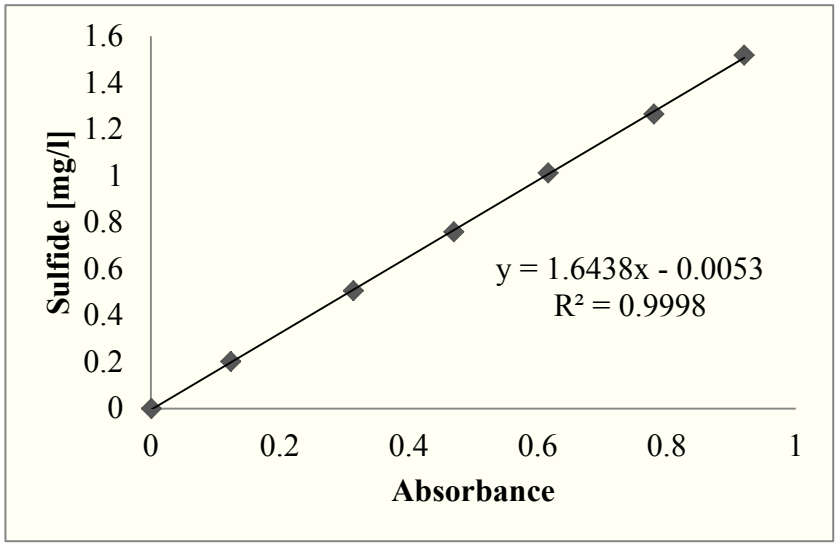

Fig. 3.8. Calibration curve of sulfide determination with a spectrophotometer at 690 nm. Sulfide is the amount of total sulfide (H_2S, HS^- and S^{2-}).

Sample preparation:
The sulfide concentrations in the samples must be below 1.5 ppm (absorbance value < 1.000) so that the sampled fluids of the experiment were diluted with dilution water reagent. The pure dilution water was measured to determine the blank values. Prior to pipetting aliquots from the preserved sample, it is important to warm up the samples to room temperature, to homogenize the samples in an ultrasonic bath and to shake the vials well, because the samples contain sulfide bound as zinc sulfide (ZnS) precipitate. Diamine reagent (color reagent) and ferric chloride reagent (catalyzer reagent) were added to the samples in cuvettes. The cuvettes were sealed and shaken thoroughly. When the diamine reagent (color reagent) is added to the suspension containing zinc sulfide, hydrogen sulfide is formed and reacts to colorless Leucomethylene blue. Then the Leucomethylene blue oxidizes through Fe^{3+} to chromatic methylene blue. The absorbance was measured after one hour reaction time with the spectrophotometer at a wavelength of 670 nanometer.

3.6 Inductively coupled plasma atomic emission spectroscopy (AES)

The inductively coupled plasma atomic emission spectroscopy (ICP-AES) was used to measure the concentration of sodium Na^{+}, Si^{4+} and Mg^{2+} dissolved in the fluids retrieved from the experiments. The sample is injected in an argon plasma which causes electrons of the ions to be transferred to higher energy levels. When these electrons return to a lower state of energy they emit electromagnetic radiation (from ultra-violet to visible range). Each element emits electromagnetic radiation at a characteristic wavelength. The result is a complex spectrum with several emission lines and a spectrometer is used to separate the element-specific wavelengths. The intensity of the radiation is proportional to the element concentration and is measured by a charged-coupled device (CCD) detector or by a segmented-array-charge-coupled device (SCD) detector. Comparison with standard materials was used for quantification. The advantage of ICP-AES is the simultaneous measurement of all elements of interest and the robustness when analyzing samples with high salt content. This method is less sensitive than the ICPMS, and the detection limits of the AES are typically the ppm range.

An atomic emission spectrometer from Perkin Elmer with a SCD-detector, model Optima 3300RL and later a AES from Agilent, series 720 ICP-AES spectrometer with a CCD-detector, were used in this work. Sodium was measured at the wavelength of 589.592 nm by the Perkin Elmer Optima 3300RL and at the wavelength of 330.237 nm by the Agilent 720 ICP-OES. Magnesium was measured at the wavelength of 280.270 nm and silica was measured at the wavelength of 251.611 nm by the Agilent 720 ICP-OES. The sodium concentrations of the fluids in the experiments are highly concentrated and had to dilute 200-fold with ultrapure nitric acid (2 %) to measure the amount of sodium. The relative standard deviation over all measurements was better than 3.5 %.

3.7 Inductively coupled plasma mass spectrometry (ICPMS)

The inductively coupled mass spectrometry (ICPMS) is a sensitive analytical method to determine the concentrations of most elements. The detection limits are in the ppt range. The ICPMS combines an argon plasma as a high efficient ion source and a mass spectrometer. A nebulizer with a spray chamber configuration is typically used for introduction of liquid samples. The nebulizer generates an aerosol of the liquid sample and a spray chamber placed behind the nebulizer removes large droplets. Only the fine aerosol is introduced into the argon plasma. The hot plasma (6000 to 10000 K) dries the aerosol, volatilizes, atomizes and ionizes the sample. Positively charged ions are generated and then accelerated by a negative voltage into the spectrometer which is operated under high vacuum. The positive ions are separated according to their mass-to-charge ratio (m/z) and detected by a secondary electron multiplier. The count rate for a specified ion is proportional to its concentration. Isobaric, polyatomic (molecular) and doubly charged ion interferences can occur; they are caused by identical mass-to-charge ratios and have to be accounted for (for example see Tab. 3.1).

In the course of the thesis work, all ICPMS-measurements were performed with a Thermo Scientific ELEMENT2, a high resolution ICPMS. The ELEMENT2 is a double focusing magnetic sector field ICPMS. Double focusing refers to the combination of magnetic and electrostatic fields. First a magnetic field separates ions according to their mass and energy, and then an electrostatic analyzer focuses ions with respect to ion energy onto the detector. There are three fixed mass resolution powers: low resolution with R = 300, medium resolution with R = 4000 and high resolution with R = 10000.

R is the abbreviation for resolution and it is calculated as R = m / (Δm), where m is the mass of the analyte and Δm is the mass difference between the analyte peak and interference it must be separated from. The detection system is a conversion dynode, which converts incoming ions to electrons. These electrons are then led to the detector for further initiation of an electron cascade in the secondary electron multiplier (SEM).

Tab. 3.1. Common molecular interferences.

isotope	abundance [%]	interfering ions
^{24}Mg	78.99	$^{23}Na^{1}H$, $^{12}C^{12}C$
^{28}Si	92.23	$^{12}C^{16}O$, $^{14}N^{14}N$, $^{27}Al^{1}H$
^{45}Sc	100.00	$^{29}Si^{16}O$
^{56}Fe	91.72	$^{40}Ar^{16}O$
^{153}Eu	52.20	$^{137}Ba^{16}O$
^{159}Tb	100.00	$^{143}Nd^{16}O$

Magnesium, silicon, iron and zinc were analyzed in medium resolution to avoid spectral interferences (see Tab. 3.1). Rare earth elements (REE) were measured in low resolution because of the low concentration. The oxide formation ratio was determined and a correction for polyatomic interferences of oxides with REE (e.g., $^{137}Ba^{16}O$ with ^{153}Eu) was applied. Argon gas flow rates and lens settings were optimized daily for maximum intensity, signal stability and minimal oxide formation. The sample introduction system consists of a PFA microflow nebulizer with an exchangeable external sample uptake capillary of about 100 µl sample flow rate in self-aspirating mode and a cyclonic spray chamber made of PEEK polymer.

Tab. 3.2. ICPMS operating conditions and measurement settings.

Parameter	Settings
Torch	semi-demountable torch (quartz glass) with torch adaption 12/6 mm (PVDF)
Injector	made of quartz glass, 1.8 mm i.d. (ball joint)
Sampler	electroformed nickel, copper cored, diameter 50 mm, 1.1 mm orifice i.d.
Skimmer	electroformed nickel, diameter 24.5 mm, 0.8 mm orifice i.d.
Forward power	1200 W
Coolant gas flow rate	16 l * min^{-1}
Auxiliary gas flow rate	0.6 - 1.2 l * min^{-1}, daily optimized
Sample gas flow rate	0.8 - 1.2 l * min^{-1}, daily optimized
Sample flow rate	100 µl * min^{-1} (self-aspirating)
Instrument tuning	daily using a 1 ppb multi-element-solution with 17 elements to obtain highly stable signal, good peak form, optimum resolution and low oxide formation
Ion transmission	1 million counts ± 200000 counts for ^{115}In (1 µg/l) in low resolution
Ion sampling depth	adjusted daily to obtain a highly stable signal and low oxide formation
Ion lens settings	adjusted daily to obtain a highly stable signal, good peak form and optimum resolution
Mass calibration	daily with using auto lock mass in MR-mode
Sample take-up time	45 sec.
Wash time	2 min.
Scan type	magnetic jump with E-scan over small ranges
Scan Optimization	mass accuracy
Mass window	100 % in LR and 110 % in MR
Detector mode	both in low and in medium resolution
Integration Typ	average
Runs and passes	10 and 1

All dilutions (sample preparation and calibration) were done with nitric acid and deionized water in ultrahigh-purity grade. The nitric acid was purified in a clean room with a PTFE double-subboiling distill and ultrapure water was obtained from a Milli-Q-System®. The fluids from the experiments were diluted with two percent ultrapure nitric acid (total dilution factor was 10.1) and spiked with scandium as internal standard. The fluids of the rare earth experiments (additional study, see appendix) were analyzed

undiluted and indium was used as internal standard. Calibration standards were prepared from certificated element standard solutions (1000 mg/l) in the expected concentration range and scandium or indium is used as internal standard. For quality control an artificial solution with all measured elements was prepared and analyzed. The analytical error was better than 3 percent.

3.8 Thermogravimetric analysis (TG)

Thermogravimetric analysis (TG) measures the change in mass of a sample as a function of temperature or time in a defined gaseous atmosphere. The method allows analyzing materials that exhibit mass loss due to dehydration or loss of volatiles and samples that exhibit a mass increase because of oxidation. The TG device contains a sensitive balance to record the changes in weight during the incremental heating process.

Differential Scanning Calorimetry (DSC) determines the deviation from a given temperature program in comparison to a reference material. Both the sample and the reference material are located in an oven and a controlled temperature program is started. Temperature-dependent phase transformation can be endothermic (e.g., loss of water) or exothermic (oxidation) reactions. When the sample undergoes a phase transformation more or less heat will need to flow to the sample than to the reference material to maintain both at the same temperature. Thermocouples are used as temperature sensors and they are located directly below the sample and the reference material or an empty crucible. The primary measured variable is the potential difference (μV) of the thermocouples as function of time (temperature) respective the proportional temperature difference. For example heat is consumed, when a sample melts (endothermic process), so increased heat flow is required to increase the temperature of the sample as same rate as the reference.

Simultaneous application of Thermogravimetry and Differential Scanning Calorimetry (TG-DSC) allows the combined examination of weight change associated with specific enthalpy changes in the same sample in one instrument at the same time. The advantages are the identical conditions for TG and DSC (for example same gas flow

rate, atmosphere and heating rate etc.) during the measurement. The method yields information on the type and quantity of minerals in rocks.

The thermal analysis in this work was performed using the thermal analyzer NETZSCH STA 449 F3 Jupiter®, Bremen University, Department of Geoscience, Research Group of Crystallographic. The analyzer combines a high sensitivity balance and a differential scanning calorimeter that allows the simultaneous measurement of TG and DSC. The resolution of the balance is one microgram and the system covers a temperature range of 30 °C to 1500 °C.

The finely ground samples were weighed accurately in a crucible made of aluminium oxid (Al_2O_3). The initial weight was about 50 mg. An empty crucible was measured as blank value simultaneous with the sample to eliminate errors related to inaccuracy of the instrument. A heating programm from 30 °C to 1440 °C at 5 °C per minute was started. Synthetic air was used as purge and protective gas.

3.9 Scanning electron microscope (SEM) fundamentals

An electron microscope works like a conventional microscope except that a focused beam of electrons is used to image the sample instead of light and that the sample is under vacuum during the measurement to allow the electrons to travel freely from the electron beam source to the sample and then to the detectors. The advantages of SEM are much higher magnification (100000x) and a greater depth of field in comparison to light microscopy. An electron gun produces a beam of electrons and an electron optical system of lenses and apertures focuses the electron beam into a thin and coherent beam onto the sample. A large number of signals are generated when an electron beam strikes the sample (different electron signals and photon signals) and they can be detected with various detectors. The electron beam is scanned in a raster over the sample surface and the emitted secondary electrons are detected for each position by an electron detector to create an image of the sample. The energy-dispersive X-ray detector (EDX or EDS) is integrated into the SEM to separate the characteristic X-rays of different elements into an energy spectrum and to determine the abundance of specific elements. The measurement can be taken place on a small spot size or over a wide raster area to create an element composition map. For SEM imaging samples must be electrically conductive. Nonconductive samples were coated with a thin film of carbon or gold to

obtain conductivity. A Zeiss SUPRA 40 with a field emission source and an EDX INCA Penta FETx3 detector was used (Bremen University, Geosciences, Research Group of Historical Geology and Palaeontology). The sample powder was mounted on a sample holder with a self-adhesive conductive surface and coated with a thin film of carbon. The holder with the sample was located in the sample chamber and a vacuum was generated before the SEM measurement was started. The presence of elements was determined with the energy-dispersive X-ray detector (EDX) and using a 1 µm beam diameter. EDX-analyses provide semiquantitative information on the relative abundance of elements, which aids in identifying mineral phases in the SEM images.

3.10 Electron probe micro analyzer (EPMA)

Electron probe micro analyzer (EPMA), also known as electron micro probe analyzer (EMPA) or electron microprobe (EMP), allows in situ quantitative analyses and mapping of qualitative element distributions in solid phases. A polished and conductive sample surface is required. The sample surface is bombarded with electrons causing inner shell electrons of the atoms in the sample material to be removed. Higher shell electrons fill the vacancy and X-rays are produced by the electron transition. The X-ray spectrum is characteristic for each element. For element quantification, intensities at specific wavelengths are determined using wavelength-dispersive spectrometers. Matrix corrections are then applied to the raw data, which correct atomic number, absorption and fluorescence (ZAF correction). Natural minerals are typically used as standards for quantification. Furthermore, secondary electrons and back-scattered electrons are detected and displayed as either secondary electron (SE) images or backscattered electron (BSE) images. These images allow for observing microstructures in the sample material and help defining the position of measurement spots.

EPMA has the advantage of being a non-destructive high resolution (1 µm spot size) measurement technique; however, it is unable to analyze light elements (H, He and Li) of the periodic system, and therefore water in minerals cannot be analyzed. Also, it cannot distinguish between different valence states of elements, e.g., between ferrous and ferric iron. Assuming that in most natural silicate and oxide minerals elements are stoichiometrically bound to oxygen, results are reported as mineral oxides, although oxygen is typically not measured. Analyses for the present work were carried out at the Institute of Geosciences, Mineralogy Department, Kiel University with a JXA 8900 R

Electron Probe Microanalyzer from JEOL. 15 kV accelerating voltage and 15 nA probe current were used for measurements on serpentine and brucite. The accelerating voltage for sulfide measurements was 20 kV and the probe current was 15 nA. The instrument was calibrated using a range of mineral standards (see Tab. 3.3 and 3.4). Element mappings as well as backscattered electron images were used for the determination of compositional variations in zoned minerals.

Tab. 3.3. Used standards for analyses of silicates and brucite.

element	standard
Al	corundum
Mn	tephroite
Ca, Si	wollastonite
Mg	forsterite
Ni	Ni metal
Fe	fayalite
Ti	rutile
K	microline
Na	tugtupite
Cr	chromite

Tab. 3.4. Used standards for sulfide measurements.

element	standard
Fe, S	pyrite
Na	anorthoclase
Ti	rutile
Si, Ca	wollastonite
Mn	tephroite
Cl	scapolite
Mg	forsterite
Ni	Ni metal
Cu	Cu metal
Co	Co metal
Zn	Willemite

The mineral grains were embedded in epoxy resin and carefully polished. Silicon carbide powder (SiC) was given on a glass plate and moistened with water. Grinding of the sample surface was done by hand with rotary movements. This process is time intensive and had to be repeated with grinding powder of successive finer grain size (start with SiC grain size 400, next SiC grain size 800 and then SiC 1200). After the process of grinding, polishing with aluminium oxide Al_2O_3 was necessary. This was done with a polishing machine using 5 µm, 1µm, 0.3 µm to 0.05 µm grain size. Before measurement, the clean sample surface was conductively coated with a layer of carbon.

3.11 Powder X-ray diffraction (XRD)

X-rays can be used for qualitative identification of minerals in all rock types. Solid material shows scattering effects when bombarded with X-rays, and diffraction patterns – in comparison with crystal structure databases – can be used to identify minerals within the rock. X-rays are generated in a cathode ray tube, sent over a monochromator to get monochromatic radiation and then focused on the sample. Bragg`s law describes the relationship between the wavelength of electromagnetic radiation, the diffraction angle and the lattice spacing in a crystal:

$$n * \lambda = 2 * d * \sin \theta$$

n = order of reflection [integer]
λ = wavelength of the X-rays [Ångstrom,]
d = distance between atomic layers in a crystal, d-spacing [Ångstrom, Å]
θ = angle between the incident ray and the scattering planes [degree, °]

If Bragg-condition is fulfilled, constructive interference is observed. Since the wavelength of the X-rays is known and the angle can be measured, the d-spacings of the crystals can be calculated and compared with values from databases. The orientation of the crystal lattice in powdered samples is random so that the powder is scanned in a range of 2theta to attain all possible diffraction directions of the lattice.

The X-ray diffractogram for the present work were carried out at the Department of Geosciences, Crystallography, Bremen University using a Philips PW 1800 or a PANalytical X'Pert Powder diffractometer. Measurement conditions are presented in the appendix.

Minerals from the hydrothermal experiments were washed with ultrapure water (from a MilliQ® system, 18.2 MΩ * cm @ 25 °C) to remove remnants of sodium chloride. The dried minerals were pulverised by hand to a fine powder with an agate mortar and pestle to prevent particle size effects. To attain finer powder grinding was carried out under acetone and propanol. Powder pellets were prepared by backloading procedure for the X-ray diffraction measurement. Backloading decreases preferred orientation on the front side of the pressed powder pellet.

3.12 Magnetic measurement

Hysteresis loops were measured at room temperature on a Princeton alternating gradient force magnetometer (PMC Micromag 2900) to quantify the concentration of ferrimagnetic magnetite. Analyses in this work were carried out at the Bremen University, Department of Marine Geophysics. The magnetite concentration is estimated by determining the percentage of the samples magnetization in a field of 1T with respect to the saturation magnetization (M_S) of pure magnetite given by Peters and Dekkers (2003). M_S-based concentration estimates require information about magnetic mineralogy, grain size and grain shape. Concentration calculations are accurate only when magnetic composition is uniform with respect to grain size. The magnetite concentrations used in this study are semi-quantitative because magnetite grain size is variable in the bulk alteration products.

4. Experimental procedures

4.1 Starting materials

4.1.1 Olivine

Commercially available olivine (peridotite, tumbled-polished stones, Mineraliengroßhandel Hausen GmbH, diameter 3 to 5 mm) was hand-picked to obtain inclusion-free olivine crystals. The X-ray confirmed that pure olivine of forsterite-rich composition was separated. Measurements by electron microprobe revealed molar ratio of magnesium to iron, (X_{Mg} = Mg / (Mg + Fe^{2+}) in the range of 0.904 to 0.911, with an average of 0.909 ± 0.005 (n = 60). The olivine starting material is hence forsterite-rich ($Mg_{1.818}Fe_{0.182}SiO_4$), which is a composition typical for peridotite from the Earth`s upper mantle (results see Tab. 4.1 and Fig. 4.1). The accuracy of microprobe analysis justifies to report X_{Mg} and cations values with only two decimal places. The use of three decimal places in this work is necessary for balancing reaction equations used for modeling and does not reflect the analytical accuracy. All measured microprobe data are given in the appendix. In the following, both terms olivine and forsterite refer to the forsterite-rich olivine (X_{Mg} = 0.909).

Tab. 4.1. Average composition of olivine analyzed by EPMA. Twelve hand-picked olivine grains were analyzed, each was measured in five points. Data are in wt. %. The whole data set is shown in the appendix.

	average	abs. st. dev.	formula (oxygens = 4)	
SiO_2	41.28	0.38	Si	1.00
TiO_2	0.00	0.01	Ti	0.00
Al_2O_3	0.03	0.02	Al	0.00
Cr_2O_3	0.02	0.01	Cr	0.00
FeO	8.83	0.44	Fe	0.18
MgO	49.60	0.67	Mg	1.80
MnO	0.13	0.03	Mn	0.00
CaO	0.06	0.03	Ca	0.00
NiO	0.39	0.02	Ni	0.01
total	100.34	-	total	3.00

Concentrations of Na_2O, K_2O, ZnO and Cl were also measured, but were below detection limit.

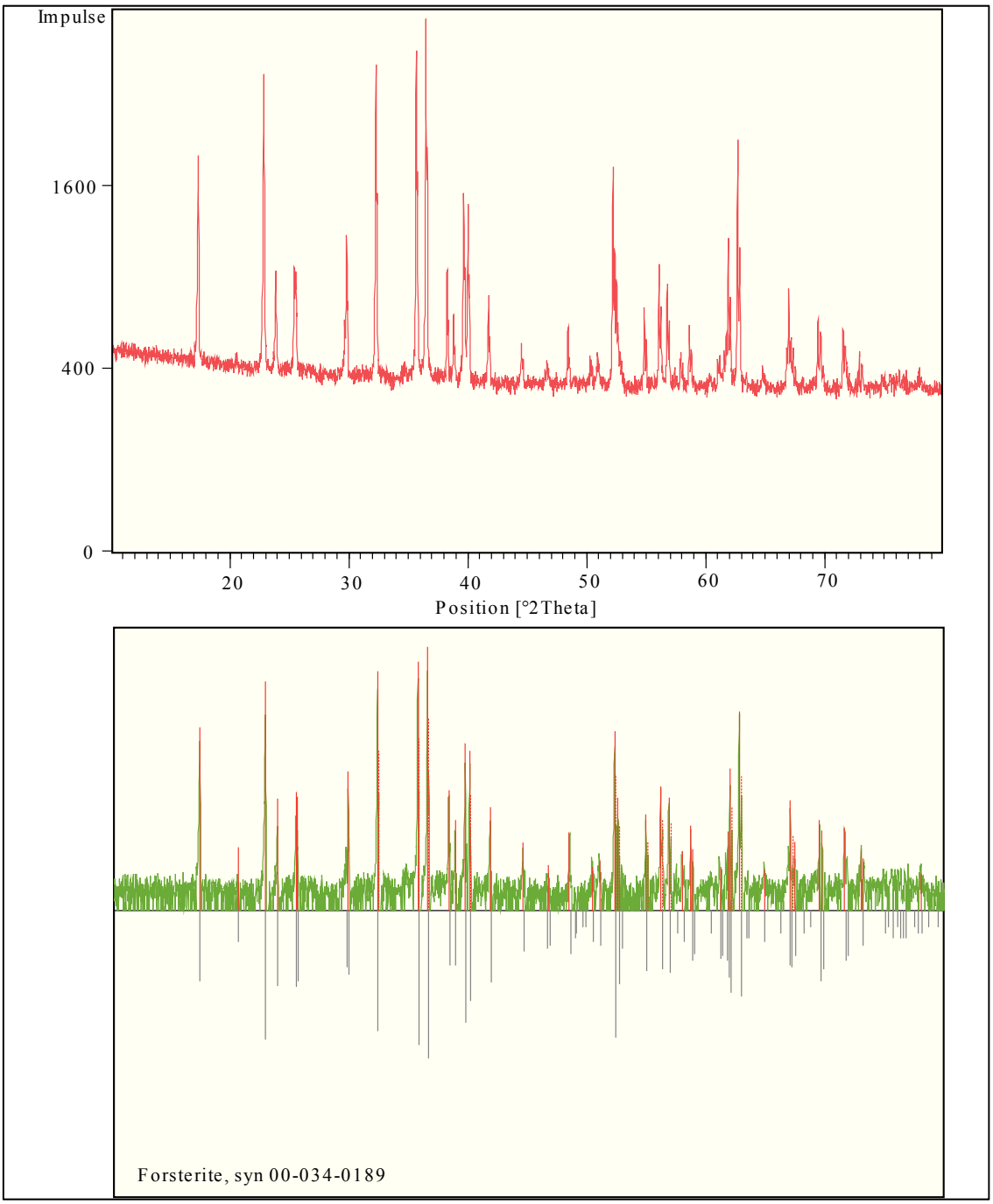

Fig. 4.1. Diffractogram of olivine starting material used for hydrothermal experiments and the powder pattern matches. The database for mineral identification was a PDF (powder diffraction file) of the International Centre for Diffraction Data (ICDD). A list of detected peaks (2theta, d-value, relative intensity) and accepted reference database entries (powder diffraction file number) is provided in the appendix.

For the first two experiments (Exp01 and Exp02) the olivine was ground with an agate mortar and a grain size between 50 to 100 µm was separated by dry sieving. In Exp03 olivine was not used and in Exp04 a grain size fraction from 25 to 75 µm was used. These fractions were washed with MilliQ®-water (18.2 MΩ * cm @ 25 °C) to remove

finer crystals and to obtain the desired grain size. After that procedure the wet grains were dried in an oven at 70 °C.

4.1.2 Pentlandite

Pentlandite with an iron to nickel ratio of 1:1 ($Fe_{4.5}Ni_{4.5}S_8$) was synthesized for use in the experiments. Pure chemicals of sulfur (Sigma-Aldrich, powder, 99.98 %, trace metals basis), nickel (Sigma-Aldrich, powder, 99.99 % trace metals basis) and iron (Merck, powder, for analysis > = 99.5 %) were used as starting material. The pentlandite was synthesized by the standard silica tube method at high temperature (Xia et al., 2008). Pentlandite with a Fe to Ni ratio of 1:1 is only stable inside a small range of sulfur variation over the whole temperature range (see Fig. 4.2). The sulfur concentration range of the batches was calculated from the phase diagram in figure 4.2 (x_1 = 46.4 at. % to x_2 = 46.8 at. %).

Tab. 4.2. Starting compositions in at. % of the pentlandite synthesis according to the phase diagram in figure 4.2.

Batch	Fe	Ni	S
A	26.8	26.8	46.4
B	26.7	26.7	46.6
C	26.6	26.6	46.8

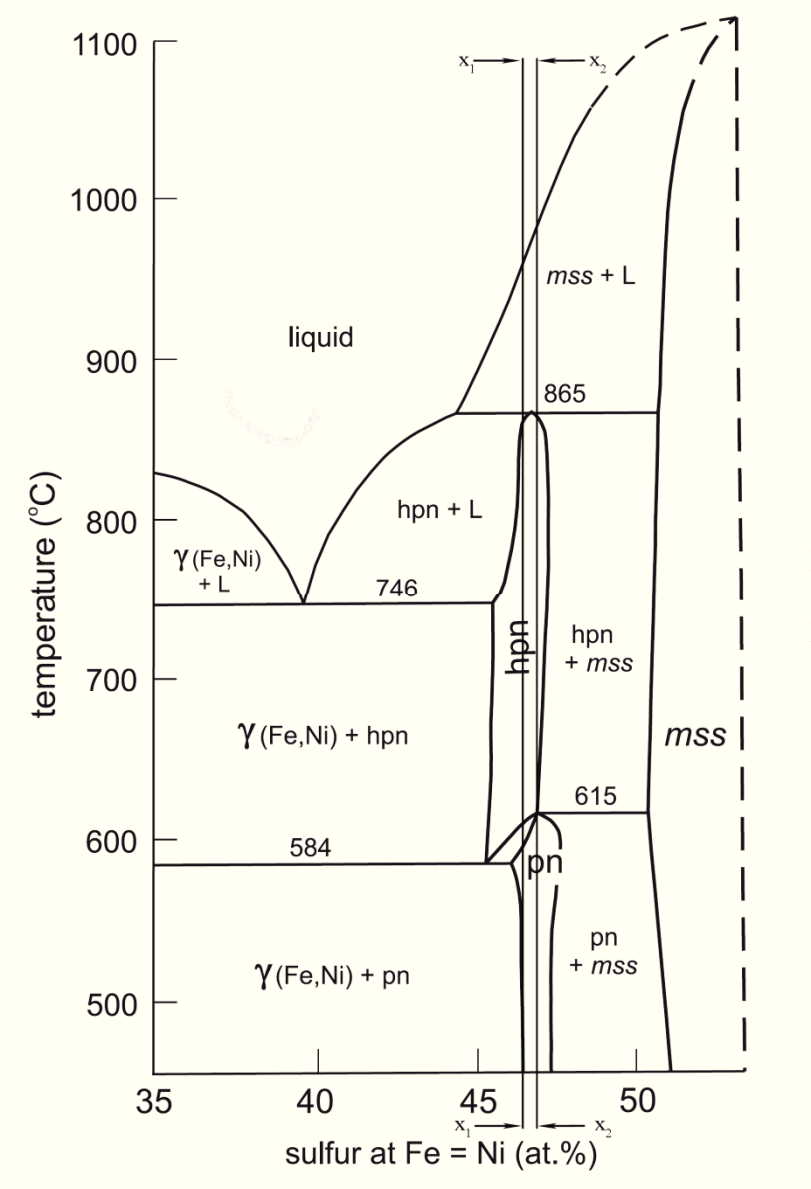

Fig. 4.2. Phase diagram of temperature versus sulfur content at atomic Fe = Ni for the Fe-Ni-S system (Sugaki and Kitakaze, 1998). Pentlandite appears as a stable phase with a limited S-composition range from about x_1 = 46.4 at. % to x_2 = 46.8 at. %. Abbreviations: pn = pentlandite, hpn = high-form pentlandite, mss = monosulfide solid solution, γ(Fe,Ni) = gamma-taenite, L = liquid.

For the synthesis of pentlandite three batches with variations in sulfur concentration were used (see Tab. 4.2). Iron, nickel and sulfur were accurately weighed and homogenized. The reactants were sealed under vacuum (~ 1 mbar) in a silica tube. The tube was placed vertically in a muffle furnace and heated to 445 °C (1 °C/min). After three hours at 445 °C the temperature was increased to 700 °C (1 °C/min) and maintained for three hours. The stepwise heating was done to prevent tube failure due to the high sulfur vapor pressure. In the last step, the tubes were heated to 1150 °C

(1 °C/min) and then annealed for further ten hours. At the end, the furnace was switched off and the batches were allowed to cool slowly down to room temperature. A thin Ni_3S_2 coating is formed on the product surface and removed by grinding. The synthetic pentlandite was characterized by Electron Probe Micro Analyses (EPMA) and by powder X-ray-diffraction (XRD, Fig. 4.3). The synthesized pentlandite is homogeneous and has a nickel to iron ratio of 1:1 (see EPMA analyses in Tab. 4.3; the complete data set is available in the appendix). Batch C was used in the experiments.

Tab. 4.3. Pentlandite data of EPMA analyses.

	Batch A		Batch B		Batch C	
	average (n = 9)	std. dev.	average (n = 7)	std. dev.	average (n = 11)	std. dev.
	wt. %	rel. %	wt. %	rel. %	wt. %	rel. %
Fe	33.17	1.48	32.90	1.83	32.62	1.39
Ni	33.43	1.36	33.67	1.39	33.97	1.00
S	32.16	0.58	32.07	0.67	32.20	0.37
total	98.75	0.29	98.65	0.31	98.79	0.27
formula (8 S)						
Fe	4.73	1.39	4.71	2.28	4.65	1.42
Ni	4.54	1.65	4.59	1.20	4.61	0.99
S	8.00	0.00	8.00	0.00	8.00	0.00
total	17.28	0.37	17.30	0.46	17.26	0.18
Fe + Ni	9.28	0.69	9.30	0.86	9.26	0.34
Fe / (Fe + Ni)	0.51	1.33	0.51	1.58	0.50	1.17

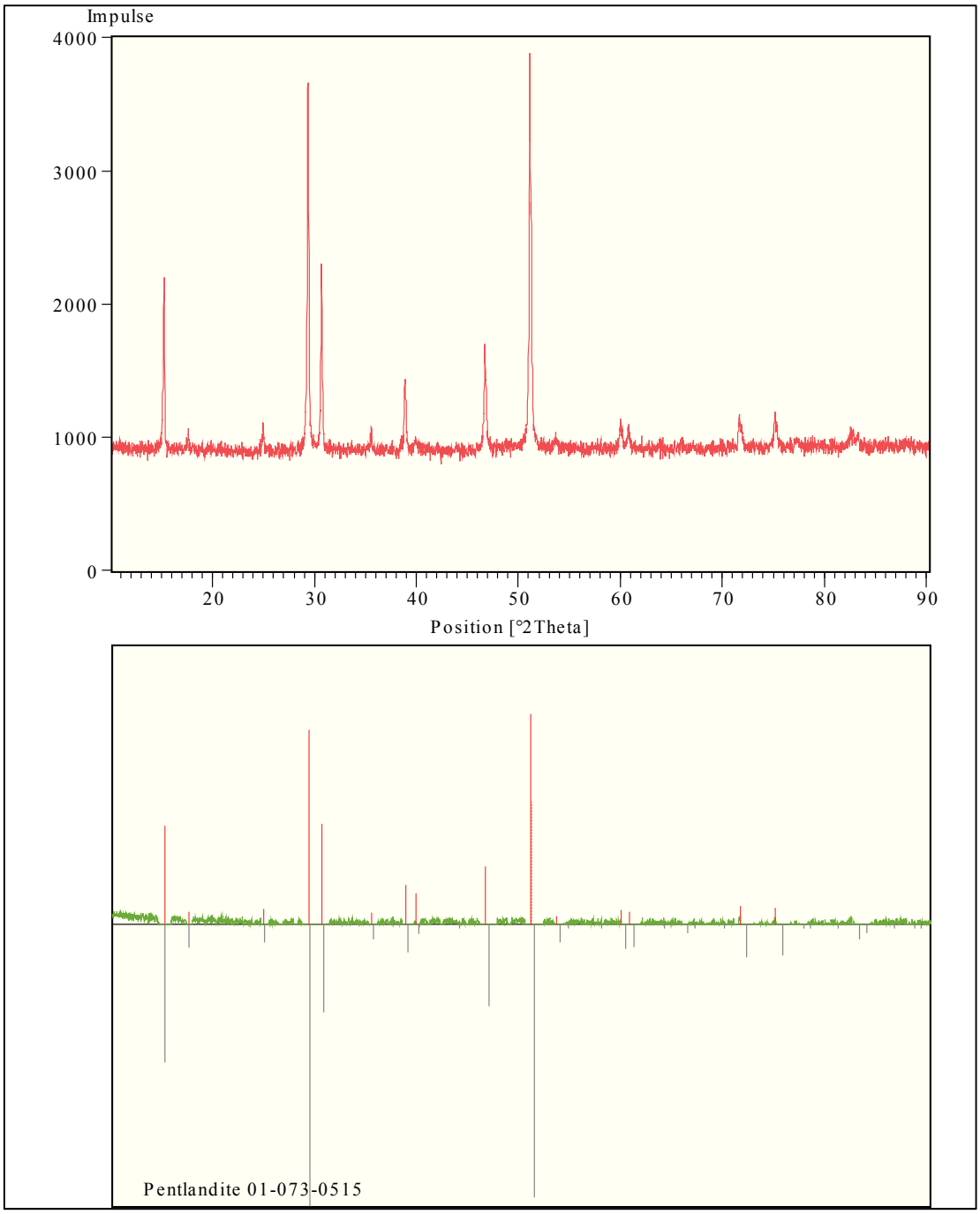

Fig. 4.3. X-ray diffraction pattern of synthesized pentlandite and the powder pattern matches. The database for mineral identification was the PDF (powder diffraction file) of the International Centre for Diffraction Data (ICDD). A list of detected peaks (2theta, d-value, relative intensity) and accepted reference database entries (powder diffraction file number) is provided in the appendix.

The synthesized pentlandite was ground as described for the olivine and a fraction of 50 to 100 µm was used in all experiments.

4.1.3 Orthopyroxene

Purchasable palm-sized orthopyroxene (Müller Mineralien, Saarbrücken, Germany) was broken up into small pieces of 250 to 500 µm, strongly magnetic grains (due to inclusions) were removed and the remaining orthopyroxene was washed with MilliQ®-water (18.2 MΩ * cm @ 25 °C). After drying in an oven at 70 °C, the orthopyroxene grains were hand-picked. Minor mineral inclusions couldn`t be removed by hand picking and were identified by EPMA and XRD analyses (see analyses Tab. 4.4 and Fig. 4.4). For all experiments the 250 to 500 µm size fraction of almost pure orthopyroxene was crushed again and sieved to obtain the 25 to 75 µm fraction. This fraction was washed with MilliQ®-water (18.2 MΩ * cm @ 25 °C) to remove smaller grains and to obtain the desired grain size and then dried in an oven at 70 °C.

The EMPA analyses revealed a homogenous composition of enstatite-rich orthopyroxene with minor mineral inclusions of talc $Mg_3Si_4O_{10}(OH)_2$, hematite Fe_2O_3 and traces of calcite $CaCO_3$ (see Tab. 4.4). The orthopyroxene is homogeneous and characterized by $X_{Mg} = Mg / (Mg + Fe^{2+}) = 0.853 \pm 0.004$ (n = 60, $Mg_{1.706}Fe_{0.294}Si_2O_6$). In the following both terms enstatite and orthopyroxene refer to the enstatite-rich orthopyroxene.

Tab. 4.4. Chemical composition of enstatite-rich orthopyroxene analyzed by EPMA. 60 measurement points at the hand-picked orthopyroxene grains were analyzed. The complete data set is available in the appendix.

	average	abs. std. dev.	formula (oxygens = 4)	
SiO_2	57.13	0.34	Si	1.99
TiO_2	0.03	0.03	Ti	0.00
Al_2O_3	0.09	0.01	Al	0.00
Cr_2O_3	0.01	0.01	Cr	0.00
FeO	9.78	0.25	Fe	0.29
MgO	32.77	0.27	Mg	1.71
MnO	0.07	0.02	Mn	0.00
CaO	0.25	0.07	Ca	0.01
total	100.13	-	total	4.00

Concentrations of Na_2O, K_2O were also measured, but were below detection limit in all analyses.

The XRD analysis confirmed that the orthopyroxene was mainly enstatite (see Fig. 4.4). Minor inclusions of calcite, hematite and talc were determined by comparison of the sample powder diffraction pattern with the powder data file database of the International Center for Diffraction (ICDD). As a result of the insignificant concentrations of the mineral inclusions only the strongest reflex (relative intensity = 100) could be seen.

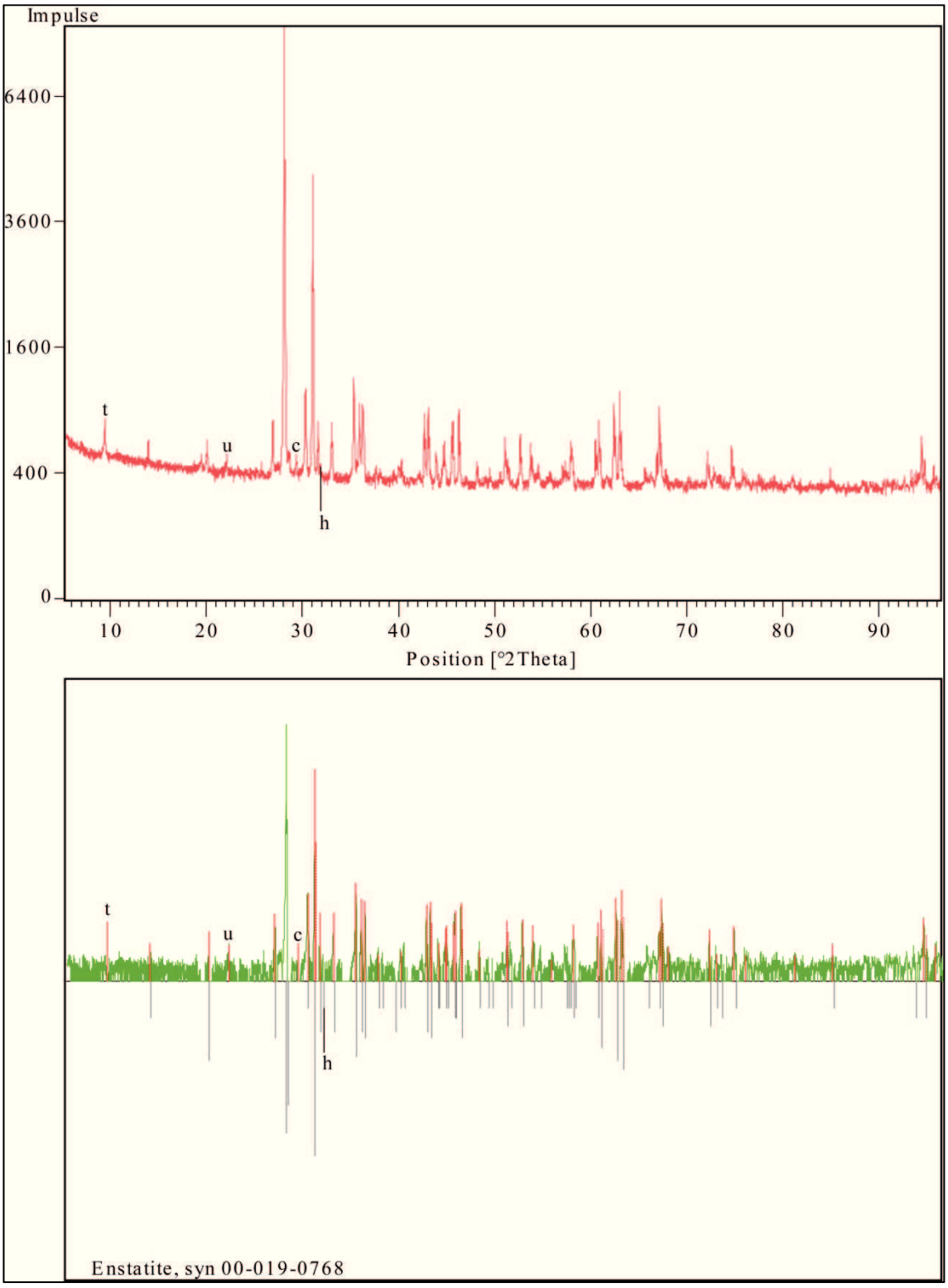

Fig. 4.4. The powder diffractogram of enstatite-rich orthopyroxene. Minor inclusions were c = calcite, h = hematite, t = talc, u = unknown. Peak matching result from the powder data file database (PDF) of the International Center for Diffraction (ICDD). A list of detected peaks (2theta, d-value, relative intensity) and accepted reference database entries is provided in the appendix.

4.1.4 Sodium chloride solution

Artificial sodium chloride solution (wt. 3.2 % = 0.55 mol/l) was prepared for the experiments rather than natural seawater to provide a reproducible composition of known elements. Sodium chloride (Merck Chemicals, Suprapur®, 99.99 %) and MilliQ®-water (18.2 MΩ * cm @ 25 °C) was weighted accurately to produce the sodium chloride solution. Argon gas was bubbled through the sodium chloride solution to remove other dissolved gases.

4.2 Execution of alteration experiments

4.2.1 Fluid-olivine-pentlandite interactions (Exp01 and Exp02)

30 grams of olivine (grain size 50–100 µm) and 100 milligrams of pentlandite (grain size 50–100 µm) were reacted with 65 grams of sodium chloride solution (wt. 3.2 % = 0.55 mol/l) at 320 °C and 400 bar in a gold reaction cell. Two identical experiments (Exp01 and Exp02) were conducted in two available hydrothermal experimental apparatuses described in chapter 2. Fluid samples were taken at intervals of time without interrupting the experiment described in chapter 2.3.11. Pressure and temperature were hold nearly constant during sampling by pumping fluid into the pressure vessel. The first experiment ran 236 days until a leakage in the outside pressure vessel forced us to shut down the heater. The reactants remained in the gold bag for 149 days and the last sampling was done after total 385 days at room temperature. The second experiment ran 424 days without any problem of leakage. During the reaction time, eight fluid samples of Exp01 were extracted and seven fluid samples of Exp02 were taken for chemical analysis. Sample handling, dilution and analysis are described in chapter 3 “Analytical methods”.

4.2.2 Fluid-orthopyroxene-pentlandite interactions (Exp03)

30 grams of enstatite-rich orthopyroxene (grain size 25–75 µm) and 100 milligrams of pentlandite (grain size 50–100 µm) were reacted with 65 grams of sodium chloride solution (wt. 3.2 % = 0.55 mol/l) at 320 °C and 400 bar in a gold reaction cell. In the following, this experiment is referred to as Exp03. Fluid samples were extracted nearly

without disturbing the pressure and temperature of the experiment. The experiment ran 154 days and five fluid samples were taken. Details about sample handling, dilution and analysis of the fluids are given in chapter 3 “Analytical methods”.

4.2.3 Fluid-olivine-orthopyroxene-pentlandite interactions (Exp04)

24 grams of olivine (grain size 25–75 µm), 6 grams of enstatite-rich orthopyroxene (grain size 25–75 µm) and 100 milligrams of pentlandite (grain size 50–100 µm) were reacted with 65 grams of sodium chloride solution (wt. 3.2 % = 0.55 mol/l) at 320 °C and 400 bar in a gold reaction cell. This experiment was identified as Exp04 in this work. The mineral mixture of olivine and orthopyroxene is analogous to that of a harzburgite composition (80 wt. % olivine and 20 wt. % orthopyroxene). Seven fluid samples were taken in the course of this experiment, which was terminated after 130 days. More information on sample handling and analysis is provided in chapter 3 “Analytical methods”.

5. Results

5.1 Foreword

Four experimental investigations of interactions between saltwater and ultramafic rocks were carried out. Two identical experiments with olivine (forsterite Mg#90.9), pentlandite and saltwater (Exp01 and Exp02) were conducted. One experimental run with enstatite-rich orthopyroxene (Mg#85.3) and pentlandite was performed (Exp03). Harzburgite composed of 80 wt. % olivine, 20 wt. % enstatite-rich orthopyroxene and trace pentlandite was used in experiment Exp04. Magnesium number (Mg#) is defined as molar ratio of magnesium to iron ($Mg\# = Mg / (Mg + Fe^{2+}) *100$). All four experiments were conducted at 320 °C and 400 bar. The starting materials and experimental procedures used for these experiments are described in chapter 4.

5.2 Changes in fluid composition

5.2.1 Fluid analyses

An overview of the fluid chemistry is presented in table 5.1. Hydrogen and iron concentrations are in µmol/kg and the other species concentrations are in mmol/kg. In experiment 01 and 02 all cations (expect for ammonium) were analyzed by inductively coupled plasma mass spectrometry (ICPMS) because of their low concentrations. In experiment 03 and 04 the positively charged species (besides ammonium and iron) were determined by atomic emission spectroscopy (AES). Iron was always analyzed by ICPMS because of its low concentration and ammonium was analyzed by flow injection analysis. All used analytical methods are described in chapter 3.

Tab. 5.1. Changes in fluid compositions during experimental runtime.

Experiment	time (days)	pH (25 °C)	H_2 (µmol/kg)	NH_4^+	Σ S	Cl^-	SO_4^{2-}	Na	Si	Mg	Fe (µmol/kg)
						(mmol/kg)					
Exp01	0	5.4	-	-	< DL	573	< DL	524	0.006	0.000	0.05
olivine	1	9.1	258	0.10	0.22	565	0.68	523	0.097	0.089	8.27
+ 0.1 g pentlandite	8	10.2	813	0.37	0.27	554	0.77	531	0.052	0.024	0.33
	29	10.2	1665	0.67	0.40	557	0.85	523	0.029	0.004	0.18
	64	9.3	878	0.79	0.38	551	0.75	523	0.067	0.008	0.37
	92	9.2	5199	0.83	0.39	557	0.84	543	0.032	0.005	0.22
	148	9.1	4273	0.90	0.28	550	0.71	539	0.012	0.013	0.12
	236	9.2	12025	0.99	0.20	543	0.30	540	0.040	0.046	0.55
	385[1)]	8.6	2102	1.01	< DL	550	0.03	505	0.017	3.163	11.17
Exp02	0	5.7	-	-	< DL	561	< DL	519	0.008	0.001	0.17
olivine	2	9.1	687	0.03	0.26	548	0.75	529	0.066	0.012	0.26
+ 0.1 g pentlandite	15	9.8	539	0.10	0.46	580	0.64	531	0.030	0.003	0.13
	50	10.0	5769	0.33	0.58	557	0.65	523	0.029	0.002	0.20
	123	9.9	5478	0.53	0.64	559	0.76	557	0.044	0.001	0.24
	222	9.9	6186	0.82	0.99	551	0.31	510	0.039	0.002	0.20
	371	9.9	1669	0.78	0.77	565	0.17	547	0.082	0.004	1.60
	424	9.7	2396	0.78	0.74	555	0.10	501	0.035	0.001	0.14
Exp03	0	6.6	-	0.02	< DL	536	0.01	487	0.02	< DL	0.01
orthopyroxene	2	5.7	720	0.28	0.29	526	0.07	486	2.29	0.14	5.02
+ 0.1 g pentlandite	25	5.5	2283	0.32	0.40	524	0.10	465	1.81	0.37	14.7
	58	5.2	2636	0.35	0.44	524	0.11	462	1.61	0.45	26.3
	154[2)]	7.2	-	0.37	0.16	511	0.05	458	1.14	2.07	114.0
Exp04	0	5.9	-	0.01	< DL	540	0.01	488	0.01	< DL	0.01
80 % olivine	1	6.9	4649	0.26	0.10	538	0.05	478	1.28	0.03	2.54
20 % orthopyroxene	34	6.0	3374	0.40	0.17	541	0.03	481	1.23	0.07	5.45
+ 0.1 g pentlandite	54	6.5	3054	0.41	0.10	512	0.01	456	1.18	0.08	4.02
	74	6.5	6667	0.46	< DL	536	0.02	498	1.15	0.08	4.99
	105	6.8	10648	0.49	0.08	537	0.01	483	1.06	0.05	3.63
	130	7.2	13694	0.54	0.04	539	0.01	478	0.97	0.04	4.04

[1)] sampling at room temperature, experiment shut off after 283 days because of leakage in the outside pressure vessel (283 days at 320 °C and 400 bar and 102 days at room temperature and pressure)
[2)] sampling at room temperature because Ti-valve was blocked (experiment shut off for one day)
DL = detection limit

5.2.2 pH and hydrogen generation

The pH of the reacting fluid varied at the beginning of the experiments from 5.4 to 6.6 despite the fact that carbon dioxide was removed via bubbling argon gas through the fluid. Mixing the crushed olivine with fluid increased the pH instantly to about 9.0. After about two weeks of reaction time at 320 °C and 400 bar the pH (at 25 °C) of the fluid was 10 in the olivine experiments (see Tab. 5.1 and Fig. 5.1). In Exp01 the pH subsequently decreased to 9.0, but in Exp02 the pH remained nearly constant at 10.0. The last pH measurement of Exp01 (pH = 8.6) was taken after the experiment remained for 102 days at room temperature and the value should only considered as an information value (the last pH value of Exp01 is not shown in Fig. 5.1). The pH in the enstatite-rich orthopyroxene experiment (Exp03) decreased slightly from 6.6 in the

beginning to 5.2 at the end of the experiment. The last pH measurement of Exp03 (pH = 7.2) was taken after the experiment remained for one day at room temperature and the value should only considered as an information value (the last pH value of Exp03 is not shown in Fig. 5.1). In the beginning of the harzburgite experiment (Exp04) the pH was increased by one unit (6.9), afterwards the value dropped a little before the pH rose to the final value of 7.2 (see Tab. 5.1 and Fig. 5.1). The mentioned pH values refer to a temperature of 25 °C measured immediately after sampling of the experiments and not to the in-situ pH.

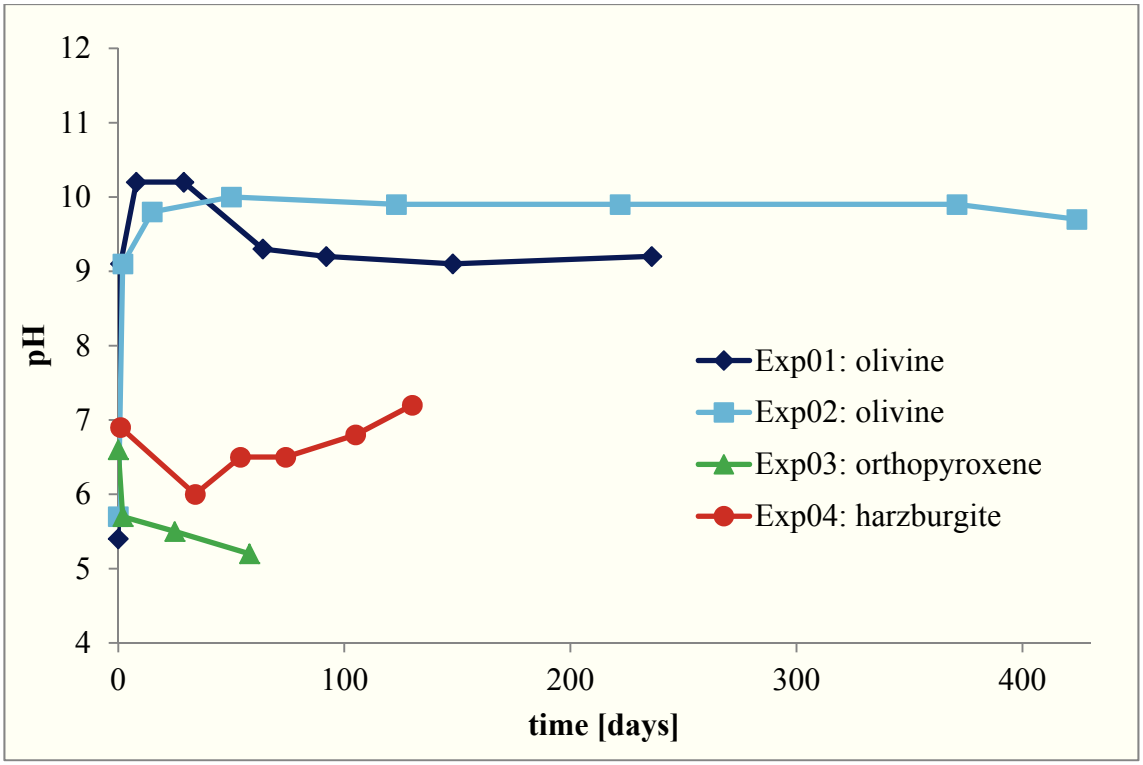

Fig. 5.1. Change in pH (25 °C) during interaction of olivine, orthopyroxene and harzburgite with pentlandite in saltwater.

In Exp01 the dissolved hydrogen concentration increased to a maximum of about 12.0 mmol/kg (Fig. 5.2). The last low value of Exp01 after 385 days is not representative and was not plotted, because at that time the heater was shut off for more than 100 days. At the beginning of the second experiment the hydrogen content was significantly increased and then almost constant over more than 170 days (of about 5.8 mmol/kg). The last two measurements indicated lower concentrations. Exp03 (orthopyroxene) showed increasing hydrogen concentrations to 2.6 mmol/kg after 58 days. Unfortunately the titanium valve was clogged, so that further sampling and analyzing of the fluid to the end of the experiment was not possible. The hydrogen

concentration in Exp04 (harzburgite) increased to 13.7 mmol/kg before the experiment was completed.

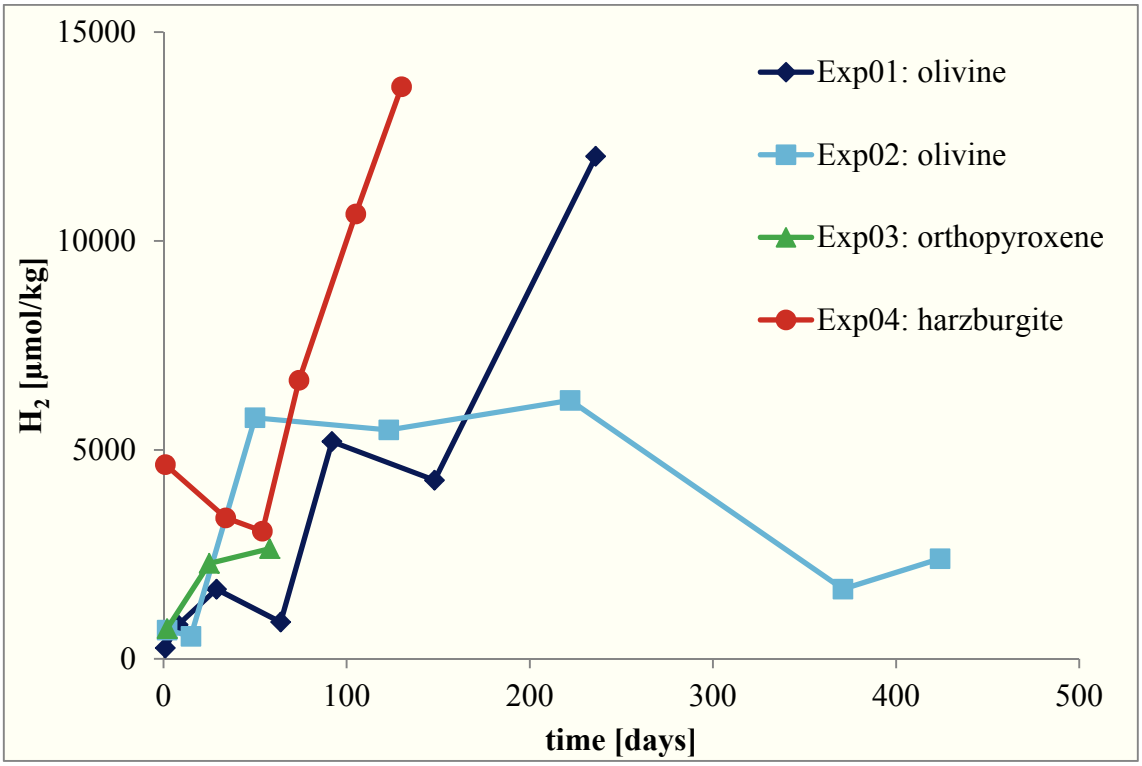

Fig. 5.2. Hydrogen concentration progression with time for the four experiments conducted during the study.

5.2.3 Anions Cl^-, SO_4^{2-}, and S^{2-}

The average concentration of chloride (Cl^-) was 556 mmol/kg in Exp01, 560 mmol/kg in Exp02, 528 mmol/kg in Exp03 and 535 mmol/kg in Exp04 with a relative standard deviation better than 2.0 %. The chloride concentrations of the fluids over a period of time varied slightly in the experiments (Tab. 5.1).

The sulfate (SO_4^{2-}) concentration in Exp01 increased within four weeks to 0.85 mmol/kg (Tab. 5.1 and Fig. 5.3). Then the concentration of sulfate was nearly constant over three months before it decreased to below detection limit after 102 days at room temperature. In Exp02 sulfate concentrations increased from below detection limit to a maximum of 0.75 mmol/kg and then it fell to 0.1 mmol/kg at the end of the experiment. Exp03 yielded almost constant low concentrations of sulfate of about 0.1 mmol/kg and Exp04 had sulfate concentrations much lower than 0.1 mmol/kg over the whole reaction progress.

The initial saltwater was free of sulfide (sum of S^{2-}, HS^- and H_2S). In the beginning of the experiments the sulfide concentrations increased immediately. The highest sulfide concentration was observed in Exp02 after 222 days (1.0 mmol/kg). Sulfide values of Exp01 and Exp03 rose and attained a value of 0.40 mmol/kg in about a month. The harzburgite experiment (Exp04) showed the lowest sulfide concentration of 0.20 mmol/kg. By the end of the experiments the sulfide concentrations tended to drop.

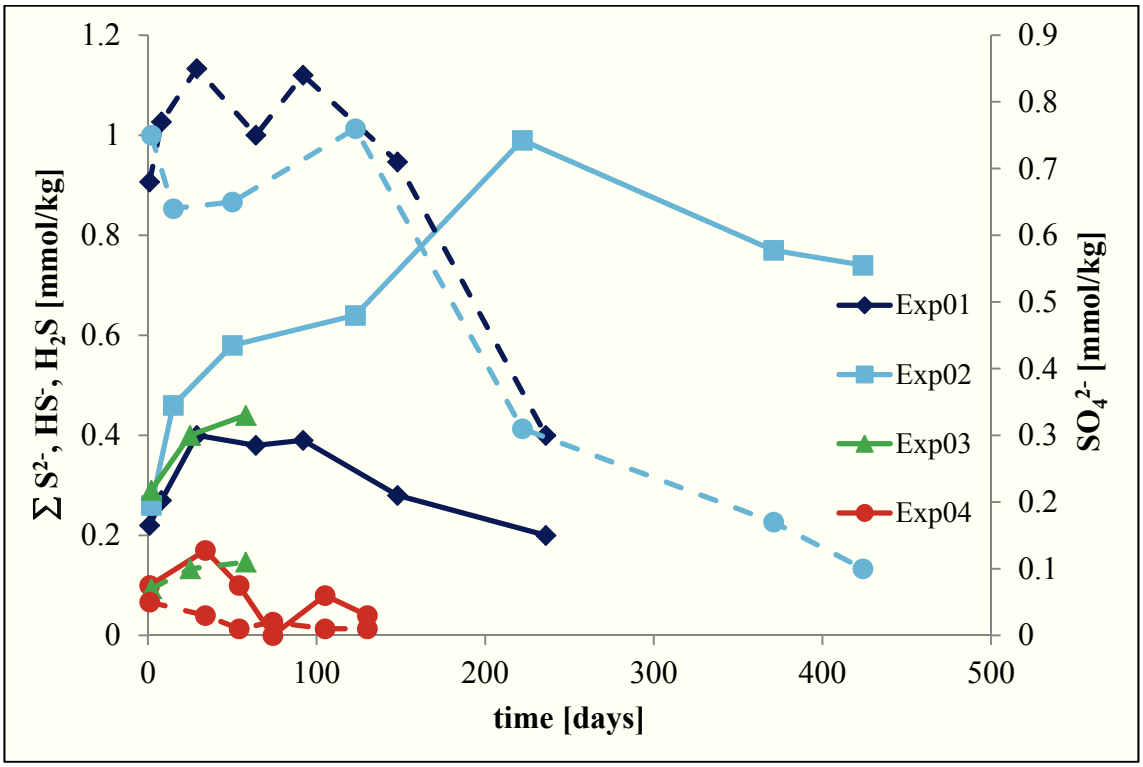

Fig. 5.3. Chronological sequence of the sulfide and sulfate concentrations in the experiments. Continuous lines denote sulfide concentrations and dashed lines indicate sulfate concentrations. The left y-axis refers to sulfide (sum of S^{2-}, HS^- and H_2S) concentrations and the right y-axis refers to sulfate concentrations.

5.2.4 Cations NH_4^+, Na^+, Si^{4+}, Mg^{2+}, Fe^{2+}

Ammonium (NH_4^+) concentrations increased within time and approached near constant values by the end of the experiments (Tab. 5.1 and Fig. 5.4). The highest ammonium concentration was in Exp01 with 1.0 mmol/kg, followed by Exp02 with 0.8 mmol/kg. Exp03 and Exp04 had lower final ammonium concentrations of around 0.3 to 0.4 mmol/kg, but the experimental runtime was shorter so that the values could possibly have increased with time.

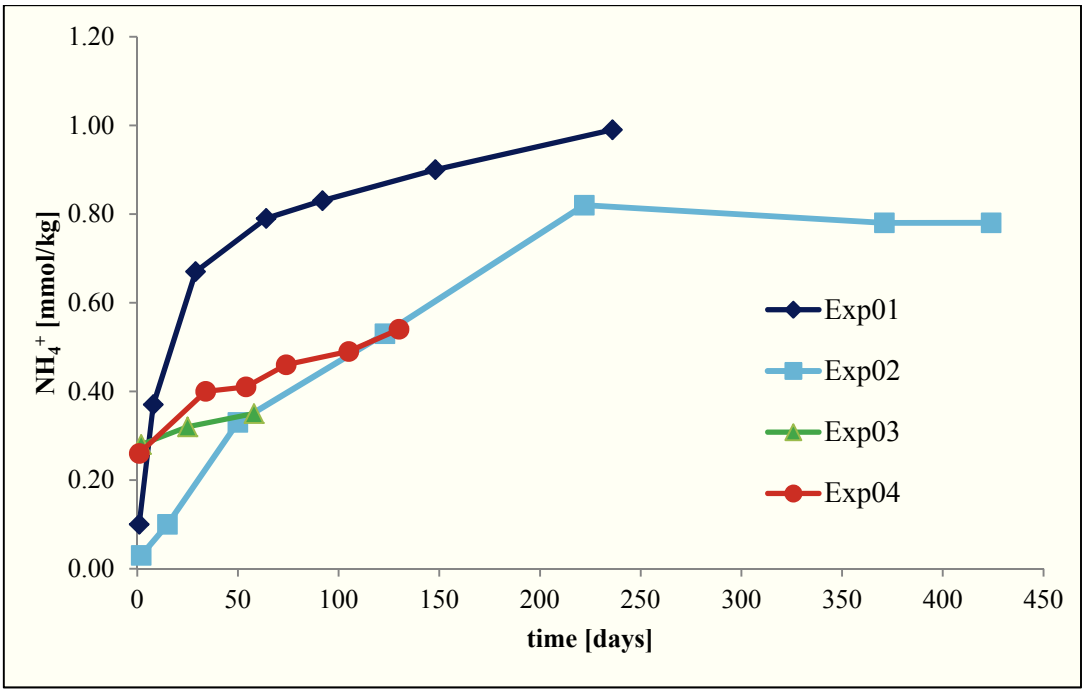

Fig. 5.4. Changes of dissolved ammonium with time in the four experiments.

The average value of sodium concentration of nine measurements in Exp01 over about twelve months was 528 mmol/kg and the average of eight measurements over 14 months in Exp02 was 527 mmol/kg both with a relative standard deviation better than of 3.5 % (Tab. 5.1). Five analyses in Exp03 yielded a sodium average value of 472 mmol/kg over five months experimental time and 480 mmol/kg sodium in Exp04 in four months of reaction time with saltwater. The relative standard deviation of the sodium analyses in Exp03 and Exp04 was better than 2.9 %. Sodium concentrations were somewhat lower than of the initial solution (566 mmol/kg).

Dissolved silica (SiO_2 (aq)), magnesium (Mg) and iron (Fe) increased initially in all experiments relative to the initial fluid composition (Tab. 5.1 and Fig. 5.5). After one month the concentrations of silica, magnesium and iron remained relatively constant throughout the experiments. The olivine long-term experiments (Exp01 and Exp02) showed toward the end of the experiments changes in the SiO_2 (aq), Mg and Fe fluid chemistry. The quantity of dissolved silica, magnesium and iron varied significantly in the different systems. The olivine experiments had the lowest concentrations. The harzburgite experiment yielded considerably higher contents of silica, magnesium and iron and the orthopyroxene assay produced the highest dissolved silica.

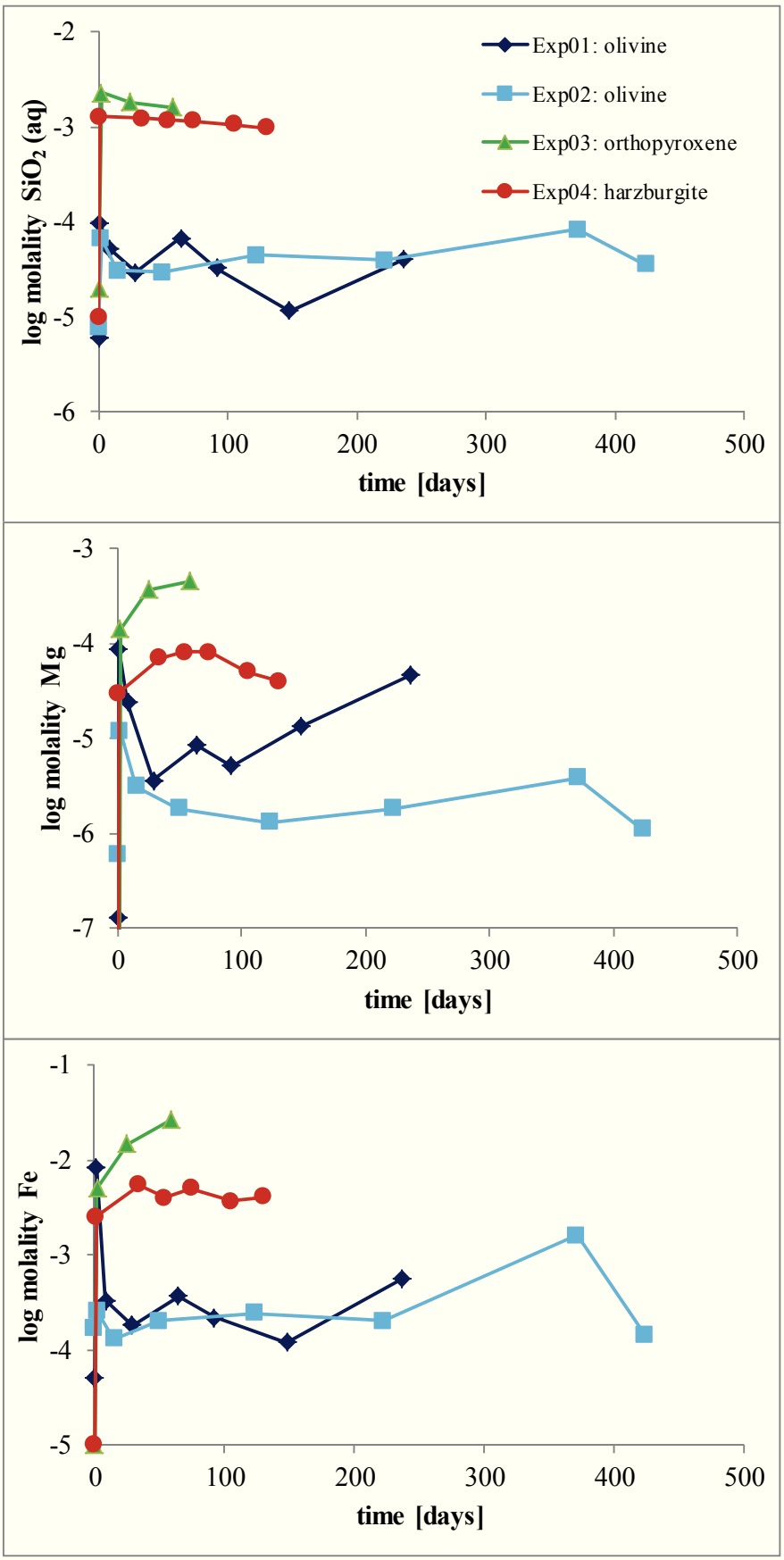

Fig. 5.5. Measured concentration variations of dissolved SiO_2 (aq), Mg and Fe in fluid as a function of time.

5.2.5 Changes in fluid composition after cooling

Fluids were sampled from Exp01 (olivine) and Exp03 (orthopyroxene), after the gold reaction cell was cooled to room temperature at the end of the experiment time. Significant changes in fluid chemistry had taken place. For example the magnesium concentrations achieved the highest measured value (see Tab. 5.1). This increase is likely due the dissolution of brucite in Exp01.

5.3 Characterization of alteration products

5.3.1 Olivine-pentlandite-saltwater (Exp01 and Exp02)

Scanning electron microscope (SEM) images and elemental abundances determined with the energy-dispersive X-ray detector (EDX) showed that the olivine surface was completely altered to brucite. Olivine crystals with an outer layer of brucite were commonly overgrown with serpentine (Fig. 5.6). Magnetite was developed in various crystal shapes and sizes (diameter from 1 to 20 μm) on the top of brucite layer and it was also partially overgrown with serpentine. Some magnetite crystals were isometric and octahedral in shape. Most magnetite grains showed a truncated octahedral habit. The hydrothermally synthesized serpentine observed in the experiments was chrysotile (identified by XRD). Small fibers of chrysotile in a rolled-cylindrical structure and conically wrapped fibrils were visible. Brucite grew as a layer on the olivine surfaces and as lamellar foliated fine sheaths (Fig. 5.6). Additionally, rare grains of secondary sulfides replacing pentlandite were visible in the SEM images.

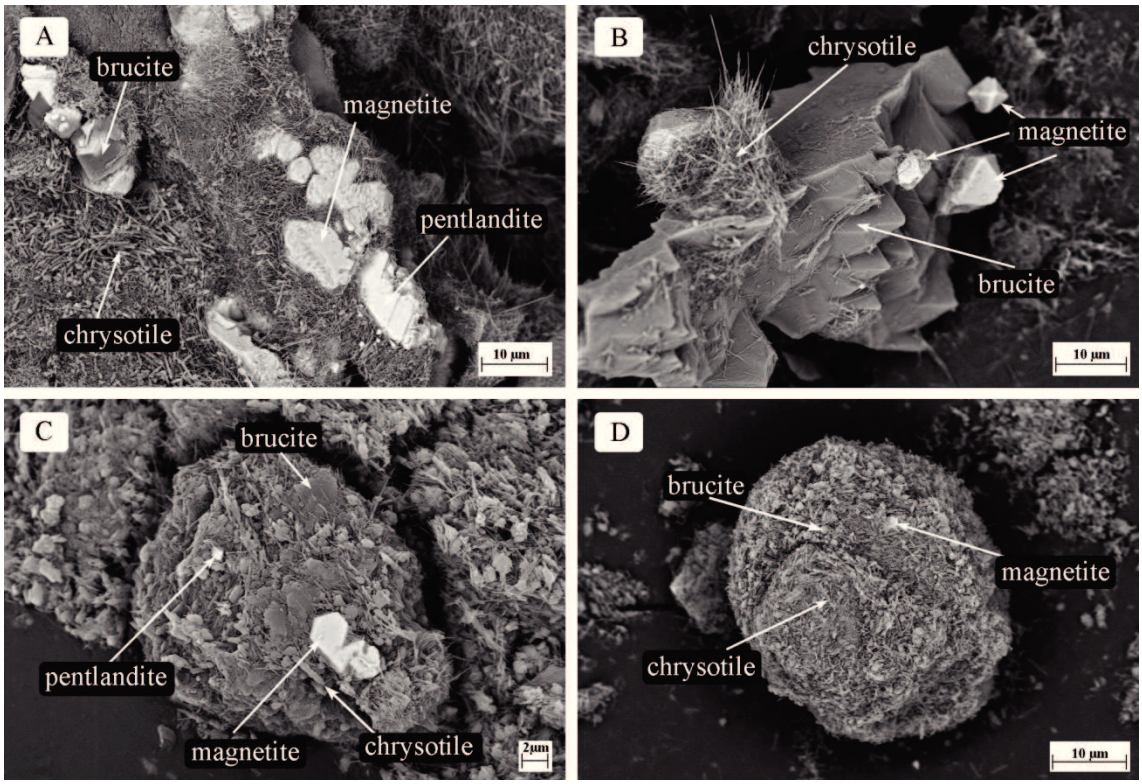

Fig. 5.6. SEM images of reaction products from alteration experiments of olivine and pentlandite. (A) and (B) after 385 days in Exp01. (C) and (D) after 424 days in Exp02.

Back-scattered electron images in Fig. 5.7, image A, show the relict of olivine, serpentine and brucite. Brucite grew as corona around olivine grains (Fig. 5.7, image B). The pentlandite reacted to form Ni-rich pentlandite (Fe^{2+} to Ni ratio of about 0.4), heazlewoodite Ni_3S_2 and magnetite. The sulfide grains are often rimmed by magnetite (Fig. 5.7 images C and D).

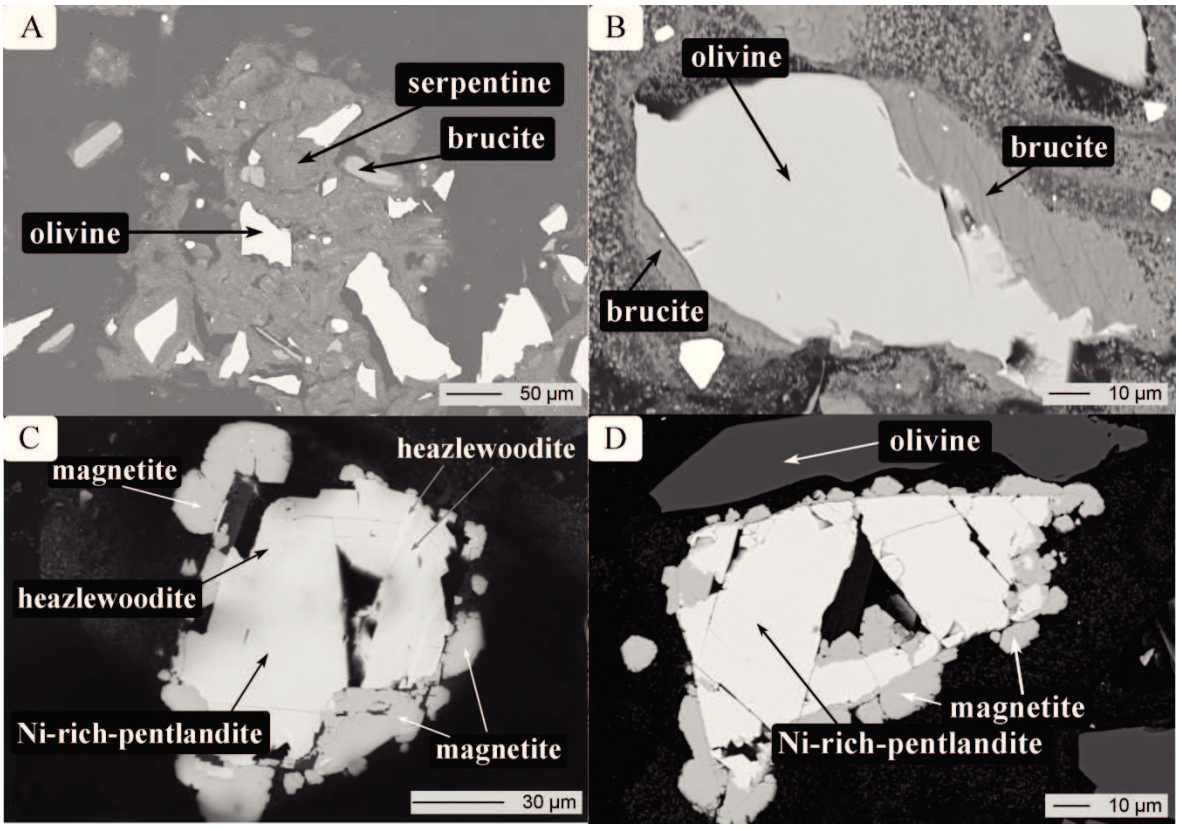

Fig. 5.7. Backscattered electron images of reaction products in Exp01 and Exp02.

Element mapping (Fig. 5.8) illustrates the element variations in the concentration of selected elements in polished sections. Si, Mg, Ni und Fe were selected to depict olivine, brucite, magnetite and Ni-Fe-alloys.

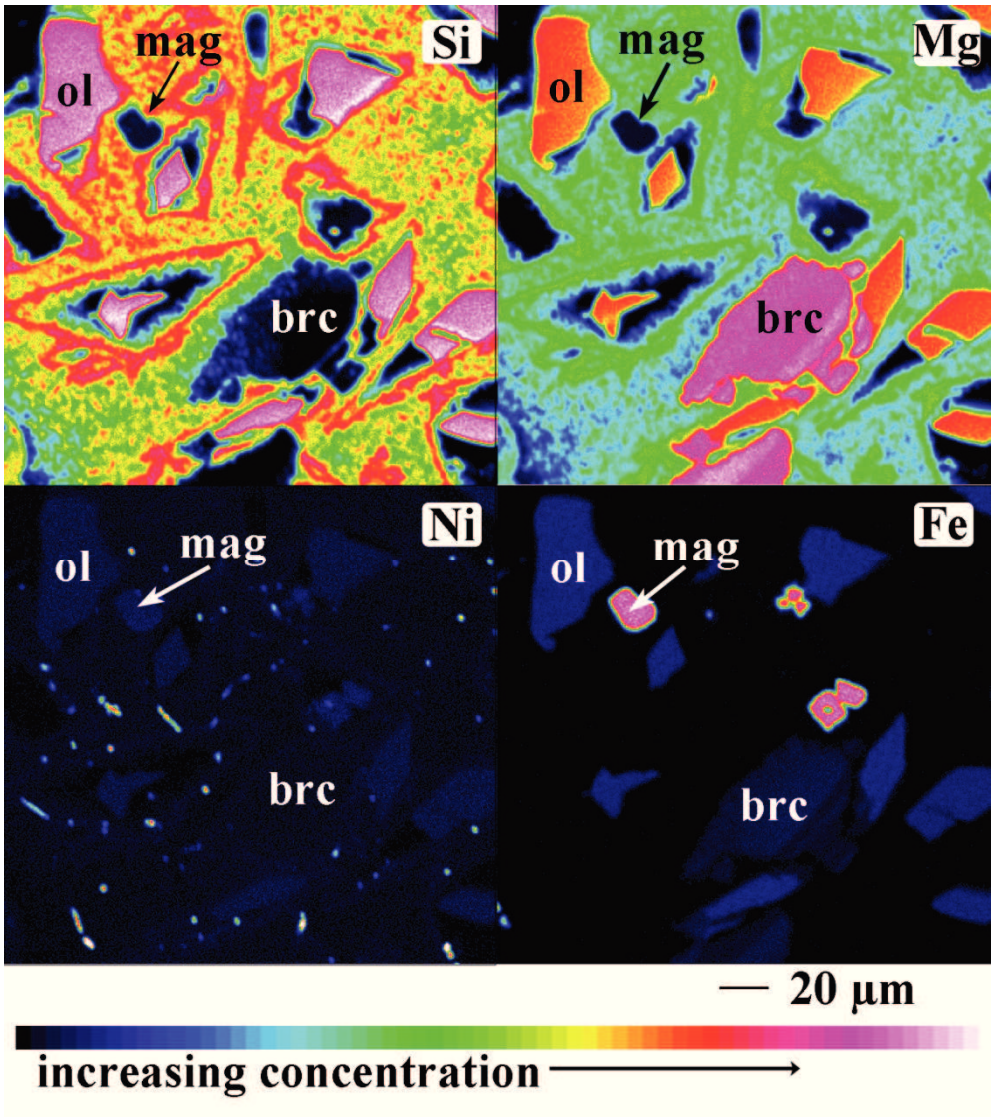

Fig. 5.8. Element mapping of the minerals after experimental runtime in Exp02. Abbreviations: ol, olivine; brc, brucite; mag, magnetite.

The reaction products were quantitatively analyzed by electron microprobe (data are listed in the appendix). Many microprobe analyses had low totals, because of the small grain size. The low totals result when the excited volume of sample includes mineral grains and the embedding epoxy. However, the evaluation of element ratios from this data provided insights into the changing phase relations during serpentinization and in particular the partitioning of iron and magnesium amongst different phases. The serpentine formed in Exp01 had an average magnesium number (Mg#) of 98.7 ± 0.19 (n = 18). Exp02 yielded a serpentine with a magnesium number (Mg#) of 98.9 ± 0.13 (n = 15). The magnesium number was calculated as molar ratio: Mg# = Mg / (Mg + Fe^{2+}) *100. The observed serpentine was more magnesian than the initial olivine (Mg#90.9).

The variability in magnesium contents of serpentine in the two identical experiments (Exp01 and Exp02) was minor and ranges from Mg# of 98.4 to Mg# of 99.2. The brucite formed in Exp01 had an average magnesium number of Mg#96.3 ± 1.4 (n = 11) and in Exp02 brucite had an average Mg# of 96.0 ± 1.1 (n = 15). The standard deviation of the magnesium number in brucite was greater than in serpentine.

Cation proportions derived from mircroprobe analysis point to $FeMg^{1-}$ as the main exchange mechanism in brucite and serpentine. The balanced serpentinization reactions in the two olivine experiments (Exp01 and Exp02), taking into account the average compositions of primary and secondary phases, are:

Exp01 balanced from microprobe analysis data:

$$Mg_{1.818}Fe_{0.182}SiO_4 + 1.400\ H_2O = 0.500\ Mg_{2.962}Fe_{0.038}Si_2O_5(OH)_4 + 0.350\ Mg_{0.963}Fe_{0.037}(OH)_2 + 0.050\ Fe_3O_4 + 0.050\ H_2$$

Exp02 balanced from microprobe analysis data:

$$Mg_{1.818}Fe_{0.182}SiO_4 + 1.399\ H_2O = 0.500\ Mg_{2.967}Fe_{0.033}Si_2O_5(OH)_4 + 0.348\ Mg_{0.960}Fe_{0.040}(OH)_2 + 0.051\ Fe_3O_4 + 0.051\ H_2$$

The use of three decimal places in the formulation of serpentinization reactions in this work is necessary for balancing and does not reflect the analytical accuracy.

Pentlandite lost iron to form a phase of Ni-rich pentlandite with an average composition of $Fe_{2.5}Ni_{6.5}S_8$. Under increased H_2(aq) activities, heazlewoodite became the stable Ni-sulfide and pentlandite reacted to heazlewoodite and magnetite:

$$Fe_{4.5}Ni_{4.5}S_8 + 6\ H_2O = 1.5\ Ni_3S_2 + 1.5\ Fe_3O_4 + H_2(aq) + 5\ H_2S(aq)$$

The chemical compositions of the sulfides were analyzed by electron microprobe. The results are plotted in the S-Ni-Fe ternary diagram (Fig. 5.9). The complete data set is presented in the appendix.

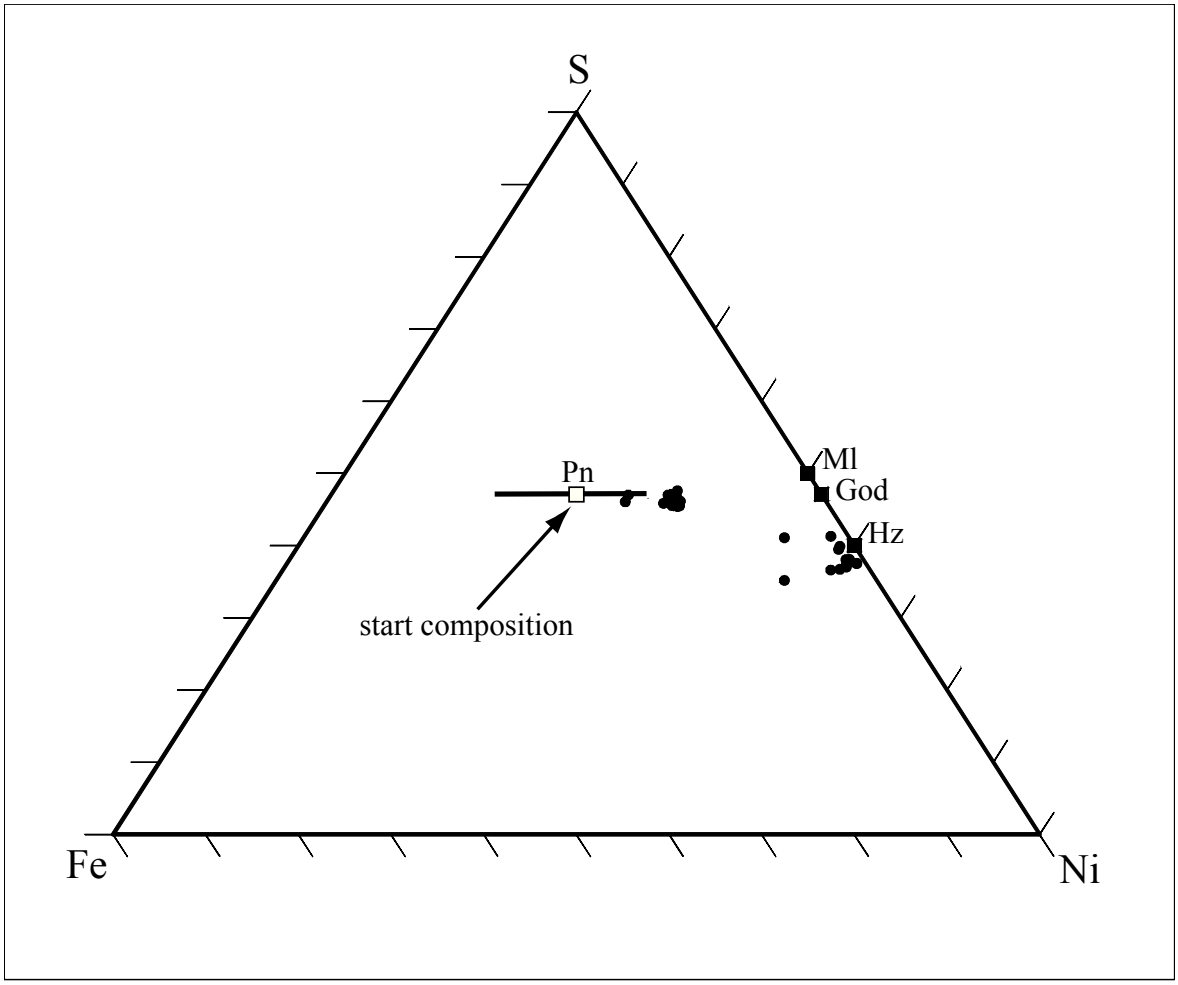

Fig. 5.9. The endmembers of nickel sulfides (squares) are plotted with the EPMA analyses data (dots) of the hydrothermally altered pentlandite (molar ratio). The solid line represents the continuous solid solution of natural pentlandite at 400 °C (Misra and Fleet, 1973). Abbreviations: Pn = pentlandite $Ni_{4.5}Fe_{4.5}S_8$, Ml = millerite NiS, God = godlevskite Ni_9S_8, Hz = heazlewoodite Ni_3S_2.

X-ray powder diffraction (XRF) investigation of the altered rock powder of Exp01 and Exp02 shows unreacted olivine besides chrysotile, brucite, and magnetite. No other phases were detected in the hydrothermally altered assemblage by XRD. The sulfides could not be identified in the XRD patterns because of the low abundance (see Fig. 5.10). A list of detected peaks (2theta, d-value, relative intensity) and accepted reference database entries (powder diffraction file number) is provided in the appendix.

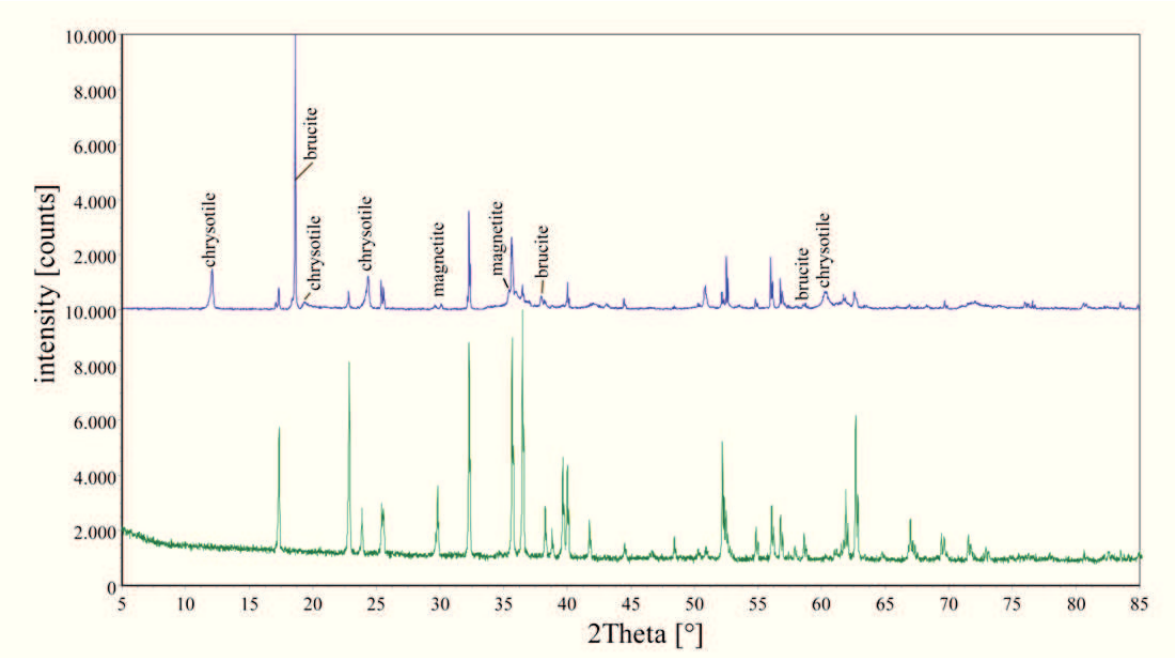

Fig. 5.10. XRD patterns of fresh (green peaks) and serpentinized olivine (blue peaks) after 14 months hydrothermal alteration (Exp02). Chrysotile, brucite and magnetite diffraction peaks are identified besides unreacted residual olivine. The diffractograms are scaled combined: the highest peak is defined as the 100 % peak and the intensity of all other peaks are measured as a percentage of the 100 % peak.

The thermogravimetric analysis confirmed the formation of brucite and serpentine (see 5.4 “Mass balance of the reaction”)

5.3.2 Orthopyroxene-pentlandite-saltwater (Exp03)

Scanning electron microscope (SEM) examinations showed that the initial orthopyroxene grains were overgrown with a fibrous thin layer of talc and chrysotile as identified by powder X-ray diffraction data and thermogravimetric analysis (Fig. 5.11). The coating was too thin to measure the Si-Mg-Fe with the energy-disperse X-ray detector of the SEM. Also the attempt to separate the thin layer of talc and serpentine in an ultrasonic bath was not successful as the products were too strongly attached to the starting orthopyroxene. Besides talc and chrysotile, magnetite was also present as alteration product. Magnetite grew in several crystal habits, but many grains were anhedral (Fig. 5.11, SEM image C).

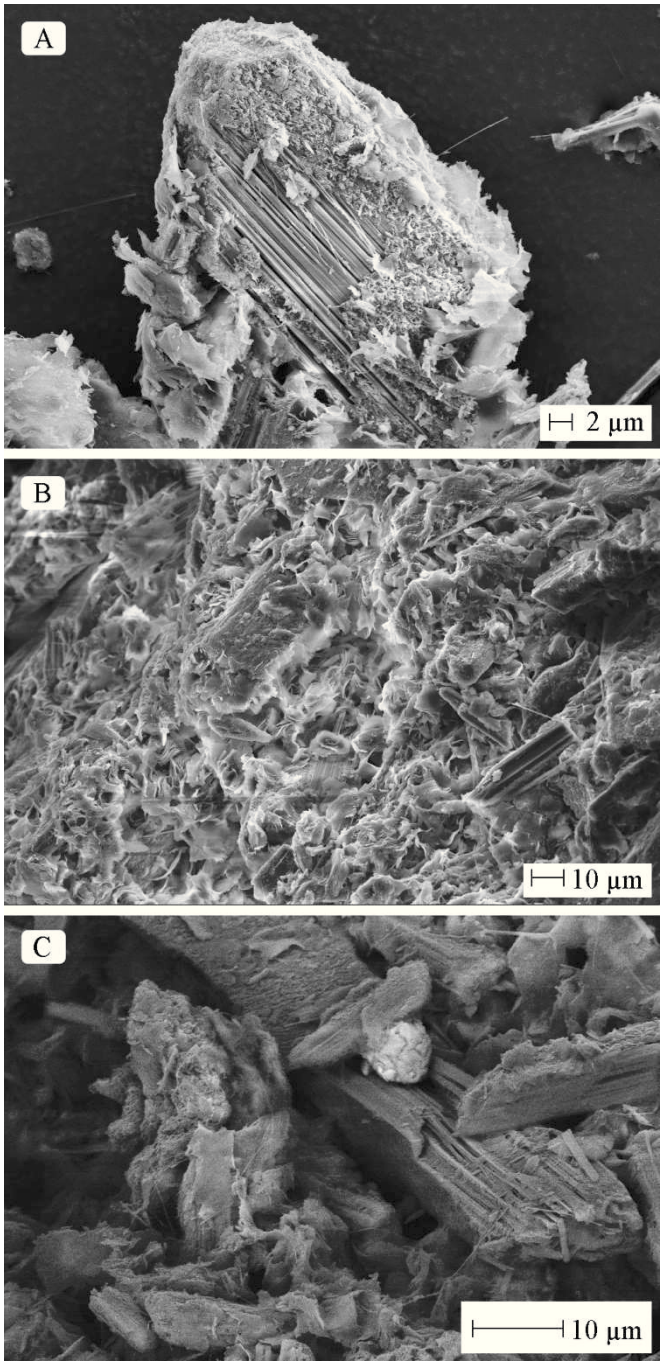

Fig. 5.11. Scanning electron microscope images of experimental products in the orthopyroxene hydrothermal alteration experiment (Exp03). Image (A) shows a grain of orthopyroxene covered by a thin layer of talc and serpentine. The orthopyroxene surfaces are partly dissolved along cleavage planes. (B) Fractures in the orthopyroxene grains were filled by chrysotile and talc. Image (C) shows a grain of anhedral magnetite between altered orthopyroxene grains.

Back-scattered electron images taken from polished sections visualize small (submicron scale) interwoven fibrous secondary products around the orthopyroxene grains (Fig. 5.12, image A). The initial pentlandite underwent incipient alteration, visible as small seam around the pentlandite (Fig. 5.12, image B).

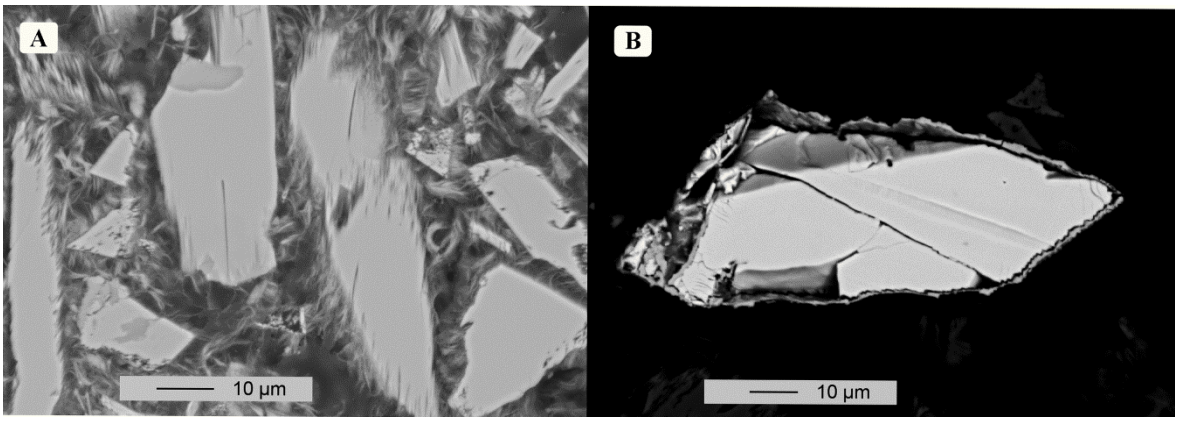

Fig. 5.12. (A) Backscattered electron microprobe images of altered orthopyroxene (Exp03). Chrysotile and talc grow as fibers on the surfaces of orthopyroxene. (B) Pentlandite taken from Exp03 (orthopyroxene experiment) indicates slight alteration of the surrounding grain boundary and formation of magnetite after 5 months reaction time at 320 °C and 400 bar.

Quantification of the composition of these alteration products with the electron microprobe failed because the aggregate size and density of alteration products was unsuitable for EMPA.

X-ray powder diffraction patterns of the starting orthopyroxene compared to patterns of the reaction products showed three phases: initial orthopyroxene, talc, and chrysotile (Fig. 5.13). The starting orthopyroxene contained traces of talc. The X-ray diffraction analyses of the transformed orthopyroxene revealed greater amounts of talc (peak at 2theta between 9 and 10 degrees). The serpentine was identified as chrysotile by peak matching routine using accepted reference database entries. No other phases were detected in the hydrothermally altered assemblage by XRD. The thermogravimetric analysis confirmed the formation of serpentine and talc (see 5.4 “Mass balance of the reactions”).

Pentlandite and magnetite was not found in the diffraction pattern because of its scarcity, but the scanning electron microscope (SEM) and magnetic measurements clearly showed the presence of magnetite. Accepted reference database entries (powder diffraction file number) and a list of detected peaks (2theta, d-value, relative intensity) are provided in the appendix.

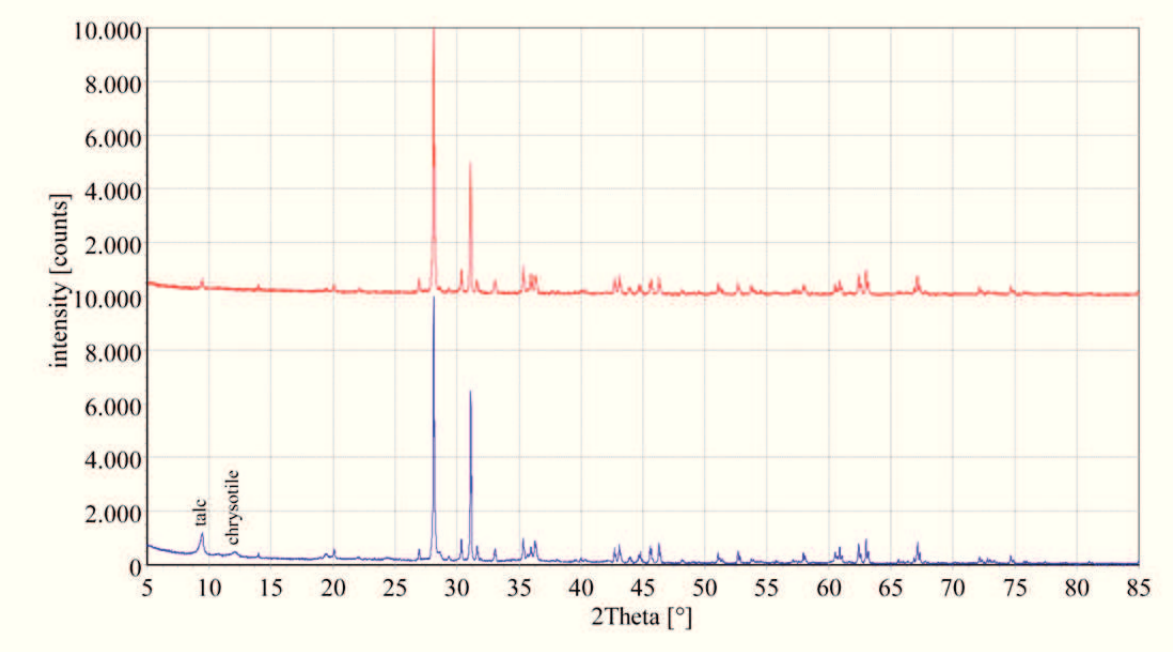

Fig. 5.13. XRD diffractogram of fresh (red patterns) and altered (blue patterns) orthopyroxene (Exp03). Chrysotile and talc diffraction peaks are identified besides unreacted residual orthopyroxene. The diffractograms are scaled combined: the highest peak is defined as the 100 % peak and the intensity of all other peaks are measured as a percentage of the 100 % peak.

5.3.3 Harzburgite-pentlandite-saltwater (Exp04)

The secondary minerals characterization of the harzburgite-pentlandite-saltwater experiment by scanning electron microscope (SEM) imaging revealed that chrysotile and magnetite were formed. It is worth noting that some initial and secondary minerals were clumped together to form large aggregates with a diameter of up to one centimeter. The average composition of these clusters was identical to the rest of altered powder as indicated by X-ray powder diffraction investigation. The starting olivine and relicts of orthopyroxene were overgrown by chrysotile in a rolled cylindrical structure as conically wrapped small fibers (Fig. 5.14). The same structure of chrysotile was also found in the pure olivine experiments (Exp01 and Exp02). The orthopyroxene was strongly corroded and mostly dissolved along cleavage planes. Olivine grains show smooth surfaces and apparent little reaction in the backscattered electron images (Fig. 5.14, image A). Pentlandite underwent hardly any alteration (Fig. 5.14, image B). Magnetite was formed in various crystal habits, often with a truncated octahedral crystal shape (Fig. 5.14, image C).

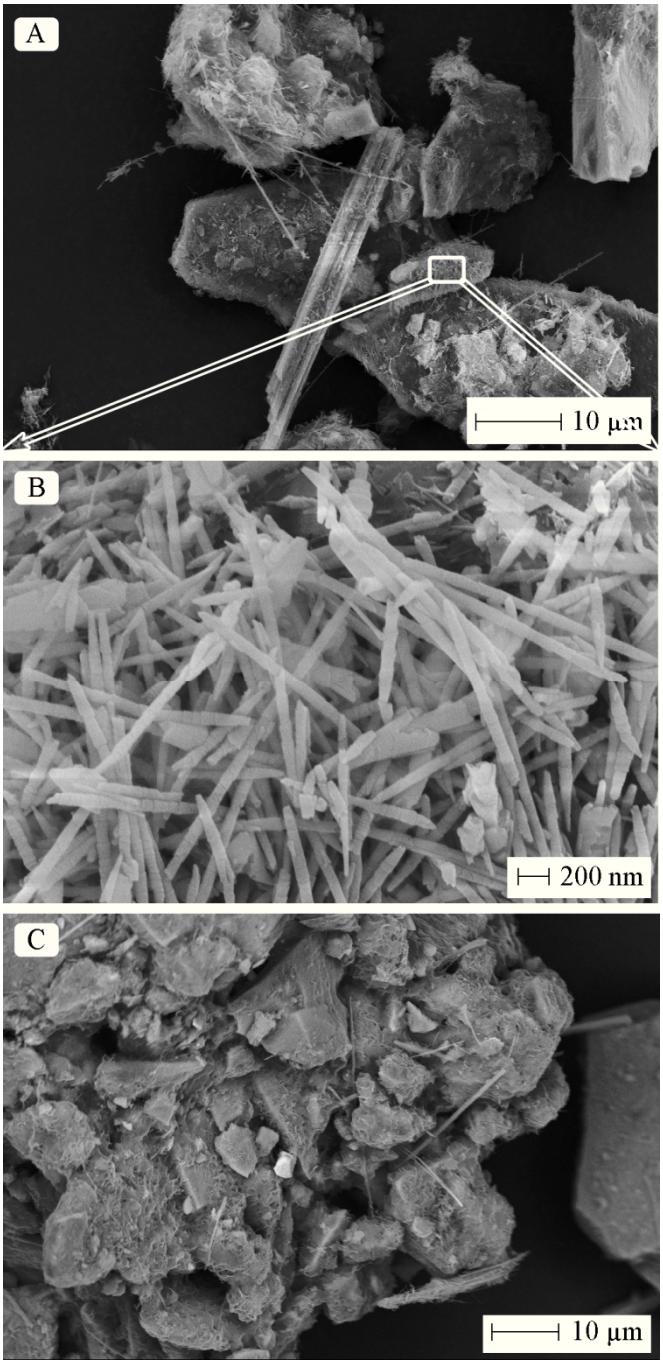

Fig. 5.14. SEM images of the reaction products in the harzburgite experiment (Exp04). (A) Olivine and relicts of orthopyroxene are overgrown by chrysotile. (B) A zoom-in image (A) shows conically wrapped small fibers of chrysotile. The zoom-in range of image (A) is marked with the white rectangle. The chrysotile fibers were < 100 nm in diameter and about 1.5 µm long. (C) Orthopyroxene and olivine grains overgrown with chrysotile and newly formed magnetite with a truncated octahedral crystal shape.

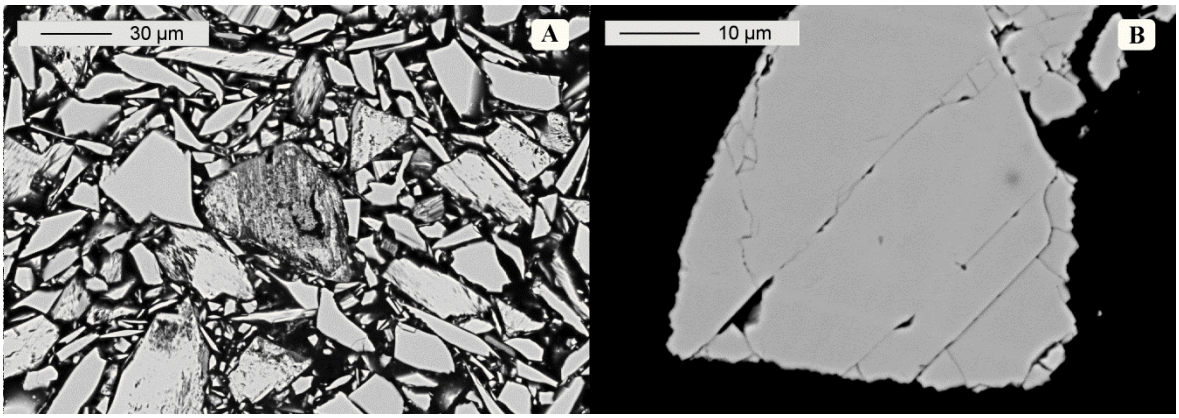

Fig. 5.15. (A) Backscattered electron images showing apparently unreacted olivine and corroded orthopyroxene after 4 months at 320 °C and 400 bar (Exp04). (B) Pentlandite underwent hardly any alteration.

The thin coatings of alteration phases on the surfaces of primary educts could not be analyzed by electron microprobe analyses (EPMA) or by the integrated X-ray detector of the SEM. X-ray powder diffraction revealed that the reaction product was mainly chrysotile (Fig. 5.16). Magnetite was not found in the diffractogram because of its scarcity, but the scanning electron microscope (SEM) and magnetic susceptibility measurements clearly showed the presence of magnetite. Olivine was apparently unreacted (i.e., did not show alteration products attached to it) and the orthopyroxene is more strongly dissolved as evidenced by elimination of characteristic X-ray patterns of this phase. The thermogravimetric analysis confirmed the formation of mainly serpentine (see 5.4 “Mass balance of the reactions”). However, the lack of talc in the reaction products indicates that olivine must have reacted.

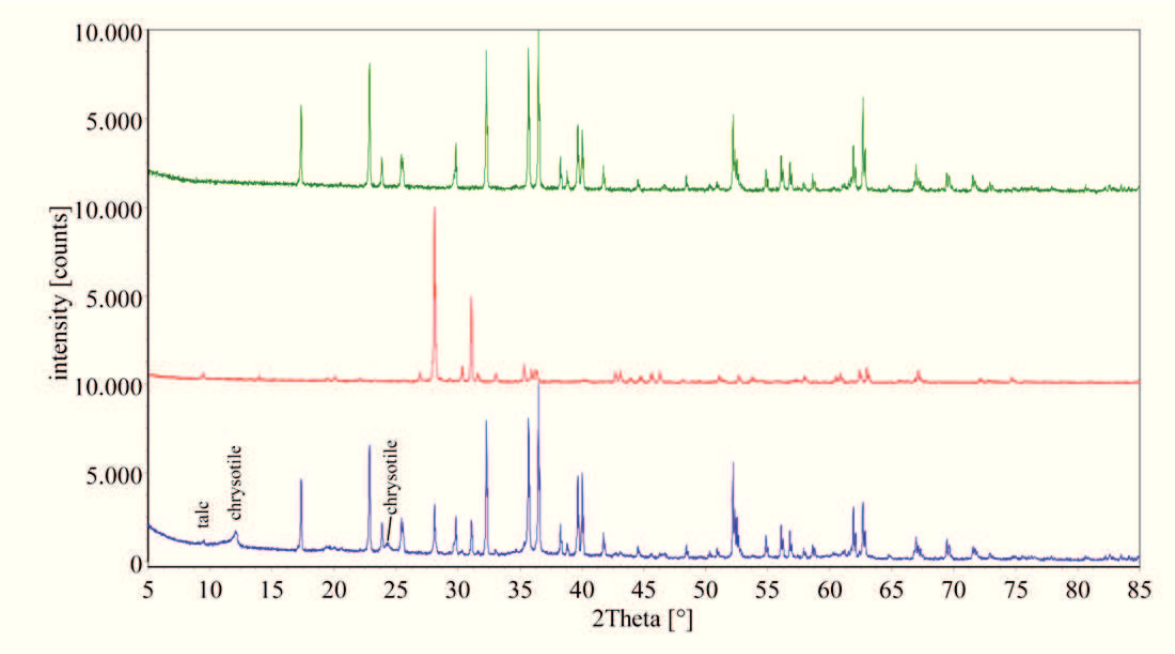

Fig. 5.16. XRD patterns of initial olivine (green peaks), orthopyroxene (red peaks) and formed secondary minerals of harzburgite-saltwater-experiment (Exp04, blue peaks). The diffractograms are scaled combined: the highest peak is defined as the 100 % peak and the intensity of all other peaks are measured as a percentage of the 100 % peak.

5.4 Mass balance of the reactions

The amounts of reaction products were calculated by thermogravimetric analyses using weight loss during dehydration (Fig. 5.17). The TG and DSC curves for the two olivine experiments (Exp01 and Exp02) were similar, but the weight loss was different because of the different reaction progress (Exp01: 9.5 months and Exp02 > 14 months reaction time). The thermogravimetric curves of the olivine experiments show two steps with significant mass changes and three caloric effects. In general the dehydration of brucite starts at about 300 °C. In the olivine experiments the mass loss due to dehydration of brucite amounts 0.97 % in Exp01 respectively 1.5 % in Exp02. Serpentine dehydrats at about 530 °C and a weight loss of 3.0 % in Exp01 and 5.0 % in Exp02 occurred. Differential scanning calorimetry (DSC) measurements were done simultaneously to the thermogravimetric analyses. Corresponding to both weight drops in the the TG curve the DSC-curve indicates two endothermic processes plus an additional exothermic sharp peak at 825 °C. The first two endothermic peaks are associated with dehydration reactions. The exothermic peak specified crystallization of residual meta-chrysotile

$(Mg,Fe)_3Si_2O_7$ (amorphous anhydrous material) into olivine $(Mg,Fe)_2SiO_4$ typically observed in TG analyses (e.g., Falini et al., 2004; Viti, 2010).

The thermal decomposition of powered reactions products in the orthopyroxene experiment (Exp03) also showed two stages of significant weight loss through dehydration. One weight loss (by 0.7 %) occurred at 530 °C where serpentine releases the chemically bound water and another weight loss (by 0.4 %) takes place at 800 °C indicating the breakdown of talc. The DSC-curve in Exp03 showed no endothermic peaks as water loss occurred cause of the small amount of serpentine forming during the 5 months of experimental runtime. A small exothermic peak of meta-chrysotile crystallization was present. The harzburgite experiment (Exp04) showed TG curve with sudden weight drop (by 2 %) at only one temperature (530 °C). This result confirms the XRD data indicating that only serpentine was formed. An endothermic peak in the DSC-curve was noticable as the exothermic characteristic peak at 825 °C. The dehydration-related weight losses indicate that 27.9 % of the olivine was reacted in Exp01 (during 9.5 months). Exp02 ran over 14 months and 46.0 % olivine were converted. Exp03 lasted over 5 months and 15.3 % of the starting orthopyroxene were altered. 16.1 % of the harzburgite was reacted in the 4 months of duration of Exp04. Triplicate thermogravimetric analyses were done and average abundances were used in the mass balance calculations. Relative standard deviations were < 2.0 % for brucite, < 4.0 % for serpentine, and < 3.1 % for talc.

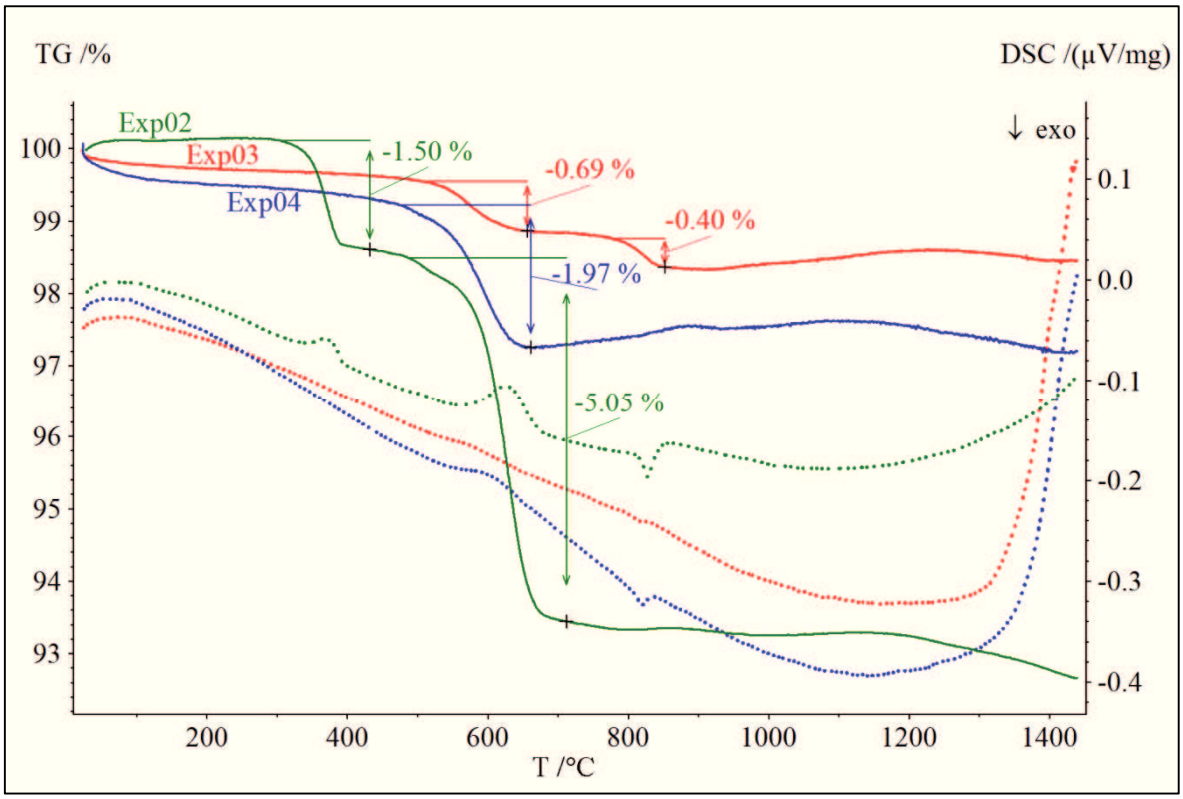

Fig. 5.17. Thermogravimetric curves of alteration products. Green lines represent the olivine reaction (Exp02), red lines indicate the orthopyroxene alteration (Exp03) and blue lines the harzburgite experiment (Exp04). Continuous lines depict weight loss during heating (TG) and dotted lines represent the differential scanning calorimetry curve (DSC). Beginning of weight loss at 300 °C shows brucite, at 530 °C serpentine and at 800 °C talc.

5.5 Magnetic susceptibility

In addition, the bulk alteration products were measured for magnetic susceptibility to quantify the amount of magnetite formed. The relation between susceptibility and amount of magnetite depends on the grain size. Because magnetite grain size is variable, the amount of magnetite calculated from susceptibility measurements is semi-quantitative only. As expected, the longest running experiment, Exp02 with olivine, generated the most magnetite of about total 4.5 wt. % in the bulk material. Exp01 has circa 2.5 wt. % after a shorter experimental run time of 4.5 months. The orthopyroxene experiment (Exp03) produced around 0.3 wt. % magnetite while magnetite concentration in the harzburgite experiment (Exp04) was twice as higher (0.6 wt. %). The greater magnetite production in the harzburgite experiment is remarkable, since the run time of Exp04 was one month shorter than that of Exp03.

6. Phase relations

6.1 Geochemical modeling

Thermodynamic equilibrium constants (log K values) of silica-, sulfur and hydrogen dependent equilibria were calculated with the SUPCRT92 software code (Johnson et al., 1992). The database of SUPCRT92 used for this study was supplemented with a thermodynamic set of data implemented by Klein and Bach (2009) and Klein et al. (2009), because some essential minerals of the Fe-Ni-O-S system were missing in the standard database of SUPCRT92. All calculations with SUPCRT92 shown here were executed for a constant pressure of 400 bar corresponding to the pressure of the experiments. The computer program EQ3/6, version 8.0 (Wolery, 1992) was used to perform geochemical reaction path modeling. For computations with EQ3/6 the thermodynamic database of Klein and Bach (2009) was included. The database consists of standard-state thermodynamic parameters for temperatures up to 400 °C at 500 bar. The reactions expected are strongly dependent on temperature, but the pressure difference of 100 bar between experiment and model is thought to have insignificant influence. The model included solid solutions (endmembers) and aqueous inorganic species in the experimental system Mg-Fe-Ni-Si-S-Na-Cl-O-H. Chrysotile was employed as the Mg-endmember of serpentine. Fluid-mineral computations were done for dissolved aqueous species and for solid solutions of the minerals in the experimental systems. The reaction path geochemical modeling of fluid-rock-reactions was simulated as a simple titration model. The variable Xi is a measure for the reaction progress. The model starts at Xi = 0 where no mineral is reacted and ends at Xi = 1 where the minerals were completely dissolved. Sodium chloride solution with the primary fluid compositions of 0.566 mol/kg water for Na^+ and Cl^- and a pH of 5.5 was used in the models. The mineral compositions of primary phases included in the models are given in table 6.1. The water-to-rock ratios were 2.2 in all experiments, and this is where each reaction path end (Xi = 1). The computation started with NaCl-solution (Xi = 0) to which solids (forsterite, fayalite, enstatite, ferrosilite, pentlandite and harzburgite) were added at a constant temperature of 320 °C. Geochemist`s Workbench® (GWB®) version 7.0.6 (Bethke, 2007) was used to construct phase diagrams. The used data file in GWB® was updated to be suitable for a pressure of 500 bar and temperatures up to 400 °C (Klein and Bach, 2009).

Tab. 6.1. Starting mineral formula compositions used in the reaction path models. Abbreviations: forsterite-rich olivine (Fo), enstatite-rich orthopyroxene (En) and pentlandite (Pn).

elements	Fo	En	Pn
Mg	1.82	1.71	
Fe	0.18	0.29	4.50
Ni			4.50
Si	1.00	2.00	
O	4.00	6.00	
S			8.00

6.2 Reaction path modeling

Water-rock reaction path modeling was performed using the EQ6 computer code to evaluate the observed mineral and fluid compositions in relation to the predicted equilibrium state as reactions progress in the experiments. The predicted changes in fluid composition along an isothermal and isobaric reaction path of adding rock to starting solution are discussed below and compared with the measured concentration of dissolved species (Fig. 6.1 to 6.4). Silica concentrations changed rapidly in the earliest stages of serpentinization experiments and reached steady-state values (corresponding to rock-buffering in fluid-rock equilibrium) in the forsterite-rich olivine (Exp01 and Exp02) and enstatite-rich orthopyroxene (Exp03) experiment (Fig. 6.1 to 6.3). In the harzburgite experiment (Exp04) a drop of silica concentration was visible shortly before 40 % reaction progress (Fig. 6.4). This drop occurs when orthopyroxene is exhausted. The model takes into account the fact that brucite was absent from secondary mineral assemblage, indicating that in the harzburgite experiment (Exp04) orthopyroxene reacted faster than olivine by a factor of 2.4. Hydrogen sulfide and iron concentrations decreased and magnesium as well as hydrogen concentrations increased.

In the reaction paths in which olivine (Exp01 and Exp02) and orthopyroxene (Exp03) were added, dissolved iron, magnesium and hydrogen sulfide reached a maximum after about 10 percent reaction progress and then decreased slightly to the end of the reaction path. Hydrogen production increased rapidly in the beginning of the reaction progress and slowly increased further to the end of the reaction path. In general, the largest changes of fluid composition occurred in the first stages of reaction and in the harzburgite model when orthopyroxene was exhausted.

The average concentrations of analyzed selected species from experimental results were compared with predicted data from the model (Fig. 6.1 to 6.4 and Tab. 6.2). The reaction progress (Xi) at experimental end was calculated from thermogravimetric analyses. Sodium, chloride and silica are in general agreement with the computed fluid composition in all experiments. Iron concentrations measured were slightly lower than predicted in the olivine experiments (Exp01 and Exp02), but higher in the orthopyroxene (Exp03) and harzburgite (Exp04) experiments. The measured magnesium concentrations in the olivine experiment (Exp01 and Exp02) were significant lower and in the orthopyroxene test (Exp03) substantial higher than the computed with values. For the harzburgite experiment (Exp04) measured and predicted magnesium data match each other. The measured hydrogen sulfide data were similar to or somewhat lower than expected based on the EQ6 computations of about 1 mmol/kg. Except for the harzburgite experiment (Exp04) hydrogen levels measured were generally lower than the computed H_2 yields.

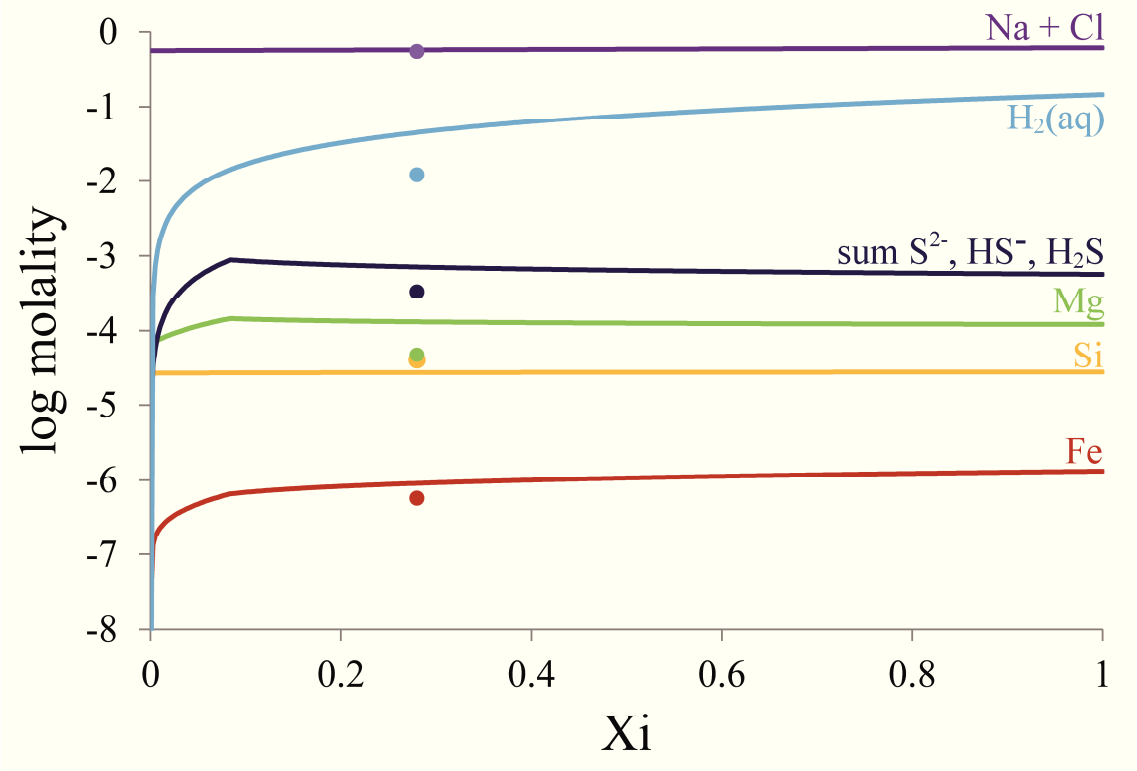

Fig. 6.1. Predicted concentrations progression of dissolved elements in Exp01 (olivine) at 320 °C and 500 bar. The points mark the analyzed dissolved species at experimental end (Xi = 0.28).

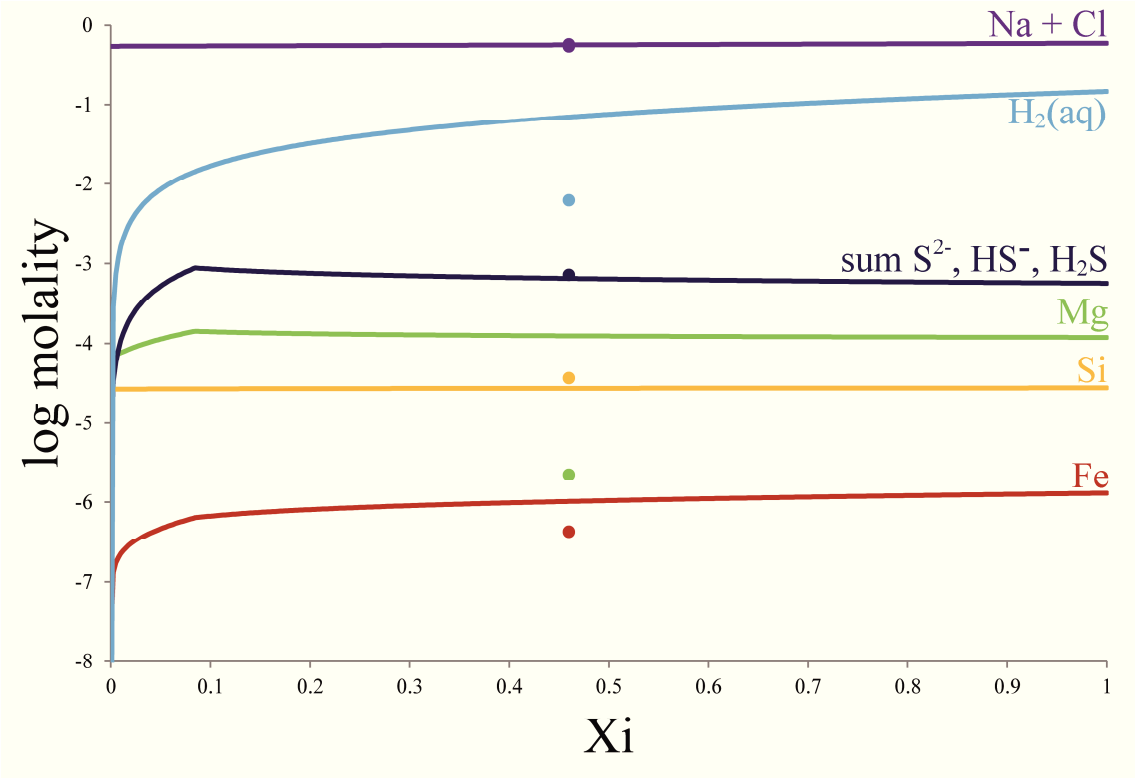

Fig. 6.2. Predicted concentrations progression of dissolved elements in Exp02 (olivine) at 320 °C and 500 bar. The points mark the analyzed dissolved species at experimental end (Xi = 0.46).

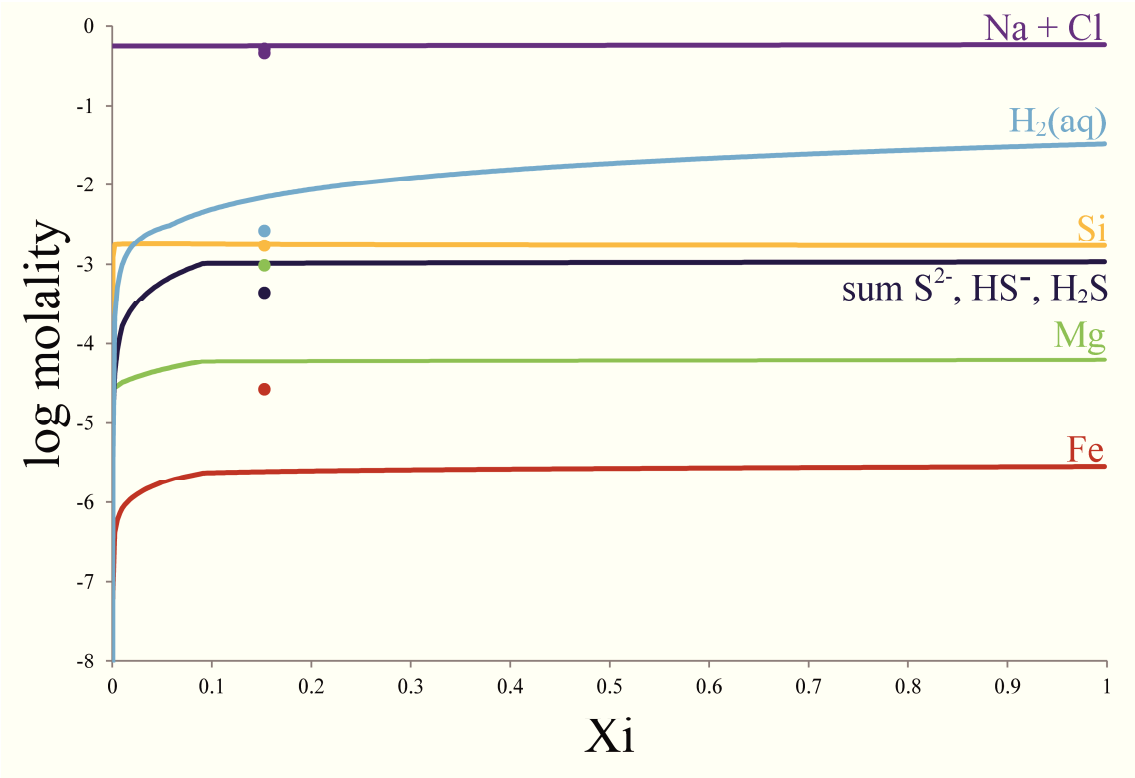

Fig. 6.3. Predicted concentrations progression of dissolved elements in Exp03 (orthopyroxene) at 320 °C and 500 bar. The points mark the analyzed dissolved species at experimental end (Xi = 0.15).

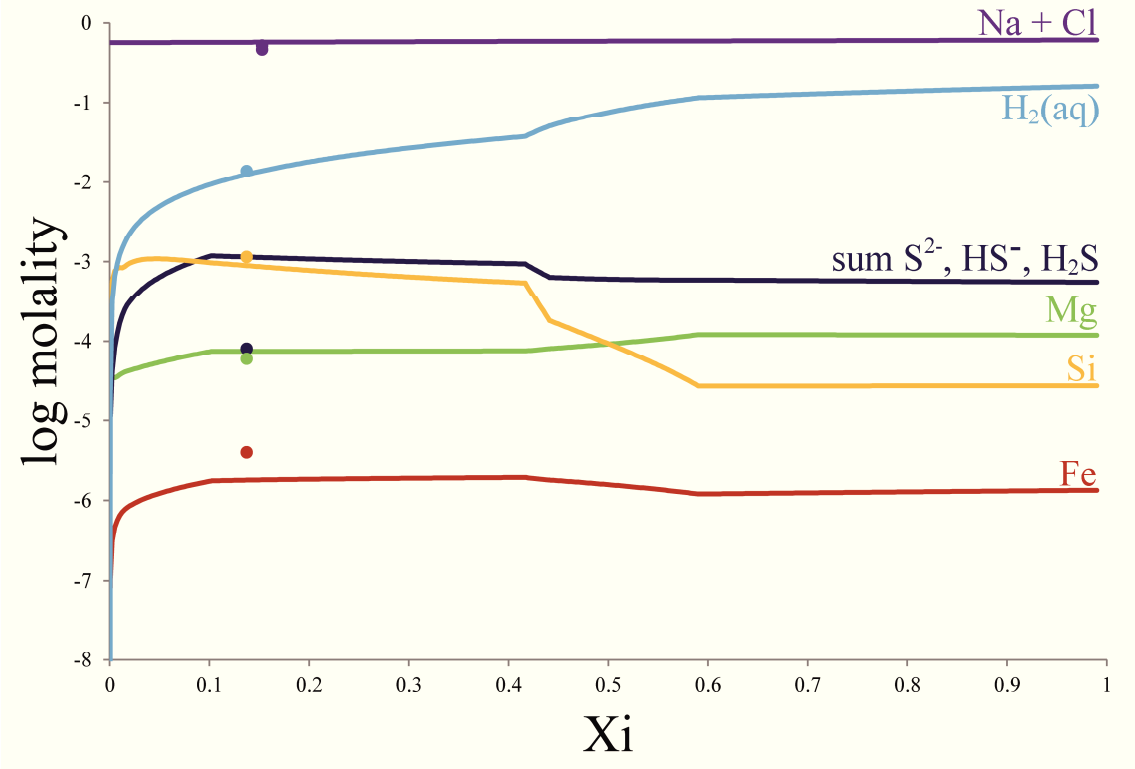

Fig. 6.4. Predicted concentrations progression of dissolved elements in Exp04 (harzburgite) at 320 °C and 500 bar. The points mark the analyzed dissolved species at experimental end (Xi = 0.14).

The observed fluid compositions in relation to predicted data using the EQ6 computer code are listed in table 6.2. Generally most of the modeled data are in good agreement with analyzed values.

Tab. 6.2. Observed fluid compositions in relation to predicted data in the experiments. Concentrations are in log molality.

	Cl	Fe	Mg	Na	Si	H_2S (aq)	$pH_{(25\,°C)}$	$pH_{(in\text{-}situ)}$	H_2 (aq)
Exp01: analyzed	-0.244	-6.515	-4.763	-0.259	-4.399	-3.776	9.5	6.9	-1.920
EQ6	-0.237	-6.043	-3.886	-0.237	-4.567	-3.258	-	6.4	-1.354
Exp02: analyzed	-0.237	-6.364	-5.648	-0.263	-4.348	-3.558	9.9	7.2	-2.209
EQ6	-0.244	-5.990	-3.906	-0.244	-4.565	-3.298	-	6.4	-1.152
Exp03: analyzed	-0.284	-4.287	-3.013	-0.326	-2.767	-3.492	5.4	5.3	-2.579
EQ6	-0.245	-5.610	-4.226	-0.145	-2.752	-3.026	-	6.0	-2.158
Exp04: analyzed	-0.273	-5.354	-4.222	-0.321	-2.943	-4.156	6.6	6.1	-1.864
EQ6	-0.241	-5.741	-4.127	-0.241	-3.072	-2.998	-	6.0	-1.840

6.3 Predicted phase relations

6.3.1 Solid solution product composition

For the olivine experiments the EQ6 model predicts formation of secondary chrysotile, brucite and magnetite from the beginning of the chemical reaction until to the complete serpentinization. In the first olivine experiment (Exp01) 27.9 % (run time 9.5 month) and in the second olivine experiment (Exp02) 46.0 % (test time 14 month) of the starting material was reacted (calculated from the thermogravimetric analyses). The solid solution compositions computed with EQ6 are chrysotile $Mg_{2.907}Fe_{0.093}Si_2O_5(OH)_4$ and brucite $Mg_{0.961}Fe_{0.039}(OH)_2$ in Exp01 and $Mg_{2.897}Fe_{0.103}Si_2O_5(OH)_4$ and brucite $Mg_{0.954}Fe_{0.046}(OH)_2$ in Exp02. The analyzed Mg-Fe-ratios in the secondary minerals of the olivine experiments were slightly different. Electron microprobe data revealed mineral formulae in Exp01 of $Mg_{2.962}Fe_{0.038}Si_2O_5(OH)_4$ for chrysotile and $Mg_{0.963}Fe_{0.037}(OH)_2$ for brucite. The analyzed chemical configuration in Exp02 was $Mg_{2.967}Fe_{0.033}Si_2O_5(OH)_4$ for chrysotile and $Mg_{0.960}Fe_{0.040}(OH)_2$) for brucite. The computations match the brucite compositions but predict too high Fe contents of serpentine. This minor discrepancy in serpentine composition is probably due to non-idealities in the chrysotile-greenalite-cronstedtite solid solution. In the balanced serpentinization reactions, model and observation lead to differences in the amount of hydrogen predicted:

Exp01 balanced from modeled data in EQ6:

$$Mg_{1.818}Fe_{0.182}SiO_4 + 1.402\ H_2O = 0.500\ Mg_{2.907}Fe_{0.093}Si_2O_5(OH)_4 + 0.379\ Mg_{0.961}Fe_{0.039}(OH)_2 + 0.040\ Fe_3O_4 + 0.040\ H_2$$

Exp01 balanced from analysis data:

$$Mg_{1.818}Fe_{0.182}SiO_4 + 1.400\ H_2O = 0.500\ Mg_{2.962}Fe_{0.038}Si_2O_5(OH)_4 + 0.350\ Mg_{0.963}Fe_{0.037}(OH)_2 + 0.050\ Fe_3O_4 + 0.050\ H_2$$

Exp02 balanced from modeled data in EQ6:

$$Mg_{1.818}Fe_{0.182}SiO_4 + 1.425\ H_2O = 0.500\ Mg_{2.897}Fe_{0.103}Si_2O_5(OH)_4 + 0.387\ Mg_{0.964}Fe_{0.046}(OH)_2 + 0.038\ Fe_3O_4 + 0.038\ H_2$$

Exp02 balanced from analysis data:

$$Mg_{1.818}Fe_{0.182}SiO_4 + 1.399\ H_2O = 0.500\ Mg_{2.967}Fe_{0.033}Si_2O_5(OH)_4 + 0.348\ Mg_{0.960}Fe_{0.040}(OH)_2 + 0.051\ Fe_3O_4 + 0.051\ H_2$$

These differences are fairly minor and are within error of the uncertainties in measurements and thermodynamic calculations involved.

The thermogravimetric investigation revealed that 15.3 % of the orthopyroxene was reacted to chrysotile and talc during five months of experimental runtime. Magnetite was also qualitatively determined by different analytical methods. The predicted mineral phases at that reaction step were chrysotile and talc. The Mg-Fe-ratios in the reaction products of Exp03 could not be analyzed by electron microprobe because of the small grain size. Based on mineral compositions predicted by EQ6, the balanced serpentinization reaction can be written as followed:

$$Mg_{1.706}Fe_{0.294}Si_2O_6 + 0.989\ H_2O = 0.323\ Mg_{2.482}Fe_{0.518}Si_2O_5(OH)_4 + 0.339\ Mg_{2.674}Fe_{0.326}Si_4O_{10}(OH)_2 + 0.005\ Fe_3O_4 + 0.005\ H_2$$

Harzburgite (Exp04) was reacted by 16.1 % after four month of experimental runtime and chrysotile as well as magnetite were found as alteration minerals. The dissolution rate determined for orthopyroxene in the harzburgite experiment (Exp04) was a factor of 2.4 faster than that of olivine. The computed reaction product was solely chrysotile at the reaction progress of 16.1 % dissolved orthopyroxene. EQ6 calculations reveal that magnetite and brucite would form in a later stage (brucite after nearly 60 % was reacted and magnetite after about 44 % of the orthopyroxene was transformed). The balanced reaction progress yielding only serpentine and magnetite with chemical compositions computed from EQ6 is:

$$Mg_{1.706}Fe_{0.294}Si_2O_6 + 2.1640\ Mg_{1.818}Fe_{0.182}SiO4 + 4.1913\ H_2O = 2.0820\ Mg_{2.709}Fe_{0.291}Si_2O_5(OH)_4 + 0.0273\ Fe_3O_4 + 0.0273\ H_2$$

In all four experiments pentlandite was added to the mafic silicates to investigate Fe-Ni-O-S phase relations during alteration processes under hydrothermal conditions at 320 °C and 400 bar. Secondary sulfide minerals in Exp01 and Exp02 were Ni-rich pentlandite and heazlewoodite as identified from compositional data collected with electron

mircoprobe. The pentlandite in Exp03 and Exp04 was apparently unreacted. The predicted sulfides from EQ6 in Exp01 and Exp02 were solely heazlewoodite and at the end of the reaction progress (about 85 % reacted olivine) pentlandite is expected to become stable, too. The modeled sulfide in Exp03 was also heazlewoodite and at the end of the mineral transformation if 97 % orthopyroxene was reacted, only pentlandite was stable. The model of the harzburgite experiment predicted heazlewoodite throughout the reaction path and pentlandite as additional phase after 10 % harzburgite was reacted to the end of the path.

6.3.2 Silica-dependent phase relations

The predicted silica-dependent phase relations of the forsterite-rich olivine experiments (Exp01 and Exp02) are shown in the phase diagram in Fig. 6.5. The measured silica activity for both experiments corresponds to a log activity SiO_2 (aq) of -4.4, which is near the univariant phase boundary between brucite and serpentine. The reaction took place at a temperature marginally lower than that of the invariant point in the system. At temperatures > 340 °C serpentine and brucite would not coexist at the measured silica activity. The influence of the Fe-partitioning into serpentine and brucite is considerable (activity Mg in chrysotile = X_{Mg}^3) and would shift the phase boundaries in the thermodynamic model shown in Fig. 6.5 slightly to higher silica values.

Tab. 6.3. Silica-dependent reactions and equilibrium constants calculated for the forsterite-rich olivine experiments (Exp01 and Exp02).

no.	reaction	log K from SUPCRT92 bei P = const. @ 400 bar							
		100 °C	150 °C	200 °C	250 °C	300 °C	320 °C	350 °C	400 °C
1	$Mg_2SiO_4 + 2\ H_2O = 2\ Mg(OH)_2 + SiO_2$ (aq)	-4.315	-4.330	-4.359	-4.401	-4.466	-4.505	-4.589	-4.921
2	$3\ Mg_2SiO_4 + SiO_2$ (aq) $+ 4\ H_2O = 2\ Mg_3Si_2O_5(OH)_4$	-14.747	-11.739	-9.274	-7.211	-5.463	-4.840	-3.987	-2.867
3	$Mg_3Si_2O_5(OH)_4 + H_2O = 3\ Mg(OH)_2 + 2\ SiO_2$ (aq)	-6.923	-6.182	-5.588	-5.104	-4.716	-4.589	-4.439	-4.408

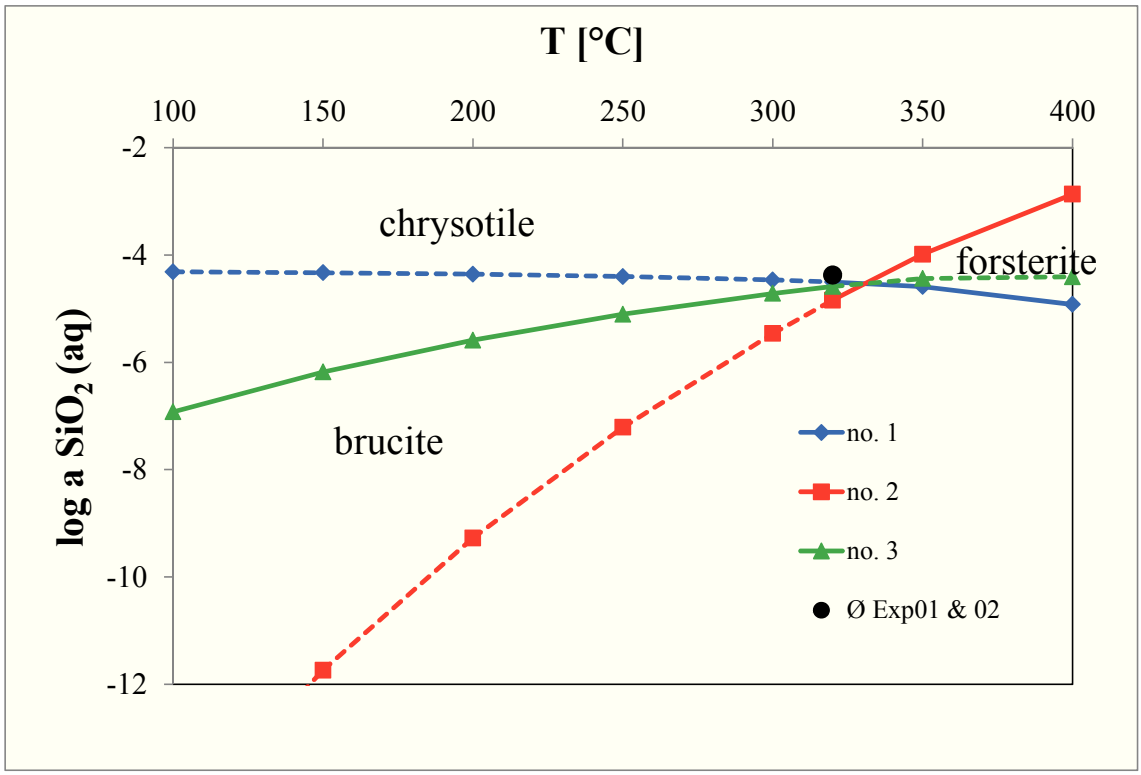

Fig. 6.5. The activity-temperature diagram representing the predicted phase equilibria during serpentinization and showing the silica buffer of the system at 400 bar. The dot placed in the diagram standing for the measured average silica activity in Exp01 and Exp02. Reaction numbers are those in table 6.3. The stable univariant equilibria reactions are given with a solid line and the metastable extensions across the invariant point with dashed lines.

Silica-dependent chemical reactions were also examined for the enstatite-rich orthopyroxene (Exp03) and harzburgite (Exp04) experiment (Tab. 6.4) The relevant equilibrium constants at different temperatures at 400 bar were calculated with SUPCRT92 (Tab. 6.4) and a temperature-silica-activity-diagram was constructed (Fig. 6.6). The silica activity observed in the enstatite-rich orthopyroxene experiment (Exp03) plots on the univariant purple line (d) which describes the equilibrium between serpentine and talc:

(d) chrysotile + 2 SiO_2 (aq) = talc + H_2O

The secondary minerals formed in Exp03 were indeed chrysotile and talc and fit to the equilibrium calculations. The only alteration mineral observed in the harzburgite experiment (Exp04) was chrysotile. The silica activity in this experiment (Exp04) was somewhat lower than the silica activity in the pure enstatite-rich orthopyroxene

experiment (Exp03) which explains the formation of chrysotile as the only secondary phase (see Fig. 6.7).

Tab. 6.4. Silica-dependent reactions and equilibrium constants calculated for the enstatite-rich orthopyroxene (Exp03) and harzburgite (Exp04) experiments.

no.	reaction	log K from SUPCRT92 bei P = const. @ 400 bar							
		100 °C	150 °C	200 °C	250 °C	300 °C	320 °C	350 °C	400 °C
a	$3\ MgSiO_3 + 2\ H_2O = Mg_3Si_2O_5(OH)_4 + SiO_2\,(aq)$	1.417	0.623	-0.023	-0.565	-1.043	-1.228	-1.512	-2.138
b	$2\ MgSiO_3 = Mg_2SiO_4 + SiO_2\,(aq)$	-3.973	-3.499	-3.109	-2.782	-2.518	-2.433	-2.339	-2.383
c	$2\ Mg_3Si_2O_{10}(OH)_2 = 3\ Mg_2SiO_4 + 5\ SiO_2\,(aq) + 2H_2O$	-6.066	-5.186	-4.468	-3.870	-3.376	-3.209	-2.999	-2.868
d	$Mg_3Si_2O_5(OH)_4 + 2\ SiO_2\,(aq) = Mg_3Si_4O_{10}(OH)_2 + H_2O$	-3.894	-3.547	-3.265	-3.033	-2.853	-2.800	-2.751	-2.867
e	$3\ MgSiO_3 + SiO_2\,(aq) + H_2O = Mg_3Si_4O_{10}(OH)_2$	-9.206	-7.717	-6.507	-5.502	-4.664	-4.373	-3.989	-3.596
f	$3\ Mg_2SiO_4 + SiO_2\,(aq) + 4\ H_2O = 2\ Mg_3Si_2O_5(OH)_4$	-14.747	-11.739	-9.274	-7.211	-5.463	-4.840	-3.987	-2.867
g	$Mg_3Si_2O_5(OH)_4 + H_2O = 3\ Mg(OH)_2 + 2\ SiO_2\,(aq)$	-6.923	-6.182	-5.588	-5.104	-4.716	-4.589	-4.439	-4.408
h	$Mg_2SiO_4 + 2\ H_2O = 2\ Mg(OH)_2 + SiO_2\,(aq)$	-4.315	-4.330	-4.359	-4.401	-4.466	-4.505	-4.589	-4.921

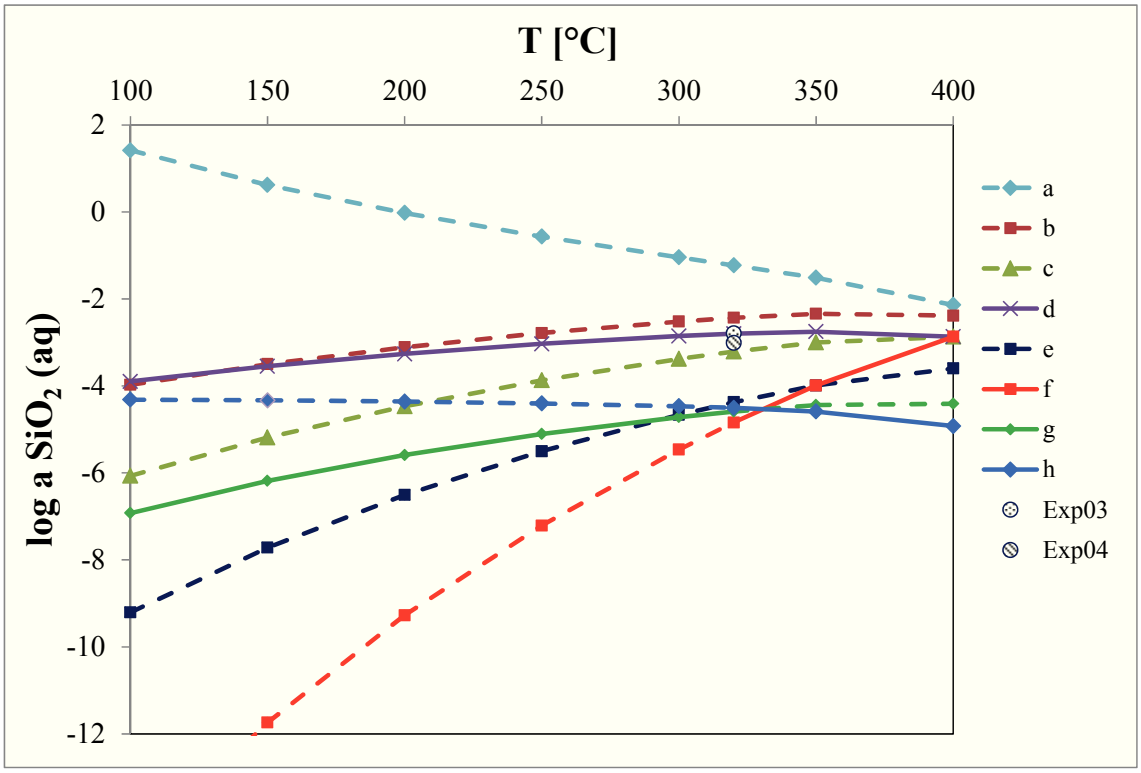

Fig. 6.6. Isobaric (P = 400 bar) univariant curves of chemical reactions given in table 6.4 for the enstatite-rich orthopyroxene and harzburgite system. The stable univariant equilibria reactions are given with a solid line and the metastable extensions with dashed lines. The silica activity in Exp03 (enstatite-rich orthopyroxene) was higher (spotted circle) than the silica activity in Exp04 (harzburgite composition, (striped circle).

Phase diagram figure 6.7 depicts the relationship of Mg-Si-O-H mineral phases to silica activity at various temperatures. The analyzed silica activities from experiments were marked. The enstatite-rich orthopyroxene experiment (Exp03) with the highest dissolved silica concentrations lies on the phase boundary between chrysotile and talc. The silica activity in the harzburgite experiment (Exp04) plotted in the mineral stability field of chrysotile near the phase boundary to talc. The forsterite-rich olivine experiments (Exp01 and Exp02) show silica activities in the mineral field of chrysotile close to the boundary line to brucite. The deviation from the phase boundary can be accounted for by the incorporation of Fe into serpentine.

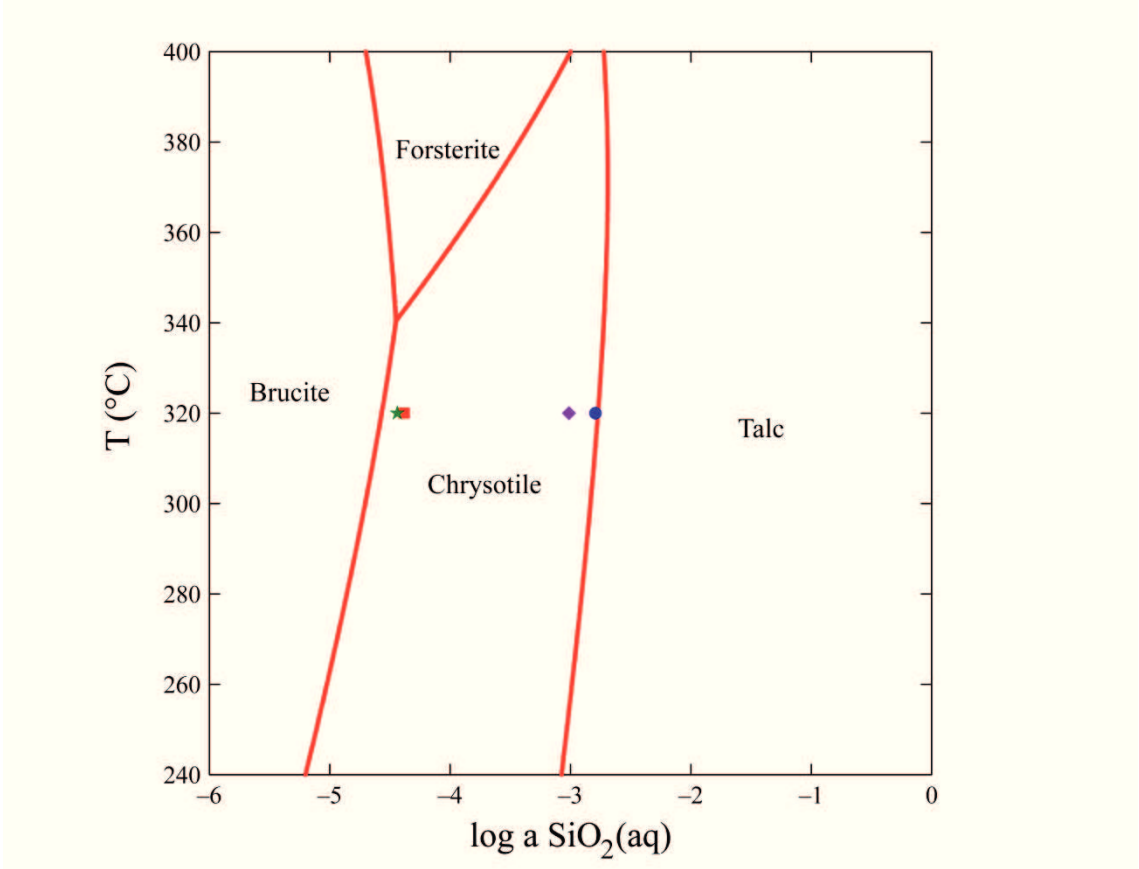

Fig. 6.7. Phase relationships in a silica-activity versus temperature diagram for the Mg-Si-O-H-system calculated for 500 bar. Observed silica activities in the experiments (400 bar and 320 °C) are also shown. Red square represents Exp01, green star shows Exp02, blue dot signs Exp03 and purple diamond indicates Exp04.

6.3.3 Magnetite

In addition to the previously mentioned silica secondary minerals, magnetite precipitated during the serpentinization reactions in all four experiments. Equilibrium constants for the magnetite forming reactions were calculated from

SUPTCRT92 (Tab. 6.5). A log activity SiO_2 (aq) – log activity H_2 (aq) – diagram was constructed to examine the relation between hydrogen and silica activities (Fig. 6.8). All experiments plot in the stability field of magnetite and match to the observed magnetite in all tests.

Tab. 6.5. Calculated equilibrium constants for the magnetite forming reactions.

no.	reaction	log K from SUPCRT92 bei P = const. @ 400 bar							
		100 °C	150 °C	200 °C	250 °C	300 °C	320 °C	350 °C	400 °C
A	$3\ Fe_2SiO_4 + 2\ H_2O = 2\ Fe_3O_4 + 3\ SiO_2$ (aq) $+ 2\ H_2$ (aq)	-17.256	-15.236	-13.478	-11.922	-10.548	-10.053	-9.387	-8.684
B	$Fe_3Si_2O_5(OH)_4 = Fe_3O_4 + 2\ SiO_2$ (aq) $+ H_2$ (aq) $+ H_2O$	-11.932	-9.953	-8.273	-6.818	-5.556	-5.104	-4.493	-3.803
C	$3\ Fe(OH)_2 = Fe_3O_4 + 2\ H_2O + H_2$ (aq)	0.701	1.855	2.867	3.773	4.606	4.927	5.406	6.284

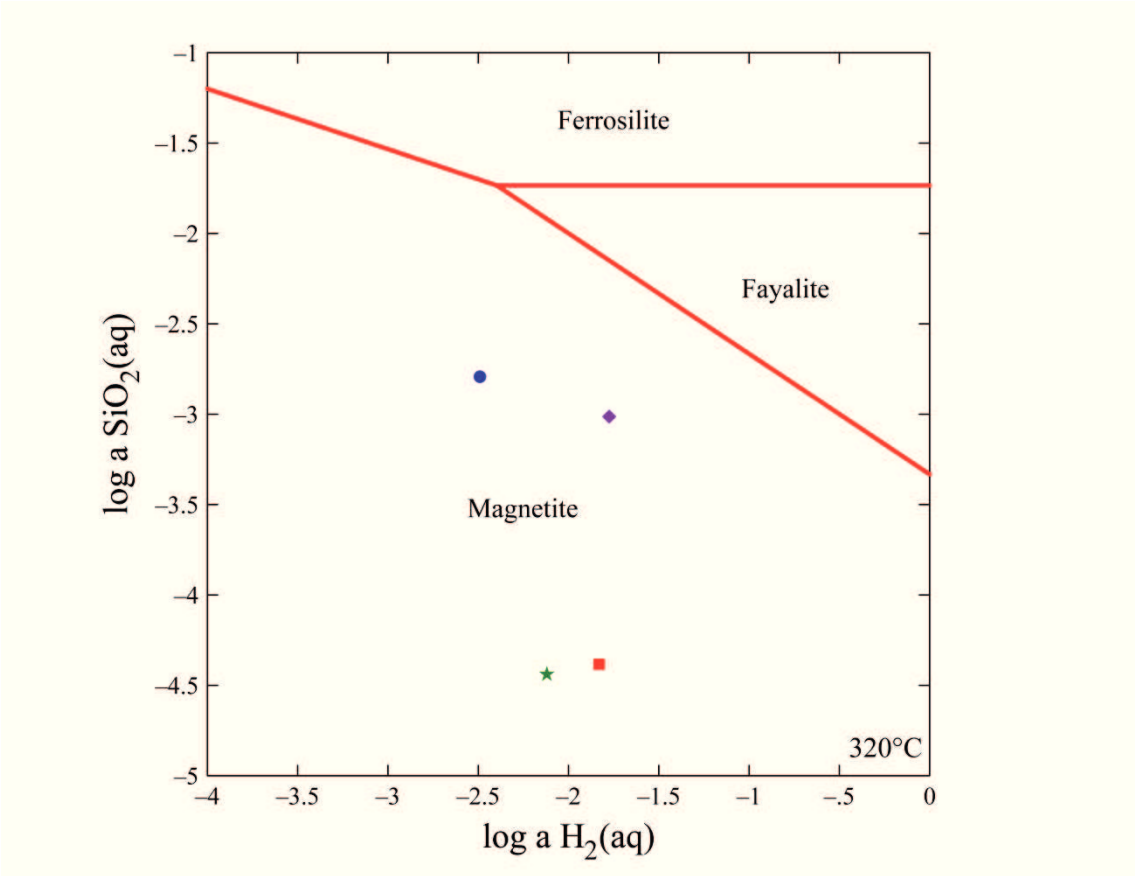

Fig. 6.8. The phase diagram shows the relationship between silica activity and hydrogen activity at 500 bar and 320 °C. All experiments are in the mineral stability field of magnetite (analyzed data). Red square represents Exp01, green star shows Exp02, blue dot signs Exp03 and purple diamond indicates Exp04.

6.3.4 Sulfur-dependent phase relations

The measured hydrogen sulfide concentration in the investigated systems resulted from reactions of the pentlandite $Fe_{4.5}Ni_{4.5}S_8$ added as starting material with the NaCl-solution. The assemblages in the experiments are consisting of initial pentlandite, Ni-rich pentlandite, heazlewoodite and magnetite. Reaction equations were formulated for the discovered secondary sulfide minerals in Exp01 and Exp02 and equilibrium constants were calculated with SUPCRT92 (Tab. 6.6). The pentlandite in Exp03 and Exp04 was not reacted and no alteration products of sulfides were discovered.

Tab. 6.6. Calculated equilibrium constants for the reaction with sulfides in the experiments.

no.	reaction	log K from SUPCRT92 bei P = const. @ 400 bar							
		100 °C	150 °C	200 °C	250 °C	300 °C	320 °C	350 °C	400 °C
I	$(Fe_{4.5}Ni_{4.5})S_8 + 6\ H_2O = 1.5\ Fe_3O_4 + 1.5\ Ni_3S_2 + 5H_2S\ (aq) + H_2$	-39.592	-32.867	-27.329	-22.650	-18.589	-17.089	-14.920	-11.162
II	$(Fe_{4.5}Ni_{4.5})S_8 + 6\ H_2O = 1.5\ Fe_3O_4 + 0.5\ Ni_9S_8 + 4\ H_2S\ (aq) + 2\ H_2$	-35.217	-29.182	-24.177	-19.916	-16.184	-14.794	-12.769	-9.178
III	$Ni_9S_8 + 2\ H_2 = 3\ Ni_3S_2 + 2\ H_2S\ (aq)$	-8.750	-7.370	-6.304	-5.468	-4.810	-4.590	-4.303	-3.968

The analyzed log activity of hydrogen (H_2 (aq)) versus temperature was plotted for all four experiments in relation to the position of phase boundaries (Fig. 6.9). The diagram represents the Fe-Ni-O-S phase equilibria in the serpentinization experiment with added pentlandite. Magnetite is stable over the whole diagram range. Godlevskite and heazlewoodite are stable at 320 °C were the experiments were carried out. The position of the boundary between godlevskite and heazlewoodite is depended on hydrogen sulfide activity (assumed 2×10^{-4} in Fig. 6.9).

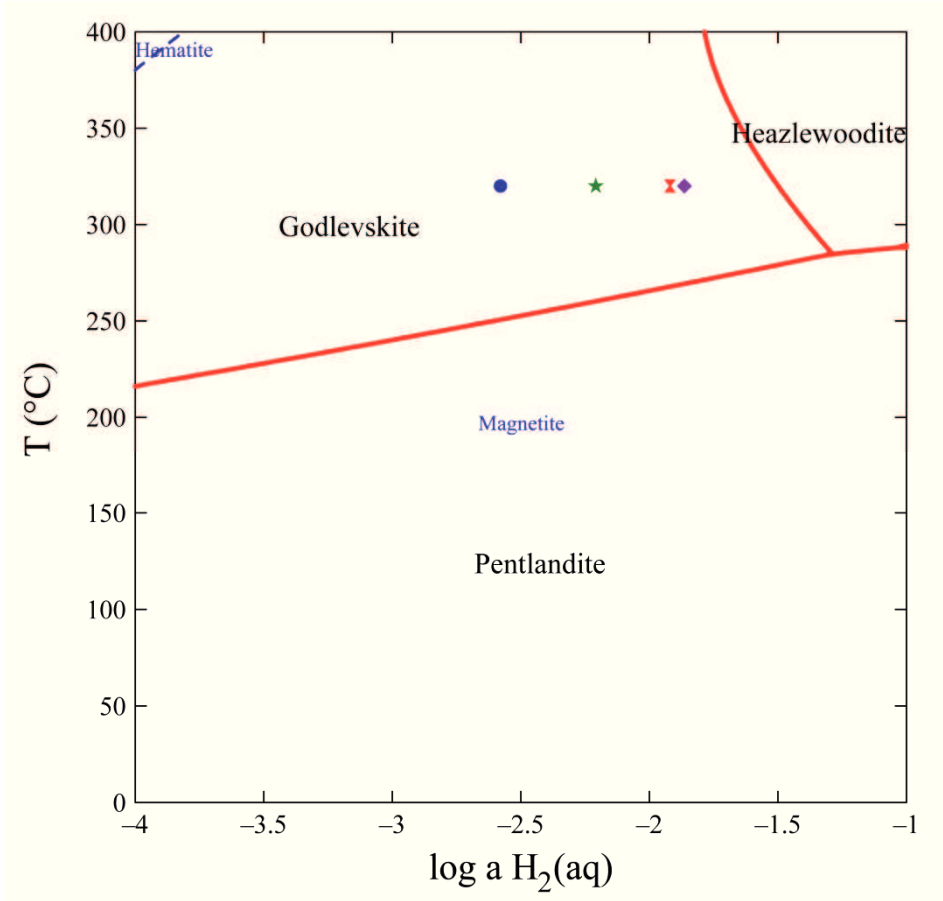

Fig. 6.9. Log activity of H_2 (aq) versus the temperature at 500 bar. The smaller blue written text indicates that the stability fields of magnetite and hematite. They are covered by the stability fields of godlevskite, heazlewoodite and pentlandite (red lines). The symbols represent the analyzed hydrogen concentrations. Red hourglass represents Exp01, green star shows Exp02, blue dot signs Exp03 and purple diamond indicates Exp04.

Maximum hydrogen concentrations expected from the reaction progress were calculated from thermogravimetric measurements. The analyzed concentrations of hydrogen of the interacting fluid and the calculated maximum hydrogen concentrations from the thermogravimetric measurements were plotted in an activity-activity-Fe-Ni-O-S phase diagram (Fig. 6.10). All plots are in the stability field of magnetite. The analytical data of Exp01, Exp02 and Exp03 plot in the stability field of godlevskite, too. Only the analyzed fluid composition of Exp04 plots in the heazlewoodite field. The calculated hydrogen concentrations based on thermogravimetric measurements relating to the reaction progress of Exp01 and Exp02 were much higher than the measured values. The calculated concentrations of hydrogen in the olivine experiments (Exp01 and Exp02) plot in the stability field of heazlewoodite near the boundary to godlevskite. The observations of magnetite and heazlewoodite as mineral products in the olivine experiments are in good correspondence with the theoretically calculated maximum

values of hydrogen from thermogravimetric analyses. In the orthopyroxene experiment (Exp03) both measured and theoretical maximum formation of hydrogen plot in the middle of godlevskite field. In Exp04 the measured hydrogen value plots in the heazlewoodite mineral stability field near to the phase boundary of godlevskite. The theoretical maximum hydrogen value lies in the godlevskite field. The theoretical hydrogen concentration in Exp01 and Exp02 is based on thermogravimetric measurements and analyzed magnesium to iron ratios from microprobe measurements. The theoretical value in Exp03 and in Exp04 is based on thermogravimetric measurements and computed magnesium to iron ratios from EQ6. The secondary minerals in the orthopyroxene and harzburgite experiment (Exp03 and Exp04) were too small for an adequate chemical analysis by electron microprobe. Hence compositions predicted in EQ6 runs were used in the mass balances of Exp03 and Exp04.

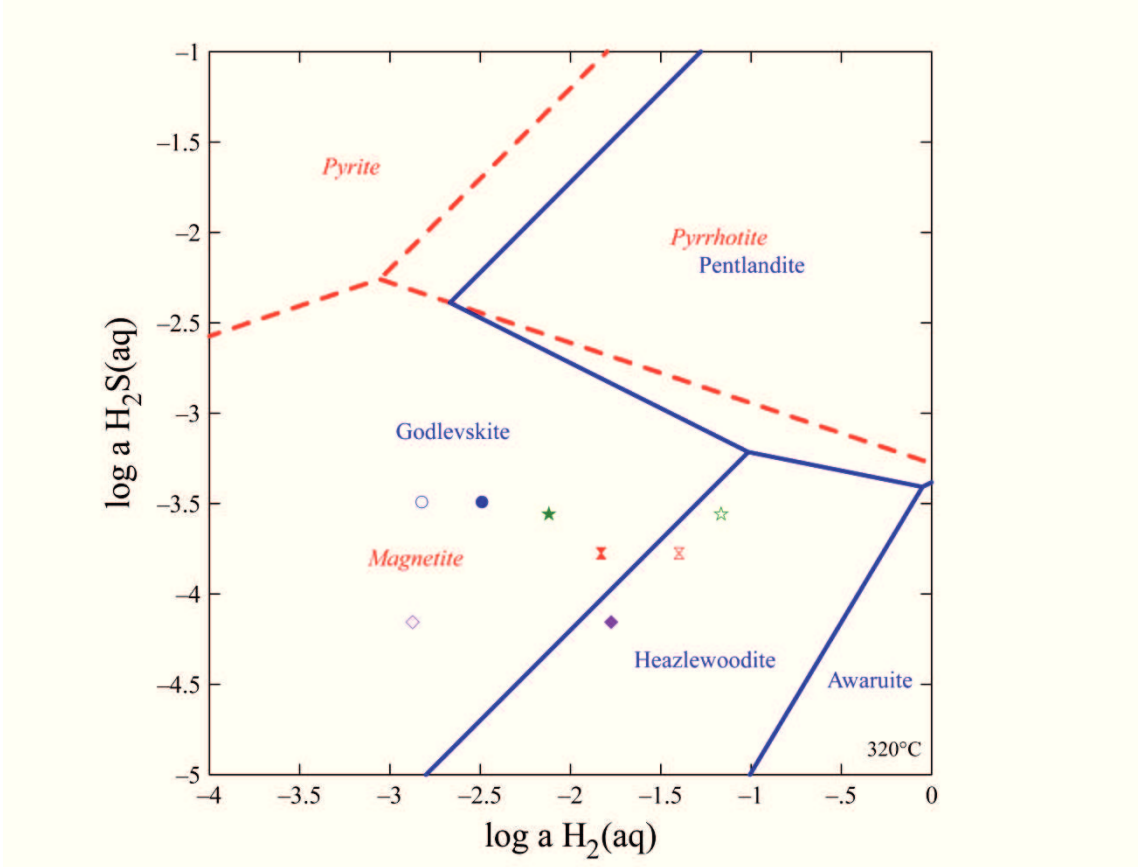

Fig. 6.10. Activity-activity diagram illustrates mineral phase relations of the Fe-Ni-O-S-system at 320 °C and 500 bar. Continuous blue lines are the boundaries of pentlandite ($Fe_{4.5}Ni_{4.5}S_8$), godlevskite (Ni_9S_8), heazlewoodite (Ni_3S_2) and awaruite (Ni_3Fe) stability fields. Dashed red lines bordered the stability fields of pyrrhotite ($Fe_{(1-x)}S$), pyrite (FeS_2) and magnetite (Fe_3O_4). The filled symbols represent the analyzed data and open symbols the calculated data based on thermogravimetric measurements relating to the reaction progress. Red hourglass represents Exp01, green star shows Exp02, blue dot signs Exp03 and purple diamond indicates Exp04.

6.4 Appraisal of modeled results

It was demonstrated that fluid compositions in the experiments are matched reasonably well by thermodynamically predicted data. The predicted mineral compositions also are in generally good agreement with the results obtained from the experiments. The calculated Mg-Fe-ratios in the secondary minerals differ slightly from the analyzed. But this causes significant differences in hydrogen generation. The predicted formation of heazlewoodite from pentlandite is corroborated by the experimental results. In addition Ni-rich pentlandite was observed in the olivine experiments. It is therefore likely that a metastable phase of Ni-rich pentlandite exists. Hydrogen and hydrogen sulfide activities control the mineral assemblages of the Fe-Ni-O-S-system (Fig. 6.10). The results indicate a substantial influence of rock composition on hydrogen production. A more detailed discussion is presented in chapter 7.

7. Discussion and conclusion

Hydrothermal vent fluids in the deep sea show remarkable chemical diversity. Basaltic rock types dominate at faster-spreading ridges and peridotites at slower-spreading ridges both at high temperatures (200 to 400 °C). Basalt-hosted systems are relatively oxidizing and produce slight acidic fluids (pH 3-5). Peridotite-hosted systems produce fluids in a wider pH range (pH 3-12) under reducing conditions. Also, systems like Lost City exist were fluids vent at low temperatures (< 90 °C) are alkaline (pH > 9), and show a completely different chemical composition. Understanding the controls of subseafloor seawater-rock reactions requires a combined experimental and theoretical approach. The results presented in this thesis shed a new light on the reactions governing the concentrations of critical chemical species in solutions interacting with ultramafic materials.

7.1 Solution chemistry

Systematic water-rock reaction experiments were conducted, in which the compositional evolution of the fluids during serpentinization was monitored. The phase relations in our experiments are controlled by the abundance of Mg, Fe, Si, H, O and S in the system. But kinetics effects also play a role in setting solution compositions. It becomes apparent from the time series analyses of solution composition that the addition of rocks to water causes dissolution reactions and therefore changes in fluid compositions. The largest changes occurred within the first days of the experiments. Quick hydrolysis of the reactive surfaces may causes the pH increasing by experimental start:

$$Mg_2SiO_4 + 2\ H_2O \rightarrow 2\ Mg^{2+} + SiO_2\ (aq) + 4\ OH^-$$

$$Mg_2Si_2O_6 + 2\ H_2O \rightarrow 2\ Mg^{2+} + 2\ SiO_2\ (aq) + 4\ OH^-$$

These reactions can explain the suddenly increase of magnesium and silica in the beginning of the experiments. Later on, serpentine, brucite and magnetite form, and the solution composition approaches steady-state, because of buffering by precipitation of chrysotile, brucite or talc. The predicted magnesium concentrations differ from analytical results in the olivine and orthopyroxene experiment. These differences can be

explained by kinetic effects or the formation of aqueous complexes which are difficult to consider in thermodynamic modeling. Our experiments were carried out with pure sodium chloride solution so an influence of other elements abundant in seawater (Mg, Ca) is prevented.

A similar experimental study of serpentinization was done by Seyfried et al. (2007) with peridotite and artificial seawater at 200 °C and 500 bar. In that experiment the pH sharply increased from 6 to 12 after about 4 months of reaction time. Simultaneously Ca, Fe and silica was decreased and a coupled relationship was suggested. Allen and Seyfried (2003) carried out an experiment with orthopyroxene and published a pH of 5 similar to our result. Earlier observation of Berndt et al. (1996) with a CO_2-bearing sodium chloride fluid and olivine also correspond to our pH results. Hence, the pH-findings in our study support experimental and field investigations of seafloor peridotite-hosted systems.

The silica activity of fluids coexisting with the minerals in our experiments corroborate the predicted changes in fluid composition, predicted abundance and composition of solid phase relations. Silica activity of the fluids appears to be an excellent monitor of the mineral phase assemblages in serpentinization reactions.

Like for silica, the dissolved sulfide concentrations in the olivine experiments are in good agreement with theoretically predicted values from equilibrium phase relations. The orthopyroxene and harzburgite investigation shows differences between model predictions and measured values of H_2S. The added pentlandite desulfurizes in the early stage of reaction progress as seen in immediately increasing hydrogen sulfide concentrations. Secondary sulfides are formed later and are most mantled by magnetite. Hydrogen sulfide concentrations increase slowly during reaction progress which differs slightly from the calculated data, where the sulfide reaches a maximum after 10 percent reaction progress and then trend to decrease slightly. Despite these small discrepancies between theoretically determined and experimentally measured fluid compositions, the predicted phase relations are in a good agreement (see a more detailed discussion below). The deviation between measurements and predictions for the analyzed species in the fluids for the olivine experiments (Exp01 and Exp02) was mostly less than 10 %. This result confirms that we possess a theoretical tool for predicting serpentinization of olivine with satisfying accuracy.

7.2 Silicate reactions

Hydrothermal alteration of ultramafic rocks forms serpentines by exothermic hydration reactions. Water reacts with minerals like olivine and / or pyroxene to form hydrous magnesia and iron silicates and hydroxides. Experimental and petrographic studies reveal that the dominant minerals are lizardite and chrysotile (e.g., Moody, 1976; Seyfried et al., 2007). Lizardite is often formed in the early stages of serpentinization (Moody, 1976; O'Hanley and Dyar, 1998). During progressive metamorphism chrysotile replaces the earlier formed lizardite as laboratory experiments have shown (Normand et al., 2002). Other field studies and laboratory experiments revealed that chrysotile is more stable at higher temperatures (Chernosky, 1975; O'Hanley and Wicks, 1995). All of our experiments were carried out at identical temperature and pressure conditions (320 °C and 400 bar) and only chrysotile was found as polymorph form independent of the reaction duration (4 to 14 month) or of different fluid chemistry. Perhaps lizardite formed in the early stages of alteration and in the course of continued reaction progress lizardite was replaced by chrysotile. These findings suggest that the temperature and pressure is not a major factor in controlling which structural types of serpentine will form. Kinetic effects and surface energy terms seem to be more relevant. Because of the very small differences in macroscopic thermodynamic properties of two serpentine polymorphs, discriminating between the two is not appropriate in model calculations.

The predicted mineral assemblages were experimentally confirmed: serpentine, brucite or talc are stable silica phases depending on the silica activity in the system. The findings of this study of olivine reaction are consistent with those of Berndt et al. (1996) who found fibrous chrysotile, brucite and magnetite in an experimental study of olivine serpentinization at 300 °C and 500 bar. Also the silica activity in the experiment of Berndt et al. (1996) is comparable with our results. The olivine alteration in our study occurred at a temperature just below the stability field of olivine at about 340 °C. Allen and Seyfried (2003) conducted an olivine alteration experiment at 350 °C which did not yield any alteration products and concluded that olivine must be stable under these conditions. The results obtained by Allen and Seyfried (2003) and in this study corroborate the predictions of thermodynamic calculations concerning temperature dependence of phase relations and aqueous silica activities.

Experimental investigations of orthopyroxene by Allen and Seyfried (2003) revealed serpentine and talc as reaction products. Orthopyroxene replacement by serpentine (chrysotile or lizardite) and talc was also confirmed in several field studies (e.g., Coleman and Keith, 1971; Katayama et al., 2010). As expected the orthopyroxene experiment in our investigation delivered serpentine as chrysotile and talc with the highest silica activity in the coexisting aqueous solution.

Only serpentine (chrysotile) formed as secondary mineral in our harzburgite experiment. Janecky and Seyfried (1986) investigated experimentally the hydrothermal alteration of harzburgite at 300 °C and 500 bar and identified lizardite and brucite as alteration products. Brucite formation is expected at low silica activity ($< 10^{-4.5}$ mol/kg) as predicted by equilibrium calculations. The silica activity in the Janecky and Seyfried (1986) experiment decreased to $10^{-5.7}$ mol/kg by the end which explains the additional brucite precipitation. In a former study from Seyfried and Dibble (1980), lizardite was present as alteration product in an experiment executed at the same conditions (300 °C and 500 bar), but with natural peridotite and a dissolved silica activity of 10^{-4} mol/kg. However the silica activity in our harzburgite experiment deviate from the predicted phase assemblage in that brucite is expected to form when the molar olivine to orthopyroxene ratio is > 1. That ratio was > 5 in the harzburgite used in the experiment, yet, brucite did not form. The only viable explanation for the lack of brucite is that orthopyroxene reacted faster than olivine. Mass balance calculations indicate that orthopyroxene reacted 2.4 times faster than olivine. This contradicts predictions of reaction rates from single-phase experiments (Martin and Fyfe, 1970) indicating that olivine reacts faster than orthopyroxene. The contrasting experimental results can be reconciled when compositional rate dependencies are taken into consideration. In experiments with both olivine and orthopyroxene, a strong activity gradient between the two reacting phases will develop. Olivine will want to turn into serpentine and brucite, while orthopyroxene will want to turn into serpentine and talc. Because brucite and talc cannot coexist, the system is highly reactive. It is this strong contrast in silica activities between the olivine and orthopyroxene that creates thermodynamic driving force for reactions. That same activity contrast will also promote diffuse mass transfer in the system. Our results hence point to interesting and previously unrecognized relations between rock composition and reaction rates that will need to be further explored in future experimental studies.

7.3 Hydrogen generation

7.3.1 Reaction path modeling and mass balance calculation

Serpentinization is accompanied by the release of hydrogen and the formation of magnetite. Hydrogen generation results from oxidation of ferrous iron (Fe^{2+}) in the primary minerals to ferric iron (Fe^{3+}) in the secondary minerals. The portion of trivalent iron accommodated within the structure of chrysotile, brucite and talc was not investigated in this study, although it contributes to hydrogen formation and hence plays an important role (e.g., Seyfried et al., 2007; Klein et al., 2009). The olivine experiments yielded reaction products with higher Mg-numbers than the starting olivine. The Mg-numbers were also slightly greater than those predicted by EQ6. The agreement between the amounts of hydrogen calculated from balanced serpentinization reactions and the hydrogen generation predicted in the reaction path models is nonetheless satisfying. Hydrogen concentrations of the olivine experiments are is shown in table 7.1. The calculated hydrogen concentrations in reaction progress calculated by mass balance in the olivine experiments (Exp01 and Exp02) are in good agreement with the thermodynamic predictions based on EQ6 computations and support the observation of Ni-rich pentlandite and heazlewoodite in the Fe-Ni-O-S-system. As the measured hydrogen concentrations by gas chromatography in the associated fluids of the olivine experiments are lower, these results should be interpreted with caution (see chapter 7.3.1).

experiment	method	H_2(aq)
Exp01:	measured	-1.920
olivine	EQ6	-1.354
	calc. from TG	-1.399
Exp02:	measured	-2.209
olivine	EQ6	-1.152
	calc. from TG	-1.165

Tab. 7.1. Calculated, predicted and measured hydrogen concentrations in the olivine experiments. Concentrations are in log molality. Measured values are based on gas chromatography analysis of the associated fluids. EQ6 are predicted values for computations with the computer program EQ3/6. The theoretical values of hydrogen (calc. from TG) are calculated from the thermogravimetric analysis at experimental end in relation to reaction progress.

The current study of hydrogen concentrations showed that thermogravimetric measurements are a valuable method to estimate hydrogen generation in serpentinization experiments and computer simulations can be used to obtain a quantitative estimate of hydrogen generation in hydrothermal systems.

7.3.2 Hydrogen analysis

Differences between predicted and measured hydrogen concentrations by gas chromatography in the systems may be explained by an analytical problem or loss of hydrogen during sampling. However, a leak in the gold bomb is improbable, because testing before and after an experiment confirmed that the system was sealed. However, the leak could have been so tiny that only volatile gases could escape. The problems of hydrogen permeation in metal walls are known, but probably no material exists that is less permeable to hydrogen than gold and, at the same time, is as workable, flexible, and chemically stable under hydrothermal conditions (Kishima, 1984; Ulmer and Barnes, 1987). Allen and Seyfried (2003) carried out an experiment at 450 °C and 500 bar to study the hydrogen diffusion using a similar gold reaction cell and concluded after that hydrogen diffusion through gold did not result in measurable losses after 3000 hours run duration. The permeation of hydrogen in gold is low and cannot explain the significantly lower hydrogen concentrations measured in the system. The connected titanium valve may be considered as a potential source of hydrogen loss. However, a plastic syringe was connected the whole time to the titanium valves to monitor a defect in tightness. Sometimes fluid could be observed in the syringes, further leakage of which could be prevented by tightening the valve. This could have been the possible reason for the unexpected low hydrogen concentrations measured in the last two samples of Exp02: after fluid sampling of Exp02 (at the 222nd day), 0.83 g fluid was observed in the syringe. The control of absolute hydrogen tightness in the course of an experiment is difficult. Besides the permeability of gold for hydrogen, there are a lot of other parameters which can cause hydrogen loss, e.g., the titanium valve, the closure of the gold bag, sampling and / or transfer of the sample to the gas chromatograph. Moreover, the limited experience in hydrogen analyses in the beginning of this study contributed to less reliable hydrogen results. Therefore, our measured hydrogen concentrations in the olivine experiments need to be interpreted with caution. The

hydrogen analyses of the orthopyroxene and harzburgite experiment are more reliable, because of the now better established analytical method.

7.3.3 Comparison with hydrogen yields obtained in previous studies

Janecky and Seyfried (1986) reported a hydrogen concentration of 0.33 mmol/kg after 17142 hours in a harzburgite alteration experiment. Experimental simulation of the serpentinization reaction of olivine by Berndt et al. (1996) at 300 °C and 500 bar yielded hydrogen generation of up to 158 mmol/kg after 69 days. McCollom and Seewald (2001) presented data of an olivine experiment at 300 °C and 350 bar with a hydrogen generation of 74 mmol/kg. In a second experiment under the same conditions, McCollom and Seewald observed only 17 mmol per kg. McCollom and Seewald presumed that the olivine in the second experiment was partially oxidized in air, or that oxygen was adsorbed on the mineral phase. In his first experiment he used olivine immediately after crushing, whereas the minerals of his second experiment were stored over a year as powder. Allen and Seyfried (2003) carried out an experimental study with different mineral compositions representative for oceanic peridotites (dunite, orthopyroxenite, websterite and harzburgite) and measured a maximum hydrogen concentrations of 26 mmol/kg in the harzburgite after 1824 hours. An additional experiment of Seyfried et al. (2007) delivered 77 mmol/kg after 7875 hours with liherzolite as starting material. Summing up, few laboratory studies on hydrogen generation were done and delivered differential results in comparable experiments. An important factor for the reaction progress and therefore for hydrogen generation as well is the grain size of the starting materials used in the experiments which was not well characterized in some publications. Worth mentioning is that, according to Klein et al. (2009), up to 50 % of the iron in chrysotile and brucite could be trivalent, which influences the hydrogen production as well as water to rock ratios. In this study, the oxidation state of iron was not investigated and all iron was assumed as ferrous. The wide influence of the hydrogen generation by Mg-Fe-ratios in the rock compositions was experimentally shown in comparison to thermodynamic reaction path models. Hydrogen generation during serpentinization depends on several parameters, which often hinders direct comparison between field observations and laboratory experiments. Difficulties in conjunction to hydrogen loss and determination were also discussed. In spite of the problems the predicted hydrogen generations in our study are in general agreement with the thermodynamic systems.

7.4 Magnetite production

The generation of hydrogen during serpentinization is accompanied by formation of magnetite (e.g., Toft et al., 1990; Oufi and Cannat, 2002). In all four experiments, magnetite is precipitated and the general hydration reaction without stoichiometric coefficients can be described as:

(Mg,Fe)-olivine + H_2O = (Mg,Fe)-Srp + (Mg,Fe)-Brc + Magnetite + H_2

Bach et al. (2006) proposed a two-stage reaction sequence of magnetite formation: (1) the reaction of olivine to serpentine and Fe-rich brucite, and (2) the reaction of Fe-rich brucite with aqueous silica to serpentine and magnetite as well as hydrogen. An external source of silica was required before magnetite could form, which was proposed to be sourced from orthopyroxene breakdown to serpentine. Frost and Beard (2007) proposed a similar sequence of magnetite formation in serpentinization reactions as Bach et al. (2006), but highlighted the importance of the breakdown of ferrous serpentine to magnetite, which would be facilitated by the low silica activities imposed to the system by the presence of brucite. The olivine experiment (Exp01 and Exp02) with low silica activity and the longest experimental runtime delivered the most magnetite, followed by the second olivine experiment. In the orthopyroxene (Exp03) and harzburgite (Exp04) experiments less magnetite was formed in shorter reaction time. The increase of magnetite content with degree of serpentinization is not linear (Toft et al., 1990), but this result may be explained by the clearly shorter experimental run durations of the orthopyroxene and harzburgite experiment. It is remarkable that the harzburgite investigation delivered twice as much magnetite than the orthopyroxene experiment although the experimental duration was one month shorter. This result may be explained by the influence of higher chemical potential in a two phase mineral assemblage. Orthopyroxene dissolves faster than olivine, which is accompanied by a relatively high silica activity. This finding supports the idea that the formation of magnetite depends on the availability of an external source of silica (Bach et al., 2006). In addition, the lack of brucite may be an indication of the reaction of brucite and aqueous silica to serpentine and magnetite. Magnetite occurred in various crystal shapes and sizes on altered grains. A remarkable reaction texture could be observed in the olivine experiments (Exp01 and Exp02) where sulfides were rimmed by magnetite. This finding supports previous research and petrographic observations of hydrothermal altered ultramafic rocks (Klein

and Bach, 2009). The starting pentlandite lost iron in the beginning of the reaction and fueled the later formation of magnetite around the Ni-rich pentlandite.

7.5 Changing Fe-Ni-S phase assemblages in pentlandite

Previous theoretical studies (Frost, 1985; Klein and Bach, 2009) had predicted changes in the assemblage of Fe-Ni-O-S-phases during serpentinization progress, but mineral phase calculations were limited by the lack of thermodynamic data for sulfides. Klein and Bach supplemented the database of SUPCRT92 with certain crucial phases of the Fe-Ni-O-S-system (Klein and Bach, 2009; Klein et al., 2009). Their theoretical calculations are consistent which observations in natural peridotite-hosted hydrothermal systems. In the course of this literature review, no experimental study could be found that focused on the combination between theoretical predictions and experimental work in Fe-Ni-O-S phase relations prior to this study.

The assemblages in the experiments consisted of primary pentlandite, heazlewoodite, Ni-rich pentlandite and magnetite. Pentlandite initially lost iron to form Ni-rich pentlandite in direction to the hypothetical endmember of godlevskite. Apparently, a metastable phase of Ni-rich pentlandite exists. The Fe-Ni-ratio changes from 1 to about 0.4. The Ni-rich pentlandite is finely intergrown with heazlewoodite and rimmed by magnetite. This mineral texture is similar to observations on natural samples of peridotites from the Mid-Atlantic Ridge (e.g., Klein and Bach, 2009). With increasing reaction progress, hydrogen concentrations built up in the fluid controlled by serpentinization in the SiO_2-MgO-FeO-Fe_3O_4-H_2O system. This increase in hydrogen concentration stabilized heazlewoodite. A Ni-rich-pentlandite, heazlewoodite and magnetite assemblage in the absence of awaruite implies hydrogen activities $< 10^{-1}$ mol/kg. Awaruite is stable at H_2,aq activities just below dihydrogen saturation of the fluids. Pentlandite reacts late in the reaction progress of serpentinization as indicated in the shorter duration of the experiments Exp03 and Exp04 by a slight alteration of the surrounding grain boundaries in pentlandite. Magnetite appears to form late in the sequence as the sulfide grains are often rimmed by this phase. Predicted secondary assemblages in relations to log activity hydrogen versus log activity hydrogen sulfide or temperature are in agreement with observed coexisting sulfides and magnetite in our experiments. The hydrogen activity in the experiments was below the stability field of

awaruite and plots near the boundary of godlevskite and heazlewoodite (in the phase diagrams godlevskite represents Ni-rich pentlandite). Increasing hydrogen sulfide activity during reaction progress would lead to transformation of heazlewoodite to godlevskite or pentlandite. But in contrast to some natural hydrothermal systems this is not observed here, because pentlandite was the only of hydrogen sulfide in the experiments. Instead the generation of hydrogen in the course of the serpentinization reactions drove the recrystallization of the sulfide mineral assemblages. The findings in our study support to previous theoretical research of Fe-Ni-O-S phase relations and lend support to validity of the thermodynamic data evaluated by Klein and Bach (2009).

7.6 Conclusion

The work presented in this dissertation comprises experimental and theoretical investigations of the alteration of ultramafic rocks in hydrothermal systems. Olivine, orthopyroxene and harzburgite were reacted with sodium chloride solution at 320 °C and 500 bar. A specific focus was on the investigation of the fate of primary added pentlandite in course of serpentinization. Prior to this study, the characteristic changes in the assemblages of Fe-Ni phases were never investigated in experimental studies.

Changes in the compositions of fluids and solids in the course of the alteration process were compared with predicted equilibrium states. This study has shown that the experimental observations are generally in agreement with thermodynamic predictions. The supplemented database of SUPCRT92 (Klein and Bach, 2009) was first experimental tested and our findings are in good agreement with the model. The detailed characterization of primary and secondary minerals linked to fluid compositions is essential to understanding serpentinization reaction. Thermogravimetric analyses of secondary mineral abundances combined with knowledge of minerals chemical compositions allow the estimation of hydrogen generation. Silica activity and particularly the strong contrast in silica activity between orthopyroxene and olivine is a key in controlling the overall reaction rates. The lack of brucite in the harzburgite experiment indicates that orthopyroxene reacted faster than olivine. Strong contrast in silica activities creates thermodynamic driving force for reactions. This research will serve as a base for future studies in hydrothermal alteration processes. Relations between rock composition and reaction kinetic will need to be further explored. Much

of the variability in terms of temperature and rock composition has not yet been investigated. Especial long-term experiments are necessary which allow a detailed characterization of Fe-Mg-ratios and iron oxidation states in the secondary minerals to understand the amount and process of hydrogen production. A number of possible future studies using the same experimental set up are apparent. The experimental setup could be improved so that it is possible to monitor in-situ hydrogen concentration during regression progress to overcome analytical problems and indicate problems with permeability. Experimental and theoretical simulations of natural systems play an important role in understanding hydrothermal alteration. They enlarge the range of applications of model predictions and assist the accuracy of thermodynamic models. Further experimental investigations are needed to further our understanding in hydrothermal processes.

References

Albertsen J. F., Jensen G. B. and Knudsen J. M. (1978) Structure of taenite in two iron meteorites. Nature 273, 453-454.

Allen D. E. and Seyfried Jr. W. E. (2003) Compositional controls on vent fluids from ultramafic-hosted hydrothermal systems at mid-ocean ridges: An experimental study at 400 °C, 500 bars. Geochimia Cosmochimica Acta, 67, 1531-1542.

Allen D. E. and Seyfried Jr. W. E. (2005) REE controls in ultramafic hosted MOR hydrothermal systems: An experimental study at elevated temperature and pressure. Geochimica et Cosmochimica Acta, 69, 675-683.

Alt J. C., Shanks W. C., Bach W., Paulick H., Garrido C. J. and Beaudoin G. (2007) Hydrothermal alteration and microbial sulfate reduction in peridotite and gabbro exposed by detachment faulting at the Mid-Atlantic Ridge, 15820'N (ODP Leg 209): A sulfur andoxygen isotope study. Geochemistry, Geophysics, Geosystems 8, Q08002, doi:08010.01029/02007GC001617.

Bach W. and Irber W. (1998) Rare earth element mobility in the oceanic lower sheeted dyke complex: evidence from geochemical data and leaching experiments. Chemical Geology, 151, 309-326.

Bach W., Roberts S., Vanko D., Binns R., Yeats C., Craddock P. and Humphris S. (2003) Controls of fluid chemistry and complexation on rare-earth element contents of anhydrite from the Pacmanus subseafloor hydrothermal system, Manus Basin, Papua New Guinea. Mineralium Deposita, 38, 916-935.

Bach W., Garrido C. J., Harvey J., Paulick H. and Rosner M. (2004) Variable seawater-peridotite interactions – first insights from ODP Leg 209, MAR 15°N. Geochemistry Geophysics Geosystems, 5, Q09F26.

Bach W., Paulick H., Garrido C. J., Ildefonse B., Meurer W. P. and Humphris S. E. (2006) Unraveling the sequence of serpentinization reactions: petrography, mineral chemistry, and petrophysics of serpentinites from MAR 15°N (ODP Leg 209, Site 1274). Geophysical Research Letters, 33, L13306.

Baker E., German C. R. and Elderfield H. (1995) Hydrothermal plumes over spreading-center axes: Global distributions and geological inferences. Pp. 47-71 in Seafloor Hydrothermal Systems: Physical, Chemical, Biological, and Geological Interactions. Humphris S. E., Zierenberg R. A., Mullineaux L. S. and Thomson R. E., eds, AGU Monograph Series, No. 91, American Geophysical Union, Washington, DC.

Berndt M. E., Allen D. E. and Seyfried W. E. (1996) Reduction of CO_2 during serpentinization of olivine at 300 °C and 500 bars. Geology, 24, 351-354.

Bethke C. M. (2007) The Geochemist'sWorkbenchVersion 7.0. Urbana, IL: University of Illinois.

Campbell A. C., Palmer M. R., Klinkhammer G. P., Bowers T. S., Edmond J. M., Lawrence J. R., Casey J. F., Thompson G., Humphris S., Rona P. and Karson J. A. (1988a) Chemistry of hot springs on the Mid-Atlantic Ridge. Nature, 335, 514-519.

Cannat M., Bideau B. and Bougault H. (1992) Serpentinized peridotites and gabbros in the Mid-Atlantic Ridge axial valley at 15°37'N and 16°52'N. Earth and Planetary Science Letters, 109, 87-106.

Chapelle F. H., O'Neill K., Bradley P. M., Methe B. A., Ciufo S. A., Knobel L. L. and Lovley D. R. (2002) A hydrogen-based subsurface microbial community dominated by methanogens. Nature, 415, 312-315.

Chernosky J. V. (1975) Aggregate refractive indices and unit cell parameters of synthetic serpentine in the system MgO-Al_2O_3-SiO_2-H_2O. American Mineralogist, 60, 200-208.

Cline J. D. (1969) Spectrophotometric determination of hydrogen sulfide in natural water. Limnology and Oceanography, 3, 454-458.

Coleman R. G. and Keith T. E. (1971) A chemical study of serpentinization - Burro Mountain, California. Journal of Petrology, 12, 311-328.

Craddock P. R., Bach W., Seewald J. S., Rouxel O. J., Reeves E. and Tivey M. K. (2010) Rare earth element abundances in hydrothermal fluids from the Manus Basin, Papua New Guinea: Indicators of sub-seafloor hydrothermal processes in back-arc basins. Geochimica et Cosmochimica Acta, 74, 5494-5513.

Dick H. J. B. (1974) Terrestrial nickel-iron from the Josephine Peridotite, its geologic occurrence, associations, and origin. Earth and Planetary Science Letters, 24, 291-298.

Dickson F. W., Blount C. W. and Tunell G. (1963) Use of hydrothermal solution equipment to determine the solubility of anhydrate in water from 100 °C to 275 °C and from 1 bar to 1000 bars pressure. American Journal of Science, 261, 61-78.

Douville E., Charlou J. L., Oelkers E. H., Bienvenu P., Jove Colon C. F., Donval J. P., Fouquet Y., Prieur D. and Appriou P. (2002) The rainbow vent fluids (36°14′N, MAR): the influence of ultramafic rocks and phase separation on trace metal content in Mid-Atlantic Ridge hydrothermal fluids. Chemical Geology, 184, 37-48.

Falini G., Foresti E., Gazzano M., Gualtieri A. F., Leoni M., Lesci I. G. and Roveri N. (2004) Tubular-shaped stoichiometric chrysotile nanocrystals. Chemistry – A European Journal, 10, 3043-3049.

Fogo J. K. and Popowsky M. (1949) Spectrophotometric determination of hydrogen sulfide – methylene blue method. Analytical Chemistry, 21, 732-734.

Frost B. R. (1985) On the stability of sulfides, oxides and native metals in serpentinite. Journal of Petrology, 26, 31-63.

Frost B. R. and Beard J. S. (2007) On silica activity and serpentinization. Journal of Petrology, 48, 1351-1368.

German C. R. and Von Damm K. L. (2004) Hydrothermal processes, in the Treatise on Geochemistry, Volume 6: The Oceans and Marine Geochemistry, pp. 181-222. Editors: Holland H. D. and Turekian K. K., Elsevier.

Haas J. R., Shock E.L. and Sassani D.C. (1995) Rare earth elements in hydrothermal systems: estimates of standard partial molal thermodynamic properties of aqueous complexes of the rare earth elements at high pressures and temperatures. Geochimica et Cosmochimima Acta, 59, 4329–4350.

Hall P. O. J. and Aller R. C. (1992) Rapid, small-volume, flow injection analysis for $\sum CO_2$ and NH_4^+ in marine and freshwaters. American Society of Limnology and Oceanography, 37, 1113–1119.

Hannigton M. D., de Ronde C. E. J. and Petersen S. (2005) Sea-floor tectonics and submarine hydrothermal systems. Pp. 111-141 in 100th Anniversary Volume of Economic Geology. Hedenquist J. et al., eds, Society of Economic Geologists, Littleton, Colorado.

Heinen W. and Lauwers A. M. (1996) Organic sulfur compounds resulting from the interaction of iron sulfide, hydrogen sulfide and carbon dioxide in an anaerobic aqueous environment. Origins of Life and Evolution of Biospheres, 26, 131-150.

Hennet R. J.-C., Holm N. G. and Engel M. H. (1992) Abiotic synthesis of amino acids under hydrothermal conditions and the origin of life: a perpetual phenomenon? Naturwissenschaften, 79, 361-365.

James R. H., Elderfield H. and Palmer M. R. (1995) The chemistry of hydrothermal fluids from the Broken Spur site, 29°N Mid-Atlantic ridge. Geochimica et Cosmochimica Acta, 59, 651-659.

Janecky D. R. and Seyfried W. E. (1986) Hydrothermal serpentinization of peridotite within the oceanic crust: experimental investigations of mineralogy and major element chemistry. Geochimia and Cosmochimica Acta, 50, 1357-1378.

Johnson J. W., Oelkers E. H. and Helgeson H. C. (1992) SUPCRT92: A software package for calculating the standard molal thermodynamic properties of minerals, gases, aqueous species, and reactions from 1 to 5000 bar and 0 to 1000 °C. Computers & Geosciences, 18, 899-947.

Katayama I., Kurosaki I. and Hirauchi K. (2010) Low silica activity for hydrogen generation during serpentinization: An example of natural serpentinites in the Mineoka ophiolite complex, central Japan. Earth and Planetary Science Letters, 298, 199-204.

Kelley D. S., Karson J. A., Früh-Green G. L., Yoerger D. R., Shank T. M., Butterfield D. A., Hayes J. M., Schrenk M. O., Olson E. J., Proskurowski G., Jakuba M., Bradley A., Larson B., Ludwig K., Glickson D., Buckman K., Bradley A. S., Brazelton W. J., Roe K., Elend M. J., Delacour A., Bernasconi S. M., Lilley M. D., Baross J. A., Summons R. E. and Sylva S. P. (2005) A Serpentinite-Hosted Ecosystem: The Lost City Hydrothermal Field. Science, 307, 1428-1434.

Kishima N. (1984) Properties of materials under hydrothermal conditions. Permeation of hydrogen through gold membrane. Papers of the Institute of Thermal Spring Research, Okayama University, Vol. 54, 55-60 (in Japanese with English abstract).

Klein F. and Bach W. (2009) Fe-Ni-Co-O-S Phase relations in peridotite-seawater interactions. Journal of Petrology, 30, 37-59.

Klein F., Bach W., Jöns N., McCollom T., Moskowitz B. and Berqué T. (2009) Iron partitioning and hydrogen generation during serpentinization of abyssal peridotites from 15°N on the Mid-Atlantic Ridge. Geochimica et Cosmochimica Acta, 73, 6868-6893.

Klinkhammer G. P., Chin C. S., Wilson C. and German C. R. (1995) Venting from the Mid-Atlantic Ridge at 37°17′N: the Lucky Strike hydrothermal site. Geological Society, London, Special Publications, 87, 87-96.

Koschinsky A., Billings A., Devey C., Dubilier N., Duester A., Edge D., Garbe-Schonberg D., German C., Giere O., Keir R., Lackschewitz K., Mai H. A., Marbler H., Mawick J., Melchert B., Mertens C., Peters M., Sander S., Schmale O., Schmidt W., Seifert R., Seiter C., Stober U., Suck I., Walter M., Weber S., Yoerger D., Zarrouk M. and Zielinski F. (2006) Discovery of new hydrothermal vents on the southern Mid-Atlantic Ridge (4°S–10°S) during cruise M68/1. InterRidge News, 15, 9–16.

Marshall W. L. (1994) Hydrothermal synthesis of amino acids. Geochimica et Cosmochimica Acta, 58, 2099-2106.

Martin B. and Fyfe W. S. (1970) Some experimental and theoretical observations on the kinetics of hydration reactions with particular reference to serpentinization. Chemical Geology, 6, 185-202.

Martin W. and Russell M. J. (2007) On the origin of biochemistry at an alkaline hydrothermal vent. Philosophical Transactions of the Royal Society B: Biological Sciences, 362, 1887-1926.

Martin W., Baross J., Kelley D. and Russell M. J. (2008) Hydrothermal vents and the origin of life. Nature Reviews Microbiology, 6, 805-814.

McCollom T. M. and Seewald J. S. (2001) A reassessment of the potential for reduction of dissolved CO_2 to hydrocarbons during serpentinization of olivine. Geochimica et Cosmochimica Acta, 65, 3769-3778.

McCollom T. M. and Seewald J. S. (2003) Experimental constraints on the hydrothermal reactivity of organic acids and acid anions: I. Formic acid and formate. Geochimica et Cosmochimica Acta, 67, 3625-3644.

McCollom T. M. and Seewald J. S. (2007) Abiotic synthesis of organic compounds in deep-sea hydrothermal environments. Chemical Reviews, 107, 382-401.

McCollom T. M. and Bach W. (2009) Thermodynamic constraints on hydrogen generation during serpentinization of ultramafic rocks. Geochimica et Cosmochimica Acta, 73, 856-875.

Menzies M., Seyfried W. E. and Blanchard D. (1979) Experimental evidence of rare earth element immobility in greenstones. Nature, 282, 398-399.

Mével C. (2003) Serpentinization of abyssal peridotites at mid-ocean ridges. Comptes Rendus Geoscience, 335, 825-852.

Michard A., Albarède F., Michard G., Minster J. F. and Charlou J. L. (1983) Rare-earth elements and uranium in high-temperature solutions from East Pacific Rise hydrothermal vent field (13°N). Nature, 303, 795-797.

Michard A. and Albarede F. (1986) The REE content of some hydrothermal fluids. Chemical Geology, 55, 51–60.

Michard A. (1989) Rare earth element systematics in hydrothermal fluids. Geochimica et Cosmochimica Acta, 53, 745–750.

Misra K. C. and Fleet M. E. (1973b) Unit cell parameters of monosulfide, pentlandite and taenite solid solution within the Fe-Ni-S system. Materials Research Bulletin, 8, 669-678.

Möller P. (2002) The distribution of rare earth elements and yttrium in water-rock interactions: field observations and experiments. In Water-Rock Interaction (eds. Stober I. and Bucher K.). Kluwer Academic Publishers, pp. 97-123.

Moody J. B. (1976) An experimental study on the serpentinization of iron-bearing olivines. Canadian Mineralogist, 14, 462-478.

Mottl M. J. and Wheat C. G. (1994) Hydrothermal circulation through mid-ocean ridge flanks: Fluxes of heat and magnesium. Geochimica et Cosmochimica Acta, 58, 2225-2237.

Normand C., Williams-Jones A. E., Martin R. F. and Vali H. (2002) Hydrothermal alteration of olivine in a flow-through autoclave: Nucleation and growth of serpentine phases. American Mineralogist, 87, 1699–1709.

O'Hanley D. S. (1992) Solution to the volume problem in serpentinization. Geology, 20, 705-708.

O'Hanley D. S. and Wicks F. J. (1995) Conditions of formation of lizardite, chrysotile and antigorite, Cassiar, British Columbia. The Canadian Mineralogist, 33, 753-773.

O'Hanley D. S. and Dyar M. D. (1998) The composition of chrysotile and its relationship with lizardite. The Canadian Mineralogist, 36, 727-739.

Ohmoto H. and Lasaga A. C. (1982) Kinetics of reactions between aqueous sulfates and sulfides in hydrothermal systems. Geochimica et Cosmochimica Acta, 46, 1727-1745.

Oufi O. and Cannat M. (2002) Magnetic properties of variably serpentinized abyssal peridotites. Journal of Geophysical Research, 107, 2095-2113.

Paulick H., Bach W., Godard M., De Hoog J. C. M., Suhr G. and Harvey J. (2006) Geochemistry of abyssal peridotites (Mid-Atlantic Ridge, 15°20'N, ODP Leg 209): Implications for fluid/rock interaction in slow spreading environments. Chemical Geology, 234, 179-210.

Perner M., Kuever J., Seifert R., Pape T., Koschinsky A., Schmidt K., Strauss H. and Imhoff J. F. (2007) The influence of ultramafic rocks on microbial communities at the Logatchev hydrothermal field, located 15°N on the Mid-Atlantic Ridge. FEMS Microbiology Ecology, 61, 97-109.

Peters C. and Dekkers M. J. (2003) Selected room temperature magnetic parameters as a function of mineralogy and grain size. Physics and Chemistry of the Earth, 28, 659-667.

Petersen J. M., Zielinski F. U., Pape T., Seifert R., Moraru C., Amann R., Hourdez S., Girguis P. R., Wankel S. D., Barbe V., Pelletier E., Fink D., Borowski C., Bach W. and Dubilier N. (2011) Hydrogen is an energy source for hydrothermal vent symbioses. Nature, 476, 176-180.

Rushdi A. I. and Simoneit B. R. T. (2005) Abiotic synthesis of organic compounds from carbon disulfide under hydrothermal conditions. Astrobiology, 5, 749-768.

Rytuba J. J. and Dickson F. W. (1974) Reaction of pyrite + pyrrhotite + quartz + gold with NaCl-H_2O solutions, 300-500 °C, 500–1500 bars, and genetic implications. In Problems of Ore Deposition: 4th IAGOD Symposium, Bulgarian Acad. Sci., Varna 1974, Vol. 2, ed. B. Bogdanov, 320–326.

Schulte M., Blake D., Hoehler T. and McCollom T. (2006) Serpentinization and its implications for life on the early Earth and Mars. Astrobiology, 6, 364-376.

Seyfried W. E. (1979) A new reaction cell for hydrothermal solution equipment. American Mineralogist, 64, 646-649.

Seyfried W. E. and Dibble W. E. J. (1980) Sea water-peridotite interaction at 300 °C and 500 bars: implications for the origin of oceanic serpentinites. Geochimica et Cosmochimica Acta 44, 309-321.

Seyfried W. E., Foustoukos D. I. and Fu Qi (2007) Redox evolution and mass transfer during serpentinization: An experimental and theoretical study at 200 °C, 500 bar with implications for ultramafic-hosted hydrothermal systems at Mid-Ocean Ridges. Geochimica et Cosmochimica Acta, 71, 3872-3886.

Stein C. A. and Stein S. (1994) Constrains on hydrothermal heat flux through the oceanic lithosphere from global heat flow. Journal of Geophysical Research, 99, 3081-3095.

Sugaki A. and Kitakaze A. (1998) High form of pentlandite and its thermal stability. American Mineralogist, 83, 133-140.

Summerhayes C. P. and Thorpe S. A. (1996) Oceanography an illustrated guide, 11, 165-181.

Sverjensky D. A. (1984) Europium redox equilibria in aqueous solution. Earth Planetary Science Letters, 67, 70-78.

Takai K., Gamo T., Tsunogai U., Nakayama N., Hirayama H., Nealson K. H. and Horikoshi K. (2004) Geochemical and microbiological evidence for a hydrogen-based, hyperthermophilic subsurface lithoautotrophic microbial ecosystem (HyperSLiME) beneath an active deep-sea hydrothermal field. Extremophiles, 8, 269-282.

Tivey M. K. (2007) Generation of seafloor hydrothermal vent fluids and associated mineral deposits. Oceanography, 20, Number 1, 50-65.

Toft P. B., Arkani-Hamed J. and Haggerty S. E. (1990) The effects of serpentinization on density and magnetic susceptibility: a petrophysical model. Physics of the Earth and planetary interiors, 65, 137-157.

Ulmer G. C. and Barnes H. L. (1987) Hydrothermal experimental techniques. A Wiley-Interscience Publication. Copyright © by John Wiley & Sons, Inc.

Viti C. (2010) Serpentine minerals discrimination by thermal analysis. American Mineralogist, 95, 631–638.

Wolery T. J. (1992) EQ3/6, a software package for geochemical modeling of aqueous systems: Package overview and Installation guide (version 7.0). Livermore, CA: Lawrence Livermore National Laboratory.

Wood S. A. (1990) The aqueous geochemistry of the rare-earth elements and yttrium: 2. Theoretical predictions of speciation in hydrothermal solutions to 350 °C at saturation water vapor pressure. Chemical Geology, 88, 99-125.

Xia F., Zhou J., Brugger J., Ngothai Y., O'Neill B., Chen G. and Pring A. (2008) Novel route to synthesize complex metal sulfides: hydrothermal coupled dissolution – reprecipitation replacement reactions. Chemistry of Materials, 20, 2809-2817.

Yanagawa K. and Kobayashi K. (1992) An experimental approach to chemical evolution in submarine hydrothermal systems. Origins of Life and Evolution of Biospheres, 22, 147-159.

Appendix

A1. Electron microprobe data of forsterite-rich olivine. Formulae calculated on the basis of 4 oxygens, assuming all Fe as Fe^{2+}. Mg# = Mg / (Mg + Fe^{2+}) *100.

sample no.	1	2	3	4	5	6	7	8	9	10	11	12	13	14	15	16	17	18	19	20
wt.%																				
SiO_2	41.52	41.16	41.19	41.06	40.73	43.04	41.25	40.95	41.18	40.92	41.18	41.17	40.97	40.98	42.03	41.10	40.99	41.00	40.98	41.14
TiO_2	0.00	0.00	0.01	0.00	0.00	0.00	0.02	0.02	0.00	0.00	0.01	0.00	0.01	0.00	0.01	0.02	0.00	0.02	0.02	0.00
Al_2O_3	0.05	0.11	0.06	0.06	0.04	0.02	0.03	0.02	0.03	0.04	0.02	0.02	0.02	0.04	0.02	0.02	0.04	0.03	0.03	0.01
Cr_2O_3	0.03	0.03	0.03	0.02	0.01	0.03	0.04	0.01	0.02	0.01	0.01	0.00	0.01	0.00	0.03	0.01	0.03	0.01	0.00	0.01
FeO	8.88	8.80	8.92	8.91	9.17	8.88	8.83	8.69	8.77	8.91	8.82	8.65	8.62	8.84	8.50	9.46	9.39	9.21	9.60	9.65
MgO	50.33	49.26	49.63	49.42	49.66	46.41	49.68	49.97	49.90	49.81	50.04	49.77	49.96	49.78	48.78	49.41	49.34	49.35	49.62	49.88
MnO	0.12	0.13	0.16	0.14	0.15	0.14	0.13	0.12	0.16	0.13	0.12	0.09	0.13	0.11	0.10	0.14	0.13	0.17	0.15	0.19
CaO	0.10	0.09	0.09	0.12	0.09	0.05	0.08	0.07	0.06	0.06	0.04	0.05	0.04	0.04	0.05	0.03	0.02	0.03	0.03	0.05
Na_2O	0.00	0.00	0.00	0.00	0.00	0.00	0.00	0.00	0.00	0.00	0.00	0.00	0.00	0.00	0.00	0.00	0.00	0.00	0.00	0.00
K_2O	0.00	0.00	0.00	0.00	0.00	0.00	0.00	0.00	0.00	0.00	0.00	0.00	0.00	0.00	0.00	0.00	0.00	0.00	0.00	0.00
NiO	0.40	0.41	0.44	0.42	0.45	0.38	0.37	0.37	0.40	0.37	0.36	0.34	0.37	0.38	0.37	0.38	0.39	0.37	0.38	0.37
ZnO	0.00	0.00	0.00	0.00	0.00	0.00	0.00	0.00	0.00	0.00	0.00	0.00	0.00	0.00	0.00	0.00	0.00	0.00	0.00	0.00
Cl	0.00	0.00	0.00	0.00	0.00	0.00	0.00	0.00	0.00	0.00	0.00	0.00	0.00	0.00	0.00	0.00	0.00	0.00	0.00	0.00
total	101.43	100.00	100.53	100.16	100.30	98.95	100.42	100.21	100.51	100.24	100.60	100.09	100.14	100.17	99.90	100.57	100.32	100.18	100.82	101.30
formula (4 O)																				
Si	1.00	1.00	1.00	1.00	0.99	1.05	1.00	1.00	1.00	1.00	1.00	1.00	1.00	1.00	1.02	1.00	1.00	1.00	1.00	1.00
Ti	0.00	0.00	0.00	0.00	0.00	0.00	0.00	0.00	0.00	0.00	0.00	0.00	0.00	0.00	0.00	0.00	0.00	0.00	0.00	0.00
Al	0.00	0.00	0.00	0.00	0.00	0.00	0.00	0.00	0.00	0.00	0.00	0.00	0.00	0.00	0.00	0.00	0.00	0.00	0.00	0.00
Cr	0.00	0.00	0.00	0.00	0.00	0.00	0.00	0.00	0.00	0.00	0.00	0.00	0.00	0.00	0.00	0.00	0.00	0.00	0.00	0.00
Fe	0.18	0.18	0.18	0.18	0.19	0.18	0.18	0.18	0.18	0.18	0.18	0.18	0.18	0.18	0.17	0.19	0.19	0.19	0.20	0.20
Mg	1.81	1.79	1.80	1.80	1.81	1.70	1.80	1.81	1.81	1.81	1.81	1.81	1.81	1.81	1.77	1.79	1.79	1.80	1.80	1.80
Mn	0.00	0.00	0.00	0.00	0.00	0.00	0.00	0.00	0.00	0.00	0.00	0.00	0.00	0.00	0.00	0.00	0.00	0.00	0.00	0.00
Ca	0.00	0.00	0.00	0.00	0.00	0.00	0.00	0.00	0.00	0.00	0.00	0.00	0.00	0.00	0.00	0.00	0.00	0.00	0.00	0.00
Na	0.00	0.00	0.00	0.00	0.00	0.00	0.00	0.00	0.00	0.00	0.00	0.00	0.00	0.00	0.00	0.00	0.00	0.00	0.00	0.00
K	0.00	0.00	0.00	0.00	0.00	0.00	0.00	0.00	0.00	0.00	0.00	0.00	0.00	0.00	0.00	0.00	0.00	0.00	0.00	0.00
Ni	0.01	0.01	0.01	0.01	0.01	0.01	0.01	0.01	0.01	0.01	0.01	0.01	0.01	0.01	0.01	0.01	0.01	0.01	0.01	0.01
Zn	0.00	0.00	0.00	0.00	0.00	0.00	0.00	0.00	0.00	0.00	0.00	0.00	0.00	0.00	0.00	0.00	0.00	0.00	0.00	0.00
Cl	0.00	0.00	0.00	0.00	0.00	0.00	0.00	0.00	0.00	0.00	0.00	0.00	0.00	0.00	0.00	0.00	0.00	0.00	0.00	0.00
Mg#	91.0	90.9	90.8	90.8	90.6	90.3	90.9	91.1	91.0	90.9	91.0	91.1	91.2	90.9	91.1	90.3	90.4	90.5	90.2	90.2

A2. Electron microprobe data of forsterite-rich olivine. Formulae calculated on the basis of 4 oxygens, assuming all Fe as Fe^{2+}. Mg# = Mg / (Mg + Fe^{2+}) *100.

sample no.	21	22	23	24	25	26	27	28	29	30	31	32	33	34	35	36	37	38	39	40
wt.%																				
SiO_2	41.26	41.33	41.24	41.39	41.91	41.36	40.90	41.14	41.18	40.96	41.24	41.15	41.13	41.44	40.80	41.52	41.53	41.58	41.65	41.40
TiO_2	0.02	0.00	0.01	0.01	0.00	0.00	0.00	0.00	0.00	0.00	0.00	0.00	0.00	0.01	0.00	0.01	0.01	0.01	0.00	0.00
Al_2O_3	0.03	0.01	0.01	0.02	0.04	0.02	0.03	0.02	0.03	0.01	0.05	0.04	0.07	0.03	0.04	0.02	0.02	0.03	0.03	0.02
Cr_2O_3	0.00	0.02	0.01	0.03	0.03	0.02	0.02	0.03	0.00	0.00	0.02	0.03	0.02	0.03	0.03	0.01	0.01	0.01	0.00	0.02
FeO	8.34	8.33	8.33	8.45	8.53	8.40	8.58	8.39	8.52	8.38	9.70	9.45	9.50	9.53	9.49	8.18	8.47	8.33	8.21	8.45
MgO	50.07	50.22	50.14	50.20	49.41	50.15	50.48	50.33	50.20	51.38	48.89	49.28	48.84	48.68	48.67	49.72	50.00	50.17	49.93	49.65
MnO	0.08	0.11	0.17	0.12	0.12	0.17	0.09	0.13	0.07	0.12	0.15	0.16	0.17	0.15	0.13	0.12	0.08	0.13	0.14	0.15
CaO	0.03	0.04	0.04	0.04	0.03	0.04	0.04	0.03	0.04	0.04	0.10	0.09	0.10	0.10	0.10	0.05	0.03	0.03	0.04	0.04
Na_2O	0.00	0.00	0.00	0.00	0.00	0.00	0.00	0.00	0.00	0.00	0.00	0.00	0.00	0.00	0.00	0.00	0.00	0.00	0.00	0.00
K_2O	0.00	0.00	0.00	0.00	0.00	0.00	0.00	0.00	0.00	0.00	0.00	0.00	0.00	0.00	0.00	0.00	0.00	0.00	0.00	0.00
NiO	0.39	0.37	0.41	0.40	0.41	0.37	0.37	0.41	0.36	0.40	0.43	0.40	0.39	0.41	0.41	0.37	0.40	0.39	0.39	0.37
ZnO	0.00	0.00	0.00	0.00	0.00	0.00	0.00	0.00	0.00	0.00	0.00	0.00	0.00	0.00	0.00	0.00	0.00	0.00	0.00	0.00
Cl	0.00	0.00	0.00	0.00	0.00	0.00	0.00	0.00	0.00	0.00	0.00	0.00	0.00	0.00	0.00	0.00	0.00	0.00	0.00	0.00
total	100.21	100.43	100.36	100.66	100.49	100.53	100.51	100.48	100.40	101.30	100.57	100.60	100.22	100.38	99.66	100.00	100.55	100.69	100.39	100.11
formula (4 O)																				
Si	1.00	1.00	1.00	1.00	1.01	1.00	0.99	1.00	1.00	0.99	1.00	1.00	1.00	1.01	1.00	1.01	1.01	1.01	1.01	1.01
Ti	0.00	0.00	0.00	0.00	0.00	0.00	0.00	0.00	0.00	0.00	0.00	0.00	0.00	0.00	0.00	0.00	0.00	0.00	0.00	0.00
Al	0.00	0.00	0.00	0.00	0.00	0.00	0.00	0.00	0.00	0.00	0.00	0.00	0.00	0.00	0.00	0.00	0.00	0.00	0.00	0.00
Cr	0.00	0.00	0.00	0.00	0.00	0.00	0.00	0.00	0.00	0.00	0.00	0.00	0.00	0.00	0.00	0.00	0.00	0.00	0.00	0.00
Fe	0.17	0.17	0.17	0.17	0.17	0.17	0.17	0.17	0.17	0.17	0.20	0.19	0.19	0.19	0.20	0.17	0.17	0.17	0.17	0.17
Mg	1.81	1.82	1.81	1.81	1.78	1.81	1.83	1.82	1.82	1.85	1.78	1.79	1.78	1.77	1.78	1.80	1.81	1.81	1.80	1.80
Mn	0.00	0.00	0.00	0.00	0.00	0.00	0.00	0.00	0.00	0.00	0.00	0.00	0.00	0.00	0.00	0.00	0.00	0.00	0.00	0.00
Ca	0.00	0.00	0.00	0.00	0.00	0.00	0.00	0.00	0.00	0.00	0.00	0.00	0.00	0.00	0.00	0.00	0.00	0.00	0.00	0.00
Na	0.00	0.00	0.00	0.00	0.00	0.00	0.00	0.00	0.00	0.00	0.00	0.00	0.00	0.00	0.00	0.00	0.00	0.00	0.00	0.00
K	0.00	0.00	0.00	0.00	0.00	0.00	0.00	0.00	0.00	0.00	0.00	0.00	0.00	0.00	0.00	0.00	0.00	0.00	0.00	0.00
Ni	0.01	0.01	0.01	0.01	0.01	0.01	0.01	0.01	0.01	0.01	0.01	0.01	0.01	0.01	0.01	0.01	0.01	0.01	0.01	0.01
Zn	0.00	0.00	0.00	0.00	0.00	0.00	0.00	0.00	0.00	0.00	0.00	0.00	0.00	0.00	0.00	0.00	0.00	0.00	0.00	0.00
Cl	0.00	0.00	0.00	0.00	0.00	0.00	0.00	0.00	0.00	0.00	0.00	0.00	0.00	0.00	0.00	0.00	0.00	0.00	0.00	0.00
Mg#	91.5	91.5	91.5	91.4	91.2	91.4	91.3	91.4	91.3	91.6	90.0	90.3	90.2	90.1	90.1	91.6	91.3	91.5	91.6	91.3

A3. Electron microprobe data of forsterite-rich olivine. Formulae calculated on the basis of 4 oxygens, assuming all Fe as Fe^{2+}. Mg# = Mg / (Mg + Fe^{2+}) *100.

sample no.	41	42	43	44	45	46	47	48	49	50	51	52	53	54	55	56	57	58	59	60
wt.%																				
SiO_2	41.46	41.52	41.51	41.29	41.79	41.29	41.28	41.42	41.57	41.26	41.07	41.15	41.27	41.07	41.16	40.04	41.48	41.40	41.25	41.73
TiO_2	0.01	0.00	0.00	0.01	0.00	0.00	0.00	0.00	0.01	0.00	0.00	0.00	0.00	0.03	0.00	0.02	0.00	0.00	0.00	0.00
Al_2O_3	0.01	0.00	0.00	0.02	0.01	0.03	0.05	0.03	0.03	0.04	0.02	0.01	0.04	0.03	0.02	0.03	0.03	0.04	0.03	0.03
Cr_2O_3	0.00	0.02	0.02	0.00	0.01	0.04	0.06	0.03	0.04	0.03	0.00	0.00	0.01	0.04	0.02	0.02	0.03	0.00	0.03	0.02
FeO	9.32	9.32	9.26	9.28	9.15	8.74	8.83	8.81	9.07	8.70	9.06	8.97	9.28	9.10	9.13	8.21	8.24	8.17	8.04	8.28
MgO	49.17	49.28	48.81	49.21	48.50	49.54	49.56	49.45	49.46	50.00	49.07	49.24	49.17	49.36	49.72	49.49	50.17	50.24	50.05	50.04
MnO	0.15	0.09	0.12	0.15	0.14	0.11	0.17	0.16	0.14	0.15	0.17	0.11	0.09	0.11	0.15	0.14	0.14	0.09	0.10	0.15
CaO	0.02	0.03	0.02	0.03	0.03	0.09	0.08	0.08	0.10	0.10	0.06	0.05	0.06	0.07	0.07	0.09	0.07	0.08	0.09	0.08
Na_2O	0.00	0.00	0.00	0.00	0.00	0.00	0.00	0.00	0.00	0.00	0.00	0.00	0.00	0.00	0.00	0.00	0.00	0.00	0.00	0.00
K_2O	0.00	0.00	0.00	0.00	0.00	0.00	0.00	0.00	0.00	0.00	0.00	0.00	0.00	0.00	0.00	0.00	0.00	0.00	0.00	0.00
NiO	0.40	0.41	0.40	0.37	0.37	0.37	0.41	0.37	0.39	0.38	0.37	0.39	0.37	0.41	0.38	0.38	0.38	0.40	0.38	0.38
ZnO	0.00	0.00	0.00	0.00	0.00	0.00	0.00	0.00	0.00	0.00	0.00	0.00	0.00	0.00	0.00	0.00	0.00	0.00	0.00	0.00
Cl	0.00	0.00	0.00	0.00	0.00	0.00	0.00	0.00	0.00	0.00	0.00	0.00	0.00	0.00	0.00	0.00	0.00	0.00	0.00	0.00
total	100.55	100.67	100.13	100.36	100.01	100.21	100.43	100.35	100.81	100.66	99.81	99.93	100.29	100.22	100.64	98.42	100.54	100.41	99.97	100.71
formula (4 O)																				
Si	1.01	1.01	1.01	1.01	1.02	1.01	1.00	1.01	1.01	1.00	1.01	1.01	1.01	1.00	1.00	0.99	1.00	1.00	1.00	1.01
Ti	0.00	0.00	0.00	0.00	0.00	0.00	0.00	0.00	0.00	0.00	0.00	0.00	0.00	0.00	0.00	0.00	0.00	0.00	0.00	0.00
Al	0.00	0.00	0.00	0.00	0.00	0.00	0.00	0.00	0.00	0.00	0.00	0.00	0.00	0.00	0.00	0.00	0.00	0.00	0.00	0.00
Cr	0.00	0.00	0.00	0.00	0.00	0.00	0.00	0.00	0.00	0.00	0.00	0.00	0.00	0.00	0.00	0.00	0.00	0.00	0.00	0.00
Fe	0.19	0.19	0.19	0.19	0.19	0.18	0.18	0.18	0.18	0.18	0.19	0.18	0.19	0.19	0.19	0.17	0.17	0.17	0.16	0.17
Mg	1.78	1.78	1.77	1.79	1.76	1.80	1.80	1.79	1.79	1.81	1.79	1.79	1.79	1.80	1.80	1.83	1.81	1.81	1.82	1.80
Mn	0.00	0.00	0.00	0.00	0.00	0.00	0.00	0.00	0.00	0.00	0.00	0.00	0.00	0.00	0.00	0.00	0.00	0.00	0.00	0.00
Ca	0.00	0.00	0.00	0.00	0.00	0.00	0.00	0.00	0.00	0.00	0.00	0.00	0.00	0.00	0.00	0.00	0.00	0.00	0.00	0.00
Na	0.00	0.00	0.00	0.00	0.00	0.00	0.00	0.00	0.00	0.00	0.00	0.00	0.00	0.00	0.00	0.00	0.00	0.00	0.00	0.00
K	0.00	0.00	0.00	0.00	0.00	0.00	0.00	0.00	0.00	0.00	0.00	0.00	0.00	0.00	0.00	0.00	0.00	0.00	0.00	0.00
Ni	0.01	0.01	0.01	0.01	0.01	0.01	0.01	0.01	0.01	0.01	0.01	0.01	0.01	0.01	0.01	0.01	0.01	0.01	0.01	0.01
Zn	0.00	0.00	0.00	0.00	0.00	0.00	0.00	0.00	0.00	0.00	0.00	0.00	0.00	0.00	0.00	0.00	0.00	0.00	0.00	0.00
Cl	0.00	0.00	0.00	0.00	0.00	0.00	0.00	0.00	0.00	0.00	0.00	0.00	0.00	0.00	0.00	0.00	0.00	0.00	0.00	0.00
Mg#	90.4	90.4	90.4	90.4	90.4	91.0	90.9	90.9	90.7	91.1	90.6	90.7	90.4	90.6	90.7	91.5	91.6	91.6	91.7	91.5

B1. Electron microprobe data of enstatite-rich orthopyroxene. Formulae calculated on the basis of 6 oxygens, assuming all Fe as Fe^{2+}. Mg# = Mg / (Mg + Fe^{2+}) * 100.

sample no.	1	2	3	4	5	6	7	8	9	10	11	12	13	14	15	16	17	18	19	20
wt.%																				
SiO_2	56.69	56.70	56.37	57.14	56.92	57.79	57.47	57.54	57.33	57.13	56.92	57.35	57.19	57.10	56.62	57.17	56.97	57.12	57.15	56.83
TiO_2	0.01	0.06	0.00	0.00	0.00	0.02	0.00	0.00	0.06	0.05	0.03	0.00	0.06	0.08	0.01	0.00	0.01	0.06	0.06	0.05
Al_2O_3	0.09	0.11	0.08	0.07	0.06	0.09	0.07	0.07	0.08	0.08	0.08	0.09	0.07	0.09	0.07	0.09	0.08	0.09	0.08	0.08
Cr_2O_3	0.00	0.03	0.03	0.00	0.00	0.02	0.00	0.01	0.00	0.00	0.00	0.00	0.00	0.02	0.02	0.00	0.00	0.00	0.01	0.00
FeO	9.91	9.88	9.83	9.79	10.41	9.72	9.48	9.45	9.76	10.00	9.93	9.95	9.80	9.61	10.12	9.98	9.94	9.72	9.50	9.67
MgO	32.78	32.53	32.49	32.54	32.74	32.36	32.71	32.78	32.93	32.58	32.50	32.73	32.09	32.43	32.66	32.35	32.76	32.31	32.83	32.74
MnO	0.05	0.07	0.09	0.07	0.07	0.14	0.02	0.06	0.05	0.09	0.05	0.07	0.06	0.05	0.03	0.05	0.12	0.08	0.04	0.09
CaO	0.06	0.29	0.27	0.30	0.14	0.27	0.05	0.29	0.26	0.32	0.31	0.05	0.31	0.32	0.28	0.30	0.28	0.28	0.10	0.11
Na_2O	0.00	0.02	0.00	0.01	0.00	0.02	0.00	0.00	0.02	0.02	0.02	0.01	0.03	0.03	0.04	0.04	0.03	0.04	0.05	0.07
K_2O	0.00	0.00	0.00	0.00	0.00	0.00	0.01	0.00	0.00	0.00	0.00	0.00	0.00	0.00	0.00	0.00	0.00	0.00	0.00	0.03
total	99.59	99.69	99.16	99.92	100.34	100.43	99.81	100.21	100.48	100.27	99.85	100.25	99.61	99.72	99.85	99.98	100.19	99.70	99.81	99.66
formula (6 O)																				
Si	1.99	1.99	1.99	2.00	1.99	2.01	2.01	2.00	1.99	2.00	2.00	2.00	2.01	2.00	1.99	2.00	1.99	2.00	2.00	1.99
Ti	0.00	0.00	0.00	0.00	0.00	0.00	0.00	0.00	0.00	0.00	0.00	0.00	0.00	0.00	0.00	0.00	0.00	0.00	0.00	0.00
Al	0.00	0.00	0.00	0.00	0.00	0.00	0.00	0.00	0.00	0.00	0.00	0.00	0.00	0.00	0.00	0.00	0.00	0.00	0.00	0.00
Cr	0.00	0.00	0.00	0.00	0.00	0.00	0.00	0.00	0.00	0.00	0.00	0.00	0.00	0.00	0.00	0.00	0.00	0.00	0.00	0.00
Fe^{2+}	0.29	0.29	0.29	0.29	0.30	0.28	0.28	0.28	0.28	0.29	0.29	0.29	0.29	0.28	0.30	0.29	0.29	0.29	0.28	0.28
Mg	1.72	1.70	1.71	1.70	1.71	1.68	1.70	1.70	1.71	1.70	1.70	1.70	1.68	1.69	1.71	1.69	1.71	1.69	1.71	1.71
Mn	0.00	0.00	0.00	0.00	0.00	0.00	0.00	0.00	0.00	0.00	0.00	0.00	0.00	0.00	0.00	0.00	0.00	0.00	0.00	0.00
Ca	0.00	0.01	0.01	0.01	0.01	0.01	0.00	0.01	0.01	0.01	0.01	0.00	0.01	0.01	0.01	0.01	0.01	0.01	0.00	0.00
Na	0.00	0.00	0.00	0.00	0.00	0.00	0.00	0.00	0.00	0.00	0.00	0.00	0.00	0.00	0.00	0.00	0.00	0.00	0.00	0.00
K	0.00	0.00	0.00	0.00	0.00	0.00	0.00	0.00	0.00	0.00	0.00	0.00	0.00	0.00	0.00	0.00	0.00	0.00	0.00	0.00
Mg#	85.5	85.4	85.5	85.6	84.9	85.6	86.0	86.1	85.7	85.3	85.4	85.4	85.4	85.8	85.2	85.2	85.5	85.6	86.0	85.8

B2. Electron microprobe data of enstatite-rich orthopyroxene. Formulae calculated on the basis of 6 oxygens, assuming all Fe as Fe^{2+}. Mg# = Mg / (Mg + Fe^{2+}) * 100.

sample no.	21	22	23	24	25	26	27	28	29	30	31	32	33	34	35	36	37	38	39	40
wt.%																				
SiO_2	57.38	57.62	57.14	57.57	57.23	57.45	57.08	56.30	56.61	56.35	56.99	57.11	57.37	57.53	57.47	57.12	56.61	56.99	56.83	57.26
TiO_2	0.02	0.10	0.07	0.08	0.06	0.05	0.00	0.00	0.00	0.09	0.00	0.01	0.00	0.03	0.05	0.06	0.04	0.05	0.02	0.07
Al_2O_3	0.11	0.08	0.06	0.10	0.08	0.06	0.08	0.08	0.08	0.10	0.10	0.10	0.10	0.11	0.09	0.09	0.11	0.11	0.11	0.07
Cr_2O_3	0.01	0.01	0.00	0.00	0.00	0.05	0.00	0.04	0.00	0.00	0.06	0.03	0.02	0.00	0.00	0.00	0.00	0.00	0.03	0.05
FeO	9.80	9.74	10.16	9.67	9.57	9.68	9.52	9.87	10.17	10.05	9.52	9.36	9.40	10.10	9.42	9.62	9.48	9.41	9.65	9.83
MgO	32.49	32.66	32.80	32.71	32.96	33.14	32.73	32.54	32.61	32.09	33.05	32.97	33.05	32.86	33.13	33.23	33.19	33.25	32.75	32.77
MnO	0.04	0.07	0.08	0.06	0.08	0.03	0.10	0.09	0.08	0.06	0.06	0.09	0.09	0.08	0.02	0.10	0.06	0.08	0.07	0.09
CaO	0.24	0.32	0.30	0.28	0.25	0.28	0.24	0.27	0.26	0.30	0.24	0.23	0.22	0.24	0.18	0.27	0.28	0.29	0.25	0.30
Na_2O	0.03	0.04	0.01	0.00	0.03	0.05	0.03	0.00	0.02	0.01	0.05	0.02	0.04	0.03	0.03	0.04	0.04	0.04	0.04	0.00
K_2O	0.02	0.00	0.00	0.00	0.00	0.00	0.00	0.01	0.00	0.00	0.02	0.00	0.00	0.00	0.00	0.00	0.00	0.00	0.00	0.00
total	100.13	100.63	100.62	100.46	100.26	100.79	99.78	99.21	99.82	99.05	100.09	99.92	100.29	100.98	100.39	100.54	99.81	100.22	99.76	100.43
formula (6 O)																				
Si	2.00	2.00	1.99	2.00	1.99	1.99	2.00	1.99	1.99	1.99	1.99	2.00	2.00	1.99	2.00	1.99	1.98	1.99	1.99	1.99
Ti	0.00	0.00	0.00	0.00	0.00	0.00	0.00	0.00	0.00	0.00	0.00	0.00	0.00	0.00	0.00	0.00	0.00	0.00	0.00	0.00
Al	0.00	0.00	0.00	0.00	0.00	0.00	0.00	0.00	0.00	0.00	0.00	0.00	0.00	0.00	0.00	0.00	0.00	0.00	0.00	0.00
Cr	0.00	0.00	0.00	0.00	0.00	0.00	0.00	0.00	0.00	0.00	0.00	0.00	0.00	0.00	0.00	0.00	0.00	0.00	0.00	0.00
Fe^{2+}	0.29	0.28	0.30	0.28	0.28	0.28	0.28	0.29	0.30	0.30	0.28	0.27	0.27	0.29	0.27	0.28	0.28	0.27	0.28	0.29
Mg	1.69	1.69	1.70	1.70	1.71	1.71	1.71	1.71	1.71	1.69	1.72	1.72	1.71	1.70	1.72	1.72	1.73	1.73	1.71	1.70
Mn	0.00	0.00	0.00	0.00	0.00	0.00	0.00	0.00	0.00	0.00	0.00	0.00	0.00	0.00	0.00	0.00	0.00	0.00	0.00	0.00
Ca	0.01	0.01	0.01	0.01	0.01	0.01	0.01	0.01	0.01	0.01	0.01	0.01	0.01	0.01	0.01	0.01	0.01	0.01	0.01	0.01
Na	0.00	0.00	0.00	0.00	0.00	0.00	0.00	0.00	0.00	0.00	0.00	0.00	0.00	0.00	0.00	0.00	0.00	0.00	0.00	0.00
K	0.00	0.00	0.00	0.00	0.00	0.00	0.00	0.00	0.00	0.00	0.00	0.00	0.00	0.00	0.00	0.00	0.00	0.00	0.00	0.00
Mg#	85.5	85.7	85.2	85.8	86.0	85.9	86.0	85.5	85.1	85.1	86.1	86.3	86.3	85.3	86.2	86.0	86.2	86.3	85.8	85.6

B3. Electron microprobe data of enstatite-rich orthopyroxene. Formulae calculated on the basis of 6 oxygens, assuming all Fe as Fe^{2+}. Mg# = Mg / (Mg + Fe^{2+}) * 100.

sample no.	40	41	42	43	44	45	46	47	48	49	50	51	52	53	54	55	56	57	58	59	60
wt.%																					
SiO_2	57.26	56.88	56.92	57.42	56.77	56.88	57.36	57.46	57.45	57.42	57.40	57.01	57.27	56.61	57.63	57.26	57.13	57.09	57.68	57.60	57.12
TiO_2	0.07	0.00	0.12	0.03	0.03	0.00	0.00	0.07	0.03	0.00	0.06	0.00	0.03	0.04	0.09	0.01	0.03	0.05	0.05	0.00	0.12
Al_2O_3	0.07	0.09	0.08	0.08	0.09	0.10	0.10	0.06	0.09	0.09	0.09	0.10	0.06	0.10	0.10	0.08	0.07	0.10	0.09	0.09	0.08
Cr_2O_3	0.05	0.01	0.04	0.01	0.00	0.02	0.02	0.00	0.02	0.00	0.01	0.03	0.00	0.01	0.01	0.01	0.00	0.03	0.02	0.02	0.02
FeO	9.83	10.22	10.17	9.98	10.15	10.10	9.59	9.63	9.75	9.56	9.86	9.63	9.85	9.60	9.64	10.01	10.13	10.12	9.52	9.45	9.47
MgO	32.77	32.61	32.72	32.54	32.56	32.82	32.85	33.30	33.12	32.91	33.12	32.68	32.84	32.77	33.00	32.52	33.07	32.85	33.11	32.97	33.00
MnO	0.09	0.06	0.08	0.09	0.08	0.07	0.05	0.03	0.08	0.04	0.08	0.05	0.07	0.10	0.09	0.03	0.06	0.09	0.05	0.05	0.08
CaO	0.30	0.28	0.29	0.29	0.31	0.26	0.28	0.25	0.28	0.26	0.28	0.27	0.26	0.25	0.26	0.33	0.04	0.29	0.28	0.26	0.28
Na_2O	0.00	0.02	0.03	0.03	0.02	0.04	0.00	0.05	0.01	0.03	0.04	0.02	0.04	0.02	0.04	0.04	0.00	0.04	0.04	0.03	0.02
K_2O	0.00	0.00	0.00	0.00	0.00	0.00	0.00	0.00	0.00	0.02	0.01	0.01	0.00	0.01	0.01	0.02	0.02	0.02	0.01	0.00	0.00
total	100.43	100.18	100.43	100.47	100.01	100.29	100.25	100.85	100.83	100.31	100.94	99.80	100.41	99.51	100.88	100.31	100.54	100.68	100.85	100.47	100.19
formula (6 O)																					
Si	1.99	1.99	1.99	2.00	1.99	1.99	2.00	1.99	1.99	2.00	1.99	2.00	2.00	1.99	2.00	2.00	1.99	1.99	2.00	2.00	1.99
Ti	0.00	0.00	0.00	0.00	0.00	0.00	0.00	0.00	0.00	0.00	0.00	0.00	0.00	0.00	0.00	0.00	0.00	0.00	0.00	0.00	0.00
Al	0.00	0.00	0.00	0.00	0.00	0.00	0.00	0.00	0.00	0.00	0.00	0.00	0.00	0.00	0.00	0.00	0.00	0.00	0.00	0.00	0.00
Cr	0.00	0.00	0.00	0.00	0.00	0.00	0.00	0.00	0.00	0.00	0.00	0.00	0.00	0.00	0.00	0.00	0.00	0.00	0.00	0.00	0.00
Fe^{2+}	0.29	0.30	0.30	0.29	0.30	0.30	0.28	0.28	0.28	0.28	0.29	0.28	0.29	0.28	0.28	0.29	0.30	0.30	0.28	0.28	0.28
Mg	1.70	1.70	1.70	1.69	1.70	1.71	1.71	1.72	1.71	1.71	1.71	1.71	1.71	1.72	1.70	1.69	1.72	1.71	1.71	1.71	1.72
Mn	0.00	0.00	0.00	0.00	0.00	0.00	0.00	0.00	0.00	0.00	0.00	0.00	0.00	0.00	0.00	0.00	0.00	0.00	0.00	0.00	0.00
Ca	0.01	0.01	0.01	0.01	0.01	0.01	0.01	0.01	0.01	0.01	0.01	0.01	0.01	0.01	0.01	0.01	0.00	0.01	0.01	0.01	0.01
Na	0.00	0.00	0.00	0.00	0.00	0.00	0.00	0.00	0.00	0.00	0.00	0.00	0.00	0.00	0.00	0.00	0.00	0.00	0.00	0.00	0.00
K	0.00	0.00	0.00	0.00	0.00	0.00	0.00	0.00	0.00	0.00	0.00	0.00	0.00	0.00	0.00	0.00	0.00	0.00	0.00	0.00	0.00
Mg#	85.6	85.1	85.2	85.3	85.1	85.3	85.9	86.0	85.8	86.0	85.7	85.8	85.6	85.9	85.9	85.3	85.3	85.3	86.1	86.1	86.1

C1. Electron microprobe data of synthetic pentlandite used in the experiments. A, B or C marks the three prepared batches. Formulae calculated on the basis of 8 sulfur.

sample no.	A1	A2	A3	A4	A5	A6	A7	A8	A9	B1	B2	B3	B4	B5	B6	B7	C1	C2	C3	C4	C5	C6	C7	C8	C9	C10	C11
wt.%																											
Fe	33.11	32.39	33.37	34.22	33.05	32.77	33.47	32.82	33.30	31.75	33.33	33.01	32.93	33.02	33.79	32.46	32.54	33.03	33.11	32.00	32.23	32.29	32.35	33.44	32.09	32.79	32.99
Ni	33.96	33.91	33.00	32.51	33.38	33.90	33.22	33.62	33.36	34.45	33.55	33.60	34.02	33.42	32.83	33.83	33.96	33.69	33.74	34.65	34.21	34.13	34.06	33.34	34.27	33.68	33.91
S	32.04	31.81	32.39	32.24	32.08	32.22	32.00	32.44	32.23	32.10	32.27	32.14	32.01	32.10	31.61	32.30	32.26	32.23	32.25	32.50	32.07	32.09	32.04	32.22	32.17	32.14	32.28
total	99.11	98.10	98.76	98.96	98.51	98.89	98.69	98.88	98.89	98.30	99.15	98.74	98.95	98.55	98.23	98.60	98.77	98.95	99.09	99.15	98.51	98.52	98.45	98.99	98.52	98.61	99.18
formula (8 S)																											
Fe	4.75	4.67	4.73	4.88	4.73	4.68	4.80	4.64	4.74	4.54	4.74	4.72	4.73	4.72	4.92	4.62	4.64	4.70	4.72	4.52	4.62	4.62	4.64	4.77	4.58	4.68	4.69
Ni	4.64	4.65	4.45	4.41	4.55	4.60	4.53	4.53	4.52	4.69	4.54	4.57	4.65	4.55	4.53	4.57	4.60	4.57	4.57	4.65	4.66	4.64	4.64	4.52	4.66	4.58	4.58
S	8.00	8.00	8.00	8.00	8.00	8.00	8.00	8.00	8.00	8.00	8.00	8.00	8.00	8.00	8.00	8.00	8.00	8.00	8.00	8.00	8.00	8.00	8.00	8.00	8.00	8.00	8.00
total	17.38	17.32	17.18	17.28	17.28	17.27	17.33	17.18	17.26	17.23	17.28	17.29	17.37	17.28	17.45	17.19	17.24	17.27	17.28	17.17	17.28	17.27	17.28	17.29	17.24	17.26	17.27
Fe+Ni	9.38	9.32	9.18	9.28	9.28	9.27	9.33	9.18	9.26	9.23	9.28	9.29	9.37	9.28	9.45	9.19	9.24	9.27	9.28	9.17	9.28	9.27	9.28	9.29	9.24	9.26	9.27
Fe/(Fe+Ni)	0.51	0.50	0.52	0.53	0.51	0.50	0.51	0.51	0.51	0.49	0.51	0.51	0.50	0.51	0.52	0.50	0.50	0.51	0.51	0.49	0.50	0.50	0.50	0.51	0.50	0.51	0.51

D1. Electron microprobe data of serpentine in Exp01. Formulae calculated on the basis of 7 oxygens, assuming all Fe as Fe^{2+}. Mg# = Mg / (Mg + Fe^{2+}) * 100.

sample no.	159	160	162	163	164	165	167	168	170	176	177	178	179	180	181	182	183	184
wt.%																		
SiO_2	28.74	29.22	28.59	21.12	20.40	16.45	22.82	22.38	17.70	22.03	13.19	18.76	18.15	20.33	16.93	15.94	19.05	19.26
TiO_2	0.00	0.03	0.04	0.00	0.00	0.02	0.00	0.04	0.05	0.02	0.05	0.03	0.00	0.00	0.00	0.03	0.00	0.07
Al_2O_3	0.04	0.04	0.05	0.02	0.01	0.01	0.01	0.02	0.02	0.05	0.00	0.03	0.02	0.02	0.02	0.01	0.02	0.00
Cr_2O_3	0.00	0.03	0.05	0.00	0.04	0.00	0.00	0.00	0.04	0.00	0.04	0.00	0.00	0.00	0.00	0.02	0.00	0.00
FeO	0.70	0.67	0.83	0.40	0.26	0.25	0.50	0.45	0.33	0.47	0.30	0.41	0.36	0.46	0.26	0.31	0.37	0.38
MgO	26.59	27.41	28.23	19.34	17.18	14.61	21.35	21.20	15.47	18.31	11.57	17.01	16.29	17.88	14.97	14.08	15.99	17.08
MnO	0.05	0.01	0.00	0.02	0.00	0.03	0.02	0.04	0.02	0.04	0.06	0.00	0.02	0.01	0.02	0.01	0.00	0.00
CaO	0.01	0.00	0.00	0.01	0.01	0.00	0.02	0.01	0.00	0.00	0.00	0.00	0.01	0.00	0.00	0.00	0.00	0.01
Na_2O	0.01	0.00	0.01	0.01	0.01	0.02	0.00	0.02	0.01	0.03	0.04	0.02	0.02	0.01	0.01	0.03	0.00	0.00
K_2O	0.01	0.01	0.00	0.00	0.00	0.00	0.00	0.01	0.00	0.01	0.00	0.00	0.00	0.00	0.00	0.01	0.00	0.00
NiO	0.10	0.12	0.09	0.06	0.04	0.03	0.06	0.03	0.06	0.11	0.07	0.06	0.09	0.05	0.06	0.05	0.04	0.08
Cl	0.23	0.28	0.22	0.39	0.47	0.44	0.38	0.38	0.51	0.39	0.58	0.47	0.39	0.46	0.48	0.61	0.49	0.43
total	56.47	57.81	58.12	41.37	38.42	31.86	45.17	44.58	34.21	41.45	25.89	36.78	35.35	39.23	32.75	31.10	35.96	37.30
formula (7 O)																		
Si	2.04	2.02	1.98	2.03	2.09	2.04	2.01	2.00	2.04	2.10	2.00	2.02	2.04	2.05	2.04	2.02	2.08	2.04
Ti	0.00	0.00	0.00	0.00	0.00	0.00	0.00	0.00	0.00	0.00	0.01	0.00	0.00	0.00	0.00	0.00	0.00	0.01
Al	0.00	0.00	0.00	0.00	0.00	0.00	0.00	0.00	0.00	0.01	0.00	0.00	0.00	0.00	0.00	0.00	0.00	0.00
Cr	0.00	0.00	0.00	0.00	0.00	0.00	0.00	0.00	0.00	0.00	0.00	0.00	0.00	0.00	0.00	0.00	0.00	0.00
Fe	0.04	0.04	0.05	0.03	0.02	0.03	0.04	0.03	0.03	0.04	0.04	0.04	0.03	0.04	0.03	0.03	0.03	0.03
Mg	2.81	2.83	2.92	2.77	2.62	2.70	2.81	2.83	2.66	2.61	2.62	2.73	2.73	2.69	2.69	2.65	2.61	2.70
Mn	0.00	0.00	0.00	0.00	0.00	0.00	0.00	0.00	0.00	0.00	0.01	0.00	0.00	0.00	0.00	0.00	0.00	0.00
Ca	0.00	0.00	0.00	0.00	0.00	0.00	0.00	0.00	0.00	0.00	0.00	0.00	0.00	0.00	0.00	0.00	0.00	0.00
Na	0.00	0.00	0.00	0.00	0.00	0.00	0.00	0.00	0.00	0.01	0.01	0.00	0.00	0.00	0.00	0.01	0.00	0.00
K	0.00	0.00	0.00	0.00	0.00	0.00	0.00	0.00	0.00	0.00	0.00	0.00	0.00	0.00	0.00	0.00	0.00	0.00
Ni	0.01	0.01	0.00	0.00	0.00	0.00	0.00	0.00	0.01	0.01	0.01	0.01	0.01	0.00	0.01	0.01	0.00	0.01
Cl	0.03	0.03	0.03	0.06	0.08	0.09	0.06	0.06	0.10	0.06	0.15	0.08	0.07	0.08	0.10	0.13	0.09	0.08
Mg#	98.5	98.7	98.4	98.9	99.2	99.0	98.7	98.8	98.8	98.6	98.6	98.7	98.8	98.6	99.0	98.8	98.7	98.8

D2. Electron microprobe data of serpentine in Exp02. Formulae calculated on the basis of 7 oxygens, assuming all Fe as Fe^{2+}. Mg# = Mg / (Mg + Fe^{2+}) * 100.

sample no.	126	127	128	129	130	131	132	133	134	135	141	142	143	144	145
wt.%															
SiO_2	23.00	30.02	30.16	31.93	28.25	32.66	27.14	29.97	28.47	24.40	28.86	28.95	35.43	30.53	33.31
TiO_2	0.08	0.02	0.00	0.05	0.05	0.03	0.06	0.03	0.01	0.00	0.03	0.00	0.00	0.05	0.01
Al_2O_3	0.16	0.26	0.35	0.20	0.12	0.11	0.23	0.10	0.10	0.16	0.21	0.25	0.24	0.16	0.17
Cr_2O_3	0.00	0.05	0.00	0.00	0.00	0.03	0.01	0.00	0.00	0.00	0.00	0.01	0.00	0.00	0.00
FeO	0.39	0.49	0.55	0.65	0.46	0.61	0.58	0.65	0.53	0.32	0.55	0.62	0.68	0.54	0.70
MgO	21.27	27.86	28.45	31.07	26.72	31.26	25.40	28.27	25.83	22.54	27.36	27.71	32.78	28.40	31.22
MnO	0.02	0.04	0.02	0.00	0.05	0.01	0.06	0.06	0.02	0.02	0.03	0.03	0.04	0.03	0.06
CaO	0.01	0.00	0.01	0.01	0.01	0.00	0.00	0.01	0.00	0.01	0.01	0.01	0.00	0.00	0.00
Na_2O	0.03	0.04	0.04	0.06	0.03	0.04	0.03	0.03	0.03	0.04	0.02	0.04	0.02	0.01	0.01
K_2O	0.02	0.02	0.00	0.00	0.00	0.01	0.01	0.00	0.00	0.02	0.00	0.00	0.00	0.02	0.00
NiO	0.07	0.06	0.09	0.07	0.01	0.02	0.10	0.41	0.04	0.06	0.06	0.07	0.08	0.11	0.13
Cl	0.34	0.34	0.33	0.19	0.28	0.22	0.28	0.21	0.27	0.32	0.27	0.29	0.18	0.25	0.20
total	45.39	59.19	60.00	64.23	55.98	64.99	53.90	59.73	55.28	47.89	57.40	57.99	69.45	60.09	65.82
formula (7 O)															
Si	2.02	2.02	2.01	2.00	2.02	2.01	2.02	2.02	2.05	2.03	2.01	2.00	2.04	2.03	2.03
Ti	0.00	0.00	0.00	0.00	0.00	0.00	0.00	0.00	0.00	0.00	0.00	0.00	0.00	0.00	0.00
Al	0.02	0.02	0.03	0.02	0.01	0.01	0.02	0.01	0.01	0.02	0.02	0.02	0.02	0.01	0.01
Cr	0.00	0.00	0.00	0.00	0.00	0.00	0.00	0.00	0.00	0.00	0.00	0.00	0.00	0.00	0.00
Fe	0.03	0.03	0.03	0.03	0.03	0.03	0.04	0.04	0.03	0.02	0.03	0.04	0.03	0.03	0.04
Mg	2.78	2.80	2.83	2.90	2.84	2.87	2.81	2.84	2.78	2.79	2.84	2.85	2.82	2.82	2.83
Mn	0.00	0.00	0.00	0.00	0.00	0.00	0.00	0.00	0.00	0.00	0.00	0.00	0.00	0.00	0.00
Ca	0.00	0.00	0.00	0.00	0.00	0.00	0.00	0.00	0.00	0.00	0.00	0.00	0.00	0.00	0.00
Na	0.01	0.00	0.01	0.01	0.00	0.00	0.00	0.00	0.00	0.01	0.00	0.01	0.00	0.00	0.00
K	0.00	0.00	0.00	0.00	0.00	0.00	0.00	0.00	0.00	0.00	0.00	0.00	0.00	0.00	0.00
Ni	0.01	0.00	0.00	0.00	0.00	0.00	0.01	0.02	0.00	0.00	0.00	0.00	0.00	0.01	0.01
Cl	0.05	0.04	0.04	0.02	0.03	0.02	0.04	0.02	0.03	0.05	0.03	0.03	0.02	0.03	0.02
Mg#	99.0	99.0	98.9	98.8	99.0	98.9	98.7	98.7	98.9	99.2	98.9	98.8	98.9	98.9	98.8

E1. Electron microprobe data of brucite in Exp01. Formulae calculated on the basis of 1 oxygen, assuming all Fe as Fe^{2+}. Mg# = Mg / (Mg + Fe^{2+}) * 100.

sample no.	156	157	158	161	169	171	172	173	174	175	185
wt. %											
SiO_2	0.82	0.73	0.77	0.06	1.65	0.09	0.11	0.55	0.16	0.07	0.44
TiO_2	0.00	0.03	0.00	0.00	0.03	0.00	0.04	0.00	0.00	0.00	0.00
Al_2O_3	0.04	0.03	0.05	0.17	0.11	0.04	0.05	0.02	0.04	0.02	0.26
Cr_2O_3	0.00	0.00	0.02	0.00	0.00	0.00	0.00	0.01	0.01	0.02	0.00
FeO	2.97	4.25	5.54	7.97	5.52	3.57	3.40	3.12	6.54	4.55	6.57
MgO	70.66	80.23	74.12	72.83	57.69	80.61	81.66	75.76	73.71	78.06	64.33
MnO	0.29	0.29	0.38	0.39	0.32	0.40	0.46	0.41	0.36	0.35	0.24
CaO	0.01	0.00	0.00	0.00	0.00	0.00	0.00	0.00	0.00	0.00	0.00
Na_2O	0.02	0.00	0.00	0.01	0.01	0.02	0.01	0.00	0.02	0.00	0.00
K_2O	0.03	0.00	0.00	0.01	0.00	0.00	0.00	0.00	0.01	0.00	0.00
NiO	0.05	0.07	0.11	0.06	0.09	0.04	0.05	0.03	0.08	0.05	0.05
Cl	0.10	0.02	0.03	0.01	0.15	0.01	0.01	0.03	0.00	0.01	0.03
total	74.97	85.64	81.02	81.51	65.58	84.78	85.80	79.93	80.95	83.14	71.92
formula (1 O)											
Si	0.02	0.01	0.01	0.00	0.04	0.00	0.00	0.01	0.00	0.00	0.01
Ti	0.00	0.00	0.00	0.00	0.00	0.00	0.00	0.00	0.00	0.00	0.00
Al	0.00	0.00	0.00	0.00	0.00	0.00	0.00	0.00	0.00	0.00	0.01
Cr	0.00	0.00	0.00	0.00	0.00	0.00	0.00	0.00	0.00	0.00	0.00
Fe	0.05	0.06	0.08	0.11	0.10	0.05	0.05	0.04	0.09	0.06	0.11
Mg	1.93	1.92	1.90	1.87	1.85	1.94	1.94	1.94	1.89	1.93	1.87
Mn	0.00	0.00	0.01	0.01	0.01	0.01	0.01	0.01	0.01	0.00	0.00
Ca	0.00	0.00	0.00	0.00	0.00	0.00	0.00	0.00	0.00	0.00	0.00
Na	0.00	0.00	0.00	0.00	0.00	0.00	0.00	0.00	0.00	0.00	0.00
K	0.00	0.00	0.00	0.00	0.00	0.00	0.00	0.00	0.00	0.00	0.00
Ni	0.00	0.00	0.00	0.00	0.00	0.00	0.00	0.00	0.00	0.00	0.00
Cl	0.00	0.00	0.00	0.00	0.00	0.00	0.00	0.00	0.00	0.00	0.00
Mg#	97.7	97.1	96.0	94.2	94.9	97.6	97.7	97.7	95.3	96.8	94.6

E2. Electron microprobe data of brucite in Exp02. Formulae calculated on the basis of 1 oxygen, assuming all Fe as Fe^{2+}.
Mg# = Mg / (Mg + Fe^{2+}) * 100.

sample no.	116	117	118	119	120	121	122	123	124	125	136	137	138	139	140
wt.%															
SiO_2	2.72	0.11	0.04	2.91	0.14	0.44	0.78	0.12	0.06	2.05	0.10	1.03	0.32	0.11	0.17
TiO_2	0.08	0.04	0.04	0.02	0.00	0.00	0.03	0.00	0.04	0.00	0.00	0.02	0.01	0.00	0.00
Al_2O_3	0.11	0.08	0.22	0.11	0.08	0.35	0.12	0.34	0.41	0.09	0.13	0.07	0.09	0.12	0.16
Cr_2O_3	0.02	0.00	0.01	0.00	0.02	0.00	0.00	0.00	0.00	0.00	0.00	0.00	0.02	0.00	0.00
FeO	6.04	5.91	7.19	3.48	2.45	6.49	5.29	7.27	7.15	4.29	4.30	5.35	7.13	4.86	7.34
MgO	74.35	82.83	76.74	74.90	69.63	76.14	77.16	73.36	74.83	77.85	80.08	79.04	73.61	78.15	75.17
MnO	0.26	0.29	0.27	0.27	0.23	0.37	0.32	0.29	0.31	0.31	0.41	0.30	0.37	0.43	0.41
CaO	0.03	0.00	0.00	0.00	0.01	0.00	0.00	0.01	0.01	0.00	0.00	0.02	0.00	0.00	0.02
Na_2O	0.03	0.03	0.03	0.02	0.00	0.01	0.02	0.01	0.02	0.02	0.01	0.00	0.00	0.04	0.01
K_2O	0.00	0.00	0.00	0.00	0.00	0.02	0.00	0.01	0.01	0.00	0.01	0.00	0.00	0.02	0.01
NiO	0.10	0.18	0.08	0.27	0.06	0.09	0.03	0.08	0.18	0.09	0.09	0.24	0.26	0.07	0.04
Cl	0.01	0.00	0.01	0.01	0.06	0.01	0.00	0.01	0.01	0.00	0.00	0.00	0.02	0.01	0.00
total	83.75	89.47	84.64	81.98	72.67	83.92	83.76	81.51	83.03	84.70	85.12	86.06	81.82	83.82	83.34
formula (1 O)															
Si	0.05	0.00	0.00	0.05	0.00	0.01	0.05	0.00	0.01	0.03	0.00	0.02	0.01	0.00	0.00
Ti	0.00	0.00	0.00	0.00	0.00	0.00	0.00	0.00	0.00	0.00	0.00	0.00	0.00	0.00	0.00
Al	0.00	0.00	0.00	0.00	0.00	0.01	0.00	0.01	0.01	0.00	0.00	0.00	0.00	0.00	0.00
Cr	0.00	0.00	0.00	0.00	0.00	0.00	0.00	0.00	0.00	0.00	0.00	0.00	0.00	0.00	0.00
Fe	0.08	0.08	0.10	0.05	0.04	0.09	0.05	0.10	0.09	0.06	0.06	0.07	0.10	0.07	0.10
Mg	1.86	1.91	1.89	1.89	1.95	1.89	1.89	1.88	1.89	1.90	1.93	1.90	1.88	1.92	1.88
Mn	0.00	0.00	0.00	0.00	0.00	0.01	0.00	0.00	0.01	0.00	0.01	0.00	0.01	0.01	0.01
Ca	0.00	0.00	0.00	0.00	0.00	0.00	0.00	0.00	0.00	0.00	0.00	0.00	0.00	0.00	0.00
Na	0.00	0.00	0.00	0.00	0.00	0.00	0.00	0.00	0.00	0.00	0.00	0.00	0.00	0.00	0.00
K	0.00	0.00	0.00	0.00	0.00	0.00	0.00	0.00	0.00	0.00	0.00	0.00	0.00	0.00	0.00
Ni	0.00	0.00	0.00	0.00	0.00	0.00	0.00	0.00	0.00	0.00	0.00	0.00	0.00	0.00	0.00
Cl	0.00	0.00	0.00	0.00	0.00	0.00	0.00	0.00	0.00	0.00	0.00	0.00	0.00	0.00	0.00
Mg#	95.6	96.2	95.0	97.5	98.1	95.4	97.5	94.7	95.4	97.0	97.1	96.3	94.8	96.6	94.8

F1. Electron microprobe data of Ni-rich pentlandite in Exp01 and 02. Formulae calculated on the basis of 8 sulfur.

sample no.	1	2	3	4	5	6	7	8	9	10	11	12	13	14	15	16	17	18	19	20	21	22	23	24
wt.%																								
Fe	19.31	19.57	19.53	19.94	19.53	20.24	19.57	19.25	21.49	20.51	16.84	17.75	18.87	18.60	18.69	19.03	18.78	19.38	19.20	19.45	19.04	18.99	19.18	19.70
Ni	48.08	47.91	48.00	47.52	46.70	46.68	45.64	45.68	33.60	44.50	42.89	45.28	46.45	46.54	46.52	46.62	46.39	45.98	45.20	46.27	46.22	46.27	45.91	45.81
S	32.96	33.11	32.62	33.02	32.71	32.91	31.23	31.22	26.19	30.55	30.01	29.93	30.17	30.12	30.51	30.28	30.46	30.27	30.43	30.49	30.57	30.70	30.29	30.41
total	100.35	100.59	100.16	100.48	98.94	99.84	96.45	96.15	81.28	95.56	89.73	92.96	95.49	95.26	95.72	95.93	95.63	95.63	94.83	96.21	95.83	95.96	95.38	95.91
formula (8 S)																								
Fe	2.69	2.72	2.75	2.77	2.74	2.83	2.88	2.83	3.77	3.08	2.58	2.72	2.87	2.84	2.81	2.89	2.83	2.94	2.90	2.93	2.86	2.84	2.91	2.98
Ni	6.38	6.32	6.43	6.29	6.24	6.20	6.39	6.40	5.61	6.37	6.25	6.61	6.73	6.75	6.66	6.73	6.66	6.64	6.49	6.63	6.61	6.59	6.63	6.58
S	8.00	8.00	8.00	8.00	8.00	8.00	8.00	8.00	8.00	8.00	8.00	8.00	8.00	8.00	8.00	8.00	8.00	8.00	8.00	8.00	8.00	8.00	8.00	8.00
total	17.07	17.04	17.18	17.06	16.98	17.02	17.27	17.23	17.38	17.45	16.82	17.34	17.60	17.59	17.48	17.62	17.49	17.58	17.39	17.56	17.47	17.43	17.54	17.56
Fe+Ni	9.07	9.04	9.18	9.06	8.98	9.02	9.27	9.23	9.38	9.45	8.82	9.34	9.60	9.59	9.48	9.62	9.49	9.58	9.39	9.56	9.47	9.43	9.54	9.56
Fe/(Fe+Ni)	0.30	0.30	0.30	0.31	0.31	0.31	0.31	0.31	0.40	0.33	0.29	0.29	0.30	0.30	0.30	0.30	0.30	0.31	0.31	0.31	0.30	0.30	0.31	0.31

F2. Electron microprobe data of heazlewoodite in Exp01 and 02. Formulae calculated on the basis of 2 sulfur.

sample no.	1	2	3	4	5	6	7	8	9	10	11	12	13	14	15	16
wt.%																
Fe	2.31	2.01	1.90	8.24	10.95	4.78	3.70	2.65	1.13	1.09	1.70	2.55	2.28	2.05	2.11	28.79
Ni	72.26	63.50	72.45	64.24	63.47	70.12	72.36	72.13	72.86	72.84	72.15	72.81	71.87	72.08	71.45	34.55
S	26.59	25.18	26.97	27.76	22.21	23.69	24.14	24.06	24.26	24.28	24.84	24.53	24.33	24.75	24.72	23.62
total	101.15	90.69	101.32	100.24	96.62	98.59	100.20	98.84	98.24	98.20	98.69	99.88	98.47	98.87	98.28	86.97
formula (2 S)																
Fe	0.10	0.09	0.08	0.34	0.57	0.23	0.18	0.13	0.05	0.05	0.08	0.12	0.11	0.09	0.10	1.40
Ni	2.97	2.76	2.94	2.53	3.12	3.23	3.28	3.28	3.28	3.28	3.17	3.24	3.23	3.18	3.16	1.60
S	2.00	2.00	2.00	2.00	2.00	2.00	2.00	2.00	2.00	2.00	2.00	2.00	2.00	2.00	2.00	2.00
total	5.07	4.85	5.02	4.87	5.69	5.47	5.45	5.40	5.33	5.33	5.25	5.36	5.34	5.28	5.26	5.00
Fe+Ni	3.07	2.85	3.02	2.87	3.69	3.47	3.45	3.40	3.33	3.33	3.25	3.36	3.34	3.28	3.26	3.00
Fe/(Fe+Ni)	0.03	0.03	0.03	0.12	0.15	0.07	0.05	0.04	0.02	0.02	0.02	0.04	0.03	0.03	0.03	0.47

G1. XRD measurement of olivine.

Measurement conditions:

instrument	PANalytical X'PERT Powder
monochromatization	Ni-Filter
start position [°2Th.]	5.008
end position [°2Th.]	144.986
step size [°2Th.]	0.017
type of divergence aperature	fixed
anode material	Cu

Powder Diffraction File (PDF) references:

PDF-no.	name of compound	chemical formula
00-034-0189	forsterite, syn	Mg_2SiO_4

Detected peaks:

Pos. [°2Th.]	d-Value [Å]	Rel. Int. [%]	Pos. [°2Th.]	d-Value [Å]	Rel. Int. [%]	Pos. [°2Th.]	d-Value [Å]	Rel. Int. [%]
17.3596	5.1085	48.26	52.4974	1.74170	18.36	77.9937	1.2241	1.94
20.5944	4.3128	5.63	52.6412	1.74160	10.25	80.6530	1.1903	3.43
22.8653	3.8894	75.09	54.8508	1.67241	13.25	82.5707	1.1675	3.65
23.8668	3.7284	17.94	55.0020	1.67231	6.91	83.5214	1.1566	4.11
25.4308	3.4996	20.17	56.0811	1.63860	22.16	85.4010	1.1359	4.02
25.5584	3.4853	18.60	56.2364	1.63850	12.24	88.9053	1.0999	6.38
29.8235	2.9959	27.61	56.7830	1.62000	18.16	91.5857	1.0746	4.54
32.2931	2.7699	82.46	56.9371	1.62000	11.16	95.9797	1.0367	10.65
32.3908	2.7686	36.64	57.8815	1.59184	4.98	96.2939	1.0367	4.96
35.6770	2.5146	88.73	58.6170	1.57361	10.26	97.8945	1.0215	5.68
35.7810	2.5137	42.49	58.8062	1.56899	5.38	101.4003	0.9954	3.72
36.4915	2.4603	100.00	61.1164	1.51510	2.66	102.6279	0.9868	1.53
36.5965	2.4596	53.05	61.7228	1.50166	8.84	103.5648	0.9804	2.61
38.2667	2.3501	20.81	61.9052	1.49768	29.00	104.6638	0.9731	3.96
38.8154	2.3182	11.55	62.0801	1.49759	15.41	110.1510	0.9395	2.19
39.6559	2.2710	39.94	62.6890	1.48082	57.07	112.2188	0.9280	4.53
40.0236	2.2509	36.75	62.8683	1.48070	25.91	116.3739	0.9065	3.35
40.1338	2.2506	19.14	64.8184	1.43723	2.38	121.5081	0.8828	3.05
41.7469	2.1619	15.32	66.9784	1.39603	17.16	123.8184	0.8732	2.68
44.5199	2.0335	6.46	67.1682	1.39600	8.19	126.7513	0.8617	3.60
46.6800	1.9443	2.93	67.3401	1.38940	6.70	128.1503	0.8565	2.08
48.4154	1.8786	8.62	69.4331	1.35255	11.76	128.6680	0.8546	1.76
50.3520	1.8108	2.62	69.6337	1.34914	9.20	129.8001	0.8506	1.87
50.9454	1.7911	3.56	71.5460	1.31771	9.83	134.9124	0.8340	3.62
52.2038	1.7508	46.23	72.9256	1.29614	5.25	136.4706	0.8294	3.12
52.3439	1.7508	26.15	73.1309	1.29301	3.81	143.3652	0.8114	0.20

G2. XRD measurement of orthopyroxene.

Measurement conditions:

instrument	PANalytical X'PERT Powder
monochromatization	Ni-Filter
start position [°2Th.]	5.008
end position [°2Th.]	124.433
step size [°2Th.]	0.017
type of divergence aperature	fixed
anode material	Cu

Powder Diffraction File (PDF) references:

PDF-no.	name of compound	chemical formula
00-019-0768	enstatite, syn	$MgSiO_3$
00-019-0770	talc-2\ITM\RG	$Mg_3Si_4O_{10}(OH)_2$
00-033-0664	burnt ochre	Fe_2O_3
00-005-0586	calcite, syn	$CaCO_3$

Detected peaks:

Pos. [°2Th.]	d-Value [Å]	Rel. Int.[%]	Pos. [°2Th.]	d-Value [Å]	Rel. Int.[%]
9.4723	9.3371	4.15	51.1994	1.7872	2.82
13.9520	6.3476	1.66	52.6583	1.7368	4.48
20.0826	4.4216	2.89	53.7422	1.7043	3.63
22.1181	4.0191	1.46	55.6986	1.6489	0.51
26.9256	3.3114	5.30	57.9476	1.5902	3.78
28.0956	3.1761	100.00	60.4845	1.5294	3.97
29.3560	3.0425	1.68	60.8542	1.5210	5.93
30.3260	2.9450	8.96	61.0377	1.5206	3.17
31.0826	2.8750	53.15	62.4093	1.4868	8.05
31.1753	2.8738	22.84	62.5870	1.4867	4.26
31.6152	2.8277	5.41	63.0029	1.4742	9.82
33.0479	2.7084	5.46	63.1836	1.4741	4.84
35.3371	2.5380	11.34	66.8761	1.3979	2.83
35.9594	2.4955	7.90	67.1460	1.3930	7.84
36.2711	2.4747	7.48	67.3214	1.3932	3.81
37.7028	2.3840	0.83	67.7843	1.3814	1.35
40.0292	2.2506	1.03	72.1495	1.3082	3.08
42.7030	2.1157	6.73	72.8578	1.2972	0.83
43.0903	2.0976	7.40	74.6738	1.2701	3.48
43.2092	2.0973	3.95	75.8693	1.2530	0.79
43.9321	2.0593	1.69	81.0007	1.1861	0.74
44.6679	2.0271	3.17	84.9377	1.1409	1.59
44.7881	2.0219	3.59	94.4057	1.0498	4.61
45.5396	1.9903	3.89	94.7304	1.0497	2.40
45.6575	1.9854	5.72	95.6654	1.0393	1.50
46.2812	1.9601	7.26	98.8606	1.0141	0.76
46.4095	1.9598	3.18	115.1113	0.9128	1.12
48.1316	1.8890	1.12	115.5675	0.9105	1.18
51.0622	1.7872	4.21			

G3. XRD measurement of pentlandite.

Measurement conditions:

instrument	PANalytical X'PERT Powder
monochromatization	Ni-Filter
start position [°2Th.]	5.008
end position [°2Th.]	144.986
step size [°2Th.]	0.017
type of divergence aperature	fixed
anode material	Cu

Powder Diffraction File (PDF) references:

PDF-no.	name of compound	chemical formula
00-008-0090	pentlandite	$(Fe,Ni)_9S_8$

Detected peaks:

Pos. [°2Th.]	d-Value [Å]	Rel. Int.[%]
15.2702	5.8025	46.57
17.6058	5.0376	5.64
24.9941	3.5627	6.94
29.3578	3.0424	92.66
30.6925	2.9130	47.41
35.5771	2.5235	5.08
38.8732	2.3168	18.33
39.9363	2.2575	14.66
46.7212	1.9443	27.45
51.1295	1.7850	100.00
51.2718	1.7848	58.16
53.6270	1.7077	3.28
60.0456	1.5395	6.70
60.7986	1.5223	5.51
71.6733	1.3157	8.35
75.1656	1.2630	7.36
96.5928	1.0318	14.07
104.1136	0.9768	2.24
119.2059	0.8931	4.12
143.3539	0.8114	29.42
143.9723	0.8100	3.32

G4. XRD measurement of Exp01 (forsterite-rich olivine) at end of experimental run.

Measurement conditions:

instrument	Philipps PW 1800
monochromatization	secondary monochromator
start position [°2Th.]	5.015
end position [°2Th.]	84.995
step size [°2Th.]	0.03
type of divergence aperature	automatic
anode material	Cu

Powder Diffraction File (PDF) references:

PDF-no.	name of compound	chemical formula
00-034-0189	forsterite, syn	Mg_2SiO_4
00-019-0629	magnetite, syn	Fe_3O_4
00-044-1482	brucite, syn	$Mg(OH)_2$
00-043-0662	chrysotile-2\ITM#c#1\RG	$Mg_3Si_2O_5(OH)_4$

Detected peaks:

Pos. [°2Th.]	d-Value [Å]	Rel. Int. [%]	Pos. [°2Th.]	d-Value [Å]	Rel. Int. [%]
12.1521	7.28339	9.26	56.7727	1.62027	3.20
17.3720	5.10488	5.39	58.6107	1.57376	3.49
18.6679	4.75335	100.00	60.3739	1.53322	2.76
19.4941	4.55371	1.15	61.9210	1.49733	21.24
22.8989	3.88374	19.92	62.6910	1.48078	45.27
24.3672	3.65295	6.91	62.8705	1.48065	20.22
25.4436	3.50080	5.15	66.9048	1.39738	2.15
29.8541	2.99289	1.99	67.3659	1.38893	13.29
32.3100	2.77079	72.02	67.5668	1.38874	5.86
35.6913	2.51567	12.20	68.3216	1.37182	1.21
36.5219	2.46034	28.75	69.6955	1.34810	10.32
38.2765	2.35150	11.23	69.8912	1.34814	4.24
39.6499	2.27316	22.12	71.5195	1.31813	4.16
40.0318	2.25235	15.50	72.1250	1.30855	0.78
41.7080	2.16563	2.41	72.8777	1.29688	3.81
44.5100	2.03559	3.97	73.1203	1.29639	3.44
46.7212	1.94428	1.38	75.8050	1.25391	1.73
48.4201	1.87995	7.51	80.5830	1.19117	1.61
50.8551	1.79551	4.24	82.2806	1.17084	2.62
52.1754	1.75169	6.73	82.5611	1.16757	2.66
52.7984	1.73248	4.69	83.5275	1.15650	5.08
54.8666	1.67335	2.07	83.7868	1.15645	1.93
56.0712	1.63886	14.13	84.1379	1.14966	1.48
56.2350	1.63448	8.43			

G5. XRD measurement of Exp02 (forsterite-rich olivine) at end of experimental run.

Measurement conditions:

instrument	Philipps PW 1800
monochromatization	secondary monochromator
start position [°2Th.]	5.015
end position [°2Th.]	84.995
step size [°2Th.]	0.03
type of divergence aperature	automatic
anode material	Cu

Powder Diffraction File (PDF) references:

PDF-no.	name of compound	chemical formula
00-034-0189	forsterite, syn	Mg_2SiO_4
00-019-0629	magnetite, syn	Fe_3O_4
00-044-1482	brucite, syn	$Mg(OH)_2$
00-043-0662	chrysotile-2\ITM#c#1\RG	$Mg_3Si_2O_5(OH)_4$

Detected peaks:

Pos. [°2Th.]	d-Value [Å]	Rel. Int. [%]	Pos. [°2Th.]	d-Value [Å]	Rel. Int. [%]
12.1204	7.30237	14.42	50.8095	1.79701	6.88
17.1004	5.18534	2.51	52.1544	1.75235	5.89
17.3397	5.11432	7.78	52.5060	1.74143	18.39
18.6289	4.76321	100.00	54.7922	1.67406	3.50
19.3358	4.59062	1.95	56.0015	1.64074	18.36
22.8305	3.89523	6.26	56.7605	1.62059	10.04
24.3486	3.65570	11.47	58.6476	1.57416	0.59
25.4118	3.50512	5.17	60.3209	1.53444	5.08
25.6004	3.47972	4.37	61.7565	1.50217	2.90
29.6348	3.01454	0.93	62.5747	1.48448	5.19
30.1166	2.96740	1.48	66.9266	1.39814	0.82
32.3137	2.77049	16.33	68.2417	1.37437	0.92
35.6439	2.51891	17.91	69.6699	1.34853	2.87
36.4727	2.46355	6.95	72.1238	1.30965	1.77
37.9628	2.37021	3.74	76.0083	1.25106	2.00
40.0080	2.25364	4.45	76.5711	1.24326	2.91
42.0476	2.14892	1.18	76.7937	1.24329	1.25
43.0931	2.09918	1.30	80.6012	1.19094	1.98
44.4688	2.03738	3.88	83.4820	1.15701	2.57
48.4327	1.87950	0.70			

G6. XRD measurement of Exp03 (enstatite-rich orthopyroxene) at end of experimental run.

Measurement conditions:

instrument	PANalytical X'PERT Powder
monochromatization	Ni-Filter
start position [°2Th.]	5.008
end position [°2Th.]	84.976
step size [°2Th.]	0.017
type of divergence aperature	fixed
anode material	Cu

Powder Diffraction File (PDF) references:

PDF-no.	name of compound	chemical formula
00-019-0770	talc-2\ITM\RG	$Mg_3Si_4O_{10}(OH)_2$
00-019-0768	enstatite, syn	$MgSiO_3$
00-043-0662	chrysotile-2\ITM#c#1\RG	$Mg_3Si_2O_5(OH)_4$

Detected peaks:

Pos. [°2Th.]	d-Value [Å]	Rel. Int. [%]	Pos. [°2Th.]	d-Value [Å]	Rel. Int. [%]	Pos. [°2Th.]	d-Value [Å]	Rel. Int. [%]
9.4940	9.31578	8.36	42.8150	2.11566	3.01	61.0551	1.52025	3.46
10.6965	8.27106	0.56	43.0891	2.09762	7.13	61.6674	1.50288	1.04
12.1518	7.28359	1.45	43.2082	2.09732	3.88	62.4014	1.48696	8.11
13.9726	6.33828	1.77	43.8962	2.06091	2.00	62.5732	1.48697	4.25
18.9470	4.68395	0.67	44.0029	2.05616	2.14	63.0059	1.47414	10.31
19.4603	4.56154	2.19	44.6742	2.02681	3.41	63.1745	1.47426	4.97
20.0905	4.41986	4.07	44.7980	2.02149	4.22	65.6220	1.42156	1.62
22.0253	4.03577	0.88	44.9144	2.02154	1.53	66.0024	1.41428	0.94
24.3400	3.65696	0.92	45.5654	1.98922	6.67	66.3538	1.40764	0.97
26.9348	3.31027	4.49	45.6770	1.98462	5.69	66.8663	1.39809	2.52
28.0997	3.17563	100.00	46.2869	1.95988	8.06	67.1599	1.39269	8.61
28.6398	3.11696	3.69	46.4107	1.95980	4.06	67.3449	1.39277	4.53
29.3727	3.04084	1.56	48.1551	1.88811	1.33	67.8018	1.38106	1.20
30.3341	2.94419	8.58	50.5799	1.80314	0.60	68.0218	1.38055	0.48
31.0926	2.87407	64.88	51.0625	1.78722	4.31	69.0177	1.35967	0.24
31.1872	2.87269	29.28	51.1974	1.78726	2.15	70.1690	1.34015	0.86
31.6212	2.82722	6.17	51.3815	1.77687	1.89	72.1615	1.30798	2.89
31.9239	2.80110	0.74	51.5182	1.77688	0.92	72.3762	1.30786	1.51
33.0540	2.70786	5.17	52.6730	1.73631	5.05	72.7944	1.29816	2.20
35.3335	2.53822	9.38	52.8162	1.73624	2.82	72.9897	1.29516	1.30
35.4398	2.53713	4.91	53.7411	1.70429	1.73	73.3474	1.29293	1.41
35.6709	2.51498	2.98	53.9374	1.69855	1.44	74.6737	1.27007	3.26
35.9593	2.49547	5.91	54.4969	1.68243	1.02	74.8853	1.27016	1.82
36.2733	2.47458	8.07	55.4499	1.65575	0.79	75.7581	1.25457	0.99
36.3843	2.47342	6.56	55.7693	1.64702	1.20	75.9619	1.25482	0.89
37.6922	2.38462	0.57	57.1151	1.61137	1.47	76.2168	1.24815	0.54
38.0697	2.36184	0.82	57.9396	1.59038	4.30	76.8899	1.23890	0.34
39.4992	2.27960	1.14	58.0675	1.58718	3.24	77.4604	1.23119	1.01
40.0049	2.25194	1.91	58.6589	1.57258	0.73	79.1021	1.20971	0.60
40.3450	2.23374	1.14	60.5139	1.52874	4.45	80.9996	1.18609	1.19
42.1966	2.13990	0.70	60.6672	1.52903	2.99			
42.6929	2.11617	5.79	60.8853	1.52030	6.69			

G7. XRD measurement of Exp04 (harzburgite) at end of experimental run.

Measurement conditions:

instrument	PANalytical X'PERT Powder
monochromatization	Ni-Filter
start position [°2Th.]	5.008
end position [°2Th.]	84.976
step size [°2Th.]	0.017
type of divergence aperature	fixed
anode material	Cu

Powder Diffraction File (PDF) references:

PDF-no.	name of compound	chemical formula
00-034-0189	forsterite, syn	Mg_2SiO_4
00-019-0768	enstatite, syn	$MgSiO_3$
00-043-0662	chrysotile-2\ITM#c#1\RG	$Mg_3Si_2O_5(OH)_4$
00-019-0770	talc-2\ITM\RG	$Mg_3Si_4O_{10}(OH)_2$

Detected peaks:

Pos. [°2Th.]	d-Value [Å]	Rel. Int. [%]	Pos. [°2Th.]	d-Value [Å]	Rel. Int. [%]	Pos. [°2Th.]	d-Value [Å]	Rel. Int. [%]
9.4971	9.31275	1.64	41.7513	2.16169	13.50	61.5309	1.50589	4.64
12.1075	7.31012	8.03	41.8683	2.16128	7.24	61.7314	1.50148	6.92
17.3670	5.10634	39.90	43.0776	2.09816	3.28	61.9143	1.49748	30.00
19.3963	4.57646	2.21	44.5207	2.03344	5.88	62.0860	1.49746	15.26
20.0544	4.42773	2.08	44.6342	2.03357	3.89	62.4001	1.48698	4.33
20.6285	4.30577	1.57	45.6114	1.98732	1.28	62.6859	1.48089	32.72
22.8711	3.88841	61.37	46.2970	1.95947	2.78	62.8614	1.48085	16.26
23.8741	3.72727	17.18	46.7395	1.94195	1.55	64.7698	1.43819	2.28
24.3629	3.65359	4.96	48.4285	1.87809	7.02	66.8095	1.39915	4.70
25.4360	3.50182	19.59	48.5717	1.87754	3.46	66.9856	1.39589	13.05
25.5766	3.48289	17.39	50.3115	1.81213	4.18	67.1501	1.39633	7.88
28.1026	3.17531	27.15	50.9163	1.79201	5.85	67.3418	1.38937	6.11
29.6551	3.01252	6.45	51.0590	1.79178	3.80	67.5486	1.38906	2.61
29.8274	2.99304	21.85	52.2142	1.75048	55.49	69.4509	1.35225	11.65
30.3532	2.94481	2.10	52.3537	1.75048	28.22	69.6728	1.34848	7.97
31.0873	2.87693	19.31	52.5101	1.74131	23.67	71.5541	1.31758	7.15
31.6499	2.82706	1.05	52.6548	1.74118	13.63	71.7413	1.31460	6.18
32.2991	2.76941	76.01	52.8049	1.73228	5.63	71.8914	1.31548	4.66
32.3959	2.76822	36.25	52.9435	1.73237	3.04	72.9240	1.29617	3.99
33.0414	2.70887	2.61	54.8551	1.67228	12.75	74.9395	1.26623	1.37
34.7150	2.58201	3.28	55.0064	1.67219	6.49	75.5324	1.25775	1.87
35.3166	2.53939	6.54	56.0841	1.63852	18.89	76.0389	1.25063	1.87
35.6855	2.51399	77.88	56.2355	1.63853	11.04	76.2842	1.24722	2.11
35.7904	2.51309	36.60	56.7869	1.61990	15.83	77.9261	1.22499	2.34
36.4976	2.45989	100.00	56.9418	1.61987	8.25	78.1546	1.22502	1.20
38.2736	2.34973	17.74	57.4386	1.60306	1.54	80.6436	1.19042	2.12
38.3882	2.34880	8.75	57.9025	1.59131	6.19	82.2364	1.17135	1.81
38.8255	2.31759	7.62	58.0610	1.59129	3.82	82.5772	1.16738	3.52
39.6640	2.27051	44.89	58.6241	1.57343	8.19	82.8435	1.16430	1.82
39.7744	2.27008	22.29	58.7931	1.57321	6.13	83.5314	1.15646	2.98
40.0270	2.25075	45.20	60.3330	1.53289	2.45	84.1471	1.14956	2.31
40.1370	2.25041	21.78	61.2123	1.51296	4.94	84.4095	1.14665	1.33

H1. Exp01 (forsterite-rich olivine): thermogravimetric curve of alteration products. Continuous line depict weight loss during heating and dotted line represent the differential scanning calorimetry curve. Beginning of weight loss at 300 °C shows brucite and at 530 °C serpentine.

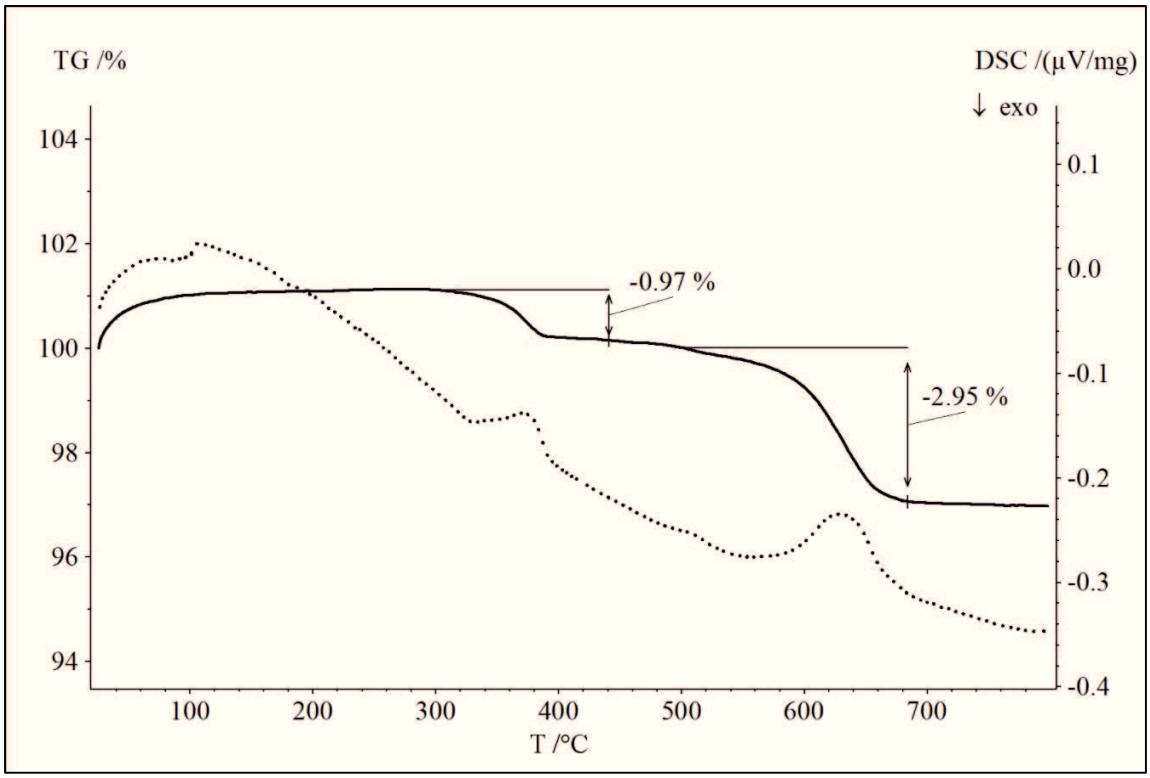

H2. Exp02 (forsterite-rich olivine): thermogravimetric curve of alteration products. Continuous line depict weight loss during heating and dotted line represent the differential scanning calorimetry curve. Beginning of weight loss at 300 °C shows brucite and at 530 °C serpentine.

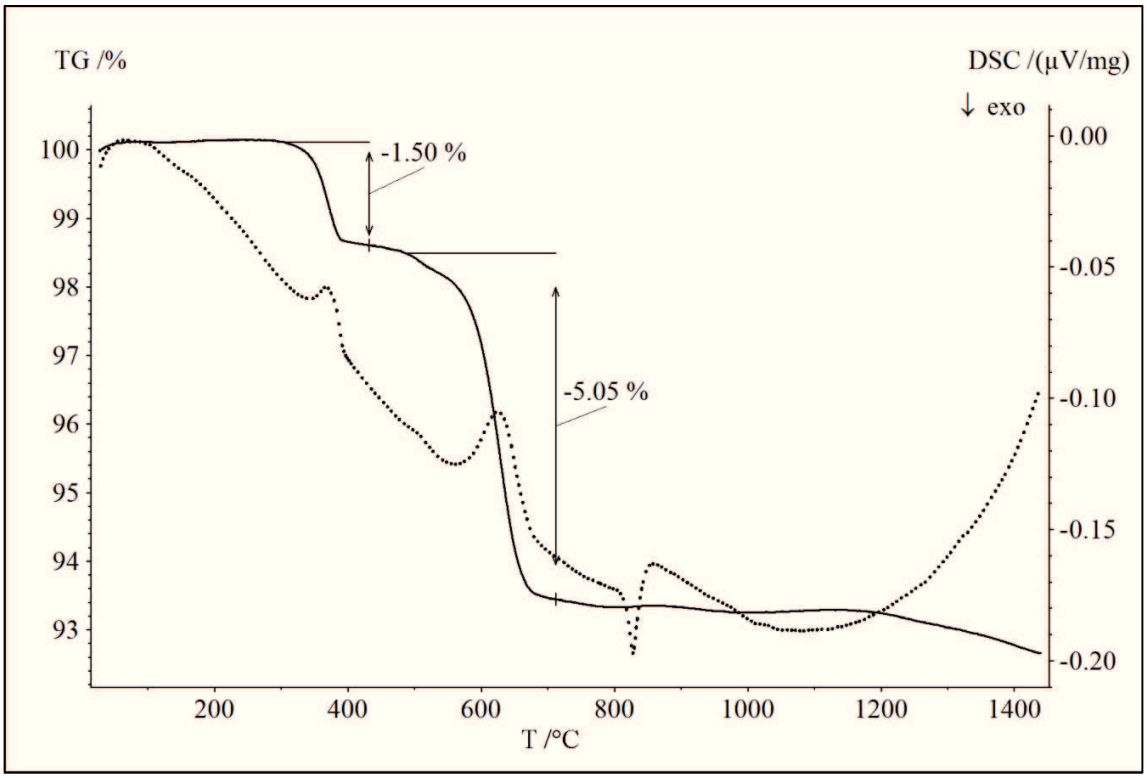

H3. Exp03 (enstatite-rich orthopyroxene): thermogravimetric curve of alteration products. Continuous line depict weight loss during heating and dotted line represent the differential scanning calorimetry curve. Beginning of weight loss at 530 °C shows serpentine and at 800 °C talc.

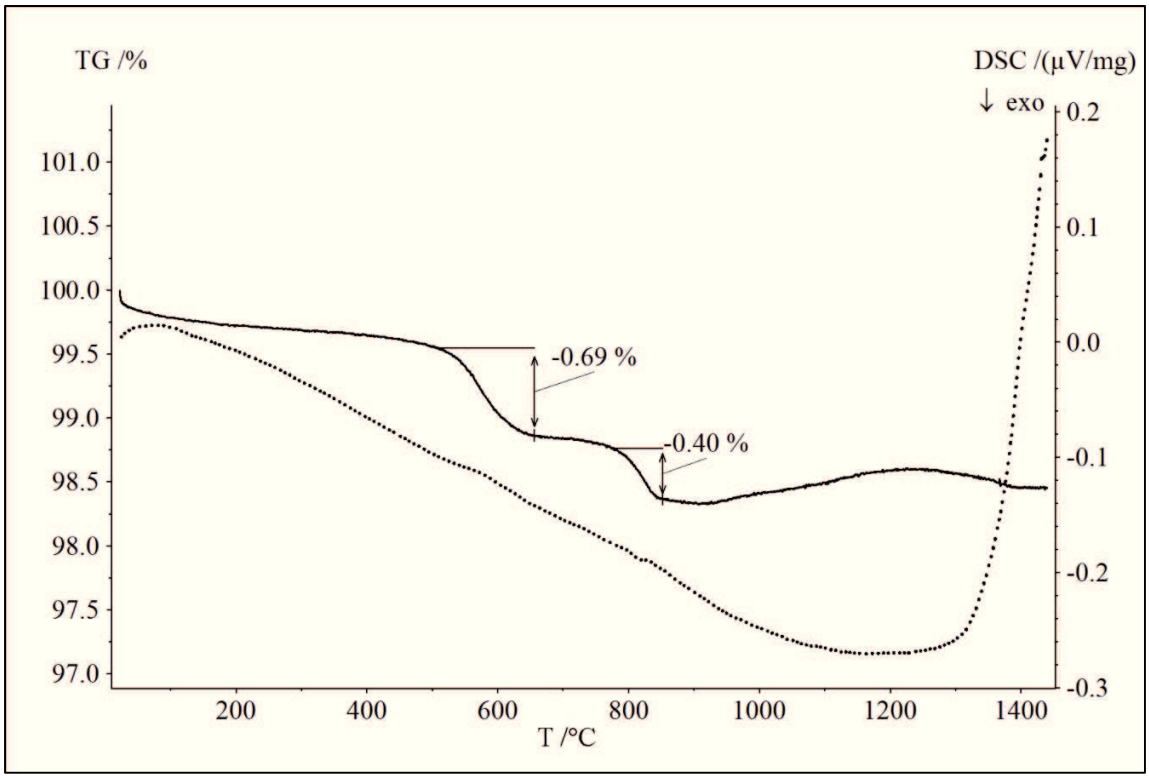

H4. Exp04 (harzburgite): thermogravimetric curve of alteration products. Continuous line depict weight loss during heating and dotted line represent the differential scanning calorimetry curve. Beginning of weight loss at 530 °C shows serpentine.

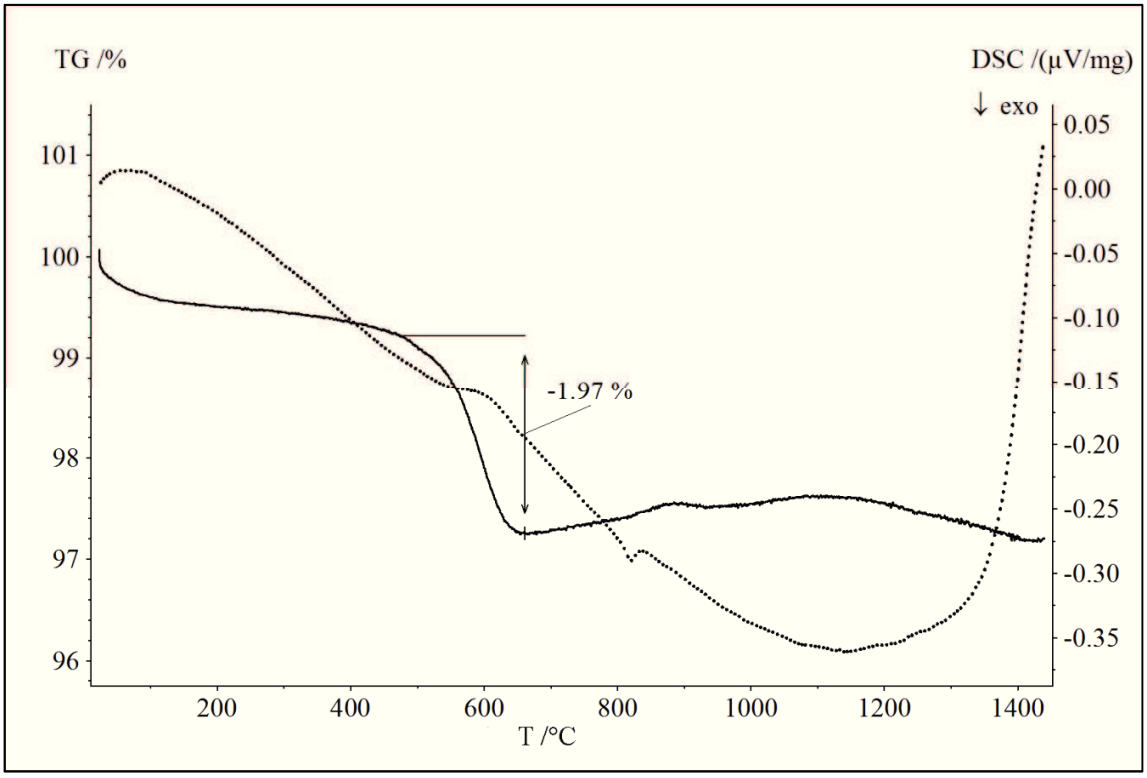

I. Hydrothermal experiments for rare earth elements

I.1 Introduction

Rare earth elements (REE) are a coherent group due to their equal ionic charges of 3+ and continuous decrease in ion radii (lanthanide contraction). Europium is usually reduced to Eu^{2+} in the specific redox environments of hydrothermal conditions below the seafloor (Sverjensky, 1984). Concentrations of hydrothermal vent fluids have been proposed to indicate interactions between seawater-derived hydrothermal solutions and specific ocean crust lithologies (e.g., Klinkhammer et al., 1995; Douville et al., 2002). Specifically, plagioclase – fluid exchange is believed by some workers to yield the light-REE enriched and heavy-REE depleted patterns with positive Eu anomalies typical for many mid-ocean ridge vent fluids. REE data for vent fluids were published by several authors from different oceanic hydrothermal areas (e.g., Michard et al., 1983; James et al., 1995; Klinkhammer et al., 1995; Douville et al., 2002; Craddock et al., 2010). High temperature chloride-dominated natural fluids show a positive europium anomaly whereas sulphate-rich fluids show no or even negative europium anomalies (Michard and Albarède, 1986; Michard, 1989). The chondrite-normalized distribution patterns of rare earth elements of fluids from different areas show significant differences: light-REE enriched, mid- and heavy-REE enriched and positive or negative europium anomalies. The rare earth element abundances in the hydrothermal fluids are often not directly related to the crustal rocks with which they interact. Based on laboratory studies, it has been proposed that fluids that reacted with specific rock types are not linked to the original host-rock REE distribution patterns (Bach and Irber, 1998; Möller, 2002; Allen and Seyfried, 2005), but influenced by fluid chemistry such as pH and ligand concentrations of chloride, fluoride and sulfate (Bach et al., 2003). Hydrothermal experiments under controlled conditions could help to examine relationships between REE distribution patterns, host rock compositions and fluid chemistry.

I.2 Experimental procedure

Experiments were conducted in an autoclave with a flexible gold reaction cell (described in chapter 2 “Experimental setup”). Despite the fact that all contact surfaces consist of unreactive gold or titanium, a blank experiment was carried out first. The

gold reaction cell was filled with 80 gram 0.001 mol/l ultrapure hydrochloric acid and reacted for 72 hours at 320 °C and 400 bar. In a second experiment an yttrium-rare-earth-element standard (Y-REE) with a concentration of 100 ng/l (ppt) was reacted for 72 hours at 320 °C and 400 bar to calculate the recovery rate and how the sampling procedure contributes to the total uncertainty of analytical results. Four aliquot fluid samples were taken after the experimental run-time. The first aliquot was to flush the titanium sample tube (discard). Subsequent fluids were taken through the titanium valve in a syringe, through the titanium valve in a sample tube and later directly out of the gold cell after cooling and opening the titanium closure of the gold cell to recognize potential contamination sources. The sampled fluids were analyzed by inductively coupled plasma mass spectrometry (ICPMS; see chapter 3 for details).

I.3 Results

The blank experiment yielded only negligible increase of REE concentrations in the fluids and indicated no significant contamination of the fluid through interaction with the reaction vessel and the titanium valve (results are presented in table 8.1). Notable is that the samples directly taken out of the gold cell contained the highest REE concentrations in the blank experiment.

Tab. 8.1. Dissolved REE in 0.001 mol/l HCl from a blank test and recovered concentrations of REE from a 100 ng/l REE standard after 72 hours reaction time at 320 °C and 400 bar. Concentrations are in ng/l.

	0.001 mol/l HCl					100 ng/l REE Standard				
Element	blank	discard	Ti-valve syr.	Ti-valve tube	gold cell	100 ppt Std	discard	Ti-valve syr.	Ti-valve tube	gold cell
Y89	0.25	0.55	0.68	0.81	1.15	107.2	6.96	6.56	6.87	6.94
La139	0.34	0.26	0.23	0.43	2.05	115.1	5.37	4.07	6.18	4.20
Ce140	0.22	0.68	0.83	0.95	1.67	113.2	6.62	5.69	7.02	7.10
Pr141	0.06	0.07	0.06	0.07	0.23	101.2	0.99	1.18	1.58	1.83
Nd146	0.06	0.17	0.24	0.39	1.86	95.1	2.31	2.02	2.18	2.35
Sm147	0.00	0.13	0.00	0.19	0.12	86.7	0.99	1.51	1.47	1.96
Eu153	0.02	0.11	0.04	0.00	0.17	88.9	7.39	9.92	10.89	10.32
Gd157	0.34	0.08	0.08	0.08	0.15	91.9	1.75	0.99	1.95	1.54
Tb159	0.01	0.02	0.02	0.02	0.03	90.3	1.02	1.09	1.12	1.06
Dy163	0.04	0.21	0.20	0.04	0.22	98.0	1.58	1.77	2.19	1.72
Ho165	0.02	0.01	0.02	0.02	0.03	92.8	1.14	1.21	1.30	1.46
Er166	0.03	0.15	0.00	0.08	0.11	89.4	1.38	1.54	1.86	1.70
Tm169	0.05	0.00	0.01	0.01	0.04	93.8	1.10	1.50	1.27	1.44
Yb172	0.13	0.09	0.05	0.09	0.08	89.9	1.48	1.47	1.69	1.60
Lu175	0.12	0.13	0.05	0.06	0.03	90.6	1.75	1.56	1.72	1.44

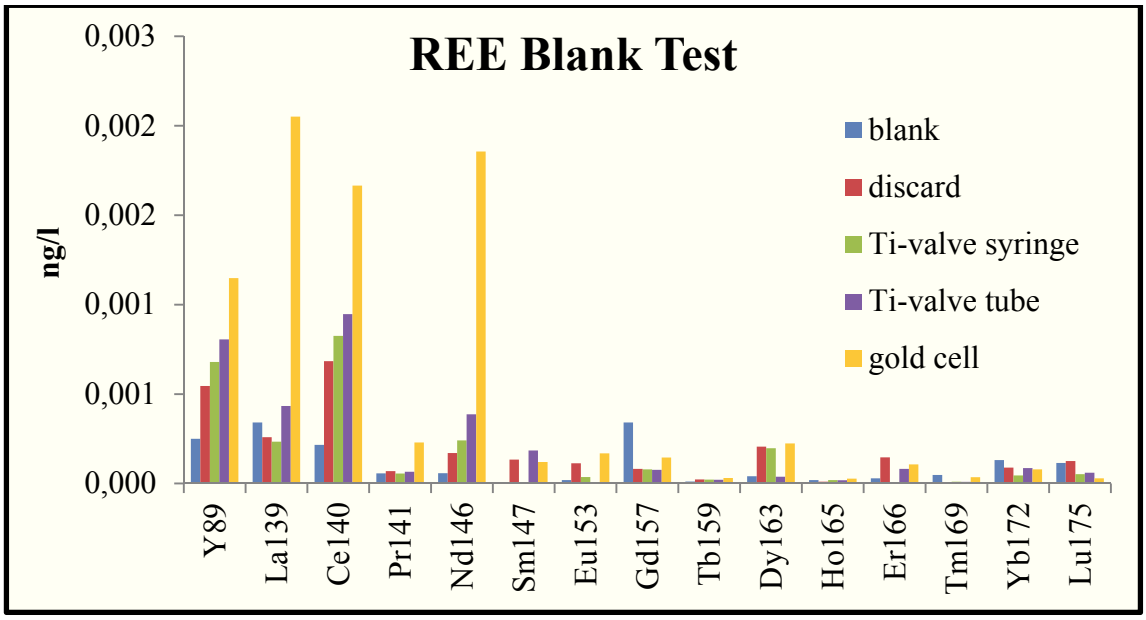

Fig. 8.1. Concentrations of the REE contamination in the blank experiment.

The ICPMS analyses of the 100 ng/l REE standard starting solution supplied a recovery rate better than 10 percent for most of the elements. The 100 ng/l REE standard solution was then reacted for 72 hours in the hydrothermal apparatus at 320 °C and 400 bar. The recovery rate after the experimental time dropped to less than 2 % for most REE elements independent of the sampling procedure.

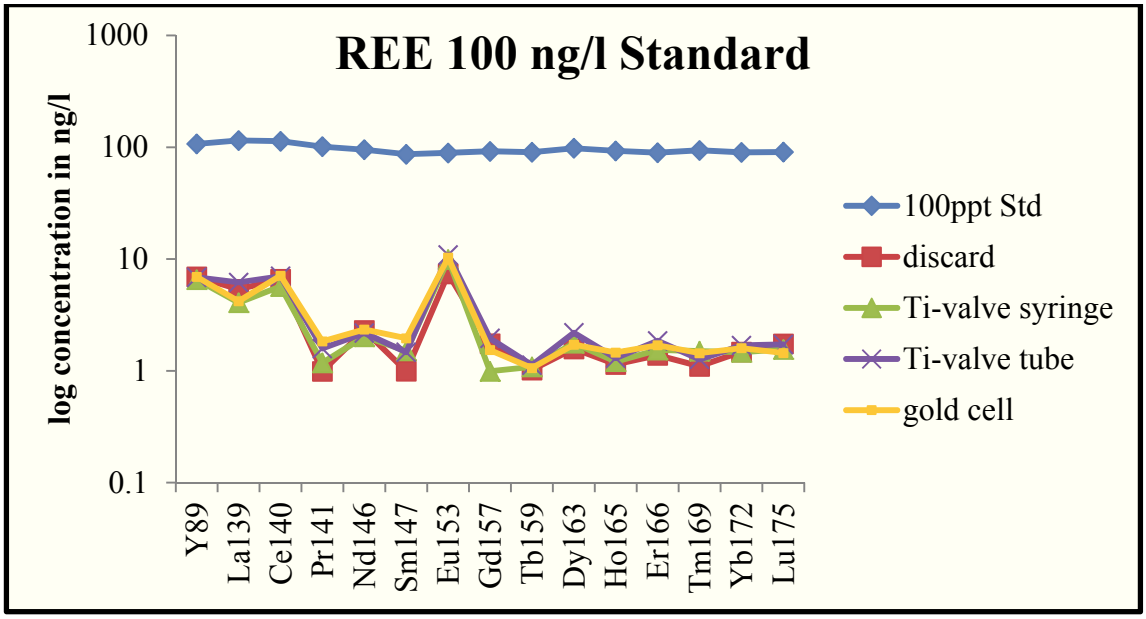

Fig. 8.2. Poor recoveries of REE after 72 hours reaction time in the hydrothermal apparatus. The blue line indicates the initial concentration of the REE standard. The loss of REE in the autoclave was significantly high.

The chondrite-normalized REE of the reacted standard solution indicated the expected natural distribution patterns but a slightly higher positive europium anomaly.

I.4 Discussion and conclusion

Experimental studies of REE distributions patterns in hydrothermal fluids within autoclaves have been executed to relate the resulting patterns to the reacted rock-REE-patterns (Menzies et al., 1979; Allen and Seyfried, 2005). The REE concentrations found in these experiments were significant greater than the starting fluid, indicating release of REEs from solid reactants into the dissolved phase. Our experimental test with a 100 ng/l REE standard solution delivered a recovery of less than 2 percent. This result indicted that the experimental set-up is not suitable for investigations of fluid-mineral partitioning, because the reaction cell walls are major scavengers for REEs. Besides the poor recovery for the REE, a positive europium anomaly was found, although only a pure REE standard solution without any rock was reacted. Wood (1990) suggested that for temperatures above 300 °C europium becomes more mobile compared to the other REE, which could causes the effect of an europium anomaly. This behavior of europium is likely due to the stability of aqueous chloro-complexes of Eu^{2+} ($EuCl^{3-}$, $EuCl_4^{2-}$), which will draw europium into solution preferentially, relative to the neighboring REE (Haas et al., 1995; Bach et al., 2003). The europium anomalies in experiments executed in an Au/Ti-autoclave controlled by the same physicochemical properties. The availability of free versus complexed ions will greatly influence the solid-fluid partitioning behavior of REE, whether the soldi is a rock or metal surfaces of a reaction cell. The recovery rate of REE using a flexible gold cell with attached Ti-valve was extremely low. This indicates that rare earth elements are surface reactive and bound strongly to contacting metal surfaces of gold and / or titanium of the test apparatus. Europium does so to a lesser extent, because the proportion of europium available as free ion in solution is smaller than that of the neighboring REEs. Our experimental setup is hence unsuitable for REE partitioning experiments. Allen and Seyfried (2005) used a similar apparatus but did not conduct blank test. It is possible that the results of that study are affected by the same type of partitioning of REE between solution and cell walls. It may well be that the pool of REE introduced in the reaction vial by adding rock powder may overwhelm the cell wall scavenging problem. Nevertheless, the blank test discussed here indicates that the utilized experimental setup

is not the method of choice for partitioning studies of extremely particle-reactive elements, such as REE and yttrium. Due to these discouraging results no further experiments regarding to REE distributions in hydrothermal fluids were carried out with our gold reaction cell autoclave system.

I.5 Outlook and conclusion

The contact surfaces in the reaction cell must be inert to the surface activity of the REE. Also, the slightly higher concentrations of REE in the blank experiment taken out directly from the gold cell may a memory effect of preceding experiments. Perhaps Teflon® material could be used, which mean the experiment temperatures are limited to about 250 °C. The use of this type of experimental setup in trace element partitioning studies has to be tested rigorously before rock-fluid interactions experiments are set-up, run, and evaluated.